THE UNIVERSITY of EDINBURGH

Particle Breakage Mechanics in Milling Operation

by

Li Ge Wang

A dissertation submitted in partial fulfilment
for the degree of
Doctor of Philosophy

in the

Institute for Infrastructure and Environment

School of Engineering

The University of Edinburgh

October 2016

Declaration of Authorship

This thesis entitled, "Particle breakage mechanics in milling operation" is submitted to the University of Edinburgh for the degree of Doctor of Philosophy. The research work described and reported in this thesis has been completed solely by Li-Ge Wang under the supervision of *Prof. Jin Y. Ooi*, *Prof. Jian-Fei Chen*, *Dr. Ian Butler* and *Dr. Jin Sun*. I confirm that:

- Where I have consulted the published work of others, this is always clearly attributed. Where I have quoted from the work of others, the source is given.
- I have acknowledged all main sources of help.
- Where the thesis is based on work done by myself jointed with others, I have made clear exactly what was done by others and what I have contributed myself. This applies in the area of material property measurement by indentation where work has been carried out jointly with Dr. Colin Hare. Also the population balance model (PBM) was carried out jointly with Dr. Xizhong Chen and Dr. Carlos Labra.

Publications based on this thesis:

L.G. Wang, J.F. Chen and J.Y. Ooi. A breakage model of particulate solids under impact loading, in preparation.

L.G. Wang, J.F. Chen and J.Y. Ooi. Assessment of particle breakage models under normal and oblique impact, in preparation.

L.G. Wang, J.F. Chen and J.Y. Ooi. Measurement of Young's modulus by nanoindentation, compression and principal curvature characterisation, in preparation.

L.G. Wang, J.Y. Ooi, A. Janda and C. Labra. Analysis of particle breakage under impact milling using a bonded discrete element method. PARTICLES 2015.

L.G. Wang, J.Y. Ooi and I. Butler. Interpretation of particle breakage under compression using X-ray computed tomography and digital image correlation. Procedia Engineering 102 2015, 240-248.

The following reports have been made:

C. Labra, J.Y. Ooi, J. Sun, L.G. Wang and J.F. Chen, IFPRI Grindability Project of Modelling, measurement and mill fingerprinting, Annual Report, 2013.

J.Y. Ooi, L.G. Wang, J. Sun, C. Hare and J.F. Chen, IFPRI Grindability Project of Modelling, measurement and mill fingerprinting, Annual Report, 2014.

C. Hare, L.G. Wang and J.Y. Ooi, IFPRI Project of Characterisation of particle grindability by indentation and impact, Final Report, 2014.

J.Y. Ooi, L.G. Wang, J.F. Chen and J. Sun, IFPRI Grindability Project of Modelling, measurement and mill fingerprinting, Annual Report, 2015.

Signed: _____

Dated: _____

Lay summary

Milling is a common unit operation in industry for intentional size reduction, which is widely recognized to be energy-intensive and highly inefficient. Despite many attempts to interpret particle breakage during a milling process, the grindability of a material in a milling operation remains aloof and the mechanisms of particle breakage are still poorly understood. Hence the optimisation and refinement in the design and operation of milling are in great need of an improved scientific understanding of the complex failure mechanisms.

This thesis aims to provide an in-depth understanding of particle breakage associated with stressing events that occur during milling. A hybrid of experimental, theoretical and numerical methods has been adopted to elucidate the particle breakage mechanics. The material grindability was first investigated by single particle loading experiments, including indentation tests, single particle impact tests and in-situ loading test under X-ray micro-computed tomography. It was found from the zeolite particle impact test that tangential component velocity plays an increasingly important role in particle breakage with increasing impact velocity.

A new particle breakage model was proposed assuming that the subsurface lateral crack accounts for the chipping mechanism. In particular, the contribution of tangential component velocity was incorporated in the new model by mobilizing the dynamic friction coefficient. Milling experiments were carried out using the UPZ100 impact pin mill to measure the comminution characteristics of the test solids, which provides the basis for the validation of numerical results. A DEM (Discrete Element Method) simulation of single particle breakage subject to impact loading was conducted to evaluate the breakage propensity which is then compared to experimental results. A recently developed new bonded contact model by Brown et al. (2014) was utilized which is based on Timoshenko beam theory considering axial, shear and bending behaviour of the bond. The upscaling procedure from laboratory scale to industrial process scale was achieved using population balance model (PBM). The DEM simulation of particle dynamics with emphasis on the impact energy spectrum was presented which sheds further insights into the coupling of PBM and DEM.

Abstract

Milling is a common unit operation in industry for the purpose of intentional size reduction. Considerable amount of energy is consumed during a grinding process and much of the energy is dissipated as heat and sound, which often makes grinding into an energy-intensive and highly inefficient operation. Despite many attempts to interpret particle breakage during a milling process, the grindability of a material in a milling operation remains aloof and the mechanisms of particle breakage are still poorly understood. Hence the optimisation and refinement in the design and operation of milling are in great need of an improved scientific understanding of the complex failure mechanisms.

This thesis aims to provide an in-depth understanding of particle breakage associated with stressing events that occur during milling. A hybrid of experimental, theoretical and numerical methods has been adopted to elucidate the particle breakage mechanics. This study covers from single particle damage at micro-scale to bulk comminution during the whole milling process. The mechanical properties of two selected materials, i.e. alumina and zeolite were measured by indentation techniques. The breakage test of zeolite granules subjected to impact loading was carried out and it was found that tangential component velocity plays an increasingly important role in particle breakage with increasing impact velocity. Besides, single particle breakage via in-situ loading was conducted under X-ray microcomputed tomography (μCT) to study the microstructure of selected particles, visualize the progressive failure process and evaluate the progressive failure using the technique of digital image correlation (DIC).

A new particle breakage model was proposed deploying a mechanical approach assuming that the subsurface lateral crack accounts for chipping mechanism. Considering the limitation of existing models in predicting breakage under oblique impact and the significance of tangential component velocity identified from experiment, the effect of impact angle is considered in the developed breakage model, which enables the contribution of the normal and tangential velocity component to be rationalized. The assessment of breakage models including chipping and fragmentation under oblique impact suggests that the equivalent normal velocity proposed in the new

model is able to give close prediction with experimental results sourced from the public literature.

Milling experiments were performed using the UPZ100 impact pin mill (courtesy by Hosokawa Micron Ltd. UK) to measure the comminution characteristics of the test solids. Several parameters were used to evaluate the milling performance including product size distribution, relative size span, grinding energy and size reduction ratio etc. The collective data from impact pin mill provides the basis for the validation of numerical simulation results.

The Discrete Element Method (DEM) is first used to model single particle breakage subject to normal impact loading using a bonded contact model. A validation of the bonded contact model was conducted where the disparity with the experimental results is discussed. A parametric study of the most significant parameters e.g. bond Young's modulus, the mean tensile bond strength, the coefficient of variation of the strength and particle & particle restitution coefficient in the DEM contact model was carried out to gain a further understanding of the effect of input parameters on the single particle breakage behavior.

The upscaling from laboratory scale (single particle impact test) to industrial process scale (impact pin mill) is achieved using Population Balance Modelling (PBM). Two important functions in PBM, the selection function and breakage function are discussed based on the single particle impact from both experimental and numerical methods. An example of predicting product size reduction via PBM was given and compared to the milling results from impact pin mill. Finally, the DEM simulation of particle dynamics with emphasis on the impact energy distribution was presented and discussed, which sheds further insights into the coupling of PBM and DEM.

Acknowledgements

I would like to express my deepest gratitude to my supervisor, Prof. Jin Y. Ooi, for the continuous support during my PhD research in the University of Edinburgh. It would be insurmountable to complete this dissertation without his remarkable supervision, guidance, encouragement and generosity. Hardly could I imagine a better supervisor who would appear more ready to help steady the ship. His influence on me is far-reaching both professionally and personally.

I am extremely grateful to Prof. Jian-Fei Chen for his incredible supervision, inspiration and moral support during the early days of my PhD. I am also very thankful to Dr. Ian Butler and Dr. Jin Sun for their excellent supervision, motivation and support throughout my PhD, to whom particular thanks are due. Great debts are owed to so many people who have generously assisted me along this exciting journey. I am very grateful to Dr. Tannaz Pak and Ms. Zeynep Karatza for their help in X-ray imaging and digital image correlation; Dr. Zhijun Zhong, Mr. Derek Jardine and Mr. Jim Hutcheson for their experimental assistance. I would like to thank Dr. Carlos Labra, Dr. J.P. Morrissey and Dr. Xizhong Chen incredibly for their many help and expertise in DEM coding. Special thanks come to Dr. Alvaro Janda, whose friendship, support and patience are overwhelming during my PhD. A very sincere thanks is due to IT support for their technique to increase the storage and solve tricky problems.

I would like to express sincere gratitude to people by whatever means of help outwith Edinburgh, Dr. Iain Crosley, Mr Stewart Bryan and other staff members (to name but a few) in Hosokawa Micron Ltd for their generosity of allowing me to conduct the impact milling tests; Prof. Mojtaba Ghadiri in the University of Leeds for the courtesy of single particle impact tester; Dr. Colin Hare in the University of Surrey for collaborating in nanoidentation tests and many helpful discussions; Prof. Cino Viggiani and Dr. Edward Ando in Universite de Grenoble for their great help in X-ray CT and digital image correlation; Prof. Luis Marcelo Tavares in Laboratório de Tecnologia Mineral for his expertise in population balance model.

I feel so honoured to spend four years with all my friends in the University of Edinburgh in particular Dr. Yi Tao, Dr. Adele Nyekachi, Dr. Colin Brett, Dr. Payam Khazaeinejad, Dr. Chuan Hong, Dr. Jinhan Xie, Dr. Rongxin Zhou, Mr. Xiaobo Cheng, Mr. Ofonime Harry. Needless to say the unforgettable moments with Dr. Giuseppe Filippone, Dr. Shane Burns, Mr. Tim Najuch and Mr. Joel Keishing etc in playing football and the unmissable games in Robins Nest.

I am also very thankful for the Scholarship provided by International Fine Particle Research Institute (IFPRI), China Scholarship Council (CSC) and the University of Edinburgh (UoE).

Last but not least I would like to thank my parents and wife, Yazhi Yu for their unwavering support, unconditional love and endless patience. Otherwise, none of this would have been possible.

Table of Content

List of Figures

List of Tables

Abbreviations

API	Application Programming Interface
BPM	Bonded Particle Model
CC	Cross Correlation
CoV	Coefficient of Variation
DEM	Discrete Element Method
DIC	Digital Image Correlation
GADO	Gadolinium Oxysulfide
LTINV	Linear Time-Invariant
LTVAR	Linear Time-Variant
PSD	Particle Size Distribution
PDF	Particle Distribution Function
PBM	Population Balance Model
QP	Quadratic Programming
RPM	Revolution Per Minute
RRB	Rosin Rammler Bennett
SEM	Scanning Electron Microscopy
SRR	Size Reduction Ratio
SSD	Sum Squared Difference
SSA	Specific Surface Area
SSE	Sum of Squared Error
TBBM	Timoshenko Beam Bond Model
TOT	Time of Transition
UFLC	Ultrafast Load Cell
XμCT	X-Ray Microcomputed Tomography

Symbols

a	Impression radius, mm
A	Area, mm^2
$b_{i,j}$	Specific breakage rate, -
BI	Brittleness index, $m^{-0.5}$
c	Length from centre of indent to tips of radial cracks, mm
C_l	Lateral crack length, mm
C_r	Radial crack length, mm
d_p	Particle diameter, mm
D	Characteristic particle size, mm
D_f	Displacement at fracture, mm
D'	Particle size when $P(D)$=1, mm
D_a	Arithmetic mean particle size, mm
$D_{50,F}$	Median size of feed particle, mm
$D_{50,P}$	Median size of product particle, mm
e	Coefficient of restitution, -
E	Young's modulus, Pa
E_B	Stressing energy before breakage, J
E_{eff}	Effective Young's modulus, Pa
E_s	Young's modulus of sample, Pa
E_i	Young's modulus of indenter, Pa
E^*	Effective modulus of elasticity
E_m	Specific breakage energy, $J\ kg^{-1}$
E_{min}	Minimum specific impact energy to yield particle breakage, $J\ kg^{-1}$

E_{max}	Maximum specific impact energy to break all particle, J kg^{-1}
E_{m50}	Median fracture energy log-normal distribution, J kg^{-1}
E_{kin}	Kinectic energy, J kg^{-1}
E_{frac}	Fracture energy, J kg^{-1}
$E_{m\infty}$	Residual fracture energy, J kg^{-1}
$f(D)$	Density distribution function, -
$f_{Mat.}$	Material parameter, kg J^{-1} m^{-1}
F	Applied force, N
F_f	Fracture load, N
F_n	Normal impact loading force, N
F_t	Tangential impact loading force, N
∇F	Gradient of implicit surface, -
G	Shear modulus, Pa
h	Displacement, mm
h_f	Final depth of indenter, mm
h_c	Vertical distance by penetration of indenter, mm
h_s	Vertical displacement of surface, mm
H	Hardness, MPa
$H(F)$	The hessian of implicit surface
k_1	Principal curvature, mm^{-1}
k_2	Principal curvature, mm^{-1}
k_3	Normal curvature, mm^{-1}
K_G	Gaussian curvature, mm^{-1}
K_M	Mean curvature, mm^{-1}

K	Stiffness, Nm^{-1}
K_c	Fracture toughness, Pa $m^{0.5}$
K_{IC}	Stress intensity factor, Pa $m^{0.5}$
l	Initial particle size, mm
l_i	Initial flaw size, mm
L	Length, m
m	Mass of particle, g
M	Moment, Nm
M	The broken mass of feed particle, g
$\bar{M}$	Fraction of broken impacted particles, %
N	Random number, -
N_0	Unbroken particles number, -
P	Indent force, N
$P(D)$	Particle size distribution, %
P_y	Yield pressure, Pa
r_c	Lateral crack merger, mm
R	Particle radius, mm
R_1	Radius of principal curvature, mm
R_2	Radius of principal curvature, mm
R^*	Effective radius, mm
S	Mean bond strength, Pa
S_i	Specific breakage rate, -
t	Time, s
t_{10}	percentage passing $1/10^{th}$ of the original mean size, mm

Δt	Time step, s
v	Impact velocity, m s^{-1}
v_d	Deformation velocity, m s^{-1}
v_{el}	Elastic wave velocity, m s^{-1}
v_{eq}	Equivalent normal velocity, m s^{-1}
v_{frac}	Crack propagation velocity, m s^{-1}
v_t	Tangential component velocity, m s^{-1}
v_{te}	Equivalent tangential component velocity, m s^{-1}
v_{50}	Median velocity breaking 50% of the particle population, m s^{-1}
V	Removal volume, mm^3
S	Breakage probability, -
S_v	Volume-specific surface area, m^{-1}
V_{det}	Detached volume due to impact, mm^3
W	Grinding energy, kWh/t
W_c	Fracture energy, J
W_i	Bond's work index, kWh/t
$W_{m,kin}$	Mass specific impact kinetic energy, J kg^{-1}
W_V	Volume-specific elastic strain energy, J m^{-3}
x	Normalised particle size, -
x_p	Feed size before grinding, mm
x_F	Product size after grinding, mm
ξ	Breakage ratio, -
ξ_i	Initial breakage ratio, -
ξ_f	Final breakage ratio, -

σ	Standard deviation, -
υ	Poisson ratio, -
I	X-ray intensity, cd/m^2
μ	Coefficient of friction, -
$\mu(x)$	Attenuation coefficient of the material, -
ε	Extent of breakage, -
ε_i	Initial breakage extent, -
ε_f	Final breakage extent, -
Φ	Timoshenko shear coefficient, -
γ	Transformation matrix, -
ς	Coefficient of variation of strength, Pa
η	Bond radius multiplier, -
w_i	Mass fraction, -
ρ	Particle density, kg m^{-3}
Γ	Specific fracture surface, J m^{-2}

Dedication

This thesis is dedicated to my PARENTS and my WIFE.

For their unconditional love, support, company and encouragement.

Chapter 1

Introduction

1.1 General background

Milling is a very common unit operation in industry for the purpose of desired size reduction. Breakage in a milling operation results from particle-particle and particle-equipment interaction, and is related to the mechanical properties of particle and the loading cases (Ghadiri and Zhang, 2002; Vogel and Peukert, 2003). Numerous comminution techniques such as air classifier mill and impact mill (Vogel and Peukert, 2004 and 2005) have been developed for the purpose of intentional size reduction. Considerable amount of energy is consumed during the grinding process and much of the energy is dissipated as heat and sound, which makes grinding as an energy-intensive and inefficient operation. Optimization of milling operations is therefore critical to minimize the energy footprint of many industrial processes. Hence in-depth understanding of particle breakage in milling operation is essential in order to achieve optimal size reduction.

Despite many attempts to interpret particle breakage during a milling process (Rumpf, 1973; Vogel and Peukert, 2005; Kwan et al., 2004), the grindability of a material in a milling operation remains aloof and the mechanism and prediction of particle breakage are still poorly understood. Hence the optimisation and refinement in the design and operation of milling are in great need of an improved scientific understanding of the complex failure mechanisms. This PhD is part of a six-year project entitled ‘Milling and Material Grindability: Measuring, Modelling and Fingerprinting’, which is supported by International Fine Particle Research Institute (IFPRI). The PhD project aims to provide in-depth understanding of particle breakage in stressing events which commonly occur during a milling operation. This study covers from single particle damage at micro-scale to bulk particles breakage during the whole milling process, both by means of experimental validation and computational modelling. This will provide the fundamental scientific basis for developing appropriate grindability tests capable of analysing particle breakage subjected to particle impact, compression,

shear and abrasion etc. pertaining to a milling process, which in turn will provide the basis for an improved particle breakage model calibrated against defined grindability.

1.2 From material grindability to milling characteristics

As the increasing demand to grind more particulate materials, the selection of most suitable grinding machine becomes even more complicated under the operating conditions (Yokoyama and Inoue, 2007). A great amount of work has been done on measuring and characterizing the grindability of particulate materials. Examples include single particle breakage measurement resulting from wear, impact and compression (Zhang and Ghadiri, 2002; Lecoq et al., 2012) and bulk measurements on attrition, shear and compression (Ghadiri et al., 2000). The prior work has provided some scientific insights relating milling characteristics to material properties and breakage mechanism under different loading conditions. Nevertheless, it is still unclear how these loading conditions relate to what actually happens in a typical milling operation and how to characterize particle breakage in the prevailing stressing events in a milling operation. There is thus a need to evaluate the appropriateness of these tests by characterizing the prevailing stressing events and establishing material grindability in the context of these stressing events. The material grindability requires a detailed study of the fundamental fracture and breakage mechanisms of individual particles under different loading regimes, and how the mechanisms relate to the mechanical properties and the final size distribution. The Discrete Element Method (DEM) has been a popular numerical approach to model the particle dynamics in a diversity of milling operations (Morrison and Cleary, 2004; Tuzcu and Rajamani, 2011). The contribution of DEM regarding comminution has been highlighted for understanding comminution fundamentals and providing information for the design, optimization and operation of comminution devices (Weerasekara et al., 2013). Although DEM can provide informative insights into the particle dynamics during a milling process, a complete and reasonable solution is still lacking because of the following key issues:

1. Currently, there is no robust breakage contact model at particle level which has been calibrated for a milling material. Published literature appears to be mainly based on empirical models involving replacing a mother particle with several progeny particles when a breakage is incurred without a robust model calibration (Tsoungui et al., 1999 and Kalman et al., 2009).

2. A huge complexity of milling operation has to be considered due to the highly heterogeneous environment in industrial mill including feed particle with wide size and shape characterisation, heat transfer and disparate local stress-strains states etc.

3. The validation in the published literature and model calibration is generally scarce. As noted by Chung and Ooi (2011), verification and validation of DEM simulations are critical to form a predictive capacity of a computational model for the intended usage of size reduction.

4. A multiscale methodology is needed to address a full scale industrial milling operation by upscaling the knowledge obtained from a smaller scale to milling. The population balance models (PBM) have been extensively used to predict the milling size distribution (King and Bourgeois, 1993). Impact energy based PBM coupled with DEM has been used to predict product size distribution (Carvalho and Tavares, 2009).

1.3 Objectives and scope of this research

This project aims to provide a fundamental understanding of the mechanism(s) for particle fracture in a milling process and develop a particle breakage model based on the findings from the experimental and theoretical studies. The material grindability test will be carried out to measure the comminution characteristics of the particulates which, when coupled with the computational modelling work to characterise the milling function, will evaluate the milling performance measures including product size distribution, breakage kernels for scale-up modelling such as population balance model of the mill. Bulk scale and particle scale experiments of different categories are conducted considering different mechanical features of materials, with the help of numerous measuring techniques. The key measurable objectives include:

1. Conduct material characterisation experiments (indentation test, compression test and impact test) on the test solids to define the relevant mechanical properties and to observe the breakage pattern in corresponding loading event.

2. Conduct in-situ X-ray μCT experiments to envisage the microstructure of selected particles, visualize the progressive failure process and evaluate the progressive failure using the technique of digital image correlation (DIC).

3. Develop a particle breakage model from a mechanistic understanding and present a systematic assessment of particle breakage models with the experimental data sourced from the published literature.

4. Conduct milling experiments at Hosokawa Ltd. (UK) to examine the material grindability during stressing events which together with the particle dynamics from DEM will form a basis to hypothesize the dominant particle loading mechanisms.

5. Develop an appropriate numerical approach such as the bonded discrete element method (DEM) to study single particle breakage subjected to impact loading, leading to an improved particle breakage model.

6. Develop the material functions, i.e. breakage function and selection function, which could be used in PBM-DEM coupling capable of characterizing particle breakage subjected to the dominant loading events identified within a milling operation.

In this work, the overarching goal is to develop a particle breakage model through a fundamental mechanics approach based on an improved understanding of particle comminution behaviour from a set of tests pertinent to milling operation. The key features of breakage mechanism in a milling operation will be deeply investigated and thus the characterization of mechanical property and prediction of milling performance can be systematically and qualitatively described.

1.4 Structure of dissertation

The thesis is divided into nine chapters. A brief outline of each chapter is stated below:

Chapter 1 illustrates the background, objective and scope of this research. The structure of the thesis is summarised.

Chapter 2 gives a literature review directly pertinent to this research. It starts with a brief introduction of comminution in milling operations. Then particle breakage is focused from three perspectives, with regards to experimental, theoretical and numerical studies. As the overarching goal of this thesis is to develop a particle

breakage model subject to loading through a fundamental mechanics approach, the theoretical studies of particle breakage will be highlighted and discussed in details.

Chapter 3 presents the selected materials and the measured response of materials from the selections of two laboratory devices. The material properties and loading response of selected particles are investigated via indentation and impact. These include indentation technology to determine the mechanical properties of selected materials and single particle impact device to measure the breakage propensity and the effects of impact velocities and impact angles.

Chapter 4 investigates single particle breakage via in-situ progressive loading under X-ray μCT. The synergy of X-ray μCT and further analysis using digital image correlation (DIC) provides new understanding of the initiation, crack propagation and damage accumulation leading to particle breakage. The breakage pattern observed under compression is thus linked with the chipping and fragmentation mechanism under impact loading. Furthermore, the influence of principal curvature on Young's modulus determination is examined.

Chapter 5 describes the distinctive breakage patterns of particle subjected to impact loading. The indentation failure process is then given which provides the physical hypothesis for breakage model development. Existing particle breakage models are summarized and classified into five categories in terms of particle comminution. The theoretical breakage models are highlighted and assessed against the experimental data from single particle impact test. The deficiencies identified from model assessment indicates that a more general breakage model is required. A new breakage model for particulate solids is proposed based on a mechanical approach, which takes the contribution of tangential component velocity into account. The proposed model as well as existing breakage models is assessed with literature data under both normal and oblique impact loading.

Chapter 6 experimentally investigates the material grindability through an impact pin mill. The influences of operational parameters and the predictive analysis of milling

output are examined. The effect of rotary speed and feed rate is examined whilst several grindability parameters are used to characterise the impact pin milling performance.

Chapter 7 presents the numerical results of single particle breakage subject to impact loading through Discrete Element Method (DEM). A bonded contact model (Brown et al., 2014) based on Timoshenko beam theory considering axial, shear and bending behaviour is utilized. The breakage behaviour of particle from chipping to fragmentation was investigated under low, medium and high impact velocities. Five factors including breakage pattern, contact force, contact evolution, failure mode, damage ratio and breakage ratio are used to characterise the impact breakage. The bonded DEM simulation results are validated against experimental results with the same breakage criterion where the disparity is discussed. A parametric study of the most significant model parameters is carried out.

Chapter 8 demonstrates the mobilisation of population balance model (PBM) by upscaling the information from lab scale (single particle impact test) to industrial scale (impact pin mill). Two important functions in PBM, namely the selection function and breakage function are discussed with regard to how to upscale the information from single particle impact test. An example of PBM to predict product size reduction is given based on the grindability results from impact pin mill in Chapter 6. Then DEM simulation of particle dynamics and particle breakage in the impact pin mill is carried out to shed some useful lights into the coupling of PBM and DEM.

Chapter 9 draws the main conclusions emerging from this thesis and highlights the recommendation for future research.

Chapter 2

Literature review

2.1 Introduction

Comminution is one of the oldest mechanical unit operations to achieve the intentional size reduction of solid materials by means of crushing, grinding, cutting or other processes (Kanda and Kotake, 2007). In a milling operation, comminution is categorized into several grinding mills depending on the fineness of the ground product and the intrinsic material properties. The grinding mechanisms can be divided to impaction, shearing, compression and attrition, which are synergic in most grinding mills. It was reported that about 3% of the global electrical energy was consumed for grinding in 1976 (Fuerstenau and Abouzeid, 2002). However, it was found that comminution is notoriously energy inefficient with less than 1% of the total energy converted into the fracture process (Alvarado et al., 1998). An example of energy distribution in a ball mill is depicted in Figure 2.1. It demonstrates that 85% of energy is dissipated as heat loss whereas the energy efficiency is in the order of 1%.

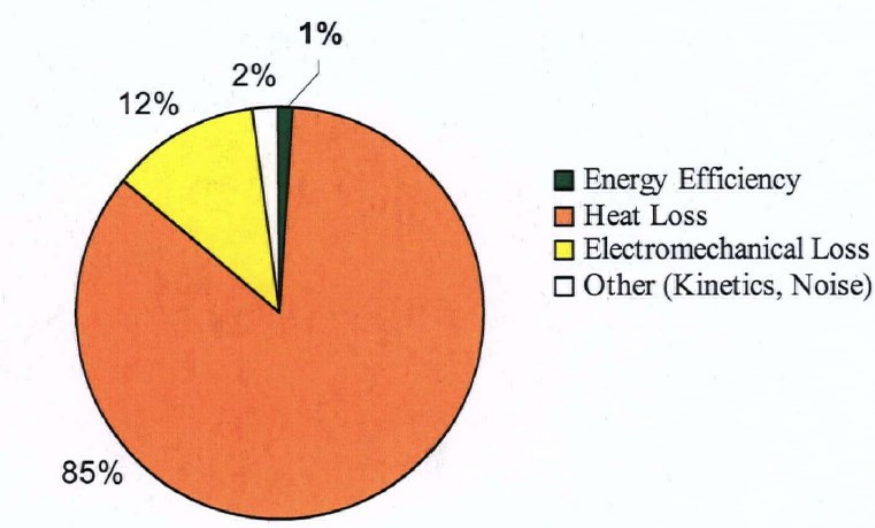

Figure 2.1 Energy distribution during comminution process of a ball mill (After Sadrai, 2007)

Considering the remarkably low energy efficiency in a milling operation, optimisation and refinement in the design and operation of milling are in great need of an improved scientific understanding of complex mechanics involved.

The objective of this chapter is to present a literature review with regard to particle breakage under stressing events pertaining to a milling operation. This review is not intended to be exhaustive and comprehensive, but concentrates upon the work conducted in this thesis. This review consists of three main parts: experimental study of particle breakage, particle breakage models in comminution and DEM modelling of particle breakage. Firstly, an overview of mechanical behaviours of particles subjected to compression, impact loading and milling process is presented in Section 2.2, which covers the breakage from particle level to bulk level in the milling operation. Secondly, existing particle breakage models are reviewed and classified into five categories in Section 2.3. As mentioned in Chapter 1, the overarching goal of this thesis is to develop a particle breakage model through a fundamental mechanics approach. Bearing this in mind, the review of existing breakage models regarding comminution will be the main body of this Chapter. Finally, a brief review of Discrete Element Method (DEM) is given and its application in milling prediction is presented in Section 2.4.

2.2 Experimental study of particle breakage

2.2.1 Compression

In a grinding process, a profound understanding of the whole operation requires a good knowledge of every particle component contributing to the overall comminution results. Therefore, compression test is usually adopted to characterize breakage of single particle subjected to compressive loading. Three types of material behavior, i.e. elastic deformation, brittle deformation and ductile deformation can be distinguished based on macroscopic stress-strain relations as shown in Figure 2.2.

In Figure 2.2 (a), particle deforms elastically when the strain is increased. The stress is linearly proportional to the deformation and is characterized by the Young's modulus (E). This process is reversible and particle could revert to original shape when the stress is released. In Figure 2.2 (b), particle fragments into smaller pieces after the elastic deformation with a certain stress reached. This stress is called fracture stress and the material is defined brittle. In Figure 2.2 (c), when the applied stress is beyond a critical point (yield strength), particle starts to behave plastically (the stress-strain curve is no longer linear) and permanent deformation is incurred. Particle with this type of deformation is defined ductile or plastic material. It should be noted that brittle materials

will exhibit ductile behaviour when a critical particle size is reached. More information about the transition from brittle to ductile behaviour can be referred in the literature (Van Veen, 2003).

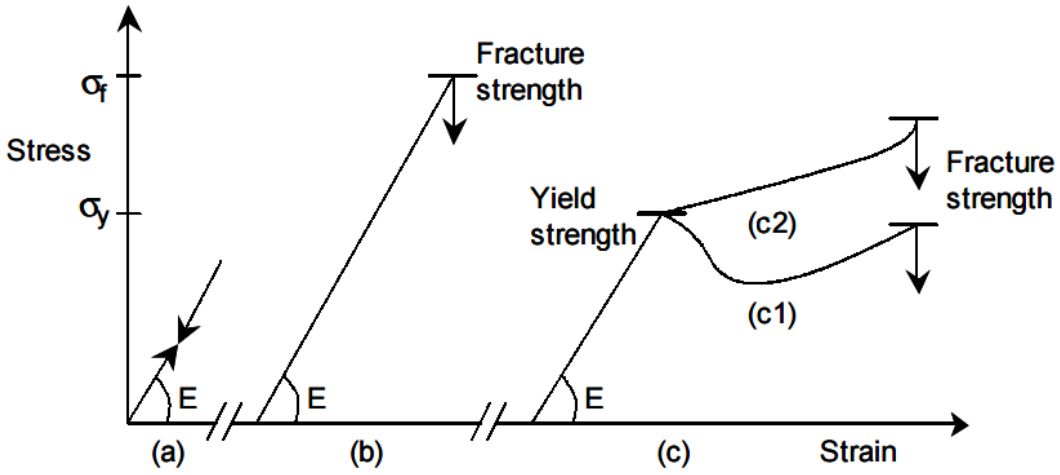

Figure 2.2 Macroscopic stress-strain relations

a. Elastic deformation b. Brittle behaviour c. Ductile behaviour (c1. normal plastic flow; c2. strain hardening) (Adapted from Van Veen, 2003)

2.2.1.1 Compressive strength characterization

Strength is a critical characterization in terms of the mechanical property since every particle experiencing collision, attrition, disintegration, and fragment is related to its mechanical stress. Also, the ultimate size distribution of particles is highly dependent on the strength distribution of the raw material. Basically, strength for particles can be characterized by four terms: crushing force, breakage energy, breakage stress, and specific energy. Each kind of term can be described by its corresponding strength distribution function.

In order to characterize the material and mechanical properties, many researchers carried out compression test to evaluate the compressive strength of single particles in a wide variety of materials. Sikong et al. (1990) tested brittle minerals and coals at micron level and showed that strength of the particles varies with particle size. Shipway and Hutchings (1993) studied the stress distribution of brittle spheres subject to uniaxial compression. It was found that failure initiates on the surface rather than internally at a critical value of tensile stress with high compliance. Danjo et al. (1994) tested 140

particles individually and showed that the crushing strength diminished exponentially with an increase of the particle size up to 500 μm. Breakage behaviors of Zeolite 4A and Al_2O_3 granules which are dominant elastic-plastic subject to compression were examined respectively (Muller and Tomas, 2012; Muller et al., 2013). The factors including particle size and moisture content were taken into account to showcase the influence on particulate breakage behavior. Aman et al. (2010) carried out the investigation of breakage probability of irregularly shaped particles and proposed that the force distribution could be transformed into energy distribution and vice versa.

2.2.1.2 Specific breakage energy

The specific breakage energy E_m refers to the mass-based stressing energy stored per mass unit until fracture and it is given by Sikong et al. (1990):

$$E_m = \frac{D_f F_f}{2m} \tag{2.1}$$

where E_m is the specific breakage energy, F_f is the fracture load and D_f is the displacement at fracture. m is the mass of the particle assumed to be a sphere. Muller and Tomas (2012) presented another equation of specific breakage energy based on stressing energy before breakage (E_B) by the integration of force with respect to the corresponding displacement in the force-displacement curve.

$$E_m = \frac{E_B}{m_p} = \frac{1}{m_p}\int_{s=0}^{s=s_B} F ds \tag{2.2}$$

Based on the dimensional analysis, a similar breakage mode can be derived from Rumpf (1973) that the product of elastically stored energy per unit volume W_v and the original particle size x is constant.

$$W_V * x = const. \tag{2.3}$$

According to $m_p = \rho * V_p$, where ρ denotes the density of the particle and V_p the volume for the single particle. Substituting Eq. (2.3) into Eq. (2.2), it can be presented as:

$$E_m = \frac{E_B}{m_p} = \frac{E_B}{\rho * V_p} = \frac{W_V}{\rho} = \frac{const.}{\rho * x} \tag{2.4}$$

It can be seen that the mass-related specific energy depends on two factors: the density of particle (ρ) and the initial particle size (x) before comminution. The distribution of specific energy and equivalent impact velocity which induce the same breakage effect were derived and compared based on the force-displacement curves obtained from the experimental results (Rozenblat et al., 2011; Muller and Tomas, 2012).

$$v_{eq} = \sqrt{2\frac{E_B}{m_p}} = \sqrt{2E_m} \tag{2.5}$$

where v_{eq} is the energetic equivalent breakage energy corresponding to the impact velocity of a particle on a rigid wall initiating breakage of the particle.

2.2.2 Impact loading

Breakage mechanism of particles subject to impact loading has been widely studied with the effect of impact velocity and impact angle investigated. Many types of test rigs have been developed to assess the breakage propensity and size distribution of particulate materials. The reason for performing impact loading test is because of the representative behavior of particle friability during comminution and its simplicity to implement in the laboratory (Petukhov and Kalman, 2003). Hence, considerable efforts have been devoted to improving the test rigs and measuring systems. Broadly the types of impact loading test can be divided as four categories, including drop weight impact test, pendulum impact test, air gun impact test, vibrational impact test, which are described as below.

2.2.2.1 Drop weight impact tests

A typical drop weight impact test consists of a long steel rod equipped with strain where a single particle is placed and impacted by a falling steel ball (Tavares and King, 1998). The Ultrafast Load Cell (UFLC) was used to investigate the deformation and fracture of single particles subject to impact. The compressive wave due to the impact loading is recorded as a function of time by a digital oscilloscope (Figure 2.3). The feature of

this test apparatus is to enable the measurement of particle fracture energy, the particle strength and the particle stiffness under impact loading, which is similar to the stressing condition in industrial ball mills. Nevertheless, the measuring process is tedious and laborious considering a large number of particles counted. Other kinds of drop weight test were developed and the relationship between breakage distribution and energy measurement were studied (Piret, 1953; Schonert, 1972; Narayanan and Whiten, 1983).

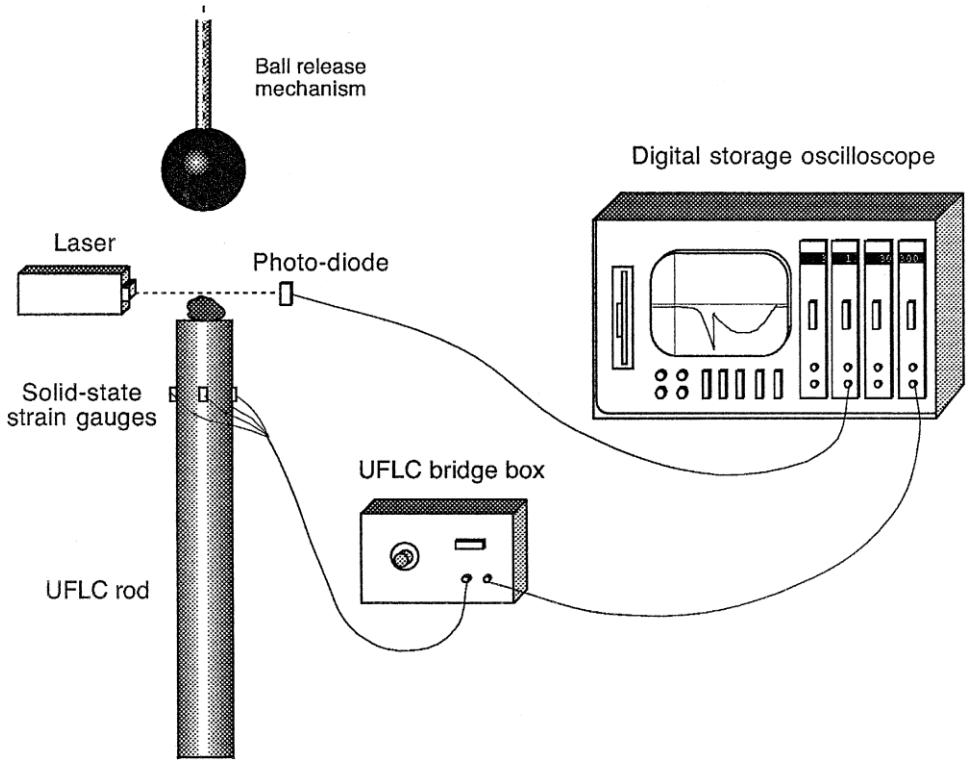

Figure 2.3 Schematic outline of a typical drop weight impact tester
(After Tavares and King, 1998)

2.2.2.2 Pendulum impact test

Pendulum impact test has been used to measure the energy utilization patterns (Narayanan, 1985), breakage energy (Weedon, 2001) and restitution coefficient (Antonyuk et al., 2010). Narayanan (1985) measured the comminution energy from twin pendulum tests and shows that the comminution energy does not increase with proportions to the input energy. Weedon (2001) developed T-lines from single particle breakage data using a laser monitored twin pendulum tester. An exponential relationship between the comminution energy and the $t_{1.4}$ parameter was developed. Restitution coefficient was measured from pendulum impact test with focus on energy absorption during compression and impact of elastic-plastic granules by Antonyuk et

al. (2010). It was found that the measured restitution coefficient is independent of the impact velocity in the examined range and independent of the load intensity by compression. A schematic outline of pendulum impact tester is shown in Figure 2.4.

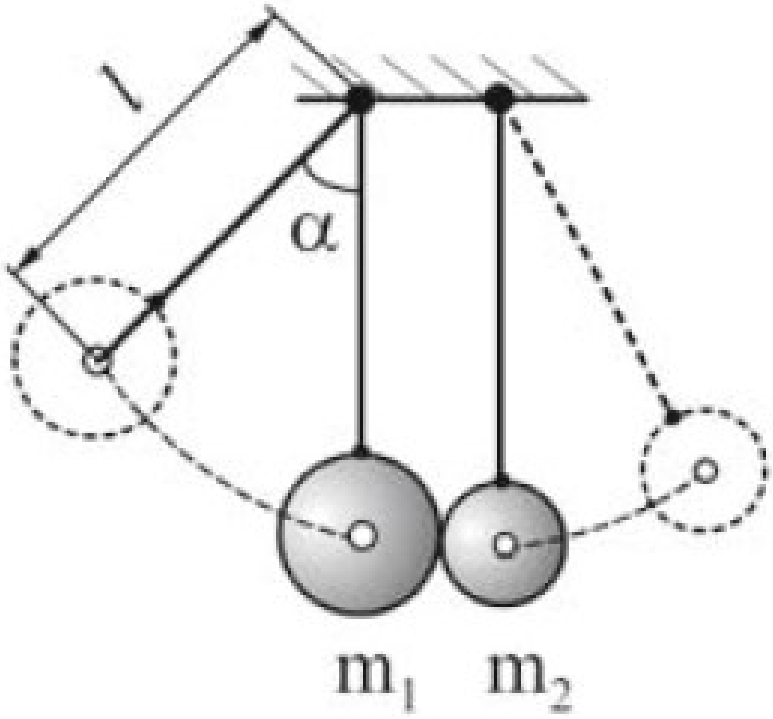

Figure 2.4 Schematic outline of pendulum tester
(After Antonyuk et al., 2010)

As shown in Figure 2.4, two particles are attached by thin wires to an overhead plate by a distance. The two particles are lifted up to a certain height and then unleashed to collide in the normal direction. The relative impact velocity can be measured from the distance between the overhead plane and impact point. The velocities of particles after impact could be measured by a high-speed video camera or photodiodes. The advantage of pendulum test enables the lower impact velocity impact, which is difficult to achieve in free-fall experiments because of small falling height (Antonyuk et al., 2010).

2.2.2.3 Air gun impact test

The principle of air gun impact system is to accelerate the individual particles through a pipe by the pressure difference and collide the particle with a target at the pipe exit. This kind of tester allows a large number of particles to be impacted for a statistical purpose. It also enables the measurement of particle breakage pattern and breakage

numbers under varying impact velocity and impact angles. Air gun impact system may be classified into two categories: horizontal impact system and vertical impact system. The horizontal impact system has been widely used by many researchers such as Salman and co-workers (1995, 2002), Tomas and co-workers (2006, 2012). It is worth noting that the original design of horizontal impact system was reported in the annual report of IFPRI by Dodds et al. (1998). A typical schematic outline of the horizontal impact system is shown in Figure 2.5.

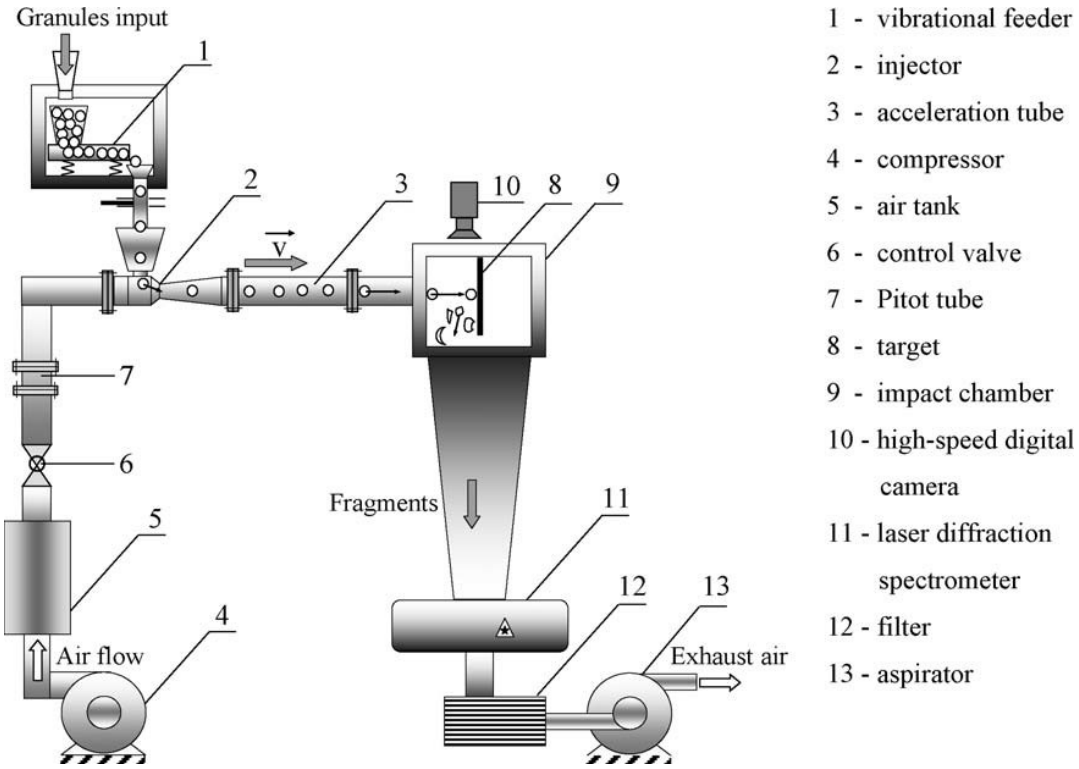

Figure 2.5 An air gun system of horizontal impact tester
(Adapted from Antonyuk et al., 2006)

The utilization of vertical impact system was extensively studied by Ghadiri and co-workers (1986, 1993, 1996, 2002, 2015). A typical vertical impact tester is schematically illustrated in Figure 2.6. Amongst these studies, the effects of impact velocity and impact angle were mainly investigated with many test materials such as aluminium oxide, catalyst beads. The index of particle breakage is characterized by broken numbers of feed particles (Salman, 1995) and the volume mass removal (Yuregir et al., 1986). A consensus was reached that normal component of impact velocity plays a key role in particle breakage.

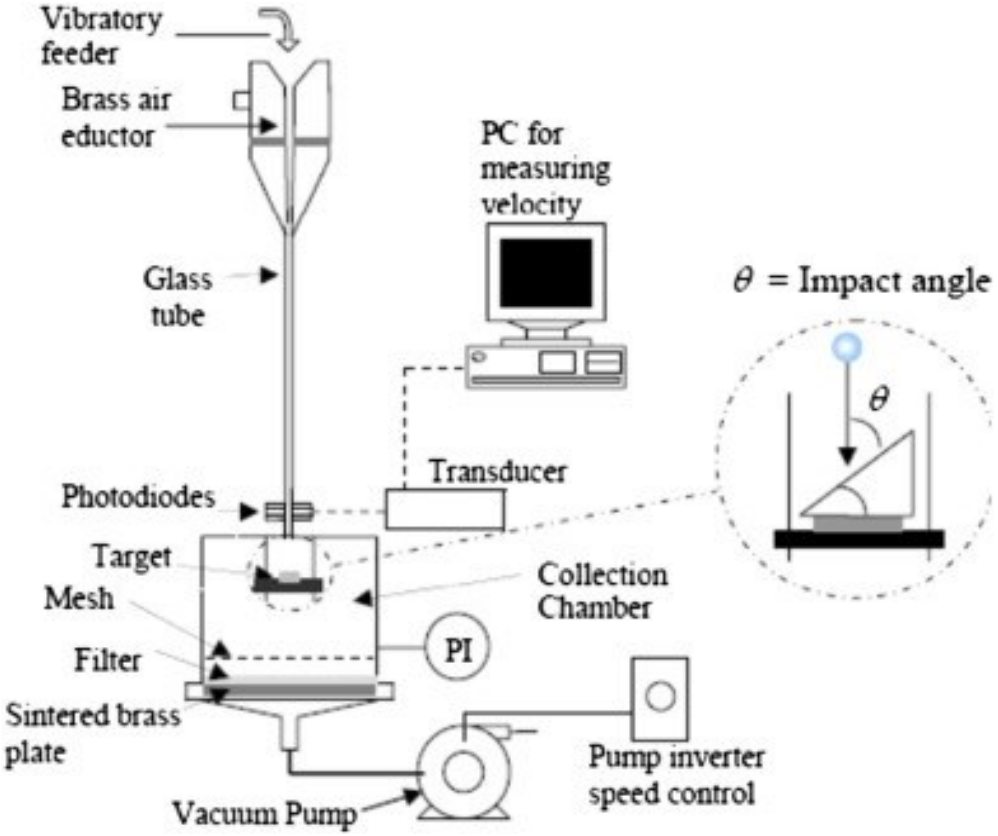

Figure 2.6 An air gun system of vertical impact tester

(After Bonakdar et al. 2015)

2.2.2.4 Vibrational impact test

Gentzler and Michaels (2004) developed a laboratory vibrational impact tester to measure the impact attrition of brittle particles as shown in Figure 2.7. This tester has a trajectory technique to elucidate average impact velocities, effective particle restitution behaviour and average losses by impact, which allows the direct comparison of data from both single particle impact and multiple particle impacts. A relatively unexplored mode of attrition was revealed and distinguished by lack of gross fragmentation at low velocities. It is speculated that the transition to gross fragmentation is related to the internal structure of the particle.

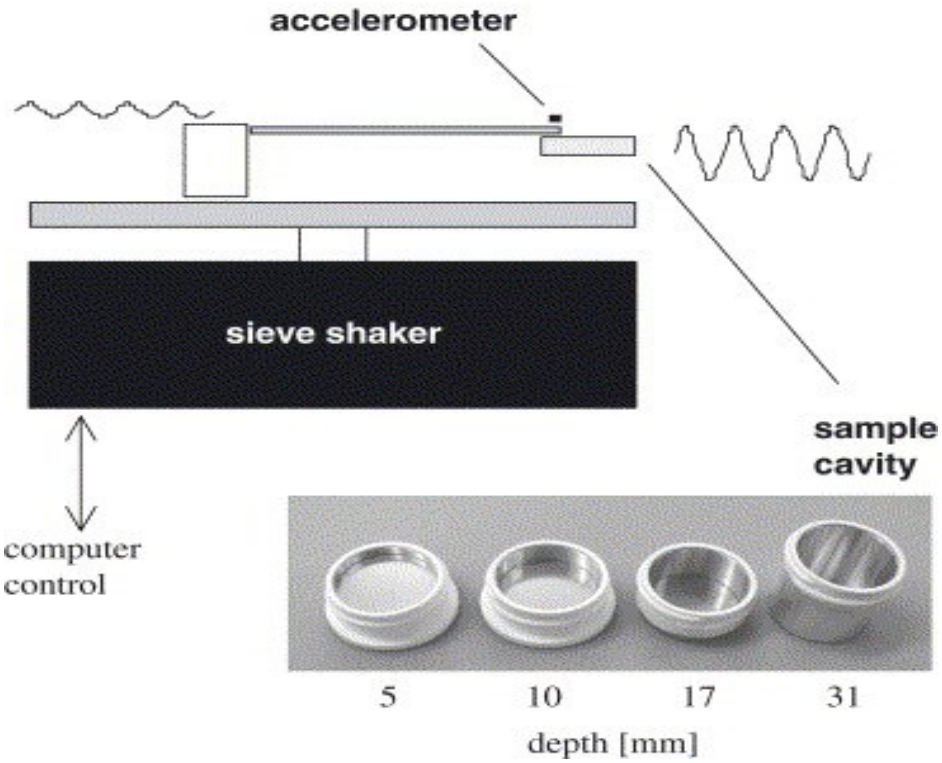

Figure 2.7 Schematic diagram of resonant cantilever impactor and pictures of the four cavities (Adapted from Gentzler and Michaels, 2004)

2.2.3 Milling operation

Milling operation can be classified as dry and wet, depending on whether water is the additional charge inside a mill. According to the fineness requirement of ground product, milling can be divided as coarse, medium and fine mills. A selection of milling types based on the fineness of product particle is shown in Figure 2.8. As the increasing demand for finer and finer product, several types of mills have been developed for fine grinding. The classification of fine grinding machines is summarized in Table 2.1 as follows (Yokoyama and Inoue, 2007). The fine grinding mills consist of five major types, i.e. impact mills, ball media mills, air jet mills, roller mills and shearing attrition mills from the perspective of grinding machines. As noted by Yokoyama and Inoue (2007), the grinding mechanisms can be expressed in terms of impaction, shearing, compression and attrition, which are combined to take place in most mills.

Numerous efforts have been done to investigate the material grindability for a variety of grinding machines. For example, the coriander seeds were ground using hammer mill and a pin mill to study the pattern of particle size distribution and their relationship with energy consumption (Shashidhar et al., 2013). Among the mathematical models for

particle size distribution, Rosin-Rammler-Bennett (RRB) gave the best fit as compared to the Gaudin-Schumann (GS) model and Log-normal function. Energy consumption for grinding was typically investigated by the classical grinding laws including Bond's law, Rittinger's law and Kick' law, which exhibit a linear relationship with particle size reduction ratio.

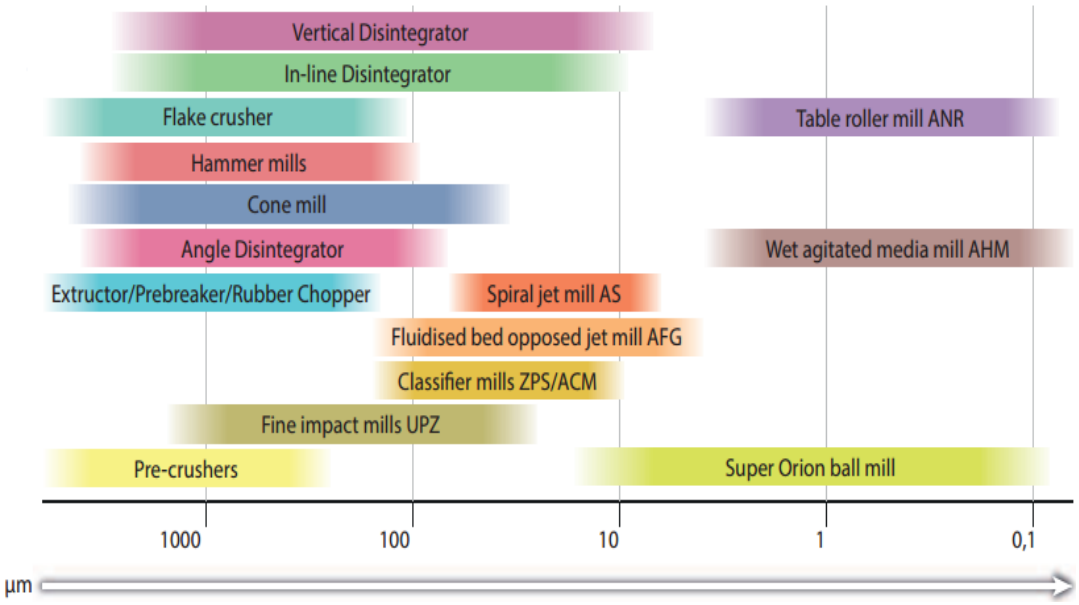

Figure 2.8 Application areas of different mill types
(Adapted from Hosokawa Micron Ltd. UK)

Manohar and Sridhar (2001) utilized a time-of-transition (TOT) technique to measure the particle size and shape of ground turmeric particles. Apart from a hammer grinding method, a cryogenic grinding system was developed for grinding and is confirmed useful in producing finer particles for heat-sensitive materials. Kwan et al. (2004) developed a method to evaluate the milling behavior of two pharmaceutical powders in an oscillatory single ball mill. The material and mechanical properties were obtained from single particle impact testing. It suggests that milling behavior of two materials is severely influenced by the particle size. The increased breakage behavior of the two materials was perceived with the increase of particle size. Noticeably, a correlation between the material properties and the milling rate was established although a unification of milling function with other material parameters is still required. A material grindability test was conducted by Lecoq et al. (1999) to study particle fragmentation under high velocity impact (up to 500 m/s) in an air-jet mill. A

classification was obtained by means of fineness criteria change and energy threshold determination. It is worth mentioning the possibility of particle fragment by successive impacts, which is presumably resulting from fatigue. Plessis et al. (2007) investigated the effect of grinding time on the particle size distribution of Portland cement clinker. It was demonstrated that the fineness and Blaine specific surface area of gasification ash and Portland cement clinker increased with the growth of grinding time though the increase was not pronounced beyond two hours.

Table 2.1 Classification of fine grinding machines (After Yokoyama and Inoue, 2007)

Group		Milling type
Impact mill		High-speed rotation disc type
		Hammer type
		Axial flow type
		Annular type
Roller mill		Roller tumbling type
		Roll type
Ball media mill	Vessel drive	Tumbling type
		Vibration type
		Planetary type
		Centrifugal fluidized-bed type
	Agitator drive	Tower type
		Agitation vessel type
		Tubular type
		Annular type
Air jet mill		Target collision type
		Fluidized-bed type
		Attrition type
Other type mills		Mortar and pestle
		Stone mill
		Powder-bed attrition-type mill
		Wet high-speed shearing mill

2.3 Particle breakage models

Milling is such a complicated unit operation which is lack of sound underlying mechanism as compared to other unit operations. However, the amount of literature dealing with milling mechanism is overwhelming. Numerous particle breakage models have been developed over the last decades. They may be classified into five categories: empirical models directly from data regression, statistical models, dimensional models, population balance models and fracture mechanics based models that make use of some simple assumptions. A review of these models is presented as below.

2.3.1 Empirical models

In the early phase, three models were proposed by Rittinger (1867), Kick (1885) and Bond (1952) as a function of particle size. Walker et al. (1937) presented a general form of the three models as following

$$dE = -C\frac{dx}{x^{\alpha}} \tag{2.6}$$

where E is the grinding energy per unit mass, x is the characteristic size of the particle, C and α are constants for a given material and mill.

Integration of the Eq. (2.6) gives

$$E = C'\left(\frac{1}{x_p^{a-1}} - \frac{1}{x_F^{a-1}}\right), a \neq 1 \tag{2.7}$$

or

$$E = C\log\left(\frac{x_F}{x_p}\right), a = 1 \tag{2.8}$$

Eq. (2.8) follows the Kick law when the exponent a is equal to 1. The equations of Rittinger and Bond are gained respectively when the value of exponent a is 2 and 1.5 accordingly. where x_p and x_F are the feed and product size. Note that there is a step change from Eq. (2.7) to Eq. (2.8) when a is assigned a value infinitesimally close to 1 in Eq. (2.7). Based on the type of grinding, it is construed that the Kick model is applicable for coarse grinding with Bond model and Rittinger model applicable for

intermediate and fine grinding respectively. Austin (1973) made a commentary on the three models of grinding and points out that Bond model and Rittinger model may be applied to the same set of grinding data.

Tavares and King (1998) investigated the deformation and fracture of single particles subject to impact using the ultrafast load cell (UFLC) from the perspective of energy. A model to describe the relationship between the mass-specific particle fracture energy (E_m) and the particle size (d_p) is given as

$$E_{m50} = E_{m\infty}\left[1 + \left(d_{p,o}/d_p\right)\right]^{\emptyset} \tag{2.9}$$

where E_{m50} is the median of the fracture energy log-normal distribution. $E_{m\infty}$, $d_{p,o}$ and $\emptyset$ are models constants estimated by the least-square method.

Datta (1999) gives an equation from data fitting obtained using a limestone

$$M = AlnI + B \tag{2.10}$$

where M is the broken mass out of the size interval of feed particles; I is the impact energy calculated from the mass of falling ball and impact velocity; A and B are parameters dependent on feed size.

By fitting the literature data, Cho and Austin (2003) derived an equation for the cumulative mass fraction of broken particles ($\overline{m_i}$) in light of specific impact energy (E):

$$\overline{m_i} = \bar{A}\ln\left(\frac{E}{K_i}\right), E_{min} \le E \le E_{max} \tag{2.11}$$

where E_{min} is the minimum specific impact energy required to yield obvious breakage of particle in size i, E_{max} is the maximum specific impact energy required to break all the particles in size i. $\bar{A}$ and $K_i = C(x_i/x_0)^{-m}$ are material-dependent constants. Cho and Austin (2003) specified that the value of $\overline{m_i}$ is zero under the specific impact energy of E_{min} and one beyond the specific impact energy of E_{max}.

Petukhov and Kalman (2004) developed an empirical model to evaluate the breakage ratio as a function of impact velocity and impact number. This gives:

$$\xi = \xi_f + \frac{\xi_i - \xi_f}{1 + (v/v_{50})^p} \tag{2.12}$$

where ξ is the breakage ratio, which is defined as the percentage of broken particles under any chosen reference size, ξ_i the initial breakage ratio and ξ_f the final breakage ratio. v is the impact velocity; v_{50} is the median velocity, which causes 50% of the particle population to break, and p is the breakage ratio distribution. For clarity, a summary of empirical models is shown in Table 2.2.

2.3.2 Statistical analysis

Many breakage functions according to statistical analysis have been found to be very practical to represent the size distribution of particle in the grinding system. The most common are:

Rosin-Rammler-Bennett function is defined by Rosin and Rammler (1933):

$$P(D) = 1 - \exp(-D/D_{63.2})^n \tag{2.13}$$

where D is the particle diameter; $D_{63.2}$ is the size of particle at which the distribution function has the value 0.632.

A model based on upper-truncated Rosin-Rammler distribution, which is detailed in King (2001) and Tavares (2004), is given by

$$P_{ij}(D) = 1 - (1 - t_{\mathrm{n}j})^{\left(\frac{\mathrm{n}-1}{\frac{D_0}{D_i}-1}\right)^{\alpha}} \tag{2.14}$$

where i, j are different size range; t_{10j} is size fraction of particle which is 10% lower than that of original particle. $D_0 = (D_j D_{j+1})^{0.5}$ and D_i is the sieve size in class i; α is

a parameter fitted from experimental data. Note that when t_{nj} is replaced by t_{10j}, the number of (n-1) evolves into 9 in Eq. (2.14).

Gaudin-Schuhmann function is expressed by (Schuhman,1940):

$$P(D) = (D/D_G)^{nG} \tag{2.15}$$

where D_G is the size when $P(D)$=1, nG is the distribution modulus determined by the slope of the log-log plot $P(D)$ and D.

Broadbent and Callcott (1956) proposed a model of breakage function:

$$P(D) = \frac{1 - e^{-\frac{D}{D'}}}{1 - e^{-1}} \tag{2.16}$$

where D' is the characteristic diameter for which 100% of the particles is smaller.

Gaudin-Meloy distribution (Gaudin and Meloy, 1962) is defined by:

$$P(D) = 1 - (1 - D/D')^n \tag{2.17}$$

where n is a parameter to characterize the steepness of the cumulative curve. Lower value of n indicates a more scatter distribution whilst higher value of n infers a more uniform particle size distribution.

The modified Gaudin-Meloy function (Harris function) is expressed as (Bergstrom, 1966; Harris 1968):

$$P(D) = \left[1 - \left(1 - \frac{D}{D_0}\right)^n\right]^m \tag{2.18}$$

where D_0 is the parameter pertinent to the maximum particle diameter, n is the fitting parameter and m is called the Schuhmann slope.

Log-normal distribution of density function is expressed:

$$f(D) = \frac{1}{\sigma\sqrt{2\pi}} \exp(-\frac{D - D_a}{2\sigma^2}) \tag{2.19}$$

where $f(D)$ is the density distribution; D_a is the arithmetic mean and σ is the standard deviation. Another log-normal distribution from impact energy perspective is given by Tavares and King (1998)

$$P(E) = \frac{1}{2}\left[1 + erf\left(\frac{lnE - lnE_{50}}{\sqrt{2}\sigma_e}\right)\right] \tag{2.20}$$

where E_{50} and σ_e are the median energy and the standard deviation of the distribution. The truncated log-normal function is given below (Klotz and Schubert, 1982):

$$P(D) = \int_{-\infty}^{u} \frac{1}{\sqrt{2\pi}} \mathrm{e}^{-u^2/2}\, \mathrm{d}_u \tag{2.21}$$

where u is the parameter relating to median and maximum progeny size. It should be mentioned that the log-normal and the upper-truncated log-normal distribution are the most commonly used function to describe particle size distribution.

Peleg and Normand (1986) developed modified beta function using the distribution density function $f_{am}(x)$ from a numerical procedure, i.e.,

$$f_{am}(x) = \frac{x^{am}(1-x)^m}{\int_0^1 x^{am}(1-x)^m dx} \tag{2.22}$$

where x is the normalized size; a and m are power coefficient determined by nonlinear regression programs. It should be noted that this function is not suitable for mixed distributions such as multimodal distributions. More terms are required to address such problems.

Austin and Luckie (1972) presented a model to calculate the breakage function from the grinding tests of a closely sized sample.

$$P(D) = \phi\left(\frac{D}{D_0}\right)^a + (1-\phi)\left(\frac{D}{D_0}\right)^b \tag{2.23}$$

where a, b and ϕ are parameters determined by the methods described in Austin and Luckie (1971).

An adjusted power law given by Vogel and Peukert (2002) is expressed as

$$P(D) = \left(\frac{D}{D_0}\right)^a . 1/2(1 + tanh\left(\frac{D - D_0}{D'}\right) \tag{2.24}$$

where D' denotes a characteristic fragment size.

Salman and co-workers (1995, 2002, 2004) studied the particle fragmentation in air gun impact system. The number of unbroken particles (N_0) is predicted by impact velocity (v) and the initial feed particle number (N).

$$N_0 = Nexp^{\left(-\left(\frac{v}{c}\right)^m\right)} \tag{2.25}$$

where c is the scale parameter and m is the Weibull modulus. It was reported that $c = 19.5$ and $m = 7.4$ for the tested aluminium oxide particle (Salman et al., 1995). However, it becomes laborious to count the number of broken particles when thousands of particles were fed under impact loads.

2.3.3 Dimensional analysis

A similarity law of breakage for geometrically similar particles was derived from dimensional analysis (Rumpf, 1973).

$$S_v l = f\left\{\frac{W_V}{E}, \frac{W_V l}{\beta_{max}}, \frac{v_{fract}}{v_{el}}, \frac{v_d}{v_{el}}, \frac{l_i}{l}, \upsilon\right\} \tag{2.26}$$

The similarity is denoted by the product of volume-specific surface area S_v and initial particle size l. where W_V is the volume-specific elastic strain energy and E is the Young's modulus of particle. v_{fract}, v_{el}, v_d=velocity of crack propagation, velocity of elastic wave and velocity of deformation; and l_i =initial flaw size, υ=Poisson ratio.

Vogel and Peukert (2003) presented an approach to quantify the grinding behaviour of different materials by constructing a mastercurve for breakage probability. Two material parameters, $f_{Mat.}$ and $W_{m,min}$ were introduced to represent the grinding property.

$$S = 1 - exp\{-f_{Mat.} lk(W_{m,kin} - W_{m,min})\} \tag{2.27}$$

where S=breakage probability; $W_{m,kin}$=mass-specific kinetic energy; l and k= particle size and impact number. The two material parameters were determined by single-particle impact tests. Meier et al. (2008) extended this model to characterize the grinding behaviour of pharmaceutical powders of size 160-500 microns. It shows that the concept of describing the milling performance by means of material functions is applicable in pharmaceutical powders. The applicability of this model is further confirmed by studying the particle size distribution of various materials under different impact velocities and angles (Meier et al. 2009). It was found that the breakage function does not depend on the impact angle. Only normal component velocity is considered under 60^o impact even though the effect of the tangential component velocity was not tested at smaller impact angles.

It may be noted that no quantitative description of particle breakage is obtained by correlating the material parameters with physical properties of the particles. The first attempt was made by Meier et al. (2009) to predict the milling behaviour by means of nanoindentation. This gives

$$f_{Mat}^* = c_1 \rho \left(\frac{H}{K_c}\right)^{2.5} \; ; \; f_{Mat}^* = f_{Mat}(1 + \frac{E}{E_{target}}) \tag{2.28}$$

where $f_{Mat}^{*}$is adjusted breakage parameter; c_1 is a proportionality constant and ρ is the particle density; H=hardness and K_c=fracture toughness.

$$lW_{m,min}^{*} = c_2 \frac{1}{\rho}\left(\frac{f_{Mat}^{*}}{\rho}\right)^{-1.5} \; ; \; lW_{m,min}^{*} = lW_{m,min}(1 + \frac{E}{E_{target}})^{-1} \qquad (2.29)$$

where $W_{m,min}^{*}$is adjusted mass-specific kinetic energy; c_2 is a proportionality constant.

However, the correlation between bulk milling behaviour and mechanical properties from nanoindentation contains some scatters due to the simplifications made and lacking of other possible important factors.

De Vegt et al. (2005) developed a particle breakage model using dimensional analysis as below:

$$S_i = c \frac{E_{kin}E_{frac}\sqrt{\frac{P_y}{\rho}}}{VH\sqrt{x_i}K_{IC}}(\frac{l_f}{x_i}) \qquad (2.30)$$

where S_i denotes the selection function of particle in the size interval of i. E_{kin} the kinetic energy of particle; E_{frac} the fracture energy, P_y the yield pressure, ρ particle density, V particle volume and H the hardness, x_i particle size in size interval of i, l_f the initial flaw size and c a constant. K_{IC} stress intensity factor. For clarity, a summary of statistical models and dimensional models is presented in Tables 2.3 and 2.4 respectively.

2.3.4 Population balance model

The breakage of particle assembly could be classified into two processes, i.e. the selection and breakage processes (Broadbent and Callcott, 1956). First of all, the breakage probability of a particle of the feed size is determined by selection function under the grinding zone. The description of selection function depends on the operation mode of the grinding machine and the intrinsic quality of the particle. Secondly, the particles are broken according to the selection function, which results in the proportions

of particles of a certain size. The breakage function demonstrates the size distribution of particles after grinding. The combination of selection and breakage functions constitute the population balance model. By means of selection and breakage functions, it demonstrates the capacity of population balance model in grinding process application. Broadbent and Callcott (1956) pointed out that the way for physical development of particle breakage is based on more appropriate selection and breakage functions.

A general form of population balance model for a batch grinding is expressed by (Austin, 1971; Herbst and Fuerstenau, 1980)

$$\frac{dw_i(t)}{dt} = -S_i w_i(t) + \sum_{j=1}^{i-1} b_{i,j}\, S_j w_j(t) \tag{2.31}$$

where i and j are the size-class indices running up to N; w_i, S_i and $b_{i,j}$ represent mass fraction in class i, specific breakage rate parameter, and breakage distribution parameter respectively.

Traditional PBMs in batch milling process exhibit linear since the specific breakage rate is assumed to be first-order. The specific breakage rate is only dependent on particle size rather than the grinding time and population density. However, the restriction of linear PBM has been noticed by Austin (1971/1972) that the linear model is not feasible for long milling times. Bilgili and Scarlett (2005) investigated the non-linear effects of PBM in milling process by categorizing the experimentally observed deviations from linear theory. It was found that the multi-particle interactions are the root cause of deviation with three types of deviations from the linear milling theory identified. Another limitation of traditional PBM is the weakness as a predictive tool especially considering the demand of scale-up from the laboratory scale to industrial scale. Due to the dependence of both intrinsic particles and grinding process, the functions suitable for one particular grinding machine cannot be directly used for the prediction of size reduction in another machine. More contents of PBM and its coupling with DEM will be introduced in Chapter 8.

Table 2.2 Summary of empirical breakage models

Authors	Model	Category	Application	Remarks
Rittinger (1867)	$E = C'\left(\frac{1}{x_p^1} - \frac{1}{x_F^1}\right)$	Empirical	Fine grinding	Energy based
Kick (1885)	$E = C\log\left(\frac{x_F}{x_p}\right)$	Empirical	Coarse grinding	Energy based
Bond (1952)	$E = C'\left(\frac{1}{x_p^{0.5}} - \frac{1}{x_F^{0.5}}\right)$	Empirical	Intermediate grinding	Energy based
Leung (1987)	$t_{10} = A(1 - e^{-bE})$	Empirical	Impact loading	Energy based
Tavares and King (1998)	$E_{m50} = E_{m\infty}\left[1 + \left(d_{p,o}/d_p\right)\right]^{\emptyset}$	Empirical	Impact loading	Drop impact test
Datta (1999)	$M = AlnI + B$	Empirical	Impact loading	Drop impact test
Cho and Austin (2003)	$\overline{m_i} = \bar{A}\ln\left(\frac{E}{K_i}\right)$	Empirical	Impact loading	Drop impact test
Petukhov and Kalman (2004)	$\xi = \xi_f + \frac{\xi_i - \xi_f}{1 + (v/v_{50})^p}$	Empirical	Impact loading	Air gun impact test

Table 2.3 Summary of breakage models: Statistical analysis

Authors	Model Equation	Model Name	Application	Remarks
Rosin and Rammler (1933); Bennett (1936)	$P(D) = 1 - \exp(-D/D_{63.2})^n$	Rosin-Rammler-Bennett	Grinding	Breakage function
King (2002) and Tavares (2004)	$P_{ij}(D) = 1 - (1 - t_{10j})^{\left(\frac{9}{\frac{D_0}{D_i}-1}\right)^{\alpha}}$	Upper truncated Rosin-Rammler	Grinding	Breakage function
Schuhmann (1940)	$P(D) = (D/D_G)^{nG}$	Gaudin-Schuhmann	Grinding	Breakage function
Broadbent and Callcott (1956)	$P(D) = \frac{1 - e^{-\frac{D}{D'}}}{1 - e^{-1}}$	Broadbent and Callcott	Grinding	Breakage function
Gaudin and Meloy (1962)	$P(D) = 1 - (1 - D/D')^n$	Gaudin-Meloy	Grinding	Breakage function

Bergstrom (1966) and Harris (1968)	$P(D)=\left[1-\left(1-\frac{D}{D_0}\right)^n\right]^m$	Modified Gaudin-Meloy	Grinding	Breakage function
Tavares and King (1998)	$P(E)=\frac{1}{2}\left[1+erf\left(\frac{lnE-lnE_{50}}{\sqrt{2}\sigma_e}\right)\right]$	Log-normal	Impact loading	Selection function
Klotz and Schubert (1982)	$P(D)=\int_{-\infty}^{u}\frac{1}{\sqrt{2\pi}}\mathrm{e}^{-u^2/2}\,\mathrm{d}_u$	Truncated log-normal	Crushing	Breakage function
Austin and Luckie (1972)	$P(D)=\phi\left(\frac{D}{D_0}\right)^a+(1-\phi)\left(\frac{D}{D_0}\right)^b$	Non-normalised	Grinding	Breakage function
Vogel and Peukert (2002)	$P(D)=\left(\frac{D}{D_0}\right)^a.1/2(1+tanh\left(\frac{D-D_0}{D'}\right)$	Adjusted power law	Impact loading	Breakage function
Salman and coworkers (1995, 2000, 2002)	$N_0=1-exp^{\left(-\left(\frac{v}{c}\right)^m\right)}$	Weibull function	Impact loading	Breakage function
Peleg and Normand (1986)	$f_{am}(x)=\frac{x^{am}(1-x)^m}{\int_0^1 x^{am}(1-x)^m dx}$	Modified beta function	Impact loading	Breakage function

Table 2.4 Summary of breakage models: Dimensional analysis

Authors	Model Equation	Model Name	Application	Remarks
Rumpf (1973)	$S_v l = f\left\{\frac{W_V}{E}, \frac{W_V l}{\beta_{max}}, \frac{v_{fract}}{v_{el}}, \frac{v_d}{v_{el}}, \frac{l_i}{l}, \upsilon\right\}$	Rumpf	Impact grinding	Selection function
Vogel and Peukert (2003)	$S = 1 - exp\{-f_{Mat.} lk(W_{m,kin} - W_{m,min})\}$	Vogel and Peukert	Impact grinding	Selection function
De Vegt et al. (2005)	$S_i = c\frac{E_{kin}E_{frac}\sqrt{\frac{P_y}{\rho}}}{VH\sqrt{x_i}K_{IC}}(\frac{l_f}{x_i})$	De Vegt	Jet milling	Selection function

2.3.5 Fracture mechanics based models

Evans and Wilshaw (1976) studied the surficial fracture by plastic indentation for a range of brittle materials in quasi-static impact regime. A material removal expression was proposed by approximate stress analysis on the postulation that material removal occurs when lateral cracks from adjacent impacts interact.

$$\varepsilon \propto \frac{\rho^{\frac{6}{5}} R G^{\frac{4}{5}}}{K_c^{3/2} H^{1/2}} v^{12/5} \tag{2.32}$$

where ε= the fraction of material loss removed due to the impact; ρ and R are the density and radius of particle respectively; K_c and H are fracture toughness and hardness of particle; G=shear modulus of the target and v=impact velocity.

Evans et al. (1978) investigated the impact fracture created in the elastic-plastic response regime, relating to surface extension and penetration. The impact damage was analysed by using simplified postulates based on key features of impact dynamics and basic fracture mechanics concepts.

A material removal expression was proposed based on the postulation that material removal is accounted for the volume encompassed by the lateral cracks.

$$\varepsilon \propto \frac{\rho^{1/4} R^{2/3}}{K_c^{4/3} H^{1/4}} v^{19/6} \tag{2.33}$$

Hutchings (1994) derived an expression to estimate the impact force on a corner of a cube, and thus calculating the dimension of impression and fractional loss resulting from impact.

$$\varepsilon \propto \frac{\rho^{4/3} R H^{2/3}}{K_c^2} v^{8/3} \tag{2.34}$$

It is assumed that the kinetic energy of particle is dissipated in the plastic deformation of the particle. The size of impression radius is expressed as a function of contact force

and then the relationship between impression radius and material property was established.

Ghadiri and Zhang (2002) proposed a breakage model based on the assumption that the detachment of subsurface lateral crack results in the chipping by impacting particle against a rigid plate.

$$\varepsilon \propto \frac{\rho v^2 RH}{{K_c}^2} \tag{2.35}$$

The lateral crack length is estimated using a linear approximation to the curve of normalised crack length as a function of fracture toughness; the depth of lateral crack is assumed to be proportional to the contact radius. It should be noted that the fracture mechanics based models are only applicable in the regime of chipping. A detailed discussion of theoretical models will be introduced in Chapter 5.

2.4 DEM modelling of particle breakage

2.4.1 A brief review of DEM

The discrete element method (DEM) was proposed by Cundall and Strack (1979) to describe the mechanical behaviour of assemblies of discs and spheres. Although DEM was first applied in the field of rock mechanics, the widespread use of DEM can be seen as many areas as possible including engineering, material science, geology, mineralogy and agriculture (to name but a few). DEM is based on an explicit scheme in which the interaction of the particles is monitored contact by contact. The motion of particles is modelled particle by particle, which makes DEM computationally intensive. Note that a small time step should be ensured so that the interactions between particles do not propagate any further than their neighbourhood. Generally DEM resolves the dynamic interaction of elements through a three-stage calculation cycle. The three stages include contact detection, calculation of interaction forces and numerical time integration. A flow chart of the three-stage calculation process is shown in Figure 2.9. As seen from Figure 2.9, DEM is dependent on two simple theories: the force displacement law and Newton's Second Law. The force displacement law calculates the internal forces from element interactions in the context of contact model. Then the resultant forces on each particle are determined by Newton's Second Law (Cundall and Strack, 1979). The

updated positions of each element including particle and geometry are used to calculate new contact forces after one time step progression.

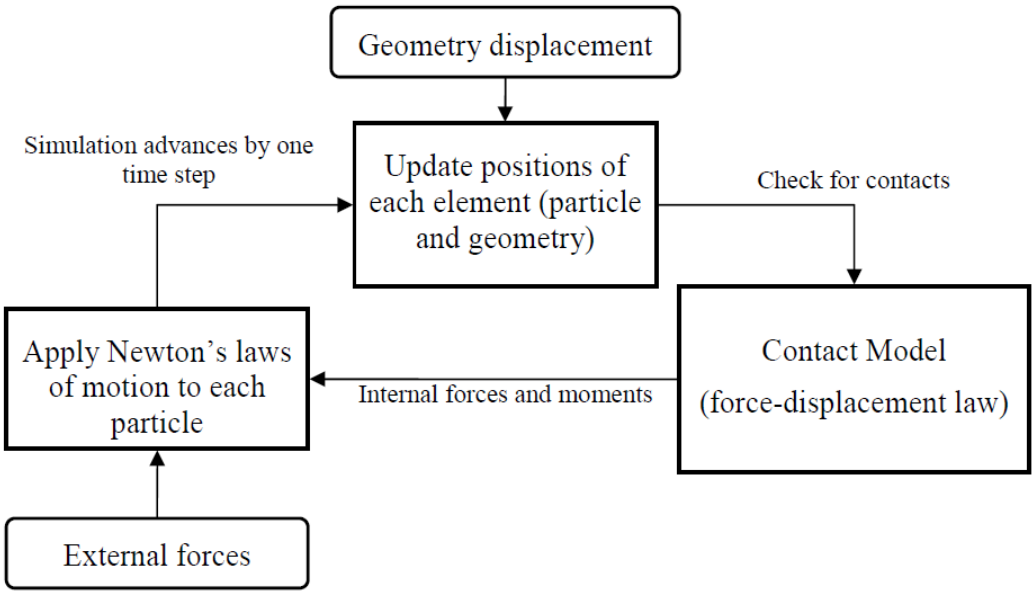

Figure 2.9 Sketch of DEM calculation cycle (After Brown 2013)

A characteristic feature of the method is that DEM can provide micromechanical insight into bulk material processing which is usually not available from experiments. On the other hand, the obvious drawbacks of DEM are the problem of scale and computational intension. Details regarding the formulation and contact force models can be referred to Zhu et al. (2007), Brown (2013) and Morrissey (2013). There have been several codes available for commercial software such as EDEM (DEM Solutions, 2015), PFC (Itasca, 2001) and DEMPACK (CIMNE, 2010). In this thesis, the DEM work was carried out to simulate single particle breakage subject to impact loading and particle breakage in UPZ100 impact pin mill using commercial software EDEM and DEMPACK respectively.

2.4.2 DEM application in single particle breakage

Due to the rapid advancement of computational power, DEM can serve as the excellent tool to envisage the breakage behaviour of individual particles without losing its fidelity. The following is a brief review of DEM modelling of single particle breakage in both compression and impact loading.

2.4.2.1 DEM modelling of compression

From the literature survey, it shows that individual particle has been usually treated as an assembly of bonded spherical micro-particles (Robertson and Bolton, 2001; McDowell and Harrireche, 2002; Cheng et al., 2003; Cil and Alshibli, 2012; Brown et al., 2014). Single sand particle was modelled in the context of DEM by bonded contact models to capture the stress variation of single particle fracture, the plastic hardening and yielding of sand under compression (McDowell and Harrireche, 2002 and Cheng et al., 2003). The agglomerate was constituted by regularly packed spheres which are connected by contact bonds. The tensile strength variation was introduced by following the Weibull distribution. However, the tensile fracture mode giving rise to particle fracture was not investigated and was yet verified by experimental measurements. An alternative method of simulating particle breakage in DEM was proposed by Hanley et al. (2015) with a crushing model. The proposed crushing model encompasses the failure criterion, the selection of appropriate input parameters and the action taken post-failure.

Potyondy and Cundall (2004) proposed a bonded-particle model (BPM) for rock which is represented by a dense packing of non-uniform-sized circular or spherical particles. The particles were bonded together at their contact points and the bonded model was implemented in 2D and 3D biaxial, triaxial and Brazilian tests. Many features of rock behaviours, including elasticity, fracturing, damage accumulation producing material anisotropy, dilation and strength increase under confinement were reproduced in this work. Particularly, a floater-elimination procedure was proposed to ensure all the particles are contacted in the assembly of particle compaction. Cil and Alshibli (2012) simulated the fracture of individual silica sand particles by adopting the bonded-particle model. Then the simulation results of crack onset and propagation were investigated and verified against 3D synchrotron micro-computed tomography images of sand. More recently, a new bonded contact model based on Timoshenko beam theory was proposed by Brown et al. (2014), which takes into account axial, shear and bending behaviour of the bond. The investigation of loading response of a concrete cylinder and comparison with the Eurocode equation prediction shows a great potential for the new bonded contact model to reproduce mechanical behaviour of cementitious materials. As a unique feature of this model, both particles and structures or deformable boundaries can be accurately represented within the framework of DEM.

2.4.2.2 DEM modelling of impact loading

As a precursor to provide a better understanding of particle breakage in a milling operation, DEM simulations of particle breakage subject to the velocity regime pertinent to milling are usually conducted to evaluate the breakage propensity and size distribution after impact incident. Potapov and Campbell (1994) studied particle breakage induced by normal impact using 2D DEM. In their work, the agglomerates were simulated by continuous contacts of convex polygons. The impact breakage was described by three parameters: Poisson's ratio, characteristic strain of the particle, impact energy. It was found that particle breakage had little dependence on the Poisson's ratio whilst the impact energy gave rise to the biggest change in the size distribution. Subero et al. (1999) investigated the mechanical strength of agglomerate materials by means of DEM with the effects of impact velocity and surface energy examined. It showed the increasing extent of breakage with increasing impact velocity and a limit of impact velocity above which an asymptotic value of damage was observed. Two forms of the Weber number were used to establish the correlation between the kinetic energy and impact velocity. It was shown that the mass fraction of debris exhibits linearly with the incidence kinetic energy at low values of modified Weber number. However, the effect of mechanical properties of primary particles, bond strength and structure of the assembly on macroscopic properties of the agglomerates was not investigated in this study. Moreno et al. (2003) examined the effect of impact angle on the agglomerates breakage and reveals that the normal component of the impact velocity plays the dominant role in controlling the breakage of contacts. Most importantly, it was concluded that the breakage pattern is dependent on the tangential component of the impact velocity. A further paper by Moreno and Ghadiri (2006) examined the effect of surface energy on damage ratio and a simple mechanistic model was proposed considering impact velocity, interparticle adhesion energy and the particle properties of the agglomerate. It indicates that the proposed mechanistic model is superior to the Weber number to describe the effect of surface energy. Antonyuk et al. (2006) studied the impact breakage of three spherical granules experimentally and then compared with the DEM results. Three breakage types were observed, namely elastic-brittle, elastic-plastic and plastic breakages. However, only 2D simulation was presented where the granule was represented as a disk. Kun et al. and co-worker (1996, 1999, 2008) focused their attention on fragmentation of brittle materials in both 2D and 3D levels. Wittel et al. (2008) performed 3D DEM to study the brittle fragmentation of

spheres inside which the agglomerated particles are connected by beam-truss elements. A detailed description of the fragmentation process is given with the underlying mechanisms involved. Then the resulting fragmentation mass distribution was described by a power law regime for small fragments and a broad peak for large fragments fitted by a two-parameter Weibull distribution.

As indicated from all the above mentioned, it is still unclear whether the large number of DEM codes have been verified against fundamental benchmark problems. No standard benchmark tests appear to exist for verifying the DEM codes. Chung and Ooi (2011) presented a set of eight benchmark tests using commercial DEM codes from particle impact level. The DEM results were then compared with analytical solutions, experimental results sourced in the literature. Good to excellent matches were achieved in all the benchmark tests with some minor discrepancies noted and resolved. Further challenges to be overcome in the large scale DEM simulations were discussed though some confidence was given in the benchmark tests.

2.4.3 DEM application in milling operation

Over the last decade, DEM has made a significant contribution in the overall understanding of comminution where particle size reduction is a key focus (Weerasekara et al., 2013). A review of tumbling mills using DEM was presented by Mishra (2003) and critically evaluates the understanding of three important aspects in DEM simulation: the inter-particle force laws, significance and choice of contact parameters, and the implementation of the numerical scheme. In particular, the influence of inter-particle force laws and associated contact parameters on the accuracy of computational results was explored. Amongst numerous milling operations, ball mills have been widely studied through DEM. For example, Mori et al. (2004) simulated the motion of balls under wet condition and established the correlation between specific impact energy and grinding rate. Tuzcu and Rajamani (2011) studied the impact breakage mode in a drop-weight apparatus (UFLC) and calculated the breakage rates via impact energy spectra by DEM. Wang et al. (2012) investigated the grinding process of ball mill using DEM based model. By linking the energy information with population balance model, the evolution of product size with grinding time was predicted and compared with the experimental data from the literature. A comprehensive review of DEM application to comminution was presented by

Weerasekara et al. (2013), in which the DEM application to other comminution devices such as crushing mill, stirred mill and SAG/AG mill has been detailed. Besides, DEM based modelling techniques, namely mechanistic ball mill model, unified comminution model and virtual comminution machine were described in great details. It is noteworthy that very few reports could be found due to the lack of prior work on DEM modelling of impact pin mill, which is chosen as the research target of milling device in this project.

2.5 Summary

The literature survey related to the research topic of particle breakage in comminution has been reviewed in this chapter. As indicated from the literature survey, comminution has been known to be energy intensive and highly inefficient. Therefore, optimisation and refinement in the design and operation of milling are in great need of an improved scientific understanding of complex mechanics involved. Experimental study covers particle breakage under compression, impact loading and milling operation. In particular, the types of single particle impact are categorized and the measurement of particle breakage in various impact tester was reviewed. It is found that breakage propensity is basically characterised by the number of broken particles or the volume loss removal.

Existing particle breakage models are deeply explored in the published literature. All these models are divided into five categories, empirical models, statistical models, dimensional models, population balance models and fracture mechanics based models. The majority of these models are empirical or practical whereas the models based on mechanistic approach are limited. It is noteworthy that the fracture mechanics based on models are merely applicable to chipping. Further details of theoretical breakage models will be more thoroughly explored in the following chapter. A brief introduction of DEM was also presented and the application of DEM into particle breakage under compression, impact loading and milling operation was reviewed.

Chapter 3

Understanding material properties via indentation and impact

3.1 Introduction

Milling is a highly inefficient and energy-intensive process which requires optimisation by the aid of material grindability test. As a prelude to understand prevailing breakage in a milling process, this chapter is to understand the material properties and loading response of particles under the stressing event of indentation and impact pertinent to a milling operation. Two materials: zeolite 4AK and alumina have been chosen as the test particles due to the isotropic and well–defined properties as well as industrial interest.

This chapter presents the measured mechanical properties of chosen particles by indentation test and subsequently the breakage propensity of zeolite particle subject to impact loading. Details about the two kinds of particles are given in Section 3.2. The principle of indentation and the experimental setup are described in Section 3.3. The results of Young's modulus and hardness measured by nanoindentation as well as fracture toughness measured by micro indentation are given and discussed in Section 3.4, which was collaborated with Dr. Colin Hare from Leeds University. Section 3.5 investigates the breakage propensity of zeolite particles subject to impact loading. The breakage behaviour was assessed in a single particle impact tester with the influence of impact velocity and impact angle examined. The detailed results are reported as below.

3.2 Materials selected

Two materials: zeolite 4AK and alumina have been chosen as the test particles with semi-brittle and brittle failure expected respectively. Figure 3.1 shows the two sourced test samples.

The selected synthetic zeolite 4AK granules have the trade name Kostrolith 4AK, which are provided by CWK Bad Kostritz GmbH. The zeolite 4AK granules are widely used as an adsorbent with pore diameter of the order of 0.4 nm. The alumina spherical granules, produced by granulation from γ-Al_2O_3 without adding a binder, are provided by Sasol GmbH, Hamburg. The alumina granules consist of approximately 98%

γ-Al_2O_3 in its chemical composition and exhibit a strong water-absorbing ability. Table 3.1 summarizes the product characteristics of zeolite 4AK and alumina γ-Al_2O_3.

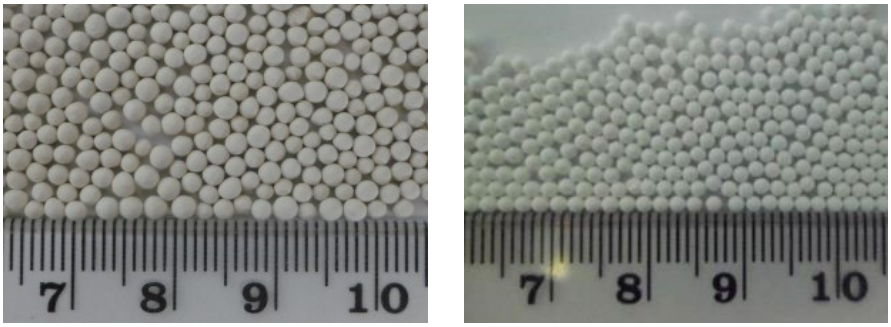

Figure 3.1 Illustration of synthetic zeolite 4AK (left) and alumina (right)

Table 3.1 Characteristics of the zeolite 4AK and Al_2O_3 granules from the suppliers

Producing Place		CWK Chemiewerk Bad Köstritz	Sasol GmbH Hamburg
Parameter	Unit	Zeolite 4AK	Alumina Al_2O_3
Diameter	mm	1.2-2.0; 2.0-2.5	1.0-1.18
Bulk density	g/ml	0.76	0.88
Specific gravity	–	2.18	3.37
Water content	≤ %wt	1.0	0.6
Fracture force	≥ N	24.9	34.49
Strength	MPa	8.34	17.84
Elastic modulus	GPa	2.45	12.23

3.3 Mechanical properties measured by indentation

Indentation test was deployed to determine three mechanical properties, i.e. Young's modulus, hardness and fracture toughness. These properties are the main characteristic of particle and are deemed to exert a key influence on particle breakage during a grinding operation (Ghadiri and Zhang, 2002). The measured mechanical properties

from indentation test provide mechanical insight into particle breakage and will be linked with the breakage model development which will be detailed in Chapter 5. This work was performed in collaboration with Dr. Colin Hare at The University of Leeds under an IFPRI (International Fine Particle Research Institute) funded collaboration project entitled 'Characterisation of particle grindability by indentation and impact'. More details of this work could be referred to IFPRI Annual Report (Colin Hare, Li Ge Wang and Jin Y. Ooi, 2014).

3.3.1 Basic principle of indentation

Nanoindentation technique provides the avenue to probe the mechanical properties of particulate materials from the micro and nano scale. Oliver and Pharr (1992) proposed a method to measure hardness and Young's modulus by instrumented indentation technique, which has been extensively adopted and used to characterize small-scale mechanical behaviour.

As indicated in a nanoindentation test (Oliver and Pharr, 2003), a prescribed load is applied by pyramidal or spherical indenter in contact with the specimen surface. As the load is increased, the penetration depth is measured accordingly. A typical form of indentation load-displacement curve consists of two stages, i.e. loading stage and unloading stage. A schematic illustration of a typical data set obtained from indenter is shown in Figure 3.2, where *P* designates the applied load and *h* the relative displacement compared to the initial undeformed specimen surface. It is assumed that the loading stage is both elastic and plastic whilst elastic displacement is recovered during the unloading stage.

As shown in Figure 3.2, there are four important parameters manifest from the load-displacement curve: the maximum load P_{max}, the maximum displacement h_{max}, the elastic unloading stiffness $S = dP/dh$, defined as the slope of the unloading curve at the initial stage of unloading and the final depth h_f, defined as the permanent depth of penetration after the indenter is completely detached.

Experiments have shown that the loading and unloading curve may be approximated by the power law relation:

$$P = \alpha h^m \tag{3.1.a}$$

$$P = \alpha (h - h_f)^m \tag{3.1.b}$$

where α and m are power fitting constants. Values of constants observed (Oliver and Pharr, 1992 and 2003) should be consulted for further details.

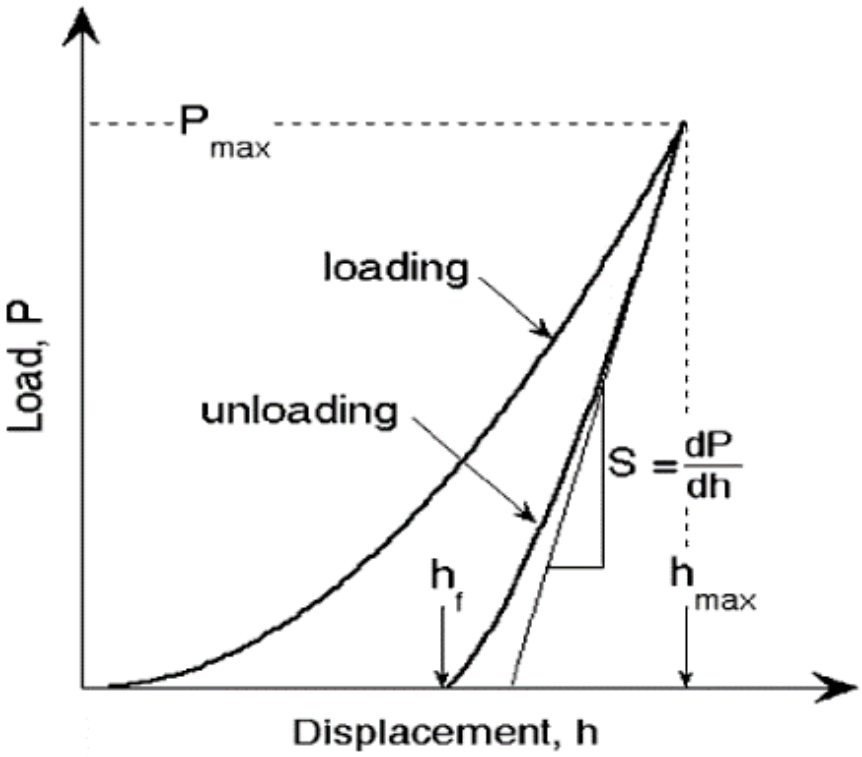

Figure 3.2 Schematic illustration of indentation load–displacement data
(After Oliver and Pharr, 1992)

Differentiation of Equation 3.1.b with respect to $(h - h_f)$ gives the contact stiffness,

$$S = \frac{dP}{d(h - h_f)} \tag{3.2}$$

Figure 3.3 shows a cross section of indentation with parameters used in the analysis. The total displacement *h* is given by

$$h = h_c + h_s \tag{3.3}$$

where h_c is the vertical distance by penetration of indenter and h_s is the vertical displacement of surface at the perimeter of the contact. a is the contact radius between the indenter and the specimen surface. Φ is the half-included angle of the indenter, which depends on the indenter geometry-$\Phi = 70.3^{o}$ for Berkovich indenter.

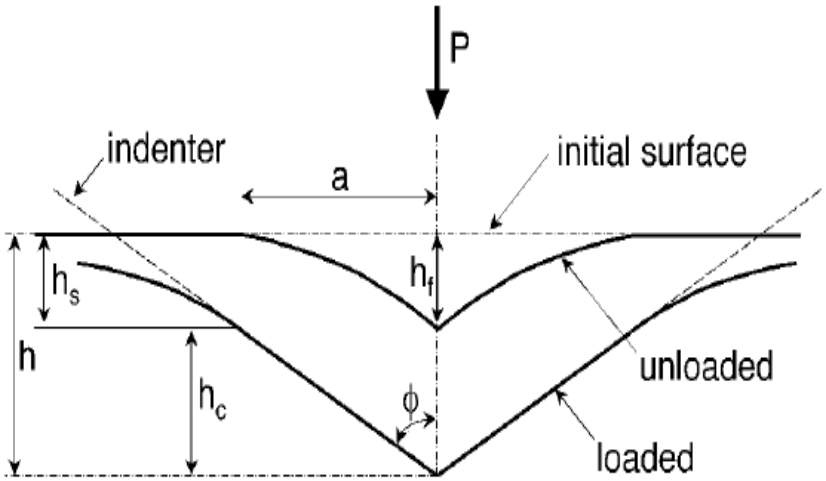

Figure 3.3 Schematic illustration of indentation with parameters characterizing the contact geometry (After Oliver and Pharr, 1992)

The contact area, A, can be expressed as a function of the plastic depth h_c

$$A = kh_c^2 \tag{3.4}$$

For Berkovich and Vickers indenters, the shape factor k is 24.5.
Once the contact area is determined, the hardness of a material is given.

$$H = \frac{P_{max}}{A} \tag{3.5}$$

where P_{max} is the maximum load applied to the sample during indentation loading and A is the corresponding contact area of P_{max}.

The unloading stiffness S can be related to contact area A and effective elastic modulus E_{eff}

$$S = \frac{2}{\sqrt{\pi}} E_{eff} \sqrt{A} \tag{3.6}$$

The effective elastic modulus E_{eff} is related to the Young's modulus and Poisson's ratio of the sample and the indenter and is defined by

$$\frac{1}{E_{eff}} = \frac{1 - \nu_s^2}{E_s} + \frac{1 - \nu_i^2}{E_i} \tag{3.7}$$

where subscripts s and i denote the sample and indenter, respectively.

The effective elastic modulus considers the fact that elastic displacement occurs in both the indenter and the sample. The Young's modulus of the sample can thus be determined with the known value of Young's modulus and Poisson's ratio for the indenter and the estimated value of Poisson's value for the sample.

Fracture toughness represents the ability of material to resist brittle fracture when a crack is present. A basic equation for evaluating the fracture toughness (K_c) of material is given (Anstis et al., 1981)

$$K_c = 0.0143 \left(\frac{E}{H}\right)^{\frac{2}{3}} \left(\frac{a}{l}\right)^{1/2} \left(\frac{P_{max}}{c^{3/2}}\right) \tag{3.8}$$

where P_{max} is the maximum applied load, E and H are the Young's modulus and hardness of the sample respectively. c is the length from the center of the indent to the tips of the radial cracks. α is an empirical constant dependent on the indenter geometry. For the Berkovich and Vickers indenter $\alpha = 0.016$. Figure 3.4 illustrates the schematic diagram of crack failure modes under Vickers indentation.

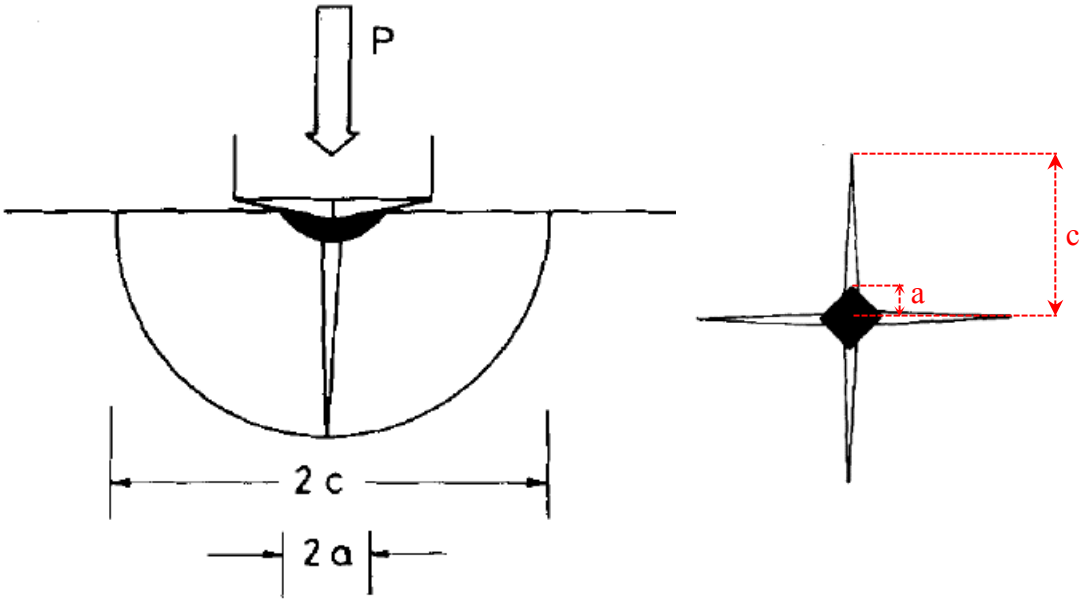

Figure 3.4 Schematic illustration of crack failure modes and dimensions for Vickers indentation (After Anstis et al., 1981)

It can be seen from Figure 3.4 that radial cracks extend outward from the boundary of indentation along the sample surface and sub lateral cracks initiate below the indentation centre and extend upward to the sample surface. It should be noted that the crack length is strongly dependent on the local microstructure and several radial cracks need to be measured for statistical reliability.

3.3.2 Measurement condition for hardness and Young's modulus

The NanoTest nanoindenter (Figure 3.5) is equipped with a video microscope for the purpose of accurate positioning of the indenter and is capable of producing well-defined load-displacement curve.

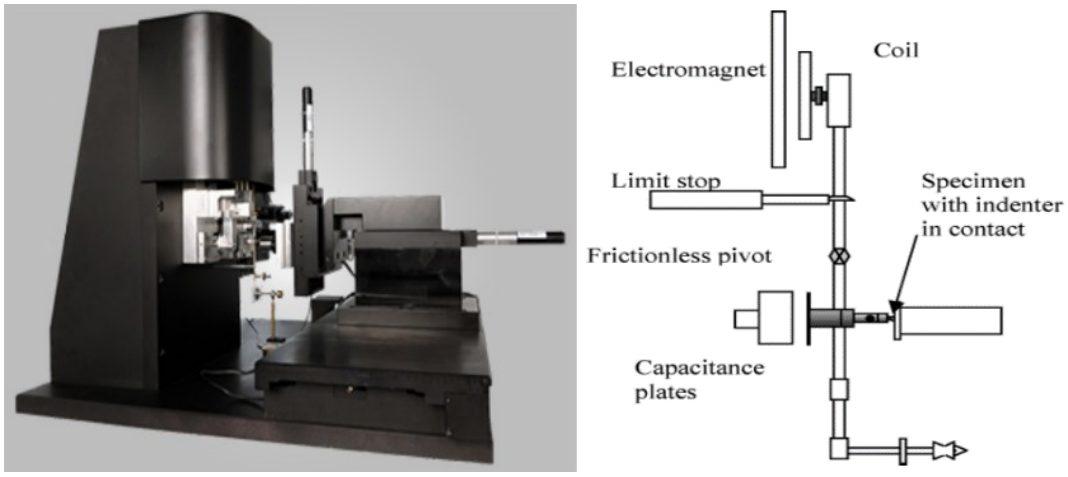

Figure 3.5 NanoTest nanoindenter (After Taylor et al., 2004)

Considering the material structure or reactions with oxygen in the air, the penetration depth of indentation is typically influential on the resulting value of hardness and Young's modulus. A preliminary set of indents up to maximum indentation load was carried out for each sample. The particle was attached to the nanoindenter by means of microscope where the central indent was placed. The focused region was considered to be the center of the particle on the indentation plane because of the high sphericity of the particle and the narrow field depth of the microscope. The initial maximum load was applied to 50 mN at a loading rate of 2 mN/s as the first stage of the preliminary test. Then the applied load was reduced to 30% of the preceding maximum load at the same loading/unloading rate, prior to reloading to a maximum load greater than the last maximum. This measuring procedure was repeated until a maximum load of 500 mN was achieved before the full unloading of the sample. Table 3.2 summarizes the whole loading and unloading procedure.

Table 3.2 Measurement scheme for multiple loading nanoindentation

Indent number	Maximum load (mN)	Unloading load (mN)
1	50	15
2	100	30
3	150	45
4	200	60

5	250	75
6	300	90
7	350	105
8	400	120
9	450	135
10	500	0

To obtain a statistical reliable value of hardness and Young' modulus, 10 particles of each material were indented under the same loading/unloading rate as mentioned above. A matrix of 3 rows by 3 columns was adopted in this procedure with a separation distance of 80 μm between neighbouring indent points to eliminate the influence by the previous indent.

3.3.3 Measurement conditions for fracture toughness

As noted in Eq. 3.8, a crack needs to be generated in order to determine fracture toughness by indentation. Due to loading capacity of 500 mN in the NanoTest, it is insufficient to generate a crack in both alumina and zeolite particle samples. Alternatively, microindentation was carried out using the Instron mechanical testing machine (Model 5566), as shown in Figure 3.6a. The SEM stubs were mounted to a sample holder which was clamped to the Instron platen. Only one indent was performed in each tested sample to eliminate the interference of neighbouring indent points. The indenter was manually aligned with the particle center before penetration. Indented particles were observed using a SEM microscope (Carl Zeiss Evo MA 15) to measure the length of generated cracks. Preliminary indents indicate that only a narrow range of indentation loads give rise to cracks which are small enough not to lead to complete particle fracture (Figure 3.6b). It was found out that indentation loads of satisfaction for small crack generation are 5 and 10 N for zeolite and alumina, respectively. The loading and unloading rate were chosen as 2% of maximum load per second.

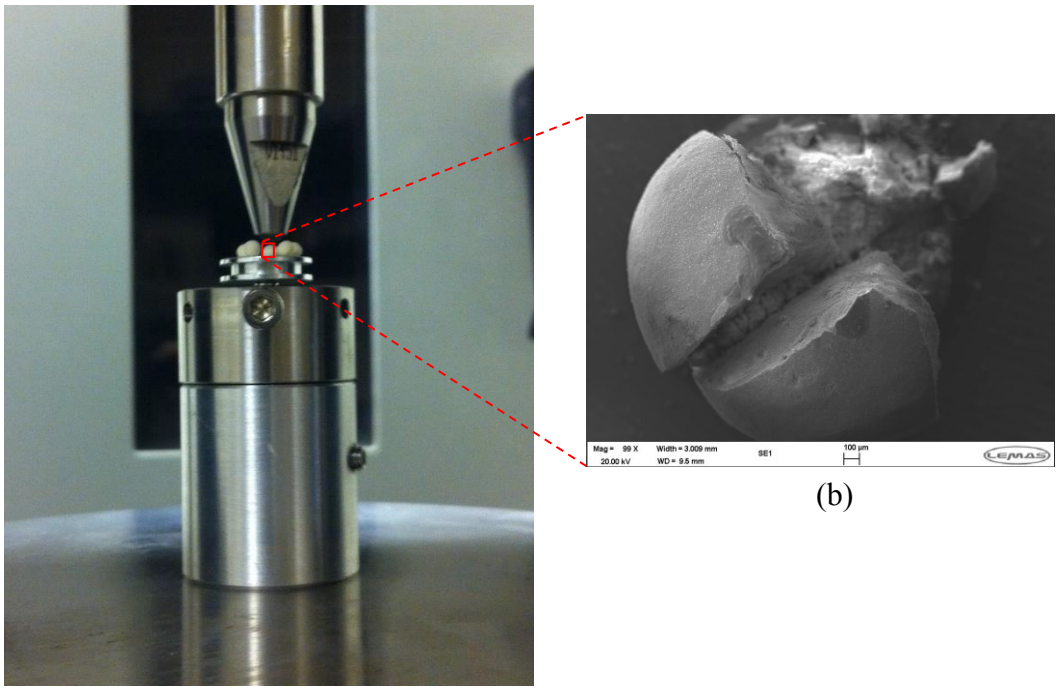

(a) (b)

Figure 3.6 (a) Microindentation measurement of fracture toughness using the Instron; (b) Fractured zeolite particle after indentation (Top view)

3.4 Results and discussion

3.4.1 Hardness and Young's modulus

Figure 3.7 shows the force-displacement curve of an alumina particle from multiple indents. It demonstrates that multiple loading does not adversely affect the overall response of the material. For each of the ten indents, an analytical expression for the unloading data could be determined by Eq. 3.1.b applied to the unloading data in the range of 40–100 % of P_{max}. The stiffness of the unloading line is then determined using Eq. 3.2 and the Young's modulus obtained through Eqs. 3.6 and 3.7 assuming the Poisson ratio of both materials to be 0.25. The hardness is measured using equations 3.4 and 3.5. By so doing, the value of hardness and Young's modulus can be determined from the multiple loading of 1.0–1.18mm alumina, 1.4– 1.7 mm zeolite and 2.0–2.36 mm zeolite, respectively.

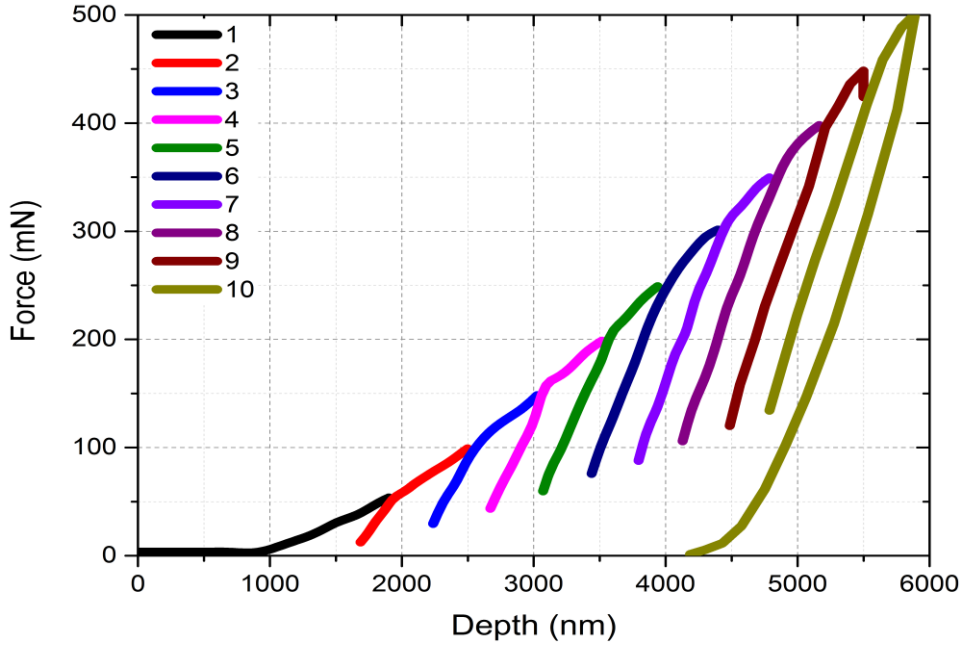

Figure 3.7 Force–displacement for multiple loads on a single alumina particle

Figures 3.8-3.10 illustrate the variation of Young's modulus and hardness for the tested materials respectively. As seen from Figure 3.8, the value of hardness for alumina particle is varied between 0.77 GPa and 0.84 GPa whilst the value of Young's modulus for alumina particle is varied between 16.5 GPa and 18.9 GPa. Figure 3.9 shows that the hardness of zeolite particle (1.4-1.7 mm) is varied from 0.11 GPa to 0.147 GPa with the Young's modulus ranging from 5.18 GPa to 5.94 GPa. Figure 3.10 shows that the hardness of zeolite particle (2.0-2.36 mm) is varied from 0.06 GPa to 0.16 GPa with the Young's modulus ranging from 6.07 GPa to 7.49 GPa. The hardness of the alumina particle increases with the increase of maximum load from 50 to 200 mN, beyond this range the value of hardness diminishes until the end load of 500mN. A similar trend is seen for the smaller zeolite particle in the load range from 50 to 200 mN and then the value of hardness keeps stable beyond that range. Nevertheless, the hardness of the larger zeolite particle continues to rise as indentation load is increased throughout the entire range. The Young's modulus exhibits similar variations for all samples, with a slight increase as maximum indentation load is increased until a maximum load of 200 mN. Beyond this range, there is a slight reduction in Young's modulus, though this is less pronounced for the larger zeolite. Considering the slight variation of Young's modulus and hardness beyond a maximum indentation load of 200 mN (excluding hardness of zeolite 2.0-2.36mm), the maximum load of 200 mN was adopted for the subsequent measurements of Young's modulus and hardness.

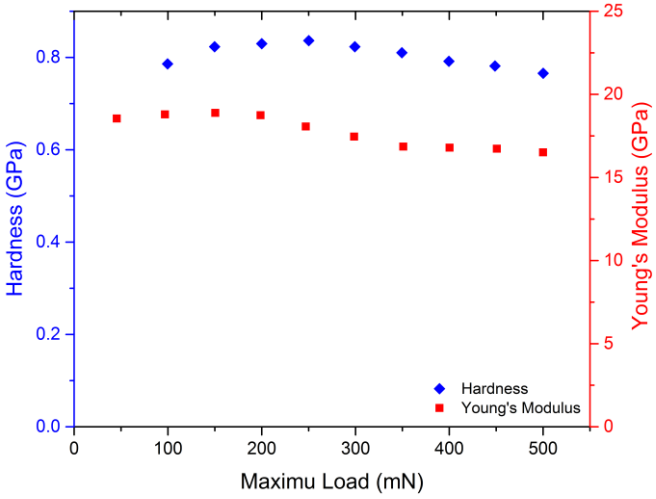

Figure 3.8 Variation of alumina (1.0-1.18 mm) mechanical properties with indent load

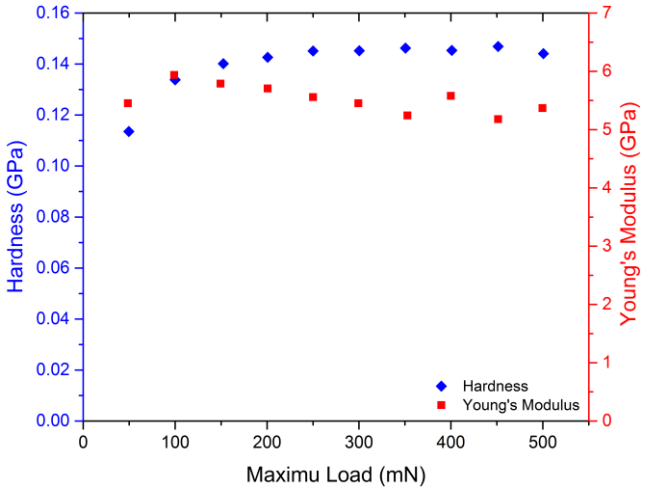

Figure 3.9 Variation of zeolite (1.4-1.7 mm) mechanical properties with indent load

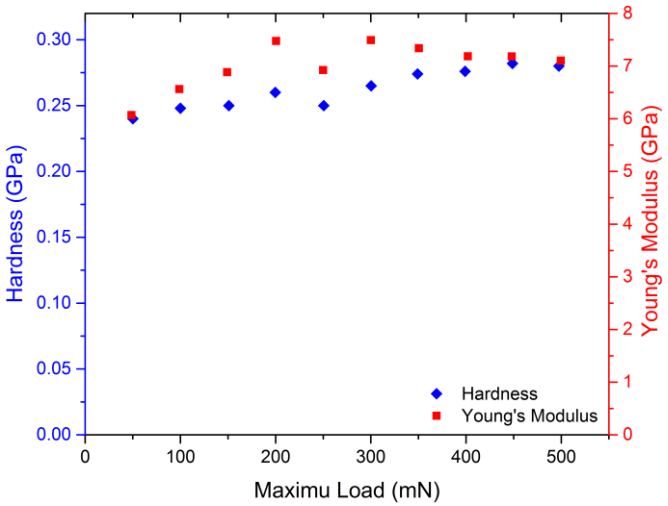

Figure 3.10 Variation of zeolite (2.0-2.36 mm) mechanical properties with indent load

Following the maximum load of 200 mN for each indentation on the same particle, the load-displacement curve for a single particle of alumina and two sizes of zeolite with total nine indentations is shown in Figures 3.11–3.13. As observed in Figure 3.11, the indent number 6 is anomalous with an incredibly large penetration as compared to other indents. Such incident may be accounted by premature detection of a very small force increase prior to the penetration of the true sample surface (e.g. by contacting dust; loose material adhered to the surface, or the tip of a highly rough area). This gives rise to artificially low values of hardness and Young's modulus due to the overestimate of penetration depth and thereby plastic area. In view of this, such incidents in alumina particle and similar incidents of two sizes of zeolite particles as observed in Figures 3.12 (Indents 6, 7) and 3.13 (Indents 1, 5 and 9) are not taken into account in this work. As compared between Figures 3.11-3.13, it infers that the penetration depth of zeolite particle is greater than that of alumina. In other words, for the same applied load zeolite particle has less resistance to deformation than the alumina particle. Hence, the hardness and Young's modulus values of zeolite are lower than that of alumina. The data of average Young's modulus and hardness for all the three particles is tabulated in Tables 3.3 and 3.4 respectively, including all the indents on a given particle.

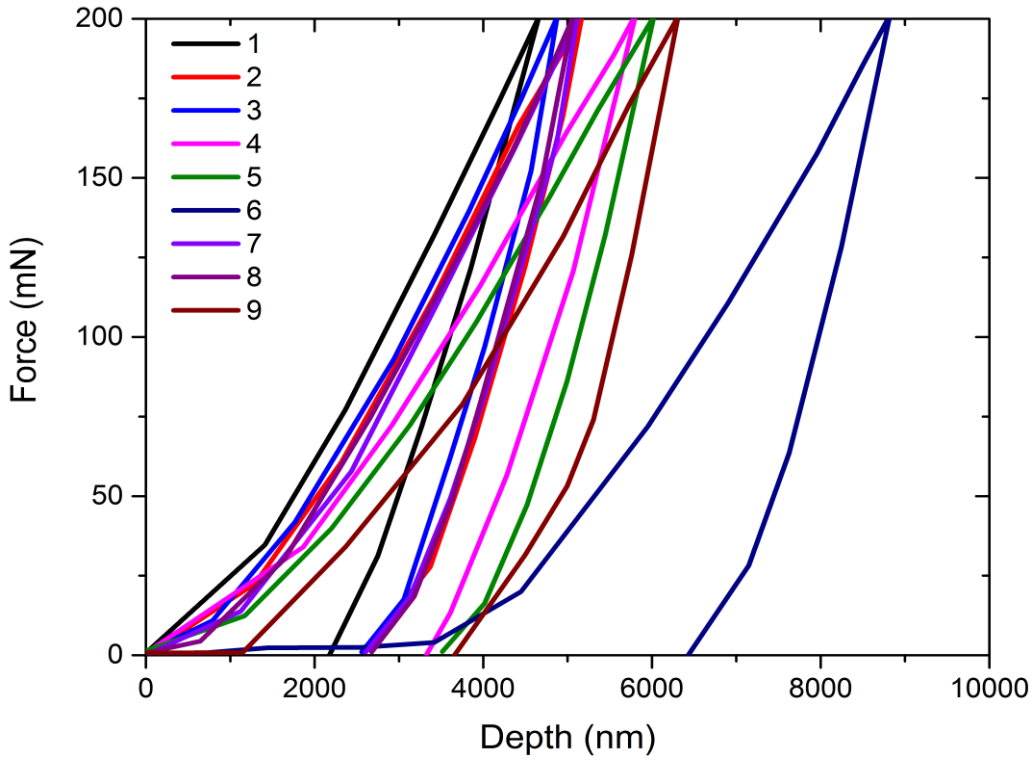

Figure 3.11 Force–displacement for several indents on a single alumina particle

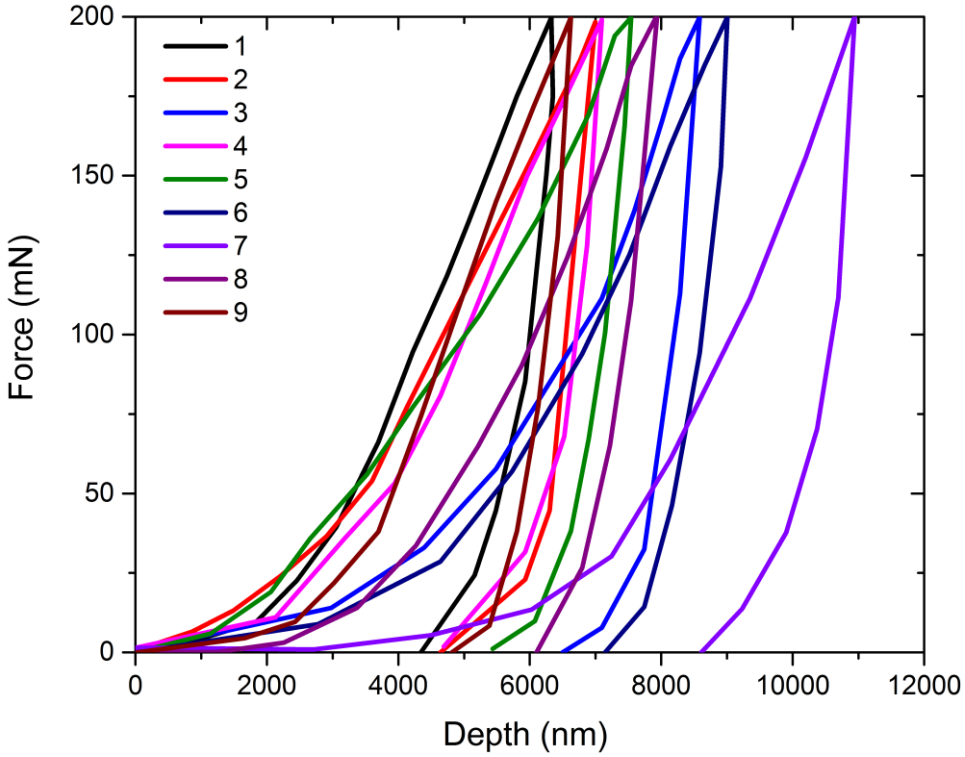

Figure 3.12 Force–displacement for several indents on a single 1.4-1.7 mm zeolite

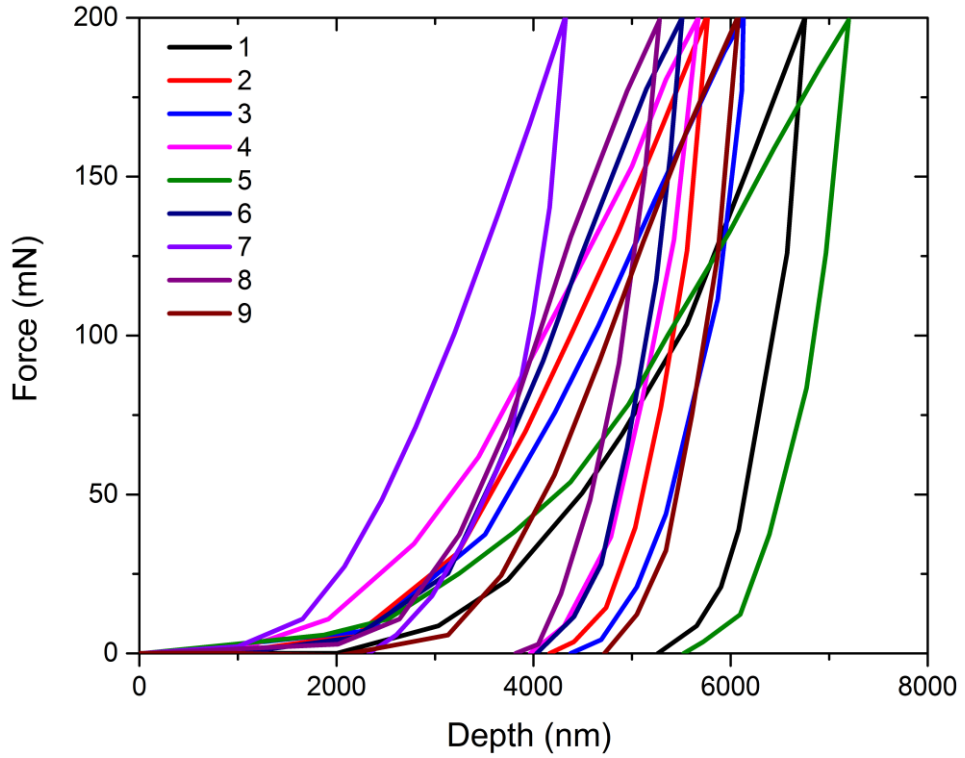

Figure 3.13 Force–displacement for several indents on a single 2.0-2.36 mm zeolite

Table 3.3 Measured Young's modulus of alumina and zeolite

Particle	Young's Modulus (GPa)		
	Alumina 1.0–1.18mm	Zeolite 1.4–1.7mm	Zeolite 2.0–2.36mm
1	22.10	6.38	7.66
2	19.54	6.19	9.89
3	18.02	5.92	8.47
4	14.24	4.89	7.06
5	15.62	6.89	7.89
6	15.61	6.72	11.86
7	4.74	6.35	8.64
8	15.16	5.74	10.03
9	15.11	6.39	9.35
10	13.43	7.74	9.27
Average	15.29	6.26	8.80

Table 3.4 Measured hardness of alumina and zeolite

Particle	Hardness (GPa)		
	Alumina 1.0–1.18mm	Zeolite 1.4–1.7mm	Zeolite 2.0–2.36mm
1	1.05	0.15	0.32
2	0.99	0.24	0.45
3	0.79	0.18	0.38
4	0.64	0.15	0.24
5	0.79	0.21	0.33
6	0.80	0.21	0.56
7	0.50	0.18	0.27
8	0.62	0.13	0.33
9	0.69	0.19	0.32
10	0.62	0.29	0.31
Average	0.75	0.19	0.34

As seen from Tables 3.3 and 3.4, the hardness and Young's modulus for alumina particle 7 is much lower than those of other particles. This behavior is not deemed to provide representative material properties. Such occurrences may be accounted by premature detection of an increase in force before the indenter begins to penetrate the true surface of the particle, which results in artificially low values of hardness and Young's modulus due to the overestimate of plastic depth. It is also noted that the difference of elastic moduli between Tables 3.1 and 3.3 is due to different measurement methods used compared to the manufacturer.

Considering a rapid reduction in penetration depth towards the end of unloading, only a portion of the unloading curve is usually considered to determine the unloading stiffness. The above results were measured using the unloading curve from 40% P_{max} to P_{max}. As a comparative analysis, the variation of Young's modulus and hardness for endpoint from 20%-60% P_{max} is investigated for 1.0-1.18 mm alumina, 1.4-1.7 mm zeolite and 2.0-2.36 mm zeolite in Figures 3.14-16. It indicates from Figure 3.14 that the variation of measured material properties of alumina is negligible (<1%) regardless of the choice of endpoint from 20%-60% P_{max}. This conclusion is also applicable to the variation of hardness for the two sizes range zeolite. However, an increase in Young's modulus is witnessed by 7% and 5% for 1.4-1.7 mm zeolite and 2.0-2.36 mm zeolite when the endpoint is moved from 40% to 60% of P_{max}. This variation is not considered as significant and the endpoint of 40 % P_{max} is chosen by default for the material property measurement.

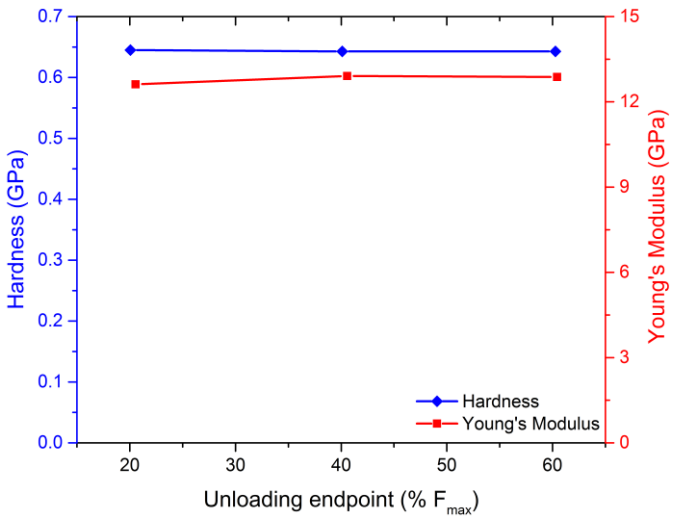

Figure 3.14 Influence of unloading endpoint on alumina properties

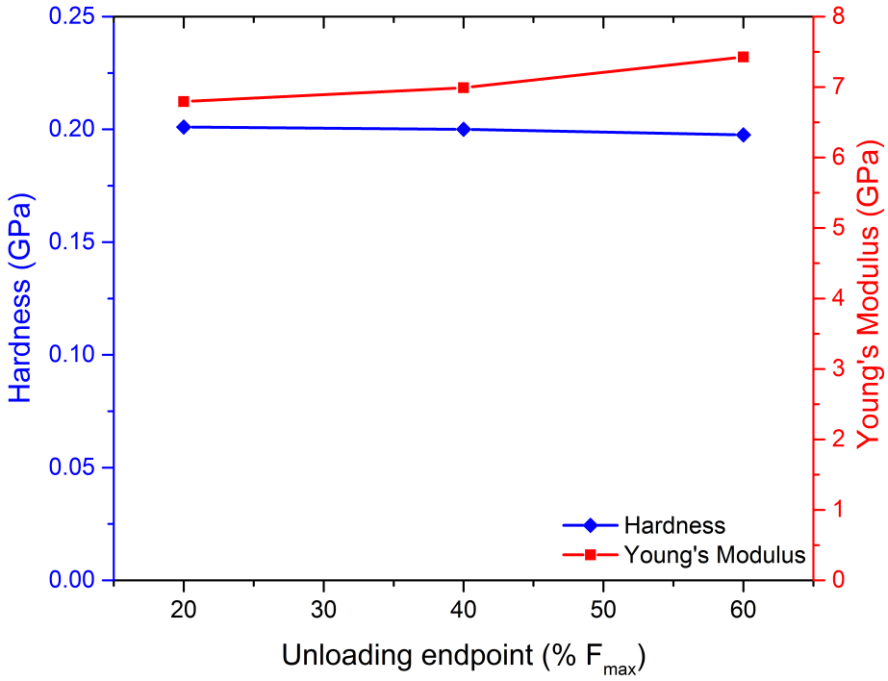

Figure 3.15 Influence of unloading endpoint on 1.4 – 1.7 mm zeolite property

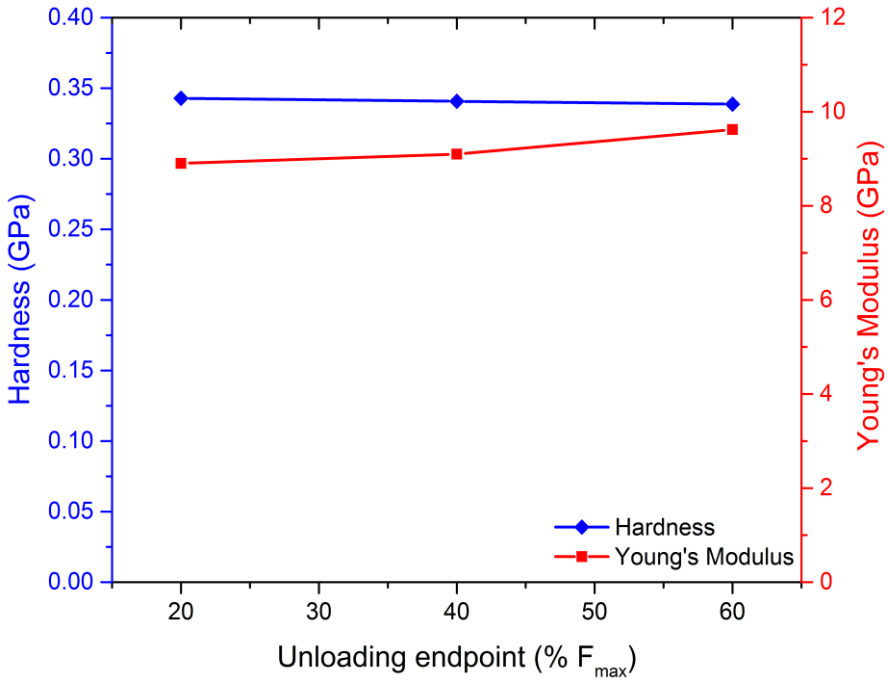

Figure 3.16 Influence of unloading endpoint on 2.0–2.36 mm zeolite property

Table 3.5 shows the statistics of hardness and Young's modulus for all acceptable indents on each of the particles. There is a wide scatter of the measured data with the maximum coefficient of variation 50.5% for alumina hardness and the minimum

coefficient of variation 20.5% for zeolite hardness. Also, the scatter of hardness is slightly larger than that of Young's modulus. This is presumably due to the discrepancy in stiffness estimate leading to an inaccuracy in h_{max} and such error is squared to determine the hardness.

Table 3.5 Statistics of measured hardness and Young's modulus

Analysis	Alumina 1.0–1.18mm		Zeolite 1.4–1.7 mm		Zeolite 2.0–2.36 mm	
	H (GPa)	E (GPa)	H (GPa)	E (GPa)	H (GPa)	E (GPa)
Average	0.75	15.29	0.19	6.26	0.34	8.80
Minimum	0.24	3.84	0.09	3.90	0.15	5.35
Maximum	2.88	46.99	0.40	9.99	0.78	16.04
Stand. dev.	0.38	6.55	0.07	1.28	0.13	2.18
Coefficient of variation	50.50%	42.87%	36.06%	20.52%	37.27%	24.75%

3.4.2 Fracture toughness

Fracture toughness was measured by the synergic action of microindentation and SEM. Initially, 40 particles of each material and size class were indented by the prescribed load (5 N for zeolite and 10 N for alumina). However, some particles were too fragile to bear the applied load and therefore were broken. The remainder was imaged by SEM to determine crack length. The number of indents and generated crack for the remaining particles is tabulated in Table 3.6.

Preliminary indents on alumina shows that the applied load up to 10 N was insufficient to generate a measurable crack. However though, many alumina particles indented at

10 N yielded cracks that were too long to measure under SEM. There is no prior knowledge of applied load required to generate a measurable crack length due to the inherent variability of particle strength. Nevertheless, several particles did result in cracks that could be readily measured, which is exemplified in Figure 3.17.

Table 3.6 Number of generated cracks

Material	Particles showing cracks	Total number of cracks
Alumina 1.0–1.18 mm	3	7
Zeolite 1.4–1.7 mm	9	19
Zeolite 2.0–2.36 mm	11	23

The distance from the center of the indent to the boundary of the indent, a, was measured as shown in Figure 3.17a using ImageJ software. The radial crack length, l, was measured at a higher magnification (Figure 3.17b) using the same software. The average value of Young's modulus and hardness for the particles were adopted to determine fracture toughness. It should be noted that the value of fracture toughness reported here is based on radial crack since only radial cracks were generated and measured for consideration.

Figures 3.18 shows examples of generated cracks in zeolite particles at 1.4–1.7 mm and 2.0–2.36 mm respectively. The values of a, l, c and the resulting K_c are evaluated and reported in IFPRI final report (Hare et al., 2014). The statistics of measured fracture toughness for particles is summarized in Table 3.7. The alumina particle has a higher average value of fracture toughness and the fracture toughness of zeolite increases with size. The fracture toughness is more scattered in zeolite, particularly in larger zeolite particles. This is probably due to comparatively small cracks generated in particles 1 and 2.

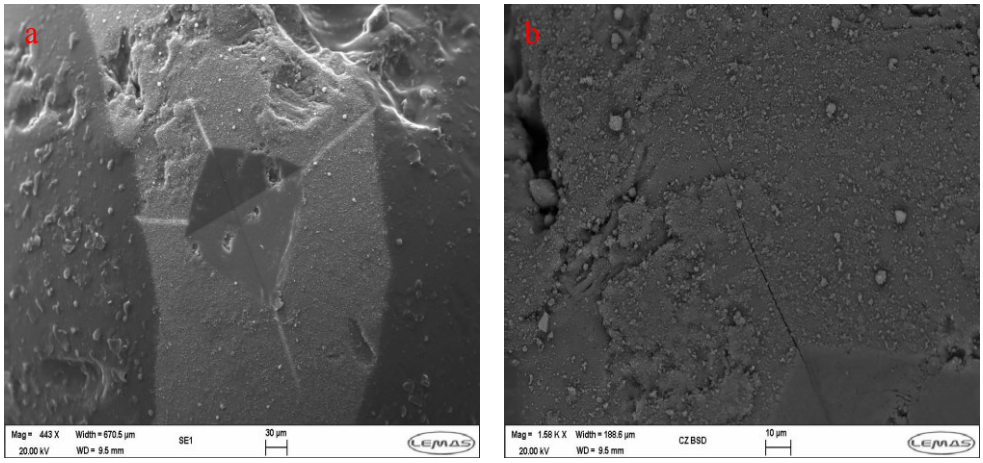

Figure 3.17 Measurable cracks generated in an alumina particle and higher magnification image of crack

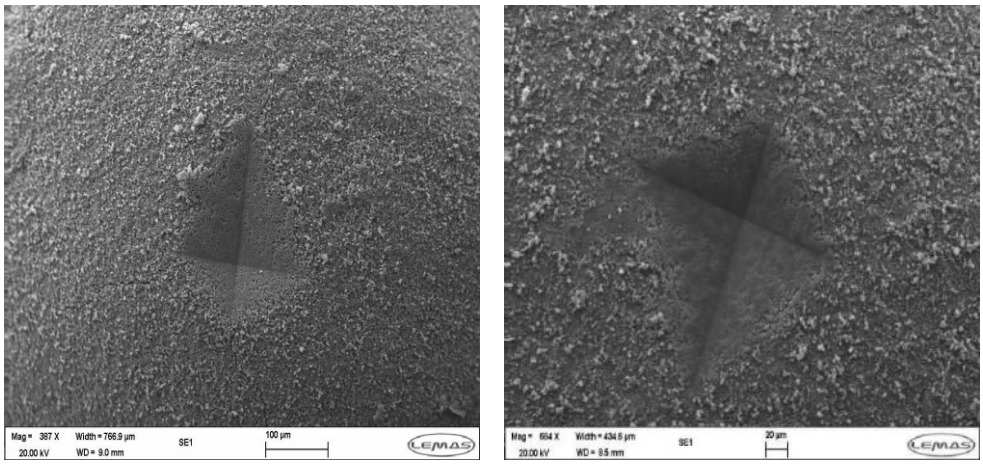

Figure 3.18 Cracks generated in a 1.4-1.7 mm zeolite particle and cracks generated in a 2.0-2.36 mm zeolite particle

Table 3.7 Summarized fracture toughness values

Material / Fracture toughness	Alumina (1.0–1.18mm)	Zeolite (1.4 – 1.7 mm)	Zeolite (2.0 – 2.36 mm)
Average ($MPa.m^{1/2}$)	0.29	0.13	0.19
Minimum ($MPa.m^{1/2}$)	0.17	0.03	0.07

Maximum ($MPa.m^{1/2}$)	0.41	0.31	0.72
Standard Deviation ($MPa.m^{1/2}$)	0.07	0.07	0.17
Coefficient Variation	24.9%	58.0%	88.9%

3.5 Single particle impact test

Single particle impact test was carried out to observe the single particle breakage behaviour subject to impact loading. The breakage pattern was identified from low to high impact velocities. The influence of impact velocity and impact angle on particle breakage ratio was investigated. The breakage event was captured by high–speed imaging technology and the particle size distribution after impact was evaluated. It is hoped to develop an improved understanding of underlying breakage mechanism based on the phenomenon observed from single particle impact test.

3.5.1 Single particle impact tester

A schematic diagram of the impact test rig is shown in Figure 3.19 which consists of a vibratory feeder to feed the particle into the glass tube automatically. The single particle impact tester was developed by Yuregir et al. (1986) as vertical impact system and subsequently used by Ghadiri and co-workers (1993, 1996, 2003 and 2015) to assess the breakage propensity. The single particle impact tester was provided by the courtesy of Prof. Mojtaba Ghadiri in the University of Leeds. Details of the impact testers are given below.

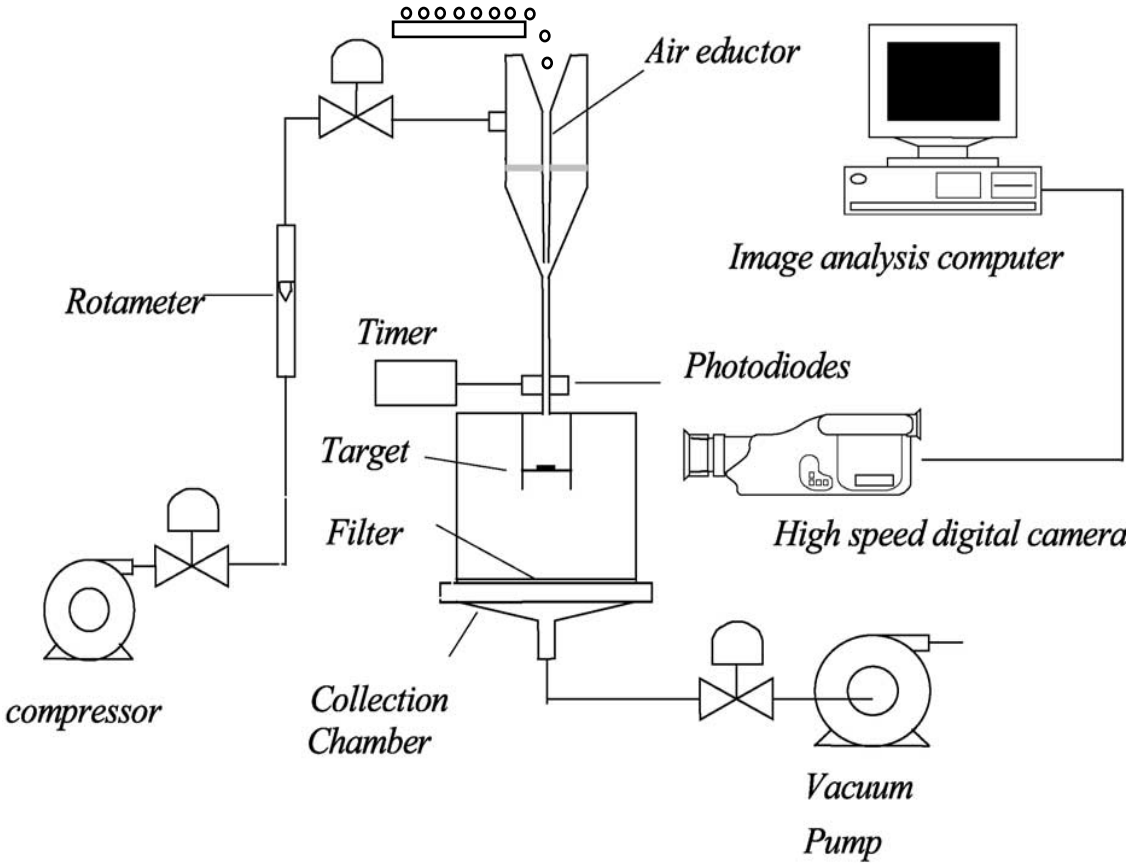

Figure 3.19 Sketch of single particle impact tester
(After Samimi et al., 2003)

The impact tester is equipped with an air eductor and a vacuum line. A line of compressed air is mounted near the top of the eductor, which accelerates the feed particles to the desired velocity. The accelerating tube is made of glass with its internal diameter 20mm and its length 1m. The particle velocity is measured by means of parallel photo–diodes with the vertical distance 28mm. When the particle travels through the photo–diodes, the duration of flight is recorded by the timer and hence the impact velocity could be determined. The impact velocity could be controlled by the air difference through the accelerating tube.

For a single particle under oblique impact, the impact angle is denoted by the acute angle between the particle impact direction and the impact target plane (Figure 3.20). By other words, normal impact refers to the impact angle 90^{o} between the impact direction and the impact target plane. The target material is made up of sapphire and stainless steel under normal and oblique impact loading respectively. The selection criteria of the target material is that it should be significantly stiffer and harder than the

impact material (Papadopoulos, 1998). Herein, the Young's modulus of sapphire (430 GPa) and stainless steel (190–200 GPa) are much higher than those of alumina (15.29 GPa) and zeolite (6.6–8.8 GPa).

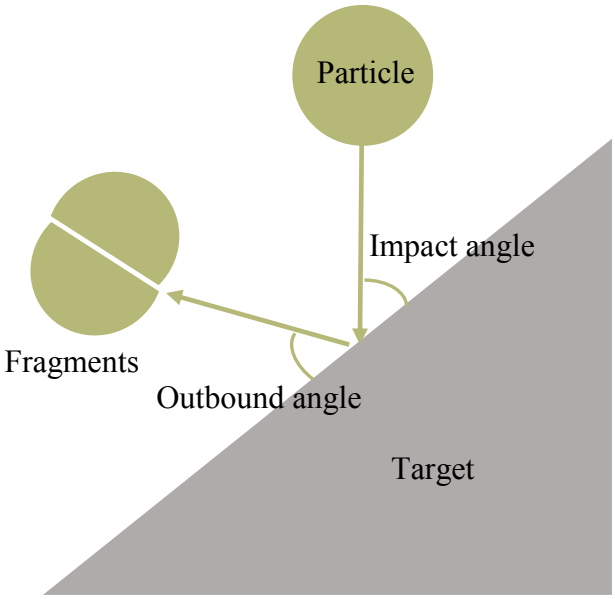

Figure 3.20 Sketch of impact angle

In this work, the feed mass of zeolite particles was typically 5 g of sieved sample (1.4–1.7 mm) consisting of more than 2000 particles. The particle was accelerated by the pressure difference between the ambient and the vacuum pump up to 30 m/s. The target was housed in a Perspex collection chamber and the impact product was collected and sieved after each impact event.

3.5.2 Particle breakage ratio definition

The breakage ratio R is calculated via the mass of debris divided by the total mass of mother particles (M_m) and debris mass (M_{de}).

$$R = M_{de}/(M_{de} + M_m) \tag{3.9}$$

where debris is defined as the particles with two sizes below the lower feed size. The initial mass of fed particles was weighed before impact and the mass of particles after impact was scaled to calculate breakage ratio as a function of the mother particles mass (M_m) and debris mass (M_{de}). The size of zeolite is sieved to the regime of 1.4–1.7 mm

beforehand to reach a comparable size ratio between neighbouring sieves. The impacted particles were sieved by using two sizes below the lower feed size according to British Standard Sieves 410. As for the zeolite (1.4–1.7 mm), the size of fragment below 1.0 mm is regarded as debris while the size of fragment above 1.0mm is regarded as mother particles.

3.5.3 Breakage ratio at varying impact velocity and impact angle

Single impact tests of feed zeolite (1.4–1.7 mm) were carried out under a laboratory condition with relative humidity of 25–30% and ambient temperature of 20–25^{o}C. The breakage ratio of zeolite was calculated over an impact velocity range from 5m/s to 30m/s under four impact angles, namely 30^{o}, 45^{o}, 60^{o} and 90^{o} (normal impact). The impact angle is denoted by the acute angle between the particle impact direction and the impact target plane. The breakage ratio of zeolite (1.4–1.7 mm) is presented in Figure 3.21 below at varying impact velocity and impact angle.

As seen from Figure 3.21, the breakage ratio of zeolite is negligible for all impact angles below impact velocity of 15 m/s. However, the breakage ratio increases dramatically over 15 m/s with increasing impact angle. The breakage ratio difference between normal impact and 60° impact is not pronounced. The breakage ratio under 45^{o} impact deviates from both preceding impact trend whereas the breakage ratio of zeolite under 30^{o} shows the slowest growth until higher impact velocity. It also demonstrates that the breakage ratio increases with the increasing impact angle. This infers that the normal component velocity plays a dominant role in particle breakage, which agrees well with previous studies (Papadopoulos, 1998; Cheong 2003).

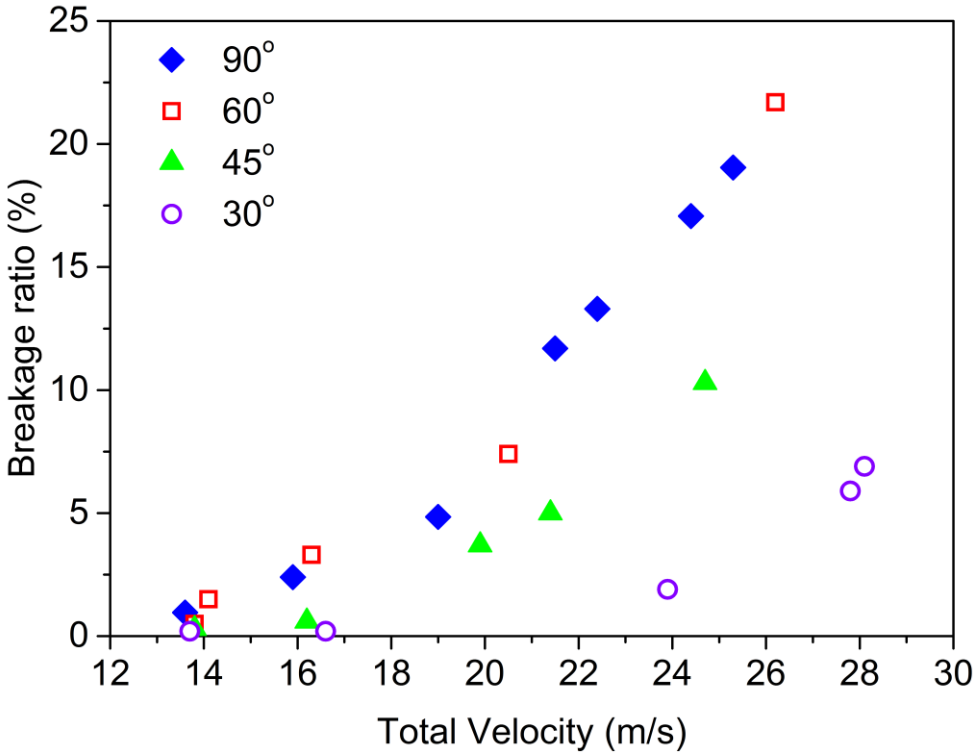

Figure 3.21 Breakage ratio of zeolite (1.4-1.7 mm) at varying impact velocity and impact angle

3.5.4 Influence of tangential component velocity

The effect of impact angle has been widely studied by previous work with the emphasis on normal component velocity. For example, Salman et al. (2002) examined the effect of impact angle on alumina particle fragmentation and found two types of fragmentation, i.e. normal fragmentation and oblique fragmentation. The noticeable difference for oblique impact is the asymmetry of oblique fragmentation as compared to normal fragmentation. Cheong et al. (2003) investigated the effect of impact angle on the size distribution and it was concluded that normal component velocity is the main driving force for breakage, which is in accordance with the work from Samimi et al. (2004) and Subero et al. (2005). Comparatively, there are few investigations of tangential component velocity as compared to normal component velocity in the published literature. Traditionally, the influence of tangential component velocity is ignored in previous research.

To investigate the effect of tangential component of impact velocity, zeolite particle was impacted at the same normal component velocity under four impact angles. Particle breakage ratio at low and high impact velocity was measured and hence the effect of

tangential component velocity could be identified. The breakage ratio of zeolite (1.4–1.7 mm) is shown in Table 3.8. The breakage ratio of zeolite particle under normal component and tangential component velocity is shown in Figure 3.22.

Table 3.8 Breakage ratio of zeolite (1.4–1.7 mm) under impact

Test	Zeolite (1.4-1.7 mm)							
Impact angle (°)	30	30	45	45	60	60	90	90
Total velocity (m/s)	16.4	28.1	12	19.9	10	16.2	8.3	13.6
Normal velocity (m/s)	8.2	14.1	8.5	14.1	8.7	14.0	8.3	13.6
Tangential velocity (m/s)	14.2	24.3	8.5	14.1	5.0	8.1	0	0
Breakage ratio (%)	0.2	6.9	0.4	3.7	0.5	3.1	0.2	1

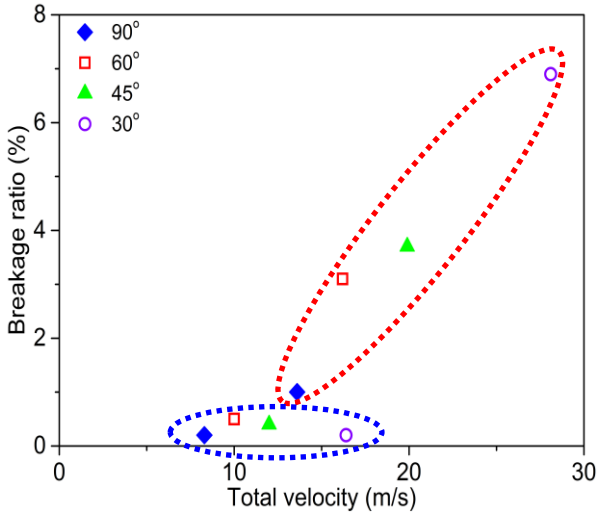

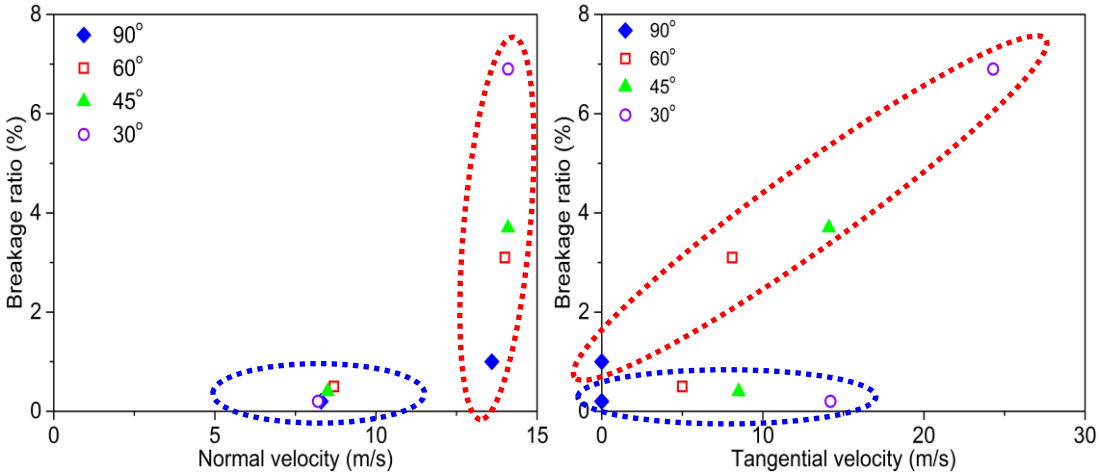

Figure 3.22 Breakage ratio versus normal component velocity (left) and tangential component velocity (right)

Figure 3.22 shows that there is no much difference of breakage ratio irrespective of the impact angle at low impact velocity whereas the breakage ratio becomes dramatically different at high impact velocity. Under a constant normal velocity, the breakage ratio increases with the increase of tangential velocity. It may be concluded that tangential velocity becomes increasingly important along with the increase of total velocity although normal velocity plays a dominant role in particle breakage. It should be noted that traditional models for predicting particle breakage predominantly consider only the normal velocity component and consequently fall short in predicting the contribution of tangential velocity component. A new particle breakage model is thus required to enable the contribution of both the normal and tangential impact velocity to be rationalized. The model development including the effect of impact angle will be described in details in Chapter 5.

3.5.5 Impact images using high-speed camera

High-speed camera was used to capture the images of single particle before and after impact. Each particle is coloured by blue and red with orthogonal circles. Zeolite particles were accelerated in the tube to impact the target at four impact angles, i.e. 30°, 45°, 60° and 90°. The successive images of zeolite (1.4-1.7 mm) which unveil the impact behaviour of particle are shown below:

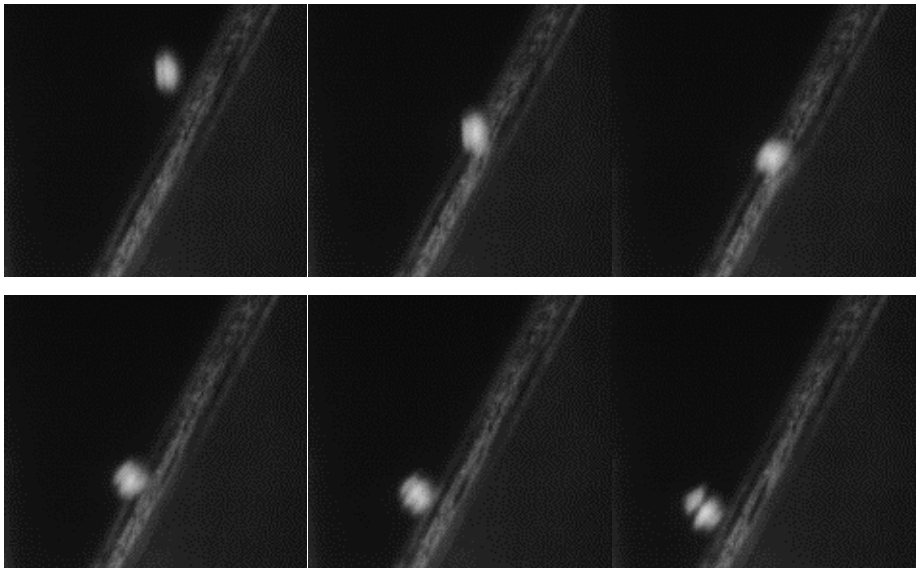

Figure 3.23 Impact sequence of zeolite (1.4-1.7 mm) under incidence angle 30^{o} impact (impact velocity=24.0 m/s) at a recording rate of 16800 fps

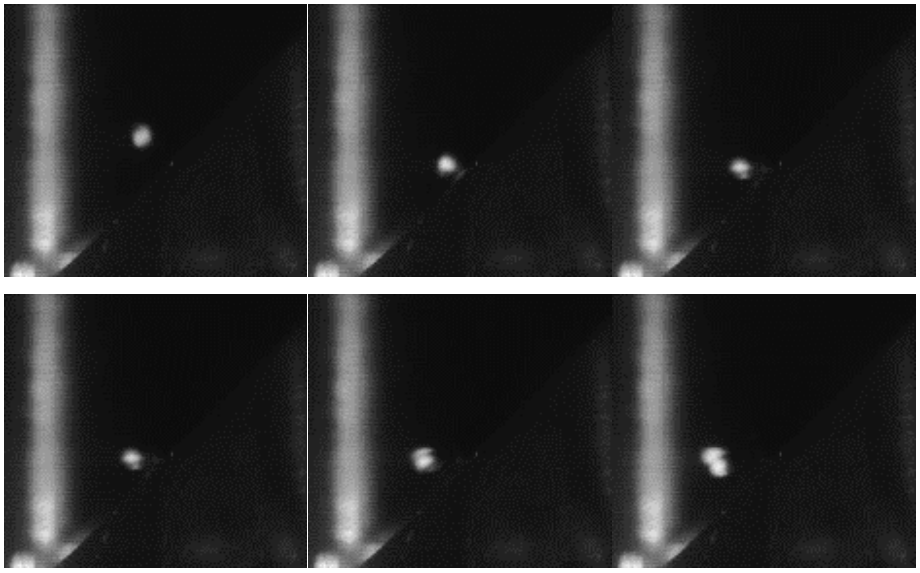

Figure 3.24 Impact sequence of zeolite (1.4-1.7 mm) under incidence angle 45^{o} impact (impact velocity=24.6 m/s) at a recording rate of 16800 fps

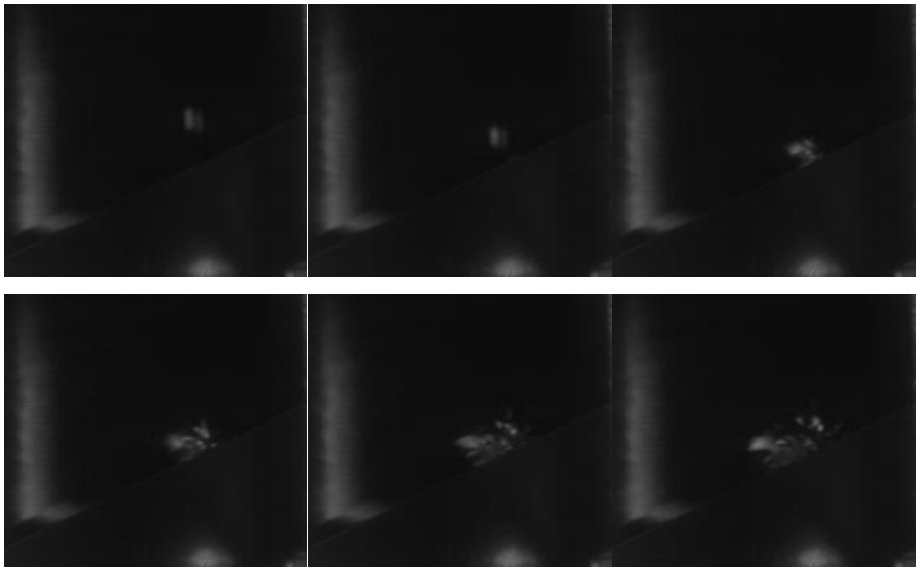

Figure 3.25 Impact sequence of zeolite (1.4-1.7 mm) under incidence angle 60^{o} impact (impact velocity=26.7 m/s) at a recording rate of 16800 fps

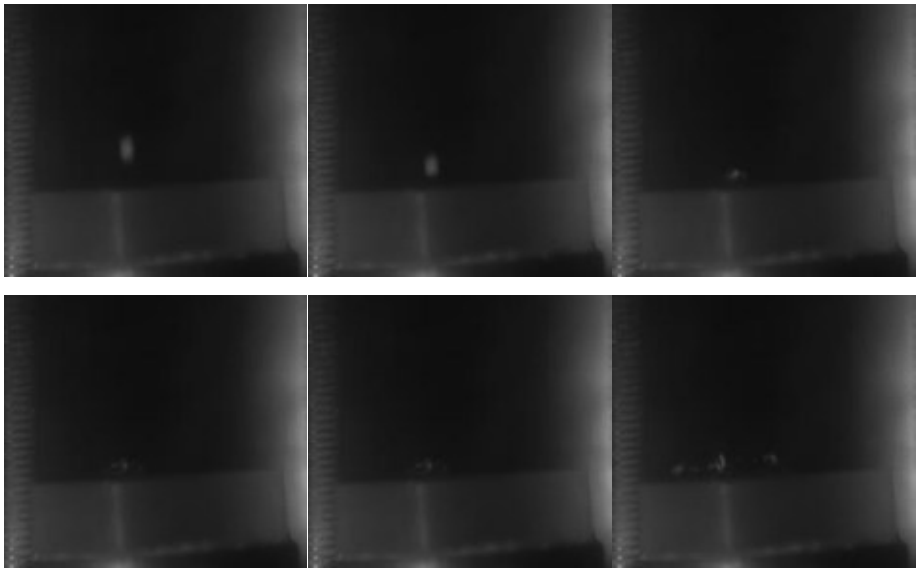

Figure 3.26 Impact sequence of zeolite (1.4-1.7 mm) under incidence angle 90^{o} impact (impact velocity=24.0 m/s) at a recording rate of 16800 fps

The images were recorded at the rate of 16800 frames per second. Figures 3.23-3.26 show the high velocity impact sequence of zeolite (1.4-1.7 mm) at four impact angles. It should be noted that the particle breaks into two pieces after contact with the target under 30^{o} and 45^{o} impact whilst the fragment happens under 60^{o} and normal impact at the instant of contact between particle and target. Particle orientation cannot always be captured in the high-speed camera since the contact location between the particle and target is randomly distributed.

Table 3.9 shows the measured values of incidence and outbound velocity of particle under impact, which are determined in ImageJ software. The impact and outbound velocity are determined from the calibrated pixel length and corresponding time elapse. The outbound velocity and angle refer to the corresponding value of main fragment of virgin particle after impact. Refer to Figure 3.20 for the impact and outbound angle.

Table 3.9 Measured value of incidence and outbound velocity and angle from high–speed camera

Impact angle (°)	Impact Velocity (m/s)	Outbound velocity (m/s)	Outbound angle (°)
30	24.0	19.79	22
45	24.6	16.19	35
60	26.7	14.39	26
90	24.0	3.07	28

It indicates that the outbound velocity is smaller than those values before impact. Note that typically only impact energy by normal component velocity is considered in grinding system in the literature. The effect of velocity component perpendicular to Figures 3.23-3.26 is not considered in this project. It will be interesting to investigate the particle breakage from the perspective of energy loss. However, research in this respect is beyond the scope of this project.

3.5.6 Particle size distribution

The size distribution of particles under the impact tests was analyzed using sieving analysis. The mass of products after impact in each sieve was measured and the mass versus sieve cut is plotted accordingly. Figure 3.27 and Figure 3.28 compare the size

distribution of zeolite (1.4–1.7 mm) for different impact velocities under normal and 30 deg. impact respectively.

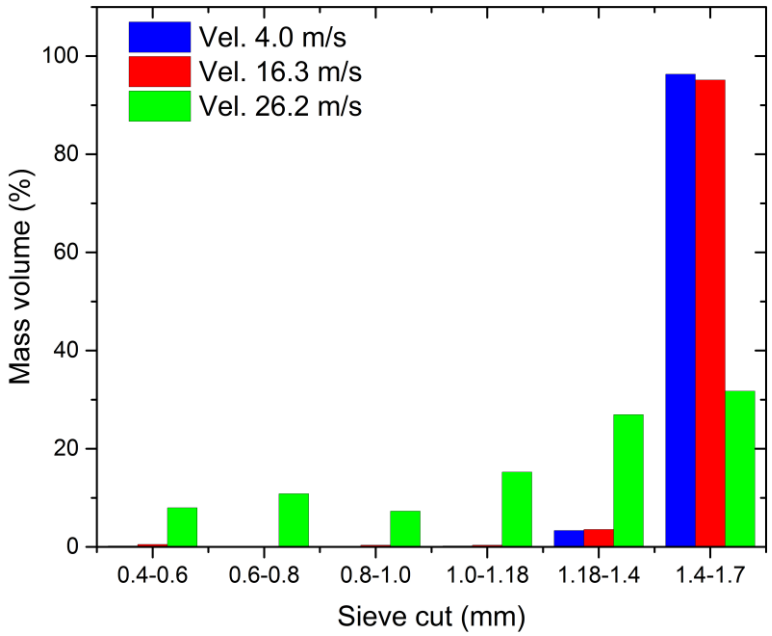

Figure 3.27 Size distribution of zeolite (1.4–1.7 mm) under normal impact

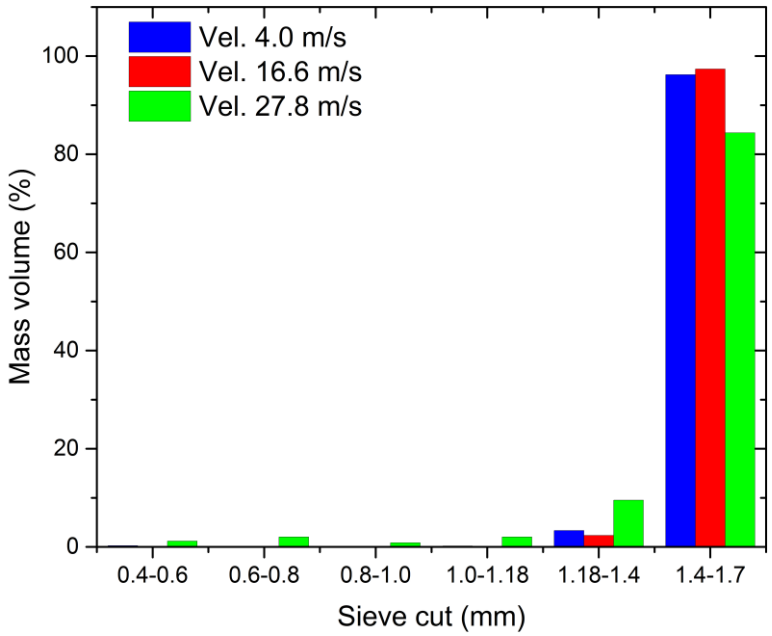

Figure 3.28 Size distribution of zeolite (1.4–1.7 mm) under 30^{o} impact

It indicates that the volume of feed particles diminishes with the increasing impact velocity. The size distribution is similar at low and medium impact velocity irrespective of impact angle.

Chipping is dominant at the low and medium impact velocity for both 30^o and normal impact since feed particles account for the majority of the mass volume proportion. However, the situation of normal and oblique impact becomes different under the high impact velocity. As for the normal impact, the volume of feed particles plummets to 32% in which fragmentation is dominant in this case. In contrast, the volume of feed particles accounts for 85% under 30^o impact. It suggests that more fragments are generated under normal impact as compared to oblique impact at high impact velocity and chipping is prone to happen under oblique impact and low impact velocity.

3.6 Summary

Grindability test was carried out to investigate the material properties and loading response of single particle subject to the stressing event of indentation and impact loading pertinent to grinding processes. Two materials: zeolite and alumina were selected as test particles considering the isotropic and well–defined properties as well as industrial interest.

The mechanical properties of alumina and zeolite particles were assessed by nano and micro indentation. Nanoindentation was used to measure the hardness and Young's modulus whilst microindentation combined with SEM was used to measure fracture toughness. It was found that alumina has the greater value of hardness and Young's modulus than zeolite. A relatively high coefficient of variation was observed with 40-50% for alumina and 20-40% for zeolite. In terms of microindentation, less measurable cracks were generated in alumina particles as compared to zeolite with the force applied because the fracture toughness of alumina was greater than that of zeolite. The coefficient of variation was relatively low for alumina (25%) but very high for zeolite (58% and 89% for the smaller and larger particles, respectively). The measured mechanical properties suggest that alumina is more resistant to breakage than zeolite.

The breakage propensity of zeolite (1.4-1.7mm) was evaluated under impact loading by observing the breakage behavior and interpreting the breakage results. Single particle impacts were performed in a range of impact velocity up to 30 m/s. The breakage ratio of zeolite increases with the growth of impact velocity and normal component velocity was found to play a key role in particle breakage. However, the significance of

tangential component velocity was identified to play an increasing role with the increasing impact velocity. Considering the lack of tangential component contribution in all existing models, it is required to incorporate the effect of impact angle in the particle breakage model. Two breakage patterns, i.e. chipping and fragmentation were observed and the breakage pattern is transformed from chipping to fragmentation alongside the increase of impact velocity.

To summarize, the measured mechanical properties from indentation test provides mechanical insight into particle breakage and the linkage with particle breakage model development. The significance of tangential component velocity identified in the single particle impact test necessitates the incorporation of tangential component velocity in particle breakage model.

Chapter 4

In-situ loading test of individual particles by X-ray μCT

4.1 Introduction

X-ray microcomputed tomography (μCT) is fast becoming a popular tool for the non-destructive 3D characterization of materials because of its micron to sub-micron ultimate resolution enabling clear and distinct visualization of a material's internal density structure. The technique of X-ray μCT is based on the attenuation of a transmitted X-ray beam as a consequence of the differing mass attenuation characteristics of the different materials comprising the sample being analyzed. Due to its high resolution, X-ray μCT has emerged as an effective solution to gain insight into micromechanical processes that occur during the deformation of granular media (Cil and Alshibli, 2012). For example, Parab et al. (2014) investigate the fracture of individual sand particles under compressive loading using X-ray imaging. Breaking into large sub-particles followed by pulverization was observed under static compressive loading. Russell et al. (2015) presented the macroscopic breakage and fragmentation pattern recorded using X-ray μCT. They made a surmise that the moisture content concentrated at the material flaws in the structure such as micro-cracks behaves as active centers of incipient stressing by transmitting stresses and causing several internal distortions at multiple locations within the granules. Zhao et al. (2015) developed a mini-loading apparatus to investigate the fracture patterns of tested particles using in-situ X-ray CT. It was found that particle morphology and initial microstructure are two important factors in determining the fracture patterns of particles.

Digital image correlation (DIC) has become a powerful and effective tool for 2D and 3D deformation measurement and is used extensively in the field of experimental mechanics (Schreier and Sutton, 2002). A variety of applications have demonstrated the versatility of this method (Schreier and Sutton, 2002). The method serves to measure full-field displacement at pixel level by establishing the correspondence of subsets between undeformed and deformed states. In particular, the combined use of high resolution X-ray computed tomography with digital image correlation (DIC) is able to

provide quantitative measurement of the three-dimensional deformations within a material when it is strained (Marrow et al., 2014). Lenoir et al. (2007) presented an example of volumetric digital image correlation applied to X-ray μCT from triaxial compression tests on argillaceous rock. Hall et al. (2010) quantified the onset and evolution of localized deformation processes in sand with grain-scale resolution using the combination of X-ray imaging and DIC. Through an incremental analysis of consecutive steps, it shows that the strain localization begins before the peak stress. More examples of the combined usage of X-ray imaging and DIC include crack propagation in quasi-brittle material, sub-indentation radial and lateral cracking growth and plastic deformation underneath indentation, which can be found in details elsewhere (Marrow et al., 2014).

The main objective of this chapter is to examine the microstructure of selected particles, to visualize the progressive failure process and to evaluate the progressive failure using the technique of digital image correlation (DIC). Section 4.2 describes the basic principle of X-ray CT and Section 4.3 presents the experimental protocol of in-situ loading tests where the in-house loading apparatus was designed and manufactured. Image processing is given in Section 4.4 including data acquisition, image reconstruction, drift correction, volume rendering and crack representation by segmentation. The stepwise loading results of six zeolite particles are presented in Section 4.5 whilst the breakage patterns of particles are discussed in Section 4.6. Section 4.7 introduces the basic principle and calculating procedure of digital image correlation (DIC). The DIC results are given to evaluate the localized deformation of particle under progressive loading in Section 4.8. As a further exploration of X-ray μCT, Section 4.9 characterizes the principle curvature using different fitting methods and investigates the influence of contact curvature on the deduced Young's modulus during the elastic deformation of a particle, which is the second part of this chapter.

Part I

4.2 Basic principle of X-ray CT

A typical CT scanner is equipped with an X-ray source and a detector with the scanned sample in between, situated on a rotating sample manipulator (Figure 4.1). During each scanning rotation, the flux of X-ray that passes through the sample is detected by the

detector and the sample is rotated through 360°. An X-ray image is collected at equally spaced points, which records the X-ray attenuation through the body of sample. For homogenous material, the attenuation of monochromatic X-rays is related to the length of the X-ray path through the sample (x) and the linear attenuation coefficient (μ) of the sample material at the X-ray energy deployed. It gives:

$$I = I_0 \exp(-\mu x) \tag{4.1}$$

where I_0 is the initial X-ray intensity.

For inhomogeneous materials, the attenuation of X-rays (I) can be expressed by:

$$I = I_0 \exp\left(-\int \mu(x)\, dx\right) \tag{4.2}$$

where $\mu(x)$ is the attenuation coefficient of the material associated with x. It should be noted that Eq. (4.2) is true for a single X-ray source energy. Since μ varies with X-ray energy for any material, in a real scanner the attenuation is the integral of Eq. (4.2) over all X-ray energies of a polychromatic source. $\int \mu(x)\, dx$ is called line integral of the linear attenuation coefficients. These integrals are defined as 'raw data', which are then passed through an image reconstruction method. The pixel values in generated cross-sectional images correspond to the value of linear attenuation coefficients. Johann Radon (1917) first stated that a three-dimensional object can be reconstructed from an infinite set of two-dimensional projections at varying angles, which laid the theoretical background for tomographic image construction.

The first generation of CT scanner was developed by Godfrey Hounsfied in 1967. Its principle is to capture a beam of X-rays using a single detector element. The beam of X-rays corresponds to the integral of linear attenuation coefficients along a single line. Then the single detector system moves horizontally to capture the integral of next line. After all the line integrals for a given position are acquired, both the detector and X-ray source are rotated with one degree by the design called as translate-rotate or pencil-beam scanner.

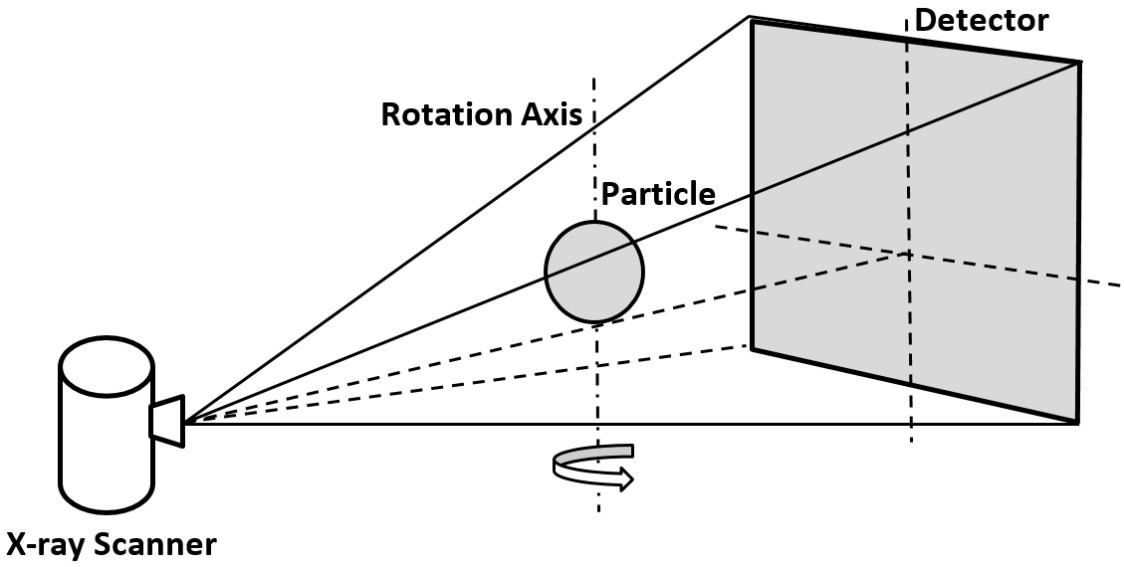

Figure 4.1 Sketch of X-ray CT principle

As a mature technology, the cone beam computed tomography has shown its promise as an alternative to conventional CT scanners like fan-beam geometry. The detector of a cone beam scanner allows, for a single rotation of the sample, to generate a scan of the full sample. The main advantage of such system is that it enables faster data acquisition acquisition and uses a comparatively less expensive radiation detector. Further details regarding the principles of first generations and cone beam CT scanners should refer to Sukovic (2003) and Goldman (2007). As for the type of scanner used in this study, cone beam CT scanner is chosen due to its scanning efficiency and lower scanning cost.

4.3 Experimental protocol

The in-situ loading test was carried out at the School of Geoscience from the University of Edinburgh. An in-situ loading apparatus was built which enables the sample to be scanned by the X-ray instrument while under load. The X-ray instrument consists of a 120keV transmission X-ray source with a diamond coated W target, a 4MP flat panel GADOX (Gadolinium Oxysulfide) x-ray camera and an air-bearing rotary table on which the in-situ loading apparatus is mounted. A complete scan is accomplished through 360^{o} rotation and approximately needs 1hr with 1000 radiographs collected. The in-situ loading apparatus and the sketch of the loading apparatus are shown in Figure 4.2 and Figure 4.3 respectively. As shown in Figure 4.3, the press base of the loading frame is attached with the rotary table, which enables the particle to be rotated

during an X-ray scan. The particle is placed between two boron nitride (BN) pistons in the loading frame and is incrementally compressed in 3-6 stages to a maximum load of 100 N by means of a manual micrometer screw thread. The plastic pillar is made of polycarbonate, which is transparent to X-rays. A recess of the plastic pillar was intentionally built so as to reduce the energy loss of X-ray although the plastic pillar is X-ray transparent. The load is measured by means of a strain gauge load cell situated below the lower BN piston. The load cell was provided by OMEGA's LCMKD series with the loading capacity of 100 N. The sketch of LCMKD-100 N is shown in Figure 4.4 and the dimension of the load cell is summarized in Table 4.1 At each static point the incremental loading, a full tomographic data set was collected. Loading proceeds until the particle fails, at which point a final data set was acquired. Between the loading sequences the loading frame is disassembled to change another particle to be tested.

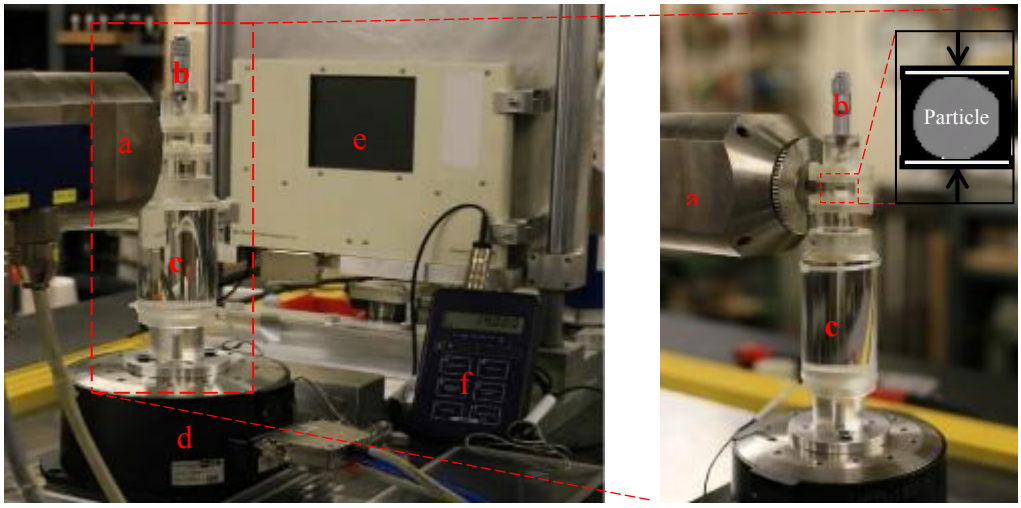

Figure 4.2 In-situ loading apparatus and X-ray scanning instrument

a: X-ray source **b**: barrel as displacement control mode **c**: plastic pillar **d**: rotary table **e**: X-ray detector **f**: meter reading

The particle is placed in a small channel of the in-situ loading rig, which levels up with the X-ray source. The samples used in this study are zeolite particles from the same batch which were tested via indentation and impact in Chapter 3. These particles were provided by CWK Bad Kostritz Gmbh and the specification of tested zeolite particle could be referred to Chapter 3. Six zeolite particles were fed into the channel respectively and compressed increasingly under displacement control loading by screwing the barrel on top of the loading rig. The applied load was recorded by the force

transducer placed beneath the bottom plate and the value of applied load was monitored by the meter reading at every loading stage.

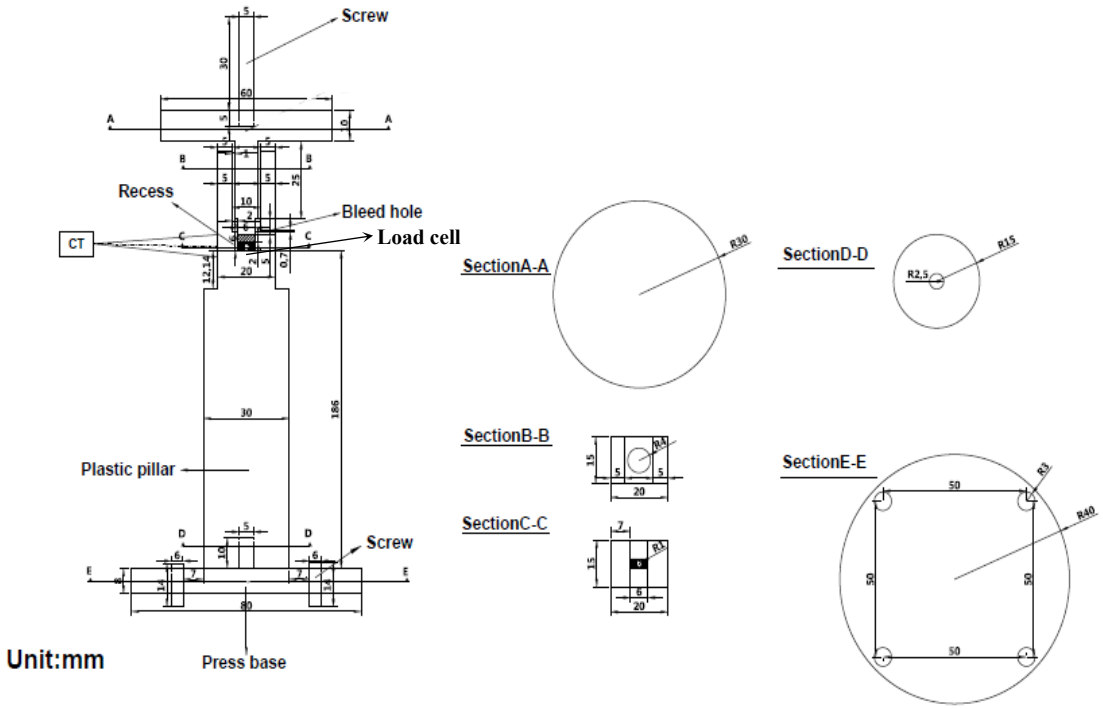

Figure 4.3 Sketch of in-situ loading apparatus

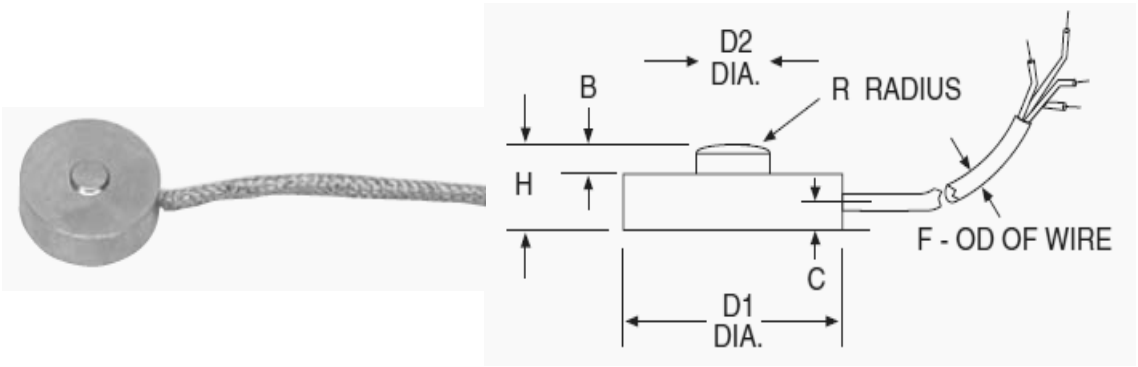

Figure 4.4 Specification of the load cell-LCMKD-100N

Table 4.1 Specification of LCMKD-100 N

Capacity	D_1 (mm)	D_2 (mm)	H (mm)	B (mm)	C (mm)	F (mm)
100 N	9.6	2.2	3.0	0.76	1.0	1.3

4.4 Image processing

4.4.1 Data acquisition

During the rotation of X-ray scan, the projection image is generated by sequential capture of attenuated X-ray beams by the detector. For cone beam geometry, it requires projections images with equal angular separation between 0^o and 360^o. In terms of projections number herein, 1000 projections are collected in the cone beam geometry, which is deemed sufficient for the quality of reconstruction. Alignment of the scanning system is a prerequisite to ensure tomography acquisition with good quality. The beam axis should be aligned with the center of the detector and the rotation axis, and the line joining the x-ray spot, the rotation axis. Apart from the projected images from X-ray scanning, to ensure successful image reconstruction in the following step, two kinds of images are needed, i.e. flat field images and dark images (also known as gain and offset images respectively). Flat field images are used to correct the beam profile and scintillator whereas dark images are used to correct detector features. More information about flat field images and dark images is given in the manual of image processing software Octopus (Octopus Imaging).

4.4.2 Image reconstruction

Image reconstruction is the mathematical process of converting raw data collected via data acquisition into two-dimensional slice images (Ketcham and Carlson, 2001). There are several methods to implement the reconstruction process such as analytical, iterative, back and filtered back projection. Amongst these, filtered back projection is the most widely used method. The advantage of filtered back projection is that blurring resulted from simple back projection could be mitigated with this method. In other words, a filter function is applied to each 2D attenuation profile before performing the back projection. More details regarding the reconstruction method could be found in Hsieh (2009). The software utilized for image reconstruction is Octopus (Vlassenbroeck et al., 2007), which was originally developed for neutron tomography. An Octopus dataset typically includes projection images (raw data), optionally beam profile images (flat images) and dark images (offset images).

4.4.3 Drift correction

In the process of scanning, the particle should be always positioned in the center of rotation axis and the rotation axis should be aligned with the detector to ensure that no spatial motion for the scanned particle occurs to obtain projection data with high quality. However, in practice, there is some shift in orientation and movements which are mainly affected by the external scanning environment, and potentially by drift of the X-ray spot of the transmission source. The sketch of rotation offset is shown in Figure 4.5. It can be seen that the particle in Figure 4.5a is positioned in the center of rotation axis at angle θ_1 whilst the particle in Figure 4.5b deviates from the rotation center at angle θ_2, which results in the spatial shift during the X-ray imaging.

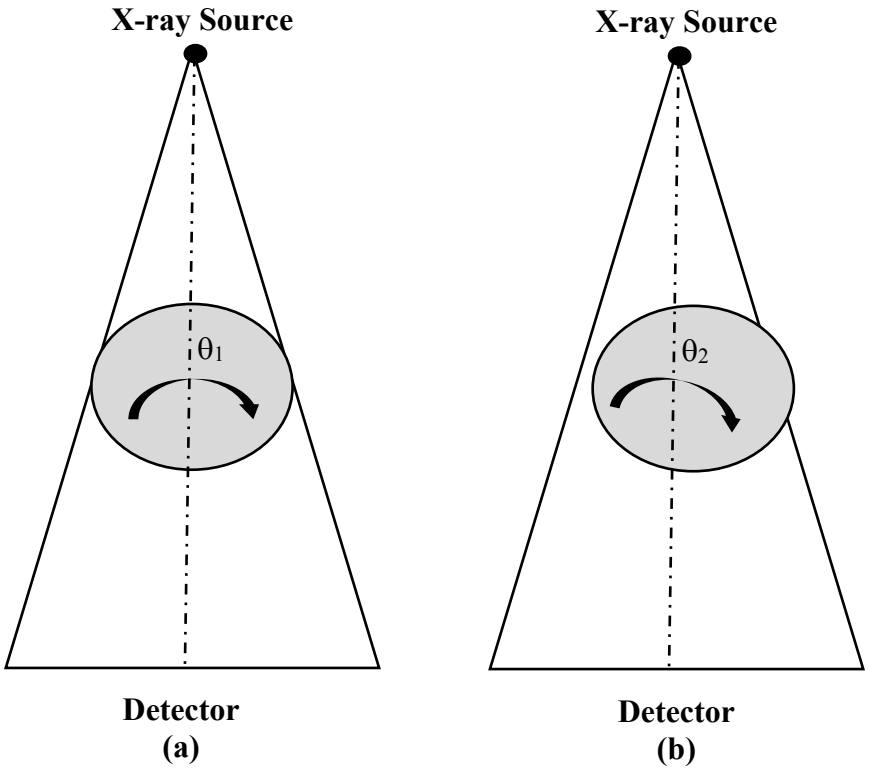

Figure 4.5 Sketch of rotation offset during CT scanning

The existence of spatial orientation during scanning can be evidenced by the comparison of normalized images with different numbers. The subtraction of sequential images and between the first and last images is performed in ImageJ. The difference between subtraction of different images is dramatic as indicated in Figure 4.6. Figure 4.6 is the phase plot in which red color represents the positive displacement whereas blue color represents the negative displacement. Figure 4.6a indicates that offset in

sequential images is trivial since no color around the particle exhibits apparent movement. However, in terms of Figure 4.6b, red color in the upper right profile of subtraction image can be obviously observed whilst blue color in the lower left profile of subtraction image is evident. This implies that the offset around rotation axis in the whole process of scanning should be non-negligible although it is not apparent in the sequential images.

To address this problem, a linear interpolation method is proposed to compensate the spatial orientation in data collection process. First, the relative movement between the first and the last images is regarded as a vector. The component in x direction and y direction is measured respectively. Then the overall movement in each direction is linearly interpolated in the whole images. After linear interpolation algorithm is applied to individual images, the bias in spatial orientation is reduced to acceptable levels. The phase plot corresponding to Figure 4.6 after offset correction is shown in Figure 4.7.

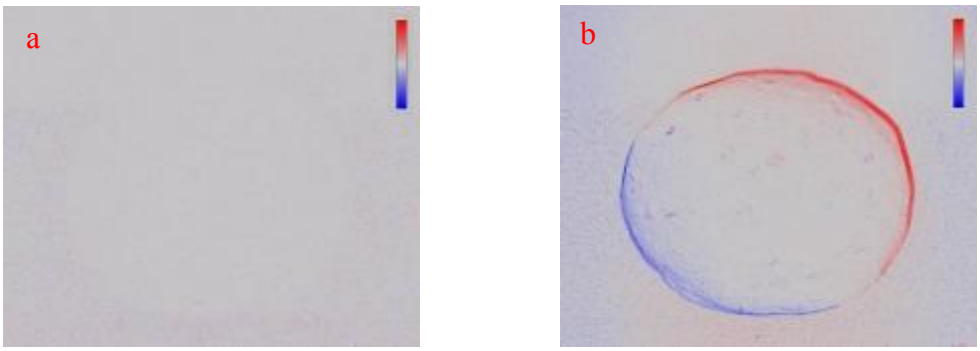

Figure 4.6 Phase plot of subtraction between No.1 and No.2 images (a); between No.1 and No.1000 images (b)

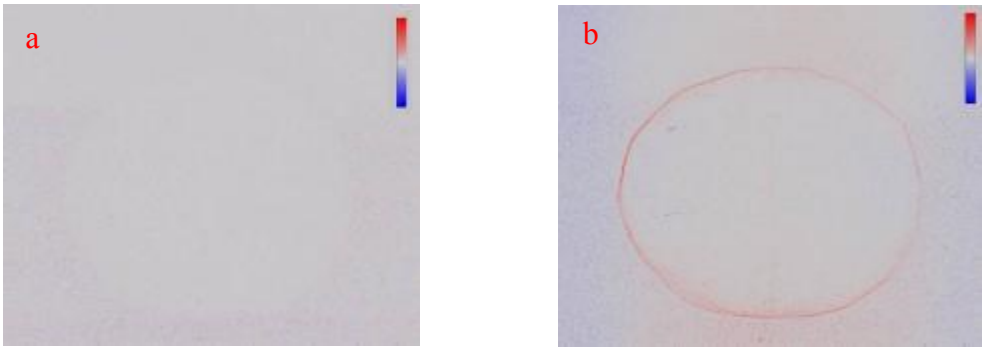

Figure 4.7 Phase plot of subtraction after offset correction between No.1 and No.2 images (a); between No.1 and No.1000 images (b)

Compared with Figure 4.6b, in Figure 4.7b, the effect of offset correction is evident and there is relatively small motion around the particle profile, which ensures that the projection data is collected around the same rotation axis to the best extent. Note that the legend in Figures 4.6 and 4.7 shows the extent of the offsets rather than the magnitude of offsets. The quantification of the offset is outside the scope of this project. Offset correction is very important in data reconstruction simply because the error introduced by improper data collection leads to erroneous reconstruction and thus results in unreliable image processing in the following stage. For example, as shown in Figure 4.8 is the reconstructed images before and after offset correction. After offset correction, the slice is created with sharp contrast and fewer stripes.

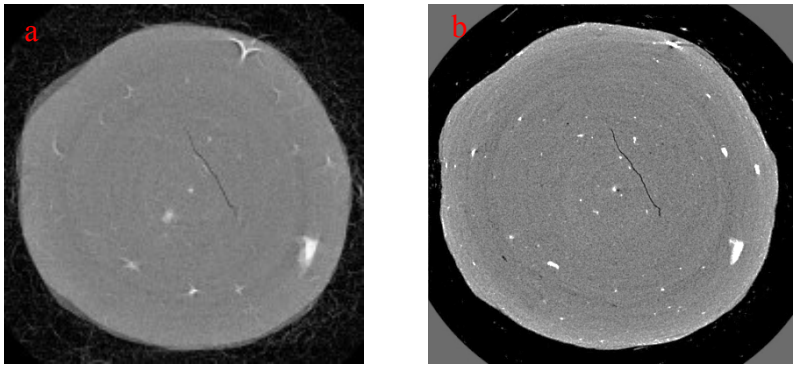

Figure 4.8 Illustration of reconstructed image from original data (a) and reconstructed image from corrected data (b) with the same number slice of particle

During image reconstruction process for both original and shifted data, the same parameters are adopted to deal with the noise filtering using Fourier filtering method and to correct beam hardening by a polynomial equation. The image quality in Figure 4.8b is greatly improved after offset correction as compared with that in Figure 4.8a. The program of addressing the spatial offset is appended in Appendix A.

4.4.4 Volume rendering

During each scanning of data acquisition, 1000 tomographic projections were collected by incremental rotation of the sample through a 360 degree rotation. Data were reconstructed by filtered back projection using Octopus 8.0, where noises were minimized and raw data was converted to be readable in Avizo (2012). Then 2D tomographic slices were stacked for 3D volume rendering using Avizo after beam

hardening and ring artifacts were filtered in post-processing. The whole image process is schematically shown in Figure 4.9.

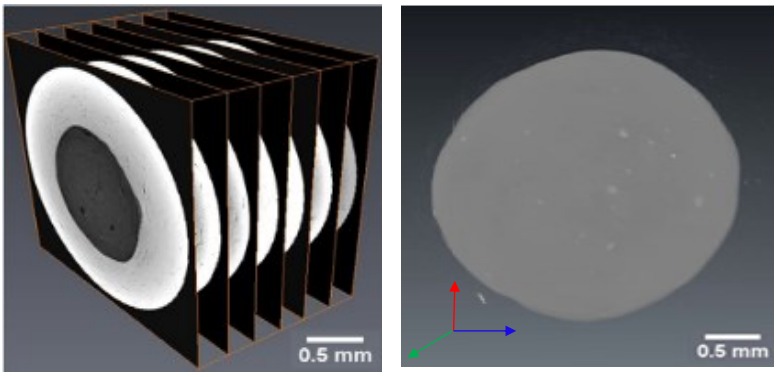

Figure 4.9 Image processing from data acquisition to 3D volume rendering

4.4.5 Crack representation by segmentation

Segmentation is an important procedure in image processing to display the region of interest. The module of interactive thresholding in Avizo Fire is used by specifying the discrete values of gray scale, which represents the value range of crack. Figure 4.10 shows selected slices and the defect region after thresholding. By so doing, the feature of crack is picked out as a function of discrete greyscale class and the 3D phase of crack in particle before and after compression can be visualized (Figure 4.11). It indicates from Figure 4.11 that the changes of 3D crack of particle before and after compression can be qualitatively observed. However, the segmentation approach used to deal with phase thresholding cannot provide quantitative information. A more advanced data processing method is required, which will be stated in the following section.

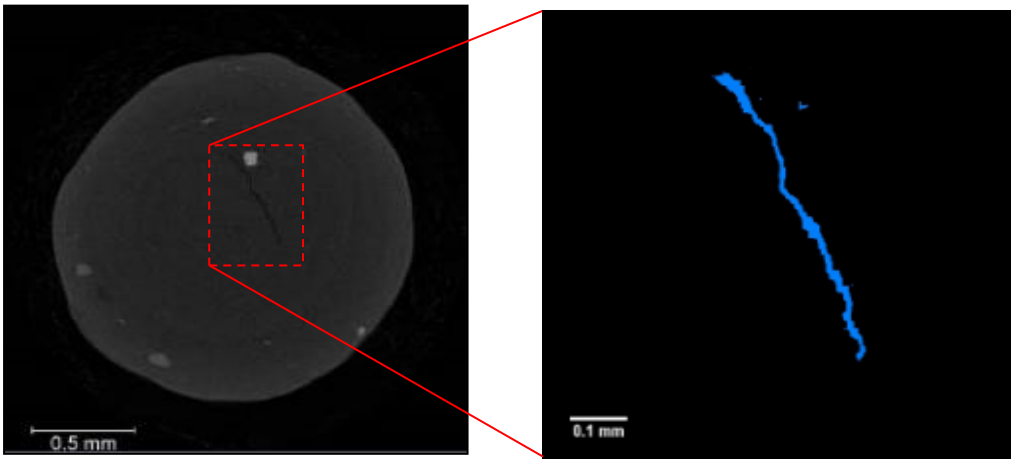

Figure 4.10 Crack representation in one slice (left) and by phase segmentation (right)

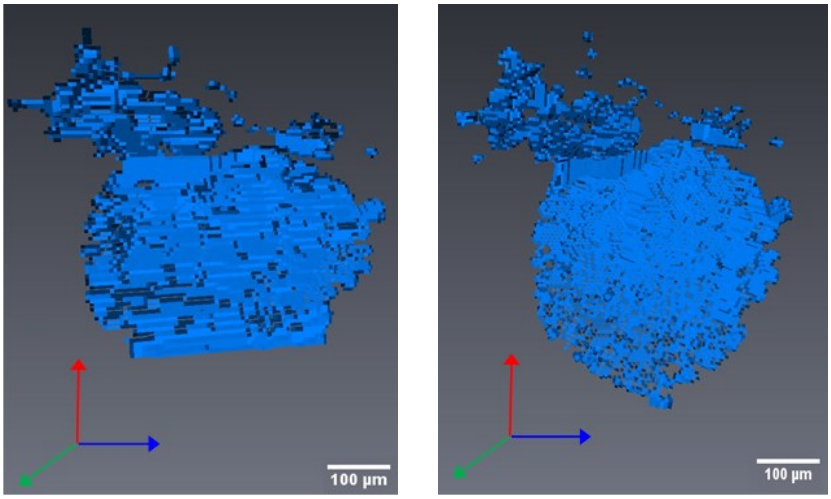

Figure 4.11 3D crack rendering of particle before (left) and after compression (right)

4.5 Stepwise loading responses

In this study, a total of six zeolite particles with similar diameters were compressed under in-situ loading and scanned using X-ray µCT. The displacement-force curve for six particles is shown in Figure 4.12. It should be noted that the in-situ loading tests were carried out twice with each time of three particles compressed. Hence, the displacement force curve of the first three particles is shown by solid line whilst the displacement force curve of the second three particles is shown by dash line. Particle I is taken as an example to show the progressive failure process under in-situ loading test. As seen from Figure 4.12, there are five loading stages for particle I with the peak force 62 N. The applied force drops slightly at each loading stage during the period of scanning due to stress relaxation. The vertical slices (slices parallel to the loading direction) of particle I under incremental loading are shown sequentially in Figure 4.13. It demonstrates that there is no visible cracking before the cleavage of the particle until the peak force, which agrees well with the failure process in Cil and Alshibli (2012). The characteristics of six particles under progressive loading are summarized in Table 4.2. It shows that the diameter of six particles is varied from 2.2 mm to 2.5 mm. Particle VI has the maximum peak force of 66 N whilst Particle III has the minimum peak force of 58 N. The average peak load is 60.8 N with a standard deviation of 3.7 N.

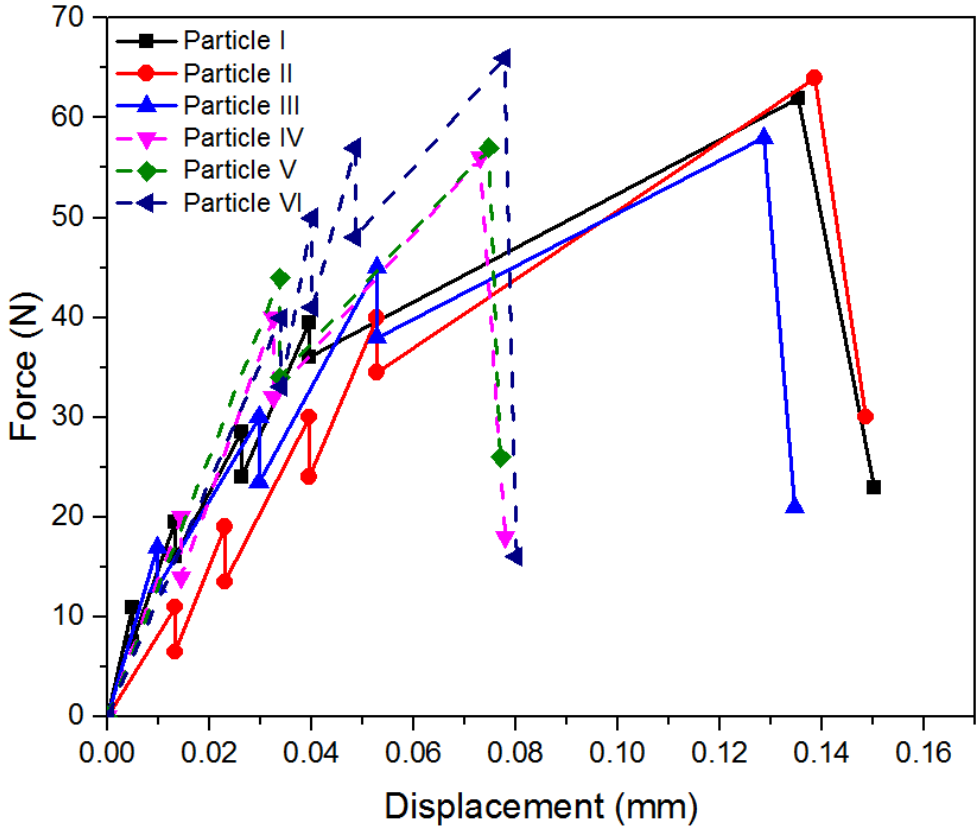

Figure 4.12 Displacement force curve of in-situ loading test

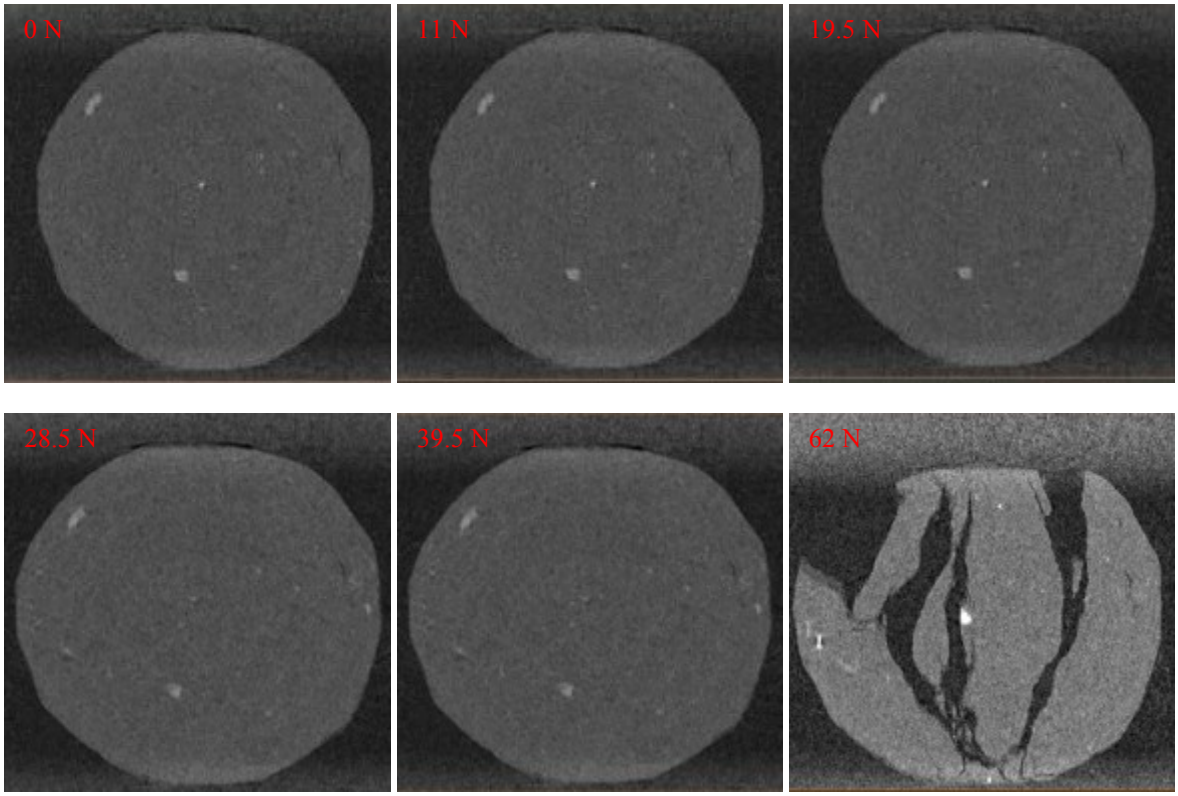

Figure 4.13 Progressive failure of Particle I under in-situ loading

Table 4.2 Loading stage for six particles

Loading Stage / Particle No.	I (N)	II (N)	III (N)	IV (N)	V (N)
I (D, 2.5mm)	11	19.5	28.5	39.5	62
II (D, 2.47mm)	11	19	30.5	40	64
III (D, 2.2mm)	17	30	45	58	#
IV (D, 2.38mm)	20	40	58	#	#
V (D, 2.35mm)	44	57	#	#	#
VI (D, 2.40mm)	40	50	57	66	#

4.6 Breakage pattern of in-situ loading test

The breakage pattern of six zeolite particles is summarized in Table 4.3, which shows the 3D view, top view and side view of broken particles respectively. It should be noted that the slice of the top view (XY Plane) and side view (YZ Plane) refers to the cross-section from 3D view perpendicular and parallel to the loading direction. Particle IV is excluded from the analysis of breakage pattern since the fragments have been detached from the mother particle. However though, the imaging of Particle IV is still shown in Table 4.3 for reference. The 3D view demonstrates that all the zeolite particles fail via several splits leading to meridian cracks. It is shown by top view that particles were broken into pieces with some gap between these pieces. Particles I, II, V are deemed to exhibit the similar breakage patterns in which a big gap throughout the particle can be observed. Particles VI shows another type of breakage where a relatively small piece was surrounded by other peripheral pieces. The third type of breakage is observed from Particle III which have three radial cracks initiating from particle center. As seen from side view, two breakage patterns can be observed with the first breakage pattern from Particle I and VI and second breakage pattern from II, III and V. The first breakage

pattern in Particles I and VI shows that the broken particle has a slim pillar fragment in the middle surrounded by another two fragments. The second breakage pattern in Particles II, III and V illustrates that particle is mainly segmented by two fragments. However, the common ground of the two breakage patterns is that some fine fragments can be found in the contact zone. These fines such as cone crack seen from Particle V are due to stress concentration which is deemed to be the crack initiation zone (Cil and Alshibli, 2012; Zhao et al., 2015). Numerous studies on the crushing of single particle under parallel compression are based on the hypothesis of tensile failure model with fractures parallel to the loading condition. Russel et al. (2015) state that a central plastically deformed cone beneath the contact area is pushed into the spherical particle under uniaxial compression. The increasing compression results in a slight lateral displacement of particle until the tensile stresses at the circumference of the contact zone split the granule by initiating meridian cracks. The depiction of X-ray µCT of a broken particle under uniaxial compression by Russel et al. (2015) is shown in Figure 4.14. Since the tested particle is the same as used in this work, the breakage pattern observed in Russel et al. (2015) is simply comparable, which could be categorized into the first breakage pattern in this work.

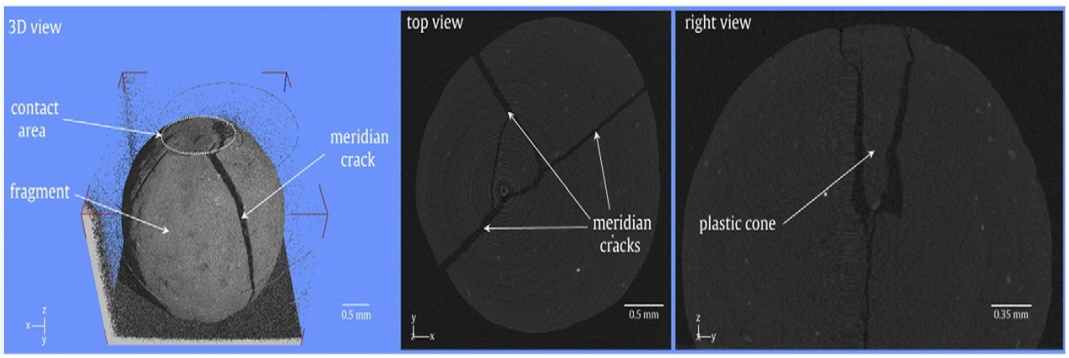

Figure 4.14 X-ray images of a broken dry granule after uniaxial compression until primary macro-breakage (After Russel et al., 2015)

As for the second breakage pattern, it is still envisaged that cracks are generated first at the contact point whilst the cracks propagate through the weakest bond path resulting in the splitting fracture of particles. Although different breakage patterns are observed for the tested zeolite particle, it is proposed that the main course for the splitting fracture should be based on the same hypothesis. It may be concluded that the cracks form from the compressive contact point due to stress concentration and grow gradually parallel

Table 4.3 Summary of breakage pattern of six zeolite particles

Particle No.	3D view	Top view (XY Plane)	Side view (YZ Plane)
I	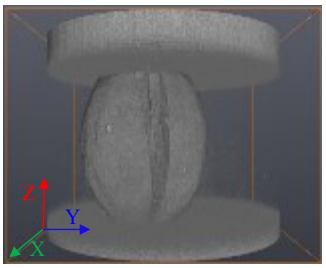	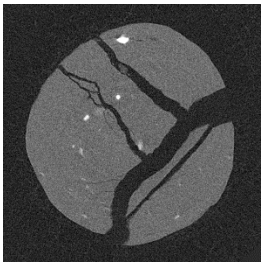	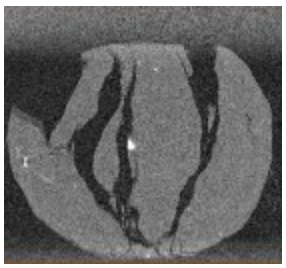
II	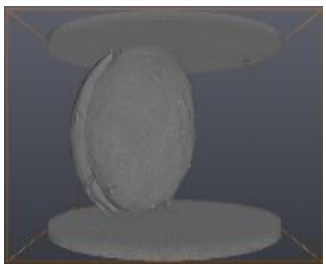	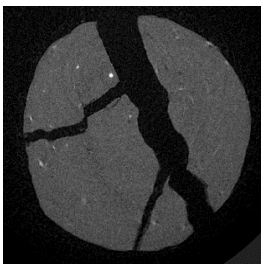	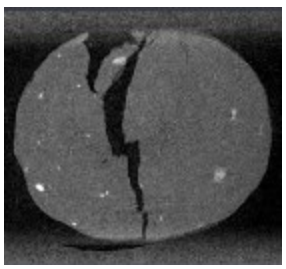
III	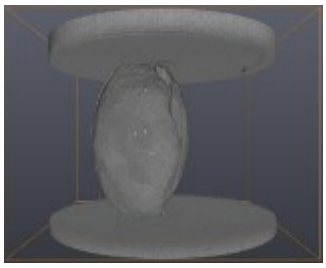	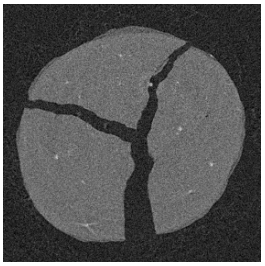	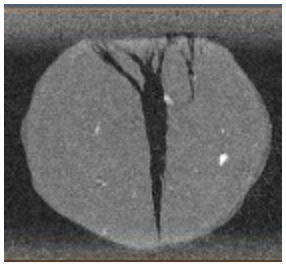
IV			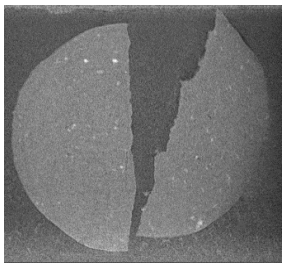
V	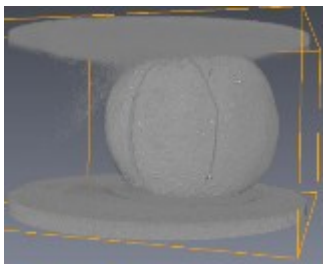	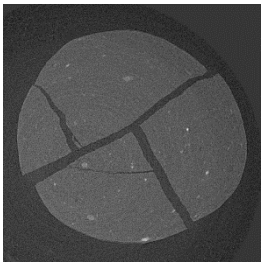	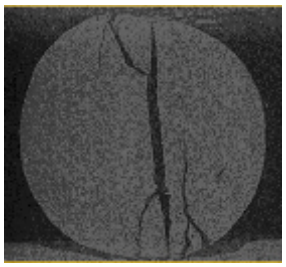
VI	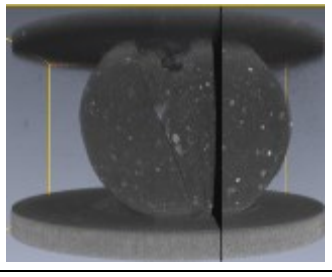	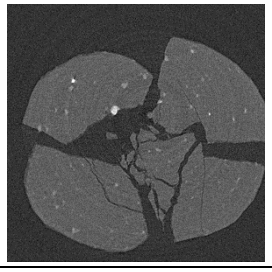	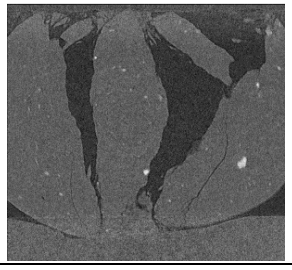

to the loading direction. Then the cracks continue to propagate through the weakest pathway due to tensile stress, which eventually results in the splitting fracture of particles. The hypothesis of tensile failure mode with fractures perpendicular to the loading direction could be referred to Jaeger (1967). Combined with Figure 4.12 and Table 4.3, it may be concluded that the compressed zeolite particles present brittle failure mode, which is in line with the finding from Russel et al. (2015).

X-ray CT images provide valuable information of progressive failure due to crack formation mechanism experimentally. However, it is difficult to provide quantitative information about the relative displacement of particle under different loading stages. Therefore, digital image correlation (DIC) was used to shed more light on the progressive failure in a quantitative way, which is described in details in the following section.

4.7 Digital image correlation

Digital image correlation (DIC) has been a well-established technique for deformation measurement in the field of experimental mechanics (Schreire and Sutton, 2002). DIC can retrieve the displacement fields of two gray-scale images by setting up the correlation window with pixel units, which calculates the relative movement of subset before and after deformation. Many applications of this technique to various disciplines can be found in terms of fracture mechanics, heat-induced deformation measurement, bio-materials and inverse stress analysis (Yoneyama and Murasawa, 2009). Examples of DIC application have been introduced in Section 4.1. The measurement accuracy of DIC is critical for interpreting the correlated results, which depends on many factors, such as subset size, image noise, sub-pixel optimization algorithm. For example, Schreire and Sutton (2002) investigated the systematic errors in DIC due to unmatched subset shape functions. Pan et al. (2006) examined the performance of sub-pixel registration algorithms in DIC on displacement estimations. Yaneyama et al. (2006) studied the effect of lens distortion on displacement measurement through DIC.

4.7.1 Basic principle

The technique of DIC was principally developed by Sutton et al. (1983). The full-field surface measurement is obtained by matching the subsets of interest before and after

deformation. A subset of (2M+1) x (2M+1) pixels centering at point (x_o, y_o) from the reference image (before deformation) is determined as compared to the subset with the same size from the target image (after deformation), as shown in Figure 4.15. The similarity between the reference and target subset is evaluated through a cross-correlation (CC) or sum-squared difference (SSD) correlation criteria (Tong, 2005). When the size of a subset is set, the similarity searching procedure is carried out by comparing the peak position of the distribution of correlation coefficients. The difference of the positions between the reference subset and the target subset yield the relative displacement *u* and *v* in x and y direction respectively. More details of the DIC technique can be found in Yoneyama and Murasawa (2008) and Pan et al. (2008).

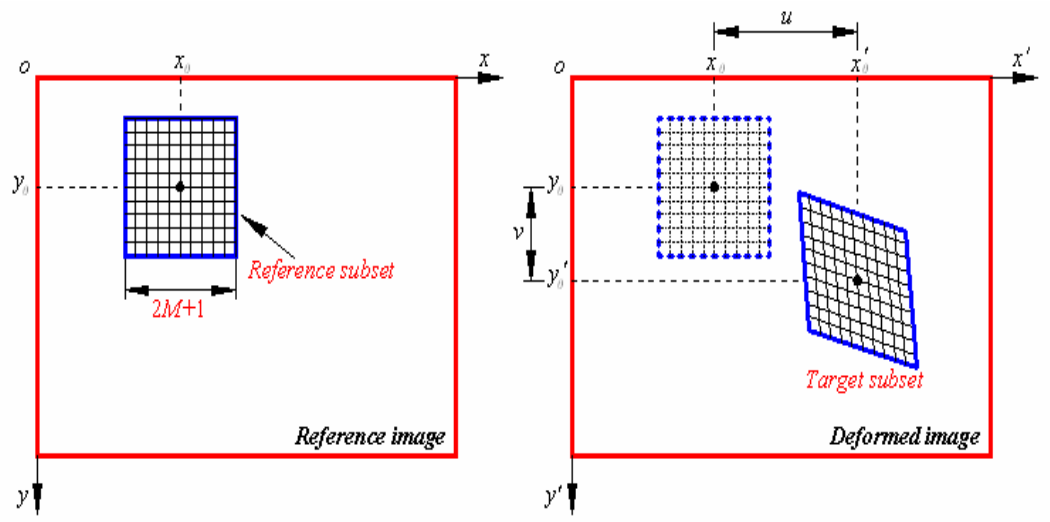

Figure 4.15 Schematic illustration of reference and target subsets in DIC (After Pan et al., 2008)

It was found by Pan et al. (2008) that the size of subset is critical to the accuracy of displacement since the subset size directly determines the area being used to track the similarity between the reference and target images. In order to achieve a correlation result of good quality, the size of the subset should be large enough to distinguish the intensity pattern contained in the subset. The subset size selection and its effect on the accuracy of measured displacement could be found in details (Pan et al., 2008).

4.7.2 DIC calculating procedure

In this work, the DIC program mapping the deformation between 3D volumes was based on the code TomoWarp, which was initially developed by Hall (2006). For a 3D

DIC analysis of two volumetric images, three components of position vectors and displacement vectors, 3D deformation and full strain tensor are calculated. The maximum shear strain (ϵ_s) is given

$$\epsilon_s = \sqrt{\frac{2}{3}[(\epsilon_1 - \epsilon_2)^2 + (\epsilon_2 - \epsilon_3)^2 + (\epsilon_1 - \epsilon_3)^2]} \tag{4.3}$$

where ϵ_1, ϵ_2, ϵ_3 denote the major, intermediate and minor principal strains.

The procedure to ensure a successful running of the DIC code TomoWarp is described in the following way.

1. Definition of image size

The first step includes the size definition of both reference and target (deformed) images which will be processed by 3D DIC. It is noteworthy that the size for reference and target images should be kept the same. The image sizes in x and y direction depend on the amount of pixels in the slice whilst the image size in z direction depends on how many slices are stacked in total.

2. Definition of the correlation window (also known as the subset size)

The shape of correlation window is cubic as shown in Figure 4.16. As mentioned above, the size of correlation window is the most important parameter for a successful performance of DIC. It should be defined with a proper estimation of the correlation window which contains enough information to be correlated between the reference and target subset. In order to guarantee a reliable displacement measurement, the size of correlation window in this work is chosen as 70 pixels.

3. Definition of search window

Search window refers to the region where the correlation window will be translated to look for a correlation coefficient for the same node in the deformed image. The value of search window could be defined by comparing the coordinate difference of slices in x, y, z directions between the reference and target image stacks.

4. Definition of node spacing

The node spacing needs to be defined in the reference image. By defining node spacing, the image is gridded and for the initial trial the definition of node spacing could be set as the same as correlation window.

5. The displacement between reference and target images will be calculated based on the aforementioned definition, which is an integer number of pixels where the highest correlation coefficient is found.

6. Subpixel refinement

Subpixel refinement is an essential step for the calculation of strains because the displacements are rarely integers of displaced pixels. The method used for subpixel refinement in this work is to interpolate the correlation coefficient field to find the best correlation. More details about this method and other types of sub-pixel refinement can be found elsewhere (Karatza, 2013).

7. The information of deformation is calculated based on the displacements through a mapping function between the subsets.

It should be noted that the strain analysis from DIC is incremental based on a continuum displacement field. As a result, good correlation won't be generated in the presence of discontinuities (Karatza, 2013). For example, the good correlation between the first image and the last image in Figure 4.13 cannot be achieved simply because discontinuities in the last image (deformed image) make it difficult to search for the similarity in the first image (reference image).

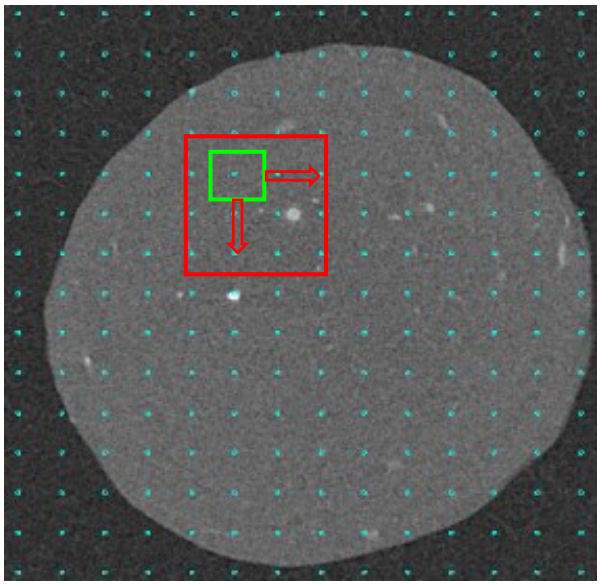

Figure 4.16 Schematic illustration of DIC calculating procedure (a) Cyan: node spacing (b) Green: correlation window (c) Red: search window
(Modified from Karatza, 2013)

4.8 Selected results from DIC

4.8.1 Correlation window

Shown in Figure 4.17 is the correlation window between two slices of the same particle before and after compression. The correlation value is varied between 0 and 1, in which 0 denotes no correlation (black) and 1 denotes complete correlation (white). Inside the particle almost full area of white color occupies the region, which indicates a high correlation result between two compared slices. It can be confirmed by plotting a straight line across the correlation window and the gray value versus line length is illustrated in Figure 4.17. In section AB the gray value along the straight line increases dramatically from 0.25 to 1.0 whilst in section CD the gray value along the line drops rapidly from 1.0 to 0.0. However, the gray value in section BC keeps constantly as the value of 1.0, which achieves perfect correlation in this region.

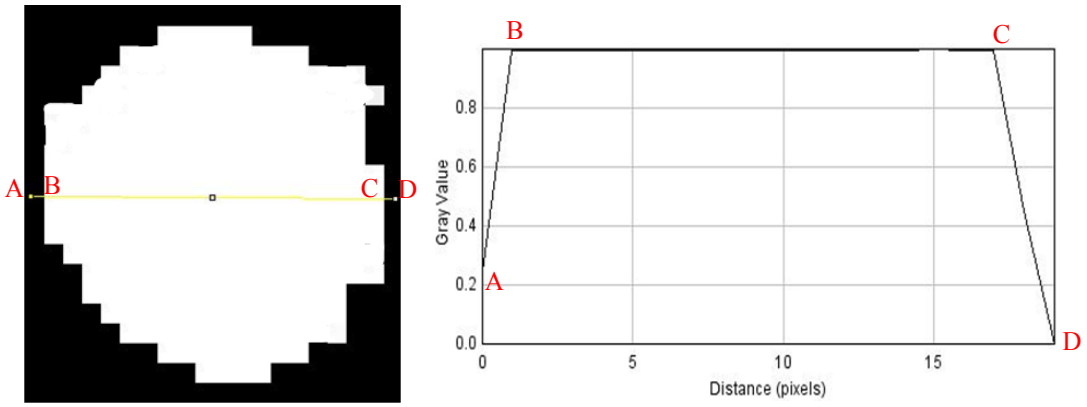

Figure 4.17 Line probe of correlation window and its variation along the line profile

4.8.2 Displacement plot

3D displacement of the deformed particle under 19.5N (loading stage 2) and 39.5N (loading stage 4) compared with the same uncompressed particle is achieved by calculating the displacement component of each correlated slice respectively. The displacement in x, y, z direction is plotted in Figure 4.18 and the histogram of gray value is accordingly shown in Figure 4.19. As can be seen from Figure 4.18, displacement component of increments 0-2 in each direction is explicitly expressed by colour map. The extent of displacement in each direction can be characterized by the color bar as indicated in Figure 4.19. The displacement of the deformed particle under 40N (increments 0-4) is shown in Figure 4.20 along with the histogram distribution in Figure 4.21.

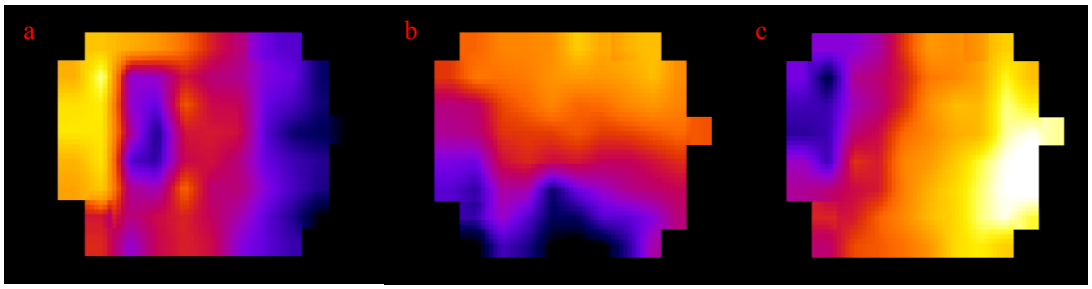

Figure 4.18 Displacement component of increments 0-2 from DIC analysis in x (a), y (b), z (c) direction

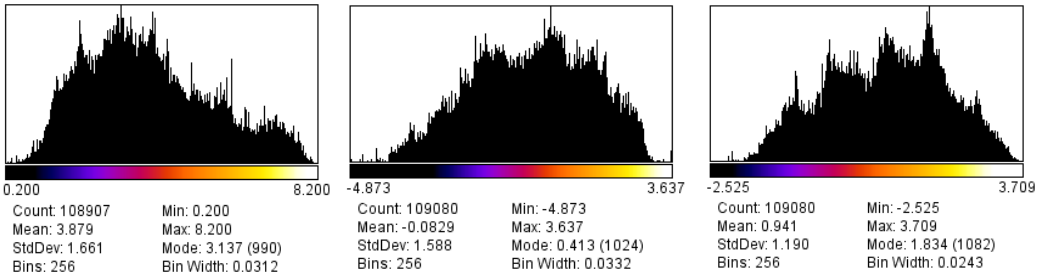

Figure 4.19 Histogram of gray value of displacement component (increments 0-2) from DIC analysis in x (a), y (b), z (c) direction

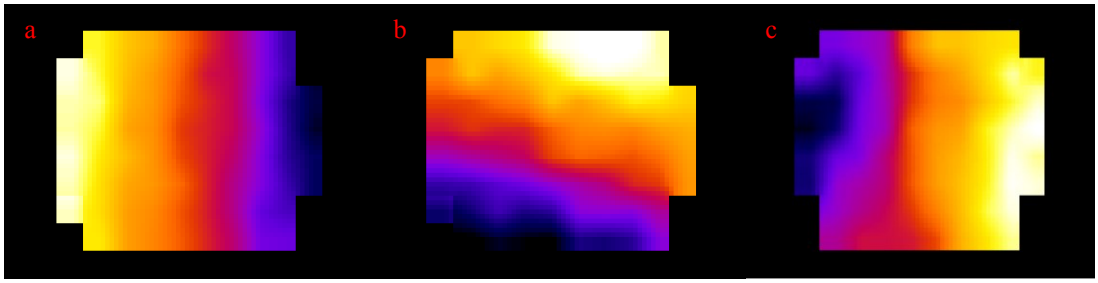

Figure 4.20 Displacement component of increments 0-4 from DIC analysis in x (a), y (b), z (c) direction

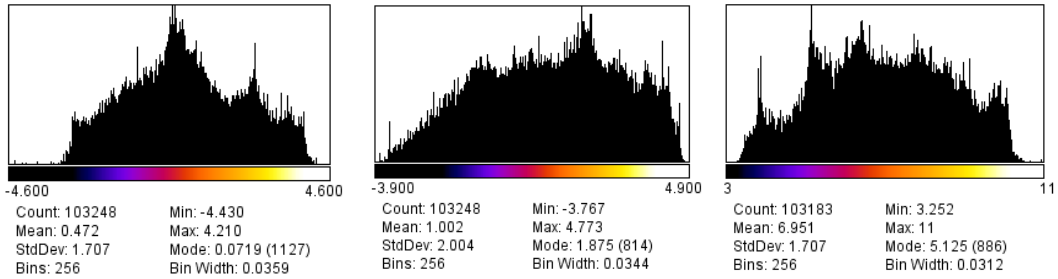

Figure 4.21 Histogram of gray value of displacement component (increments 0-4) from DIC analysis in x (a), y (b), z (c) direction

4.8.3 Maximum shear strain

Figure 4.22 shows the maximum shear strain for increments 0-2 and 0-4 (vertical section parallel to the loading direction). The maximum shear strain of increments 0-2 shows that the majority of the particle is covered by blue whereas only a few areas present relatively high value of shear strain. As for the increments 0-4, it is manifest that the maximum shear field in each subset becomes increasingly large with the incremental loading. The two strain images in Figure 4.22 clearly show the evolution of a localized band that traverses perpendicular to the loading direction. It is also clear that the localized zone is not uniform. On the other hand, the radiographic sections of specimen in Figure 4.13 do not show distinctive evidence of localized deformation. As compared to Figure 4.13 displaying the vertical slices under incremental loading, direct observation of the radiographic cross section at each loading stage is unable to reveal any sign of strain localization in a specific region.

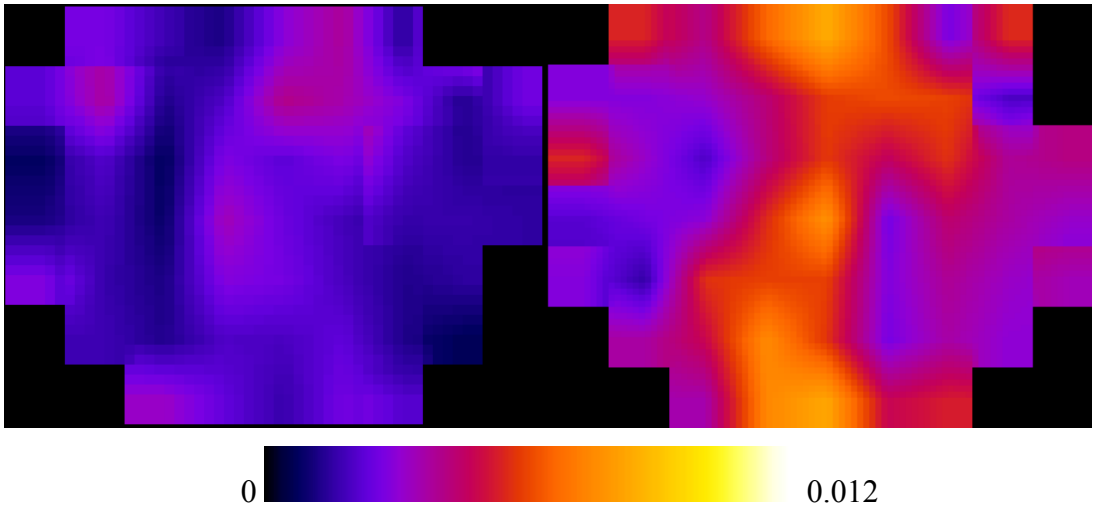

Figure 4.22 Maximum shear strain field of increment 0-2 (left) and increments 0-4 (right)

In summary, X-ray μCT complimented with DIC is able to show some important information which is difficult to detect in the tomographic images. The strain fields obtained via 3D DIC indicate that localized strain field in the particle has already formed prior to the peak force. However, it should also be noted that the quality of the DIC results critically depends on the quality of images such as the subset size, the signal-to-noise ratio. The finding from this study highlight that the localized zone formation before the peak force and the localized zone is not uniform.

4.8.4 Crack growth evaluation by DIC

The application of DIC is further exemplified by the evaluation of crack growth inside a particle under uniaxial compression. Remember that the crack detected inside a particle is randomly distributed, the particle with inside crack is another testing sample since there are no visible cracks detected inside the particles under in-situ loading test. However, the crack growth inside a particle could be evaluated through DIC, which is described below. The crack tips of slice No. 420 from the same uncompressed and compressed particle along which the crack propagate are marked in Figure 4.23 a and b respectively. It is observed that crack tip of particle has extended under compression from the zoomed images in Figure 4.23c. The propagation route from point A to point B is depicted in Figure 4.23c and the propagation angle is calculated in ImageJ with the value of 25 degrees. The crack growth is only observed from the crack tip A in the lower left corner although the loading is applied to 76% of the crushing force. It could be interpreted that the stored strain energy during compression is not large enough to generate a new surface and only slight crack growth is observed with pixel units.

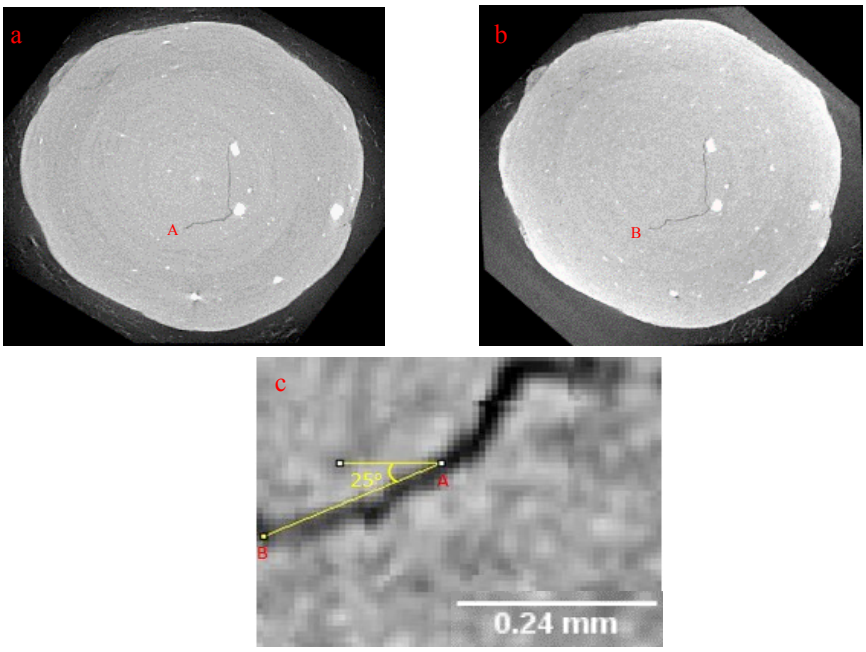

Figure 4.23 No. 420 slice of the same particle before (a) and after (b) compression with marked crack tip and propagation path after 76% loading of crushing force (c)

A particle with inherent crack was compressed to investigate how crack growth occurs under loading. The plane displacement field surrounding the propagating crack was obtained using in-house generated and tested DIC code (Hall et al., 2010). The plot of plane displacement vector of slice No. 420 in virgin particle and the plot of plane

displacement vector surrounding crack are shown in Figure 4.24. The length of arrow represents the degree of displacement in the node. It is noticed that the displacement surrounding the inherent crack inside the particle after compression is not as distinct as that in other regions.

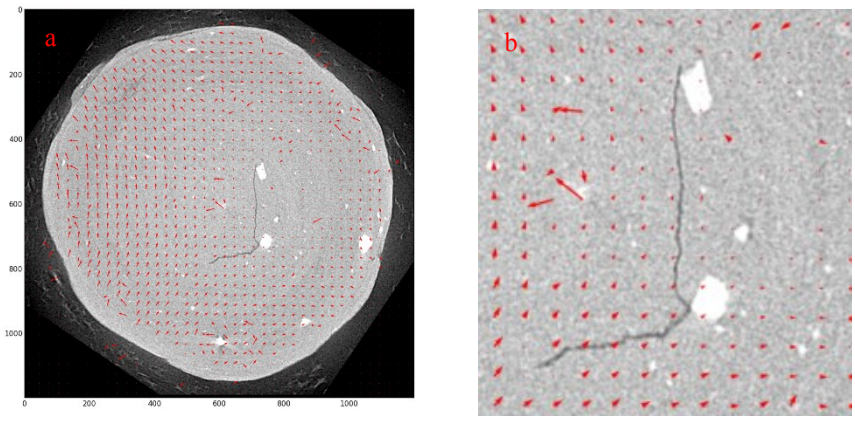

Figure 4.24 Plot of plane displacement vector of slice No. 420 in virgin particle (a) and plot of plane displacement vector surrounding crack (b)

Part II

4.9 Principal curvature characterisation and its influence on deduced Young's modulus

Contact curvature plays an important role in the determination of the Young's modulus and the mechanical response of a particle (Misra and Huang 2012; Zhao et al., 2015). Over the past decade, particle characteristics and their influence on the behaviour of particulate materials have been extensively studied. Complex imaging-based methods have been proposed to quantitatively describe the particle morphology and texture (Bowman et al. 2001; Sukumaran and Ashmawy 2001; Hu and Stroeven 2006). Clayton and Heymann (2001) showed that the particle shape can impose a significant impact on the stiffness. The influence of geometrical properties of constituent grains on the overall granular material response was experimentally examined (Cavarretta et al, 2010). The Young's modulus of particle is routinely determined by using the Hertz equation (Hertz, 1881), in which the averaging method of the principal curvature is adopted regardless of the true profile of the particle. Given a natural particle with imperfect roundness, it may be problematic to choose the averaging radius as the equivalent radius. Furthermore, the effect of particle roughness on the elastic stiffness may not be

negligible especially when the sphericity of a particle exceeds certain tolerance levels. Few studies are available to demonstrate how the contact curvature influences the determination of the elastic stiffness even though the importance of the particle shape has been recognized by aforementioned studies.

This section aims to study the sensitivity of a particle shape to the contact curvature and then the variation of the Young's modulus determined by the contact curvature during elastic deformation of a particle. The X-ray microcomputed tomography (μCT) was used to obtain the accurate geometry of a single particle. The digital information of the scanned particle, including 2D slices and 3D rendering was processed and the variation of the contact curvature of the particle was examined using the circular (spherical at 3D) and polynomial fitting methods. The fitting sections and fitting scopes of the particle were taken into account. The effect of the contact curvature on the Young's modulus was investigated via 2D and 3D fitting methods based on image processing technology.

4.10 Underlying theories

4.10.1 The Hertz contact theory

Hertz (1881) pioneered the contact mechanics investigating the contact of two elastic isotropic solids. He considered geometrical effects on local elastic deformation properties but neglected surface interactions. The radius of elastic contact r_{ce} is given by Hertz (1881)

$$r_{ce}{}^3 = \frac{3R^*F}{2E^*} \tag{4.4}$$

where R^* and E^* are the effective radius and effective modulus of elasticity respectively; F is the contact force.

The depth of indentation δ is:

$$\delta = \left[\frac{9F^2}{4R^2(E^*)^2}\right]^{\frac{1}{3}} \tag{4.5}$$

The relationship between the contact force F and the maximum pressure p_{max} is (Johnson, 1992):

$$F = 2\pi \int_0^{r_{ce}} p(r_c)\, r_c dr_c = \frac{2}{3}\Omega {r_{ce}}^2 p_{max} \tag{4.6}$$

where r_{ce} is the radius of a circular contact area and $p(r_c)$ is the contact pressure:

$$P_{max} = \frac{3}{2}\frac{F}{\pi r_{ce}^2} = \frac{3}{2}p = \frac{3}{2}\frac{F}{A_{ce}} = \left(\frac{3}{2}\frac{F}{\pi^3}\frac{E^{*^2}}{R^{*^2}}\right)^{1/3} \tag{4.7}$$

It shows that the maximum contact pressure is 1.5 times the mean pressure p on the elastic contact area A_{ce}. The effective radius R^* of both solids is given by

$$R^* = \left(\frac{1}{R_1} + \frac{1}{R_2}\right)^{-1} \tag{4.8}$$

where R_1 and R_2 are the radius of the principal curvatures of two solids before flattening, and E^* the effective modulus of elasticity:

$$E^* = 2\left(\frac{1-\upsilon_1^2}{E_1} + \frac{1-\upsilon_2^2}{E_2}\right)^{-1} \tag{4.9}$$

In the case of a particle under compression by two parallel platens, the equation for calculating the modulus of elasticity, based on Hertz contact stress, is expressed as (ASAE, 1998):

$$E = \frac{0.338F(1-\upsilon^2)}{D^{3/2}}\left[K_u\left(\frac{1}{R_1} + \frac{1}{R_1'}\right)^{1/3} + K_L\left(\frac{1}{R_2} + \frac{1}{R_2'}\right)^{1/3}\right]^{3/2} \tag{4.10}$$

where E and D denote the Young's modulus and indentation displacement; υ and F Poisson's ratio and applied force. R_1 and R_1', R_2 and R_2' are radii of principal curvature at the corresponding point of contact respectively. The Hertz equation assumes that

deformation is very small and the material being compressed is elastic. The particle under compression between two parallel platen is schematically shown in Figure 4.25.

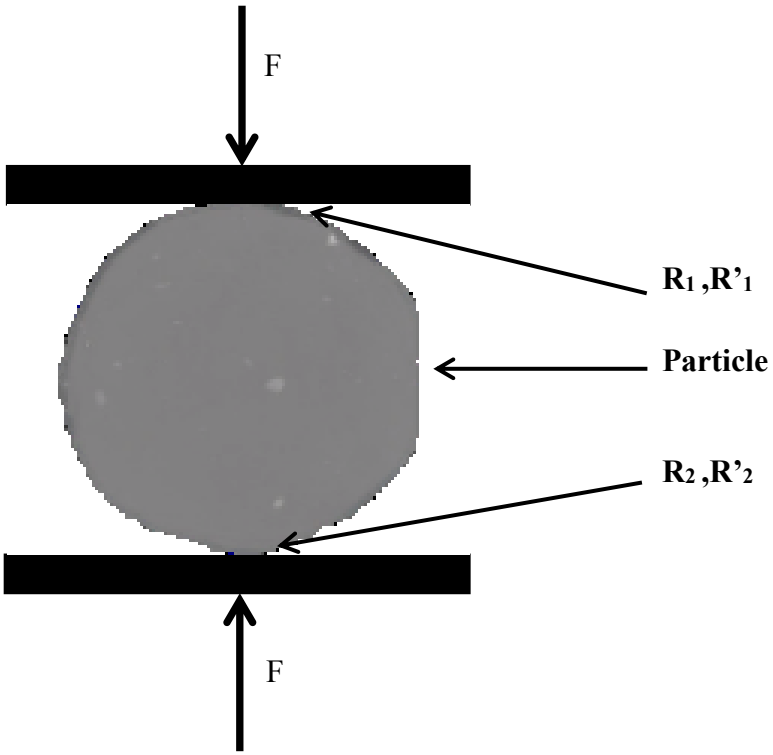

Figure 4.25 Sketch of a particle under compression between parallel platens

The constants K_u and K_L in equation are determined by $cos\theta$. The value of K_u and K_L gives inverse correlation with $cos\theta$ and the variation between K and $cos\theta$ is given in Appendix B; $cos\theta$ is calculated from the following formula (ASAE, 1998):

$$cos\theta = \frac{\left[\frac{1}{R_1} - \frac{1}{R_1'}\right]}{\left[\frac{1}{R_1} + \frac{1}{R_1'} + \frac{1}{R_2} + \frac{1}{R_2'}\right]} \tag{4.11}$$

4.10.2 Euler's theorem

In the field of differential geometry, the Euler's theorem (Euler, 1760) is a result of the curvature of curves on a surface. For each point p on a surface, there exist two such particular directions. They are mutually perpendicular and the curvatures k_1 and k_2 of the normal sections in these directions are the minimum and maximum values of all normal sections at point P (Figure 4.26a). k_1 and k_2 are named the principal curvatures.

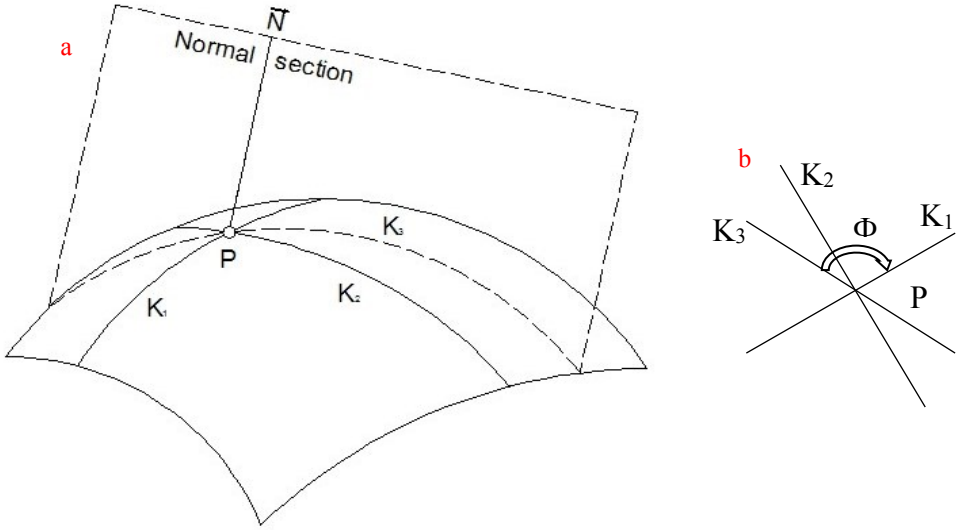

Figure 4.26 Sketch of principal curvature on a surface in 3D Euclidean space

A normal plane through p is a plane passing through the point p containing the normal vector. Let Φ be the angle in the tangent plane (Figure 4.26b), the normal curvature k_3 in direction Φ is given by:

$$k_3 = k_1 cos^2\Phi + k_2 sin^2\Phi \tag{4.12}$$

Eq.4.12 is thus called Euler's equation (Eisenhart, 2004).

4.10.3 Curvature formula

Curvature is the amount by which a geometric object deviates from being flat with the equivalent definition as the reciprocal of the radius of the osculating circle. For a planar curve given explicitly as y $= f(x)$, and using primes for derivatives with respect to coordinate x, the curvature is:

$$k = \frac{|y''|}{(1 + y'^2)^{3/2}} \tag{4.13}$$

For an implicit surface $F(x, y, z) = 0$, three notations including the gradient ∇F, the Hessian $H(F)$, and the adjoint of the Hessian for surface are needed to derive curvature formula (Ron Goldman, 2005).

$$\nabla F = \left(\frac{\partial F}{\partial x}\ \frac{\partial F}{\partial y}\ \frac{\partial F}{\partial z}\right) = (F_x\ F_y\ F_z) \tag{4.14}$$

$$H(F) = \begin{pmatrix} \frac{\partial^2 F}{\partial x^2} & \frac{\partial^2 F}{\partial x \partial y} & \frac{\partial^2 F}{\partial x \partial z} \\ \frac{\partial^2 F}{\partial y \partial x} & \frac{\partial^2 F}{\partial y^2} & \frac{\partial^2 F}{\partial y \partial z} \\ \frac{\partial^2 F}{\partial z \partial x} & \frac{\partial^2 F}{\partial z \partial y} & \frac{\partial^2 F}{\partial z^2} \end{pmatrix} = \begin{pmatrix} F_{xx} & F_{xy} & F_{xz} \\ F_{yx} & F_{yy} & F_{yz} \\ F_{zx} & F_{zy} & F_{zz} \end{pmatrix} = \nabla(\nabla F) \tag{4.15}$$

$$H*(F) = \begin{pmatrix} Cofactor(F_{xx}) & Cofactor(F_{xy}) & Cofactor(F_{xz}) \\ Cofactor(F_{yx}) & Cofactor(F_{yy}) & Cofactor(F_{yz}) \\ Cofactor(F_{zx}) & Cofactor(F_{zy}) & Cofactor(F_{zz}) \end{pmatrix} = \begin{pmatrix} F_{yy}F_{zz} - F_{yz}F_{zy} & F_{yz}F_{zx} - F_{yx}F_{zz} & F_{yx}F_{zy} - F_{yy}F_{zx} \\ F_{xz}F_{zy} - F_{xy}F_{zz} & F_{xx}F_{zz} - F_{xz}F_{zx} & F_{yx}F_{zx} - F_{xx}F_{zy} \\ F_{xy}F_{yz} - F_{xz}F_{yy} & F_{yx}F_{xz} - F_{xx}F_{yz} & F_{xx}F_{yy} - F_{xy}F_{yx} \end{pmatrix} \tag{4.16}$$

Here ∇ applied to a row vector refers to taking the gradient of each component and store these component gradients in a matrix as consecutive column vectors. The gradient ∇F is parallel to the normal of the surface $F(x, y, z) = 0$.

The following curvature formulas for implicit surfaces appear in Spivak (1975):
Gaussian curvature

$$K_G = \frac{\nabla F * H(F) * \nabla F^T}{|\nabla F|^4} = -\frac{\begin{vmatrix} H(F) & \nabla F^T \\ \nabla F & 0 \end{vmatrix}}{|\nabla F|^4} \tag{4.17}$$

Mean curvature

$$K_M = \frac{\nabla F * H(F) * \nabla F^T - |\nabla F|^2 Trace(H)}{2|\nabla F|^3} = \frac{-coeff(\lambda) in \begin{vmatrix} H(F) - \lambda I & \nabla F^T \\ \nabla F & 0 \end{vmatrix}}{2|\nabla F|^3} \tag{4.18}$$

The principal curvatures k_1 and k_2 can be computed from the mean and Gaussian curvature K_M and K_G from

$$k_1, k_{2=} K_M \pm \sqrt{K^2{}_M - K_G} \tag{4.19}$$

The detailed derivation for Gaussian and mean curvatures of implicit surfaces can be found in Ron Goldman (2005).

4.11 Methodology

A single zeolite particle (Diameter 2.27mm) was imaged by X-ray μCT, which was carried out in X-ray μCT laboratory in the School of Geoscience, Edinburgh University. The projection data are collected by incrementing a small the rotation angle around the rotation axis during X-ray scanning. The collected data were processed in an image processing software Avizo Fire. This way the imaged particle could be visualized in 3D by data reconstruction and the digital information of the reconstructed particle could be captured and processed. The global and local curvature estimation at the contact point was conducted with two different fitting methods. The effects of fitting scope and fitting section are also investigated. The detailed procedure for image processing is described as follows.

4.11.1 Image representation

A sequence of slices in XY cross-section is stacked in Avizo and orthogonal planes around the vertex of particle are displayed as shown in Figure 4.27.

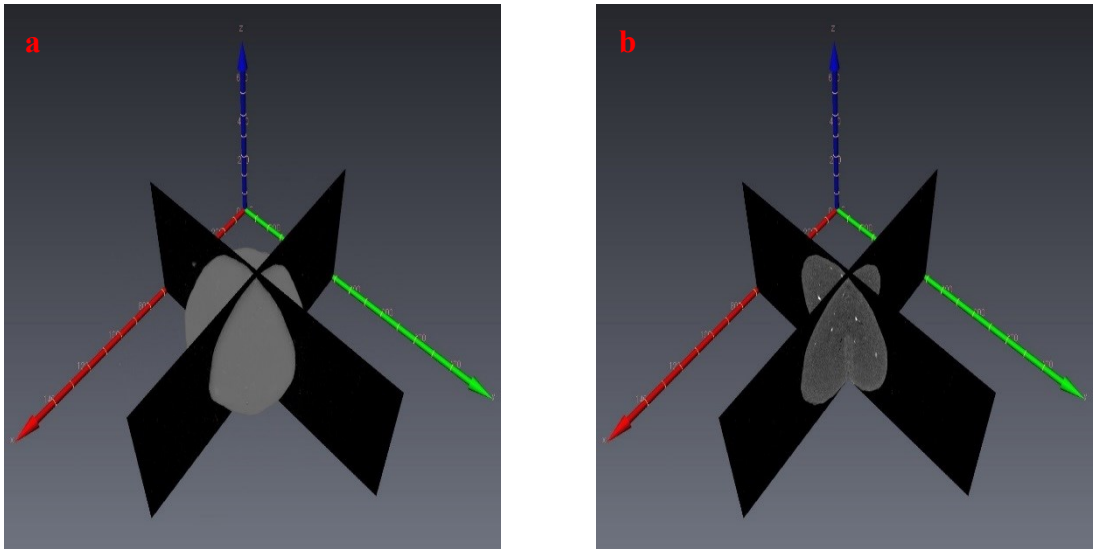

Figure 4.27 Schematic of X-ray CT of a zeolite particle: (a) volume rendering (b) dual orthogonal slices

The orthogonal planes are rotated every 5, 10, 20 and 45 degrees and totally 18, 9, 5 and 2 pairs of orthogonal planes which cross the particle around the same vertex are generated.

4.11.2 Image binarization

Image binarization is a process to convert a grey image to a black and white one. The binarized image has only two colours, black and white in which the black (background) is represented by "0" whilst white (the object) is represented by "1". Figure 4.28 shows that a grayscale image is binarized using an image processing software Fiji in order to get the outline of slice.

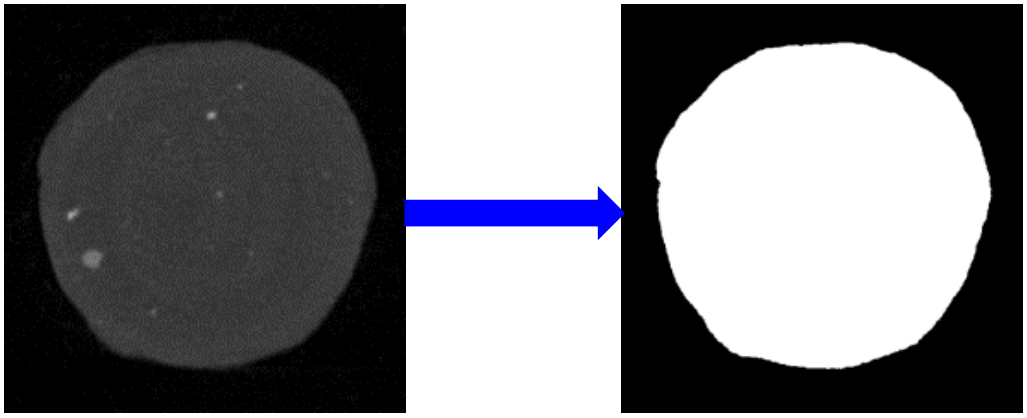

Figure 4.28 Binarization from grayscale to black and white

Figure 4.29 shows binary images of two orthogonal slices after binarization. Binary images require lower storage and simple processing algorithm compared to greyscale images.

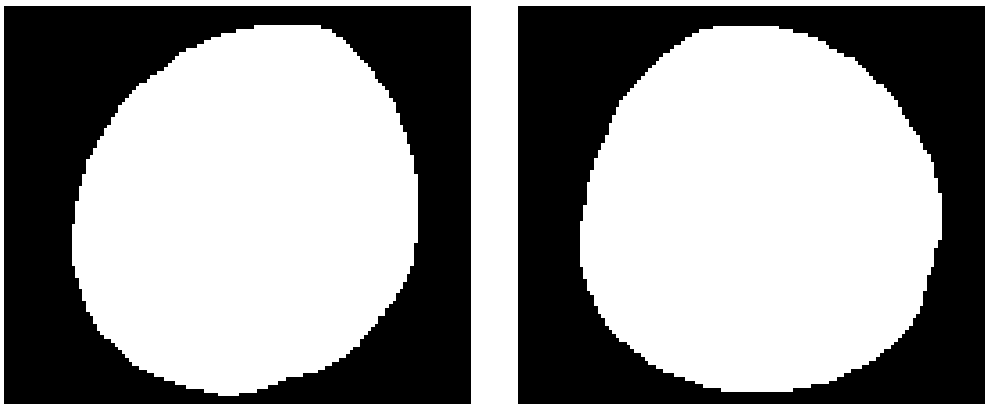

Figure 4.29 Binarization images of orthogonal slices

4.12 Curvature estimation

The polynomial and circular (spherical) fitting methods are used here to compute the principal curvatures of the vertex in 2D and 3D. The effects of fitting section and fitting scope of tomography were investigated. Section 1 in Figure 4.30 represents the centre position of the tomography: the geometry above the section is fitted. The fitting scope is thus becoming increasingly smaller from the centre position until section 10 with equal section spacing. The fitting section is divided by 10, 20 and 50 respectively in the fitting scope of the semi-particle. The fitting scope is varied by semi-particle, quarter particle, one-eighth particle and one-sixteenth particle. The program of curvature estimation in 3D is appended in Appendix B. The corresponding results from different fitting circumstances are presented as follows.

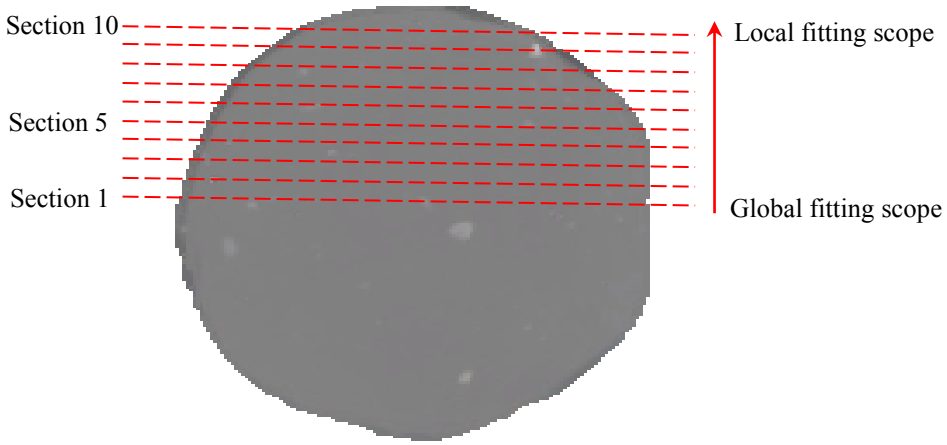

Figure 4.30 Sketch of fitting section from global fitting to local fitting

The parameters used to calculate the Young's modulus and the indentation depth during deformation are summarized in Table 4.4 below. In Table 4.4 *R* was the averaged value of 6 times-measurement using the caliper ruler.

Table 4.4 Parameters for calculation of Young's modulus and indentation depth of a zeolite 4AK particle

Radius (mm)	Applied force (N)	Displacement (mm)	Poisson's ratio
1.135	6	0.02	0.25

4.13 Results

4.13.1 Effect of angular division on principal curvatures

Eighteen pairs of orthogonal planes around the vertex were obtained from stacked slices by an incremental rotation of 5 degrees. The curvature value of individual orthogonal plane using the 3rd polynomial and circular fitting methods are tabulated in Table 4.5 using fitting section 1. Note that the curvature using the 3rd polynomial fitting is determined by Eq. (4.13). As in Eq. (4.10), the Young's modulus is determined by the summation of maximum and minimum principal curvature, thus the summation of principal curvature is shown in Table 4.5 as well.

Table 4.5 Estimated curvature in orthogonal planes using the 3rd polynomial and the circular fitting method in section 1

Rotation degree (^{0})	Plane XZ		Plane YZ		Sum_K (mm^{-1})	Sum_Kc (mm^{-1})
	K (mm^{-1})	Kc (mm^{-1})	K (mm^{-1})	Kc (mm^{-1})		
0	1.376	0.864	1.593	0.897	2.970	1.761
5	1.412	0.852	1.599	0.890	3.011	1.742
10	1.404	0.851	1.599	0.885	3.002	1.736
15	1.404	0.851	1.615	0.882	3.018	1.734
20	1.368	0.848	1.627	0.883	2.995	1.732
25	1.321	0.839	1.628	0.887	2.949	1.726
30	1.268	0.830	1.615	0.887	2.883	1.717
35	1.206	0.822	1.597	0.885	2.802	1.707
40	1.198	0.822	1.564	0.881	2.763	1.703
45	1.397	0.857	1.595	0.896	2.992	1.752
50	1.215	0.818	1.520	0.876	2.735	1.694
55	1.208	0.817	1.478	0.870	2.686	1.687
60	1.231	0.817	1.486	0.873	2.717	1.690
65	1.296	0.820	1.490	0.874	2.786	1.694

70	1.396	0.830	1.496	0.876	2.892	1.706
75	1.470	0.837	1.494	0.874	2.964	1.711
80	1.542	0.841	1.485	0.870	3.027	1.711
85	1.590	0.851	1.477	0.865	3.067	1.716

According to the Euler's theory, there exists principal curvatures around one point on a smooth surface, which represents the maximum and minimum curvature. The non-linear least square approach was used to optimise the principal curvature based on the curvature value listed in Table 4.6. The principal curvatures were found to be 1.612 and 1.275 using the 3rd polynomial fitting method, while they were found to be 0.892 and 0.829 using circular fitting method. The same method is applied to optimise the principal curvature calculated by 3rd fitting method and circular fitting method under different incremental rotation angles. The optimised results are shown in Table 4.6 and the corresponding plot is shown in Figure 4.31.

Table 4.6 Optimised principal curvature with varying incremental rotation angle using two fitting methods

Incremental rotation angle (^{0})	3rd polynomial fitting method		Circular fitting fitting method		K_sum (mm^{-1})	Kc_sum (mm^{-1})
	Kmax (mm^{-1})	Kmin (mm^{-1})	Kmax (mm^{-1})	Kmin (mm^{-1})		
5	1.612	1.275	0.892	0.829	2.887	1.721
10	1.613	1.274	0.894	0.827	2.888	1.721
20	1.619	1.274	0.883	0.832	2.893	1.715
45	1.671	1.264	0.888	0.824	2.935	1.712

In Figure 4.31, as the incremental rotation angle is increased, the summation of the principal curvatures using 3rd polynomial fitting method increases slightly whereas that using the circular fitting method decreases lightly. The curvature estimate thereafter is obtained by 5 degree of incremental rotation angle under different fitting sections.

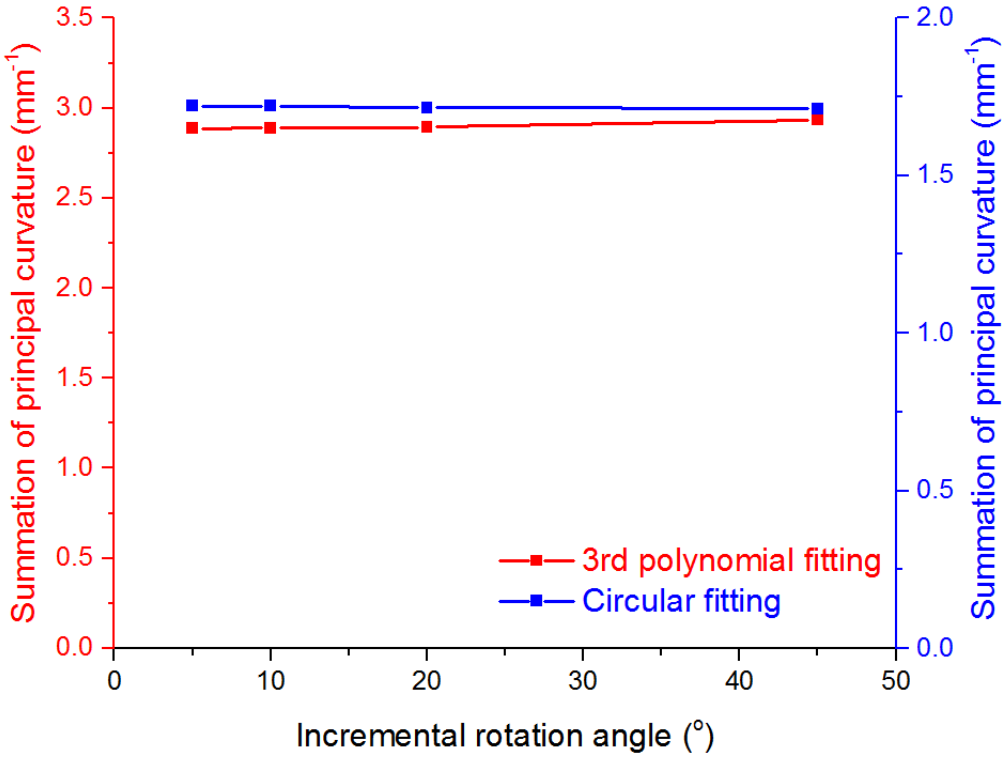

Figure 4.31 Variation of incremental rotation angle versus summation of principal curvature under 3rd polynomial and circular fitting methods

4.13.2 Effect of fitting section on the principal curvatures

The fitting section is varied in the spectrum of 10, 20, 50 respectively, within the fitting scope of the semi-particle. The estimated principal curvature summation from 2D and 3D 3rd polynomial fitting methods within 10 sections is shown in Figure 4.32 whilst the estimated principal curvature summation from the circular and spherical fitting methods is shown in Figure 4.33. Note that the relative variation is defined by the difference of principal curvature summation under 2D and 3D fitting conditions divided by the principal curvature summation from 3D fitting condition. Take 3rd polynomial fitting for example, the relative variation is defined as (K_sum_{3D}- K_sum_{2D})/ K_sum_{3D}, where K_sum_{3D} and K_sum_{2D} are the principal curvature summations in 3D and 2D fitting using the 3rd polynomial fitting method.

As seen from Figure 4.32, the principal curvature summation obtained in 2D and 3D from the 3rd fitting methods are generally in good agreement. The principal curvature summation decreases and the relative variation is increasingly large as the fitting section is increased. Similarly, the principal curvature summation through circular fitting agrees well with that through spherical fitting. However, the principal curvature

summation increases slightly and then reduces as the fitting section is increased. In particular, the principal curvature summation by the 3rd polynomial fitting is larger than that by circular or spherical fitting. Likewise, the principal curvature calculated in 20 sections through the 3rd polynomial fitting is plotted in Figure 4.34. The principal curvature calculated in 20 section through the circular and spherical fitting method is plotted in Figure 4.35.

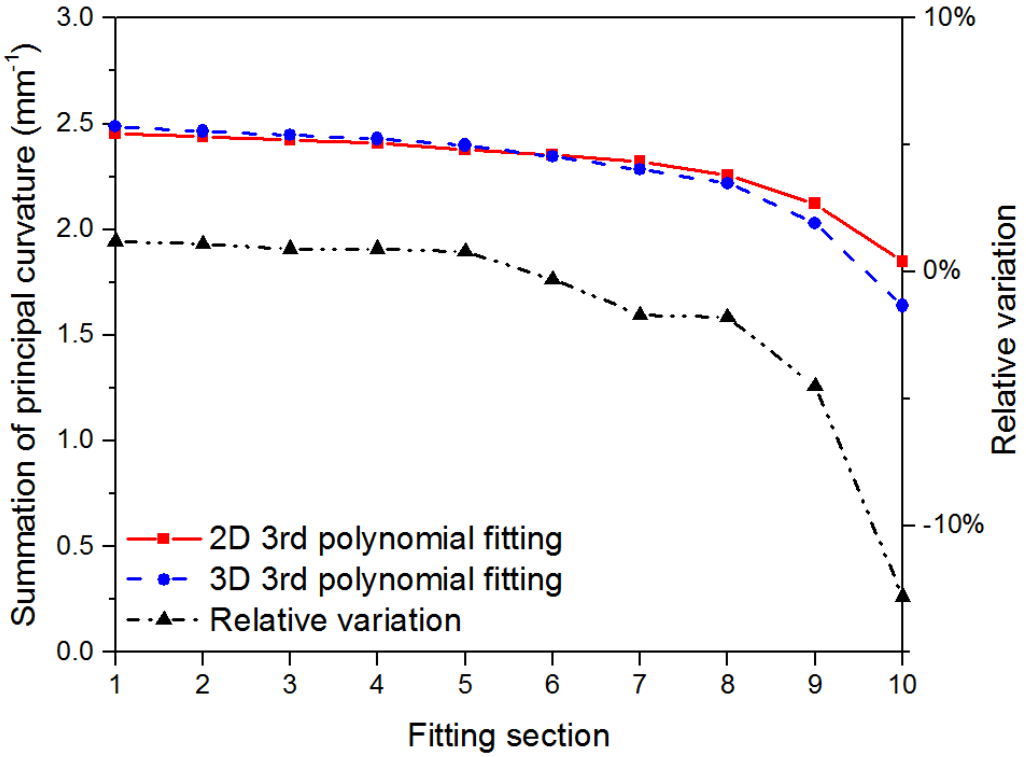

Figure 4.32 Variation of fitting section versus summation of principal curvature using 2D and 3D polynomial fitting methods

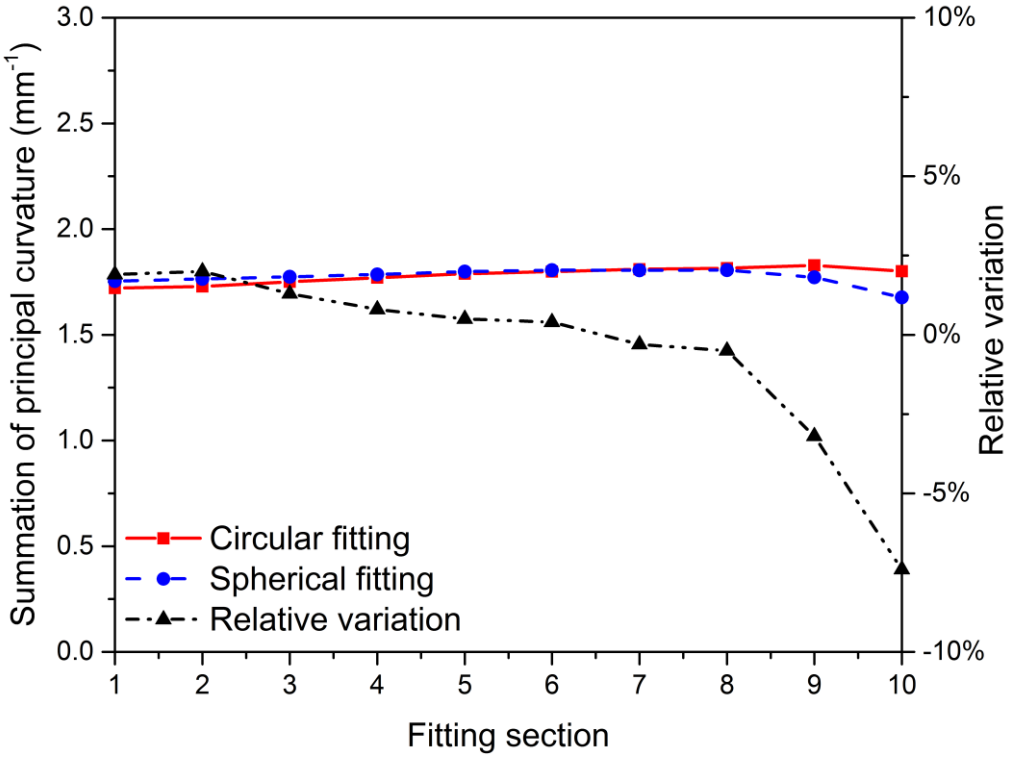

Figure 4.33 Number of fitting section versus summation of principal curvature under circular and spherical fitting methods

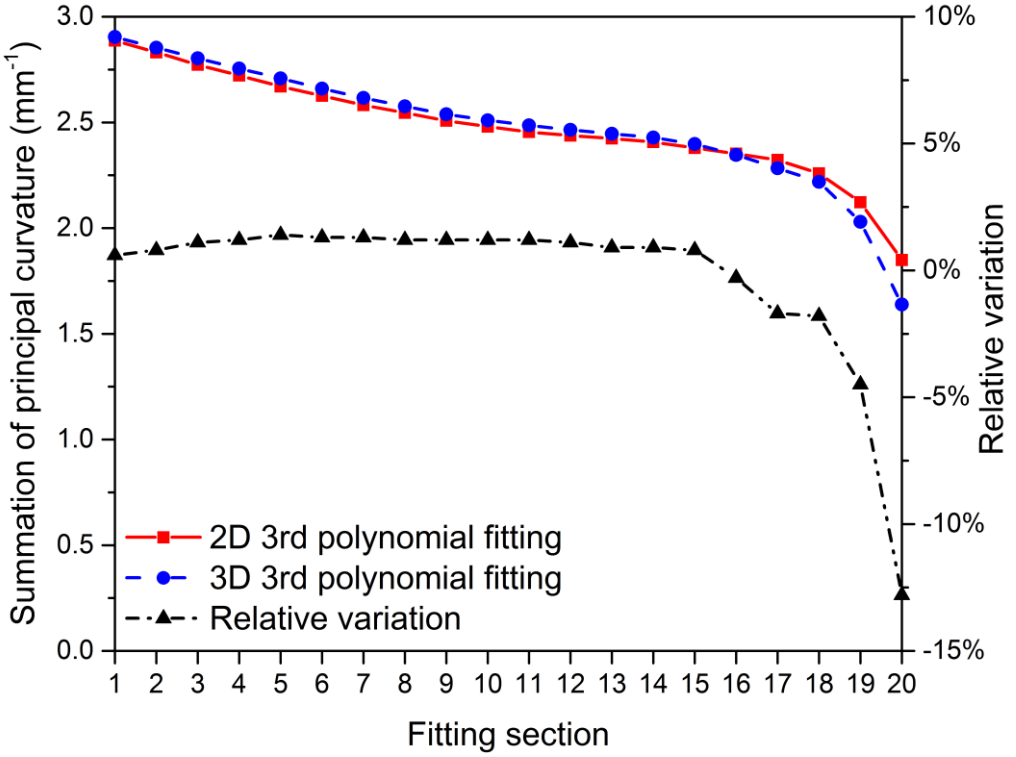

Figure 4.34 Number of fitting section versus summation of principal curvature under 2D and 3D polynomial fitting methods

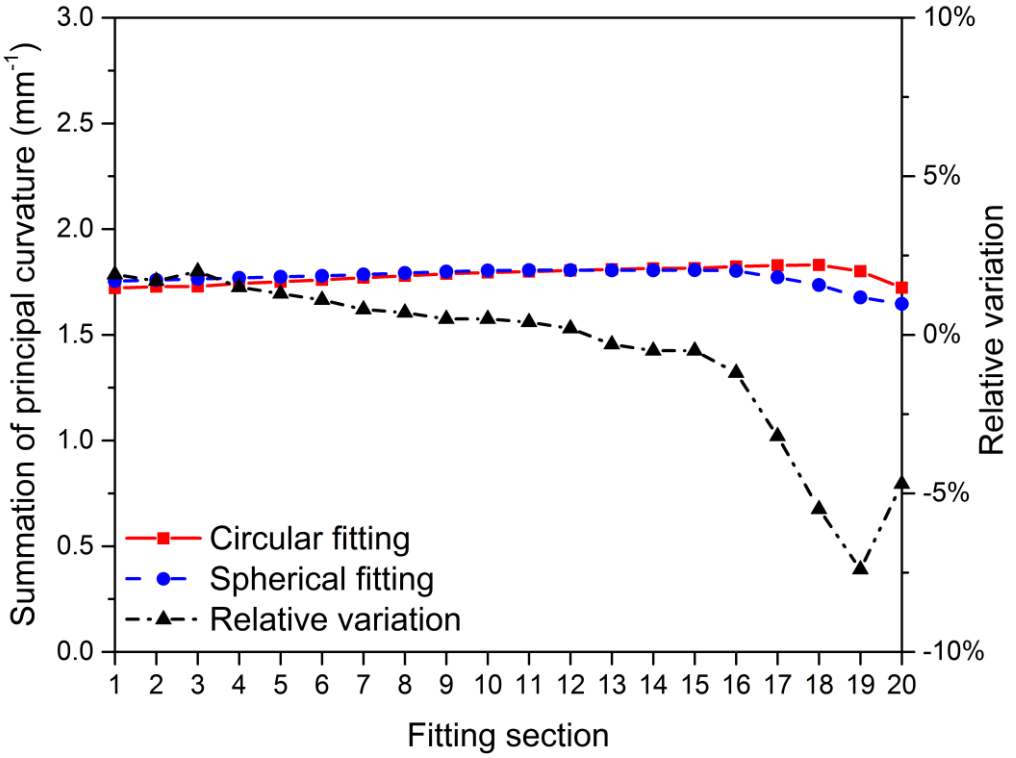

Figure 4.35 Number of fitting section versus summation of principal curvature under circular and spherical fitting methods

In Figure 4.34 of the 3rd polynomial fitting, the principal curvature summation with 20 sections decreases with the increase of fitting section, which follows the trend in 10 sections. However, the relative variation in 20 sections is more deviated as compared to that in 10 sections. Despite some fluctuations of principal curvature summation in Figure 4.35, it shows that the principal curvature summation through circular and spherical fitting is more stable than that from the 3rd polynomial fitting. A good agreement is reached under 2D and 3D conditions irrespective of the fitting method.

Similarly, the principal curvature calculated in 50 sections through the 3rd polynomial fitting is plotted in Figure 4.36. The principal curvature calculated in 50 section through circular and spherical fitting is summarized plotted in Figure 4.37 respectively.

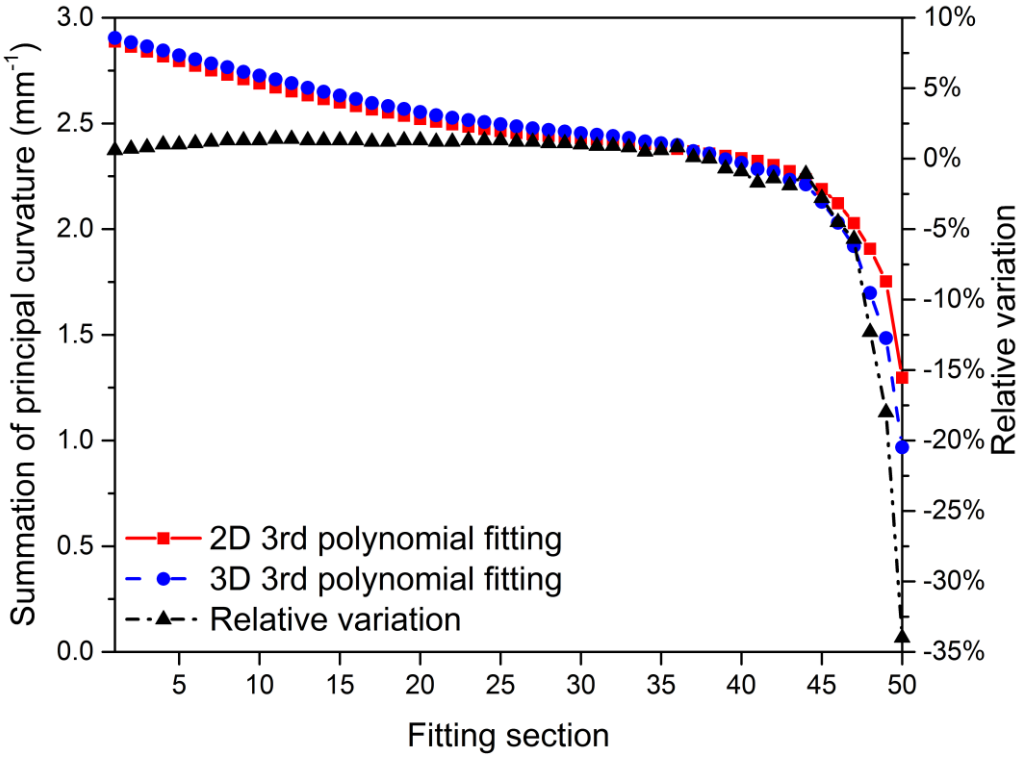

Figure 4.36 Number of fitting section versus summation of principal curvature under 2D and 3D polynomial fitting methods

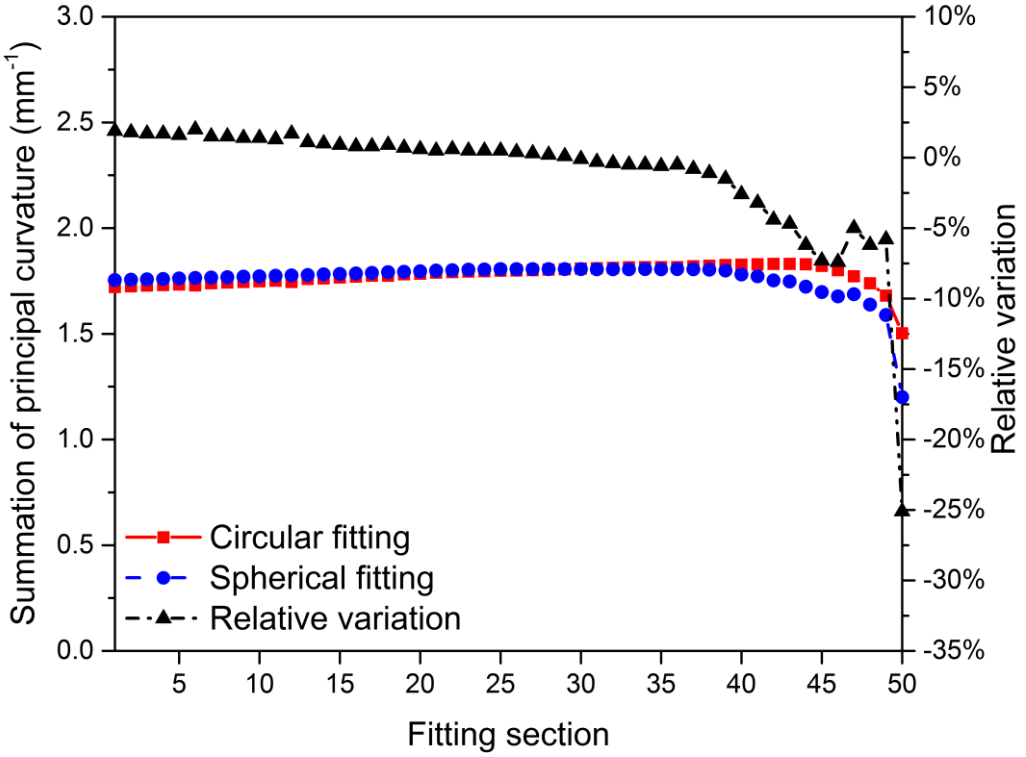

Figure 4.37 Number of fitting sections versus summation of principal curvatures using the circular and spherical fitting methods

The principal curvature summation in 50 sections generally follows the trend in 10 and 20 sections. Amongst Figures 4.32, 4.34 and 4.36, it is found that the principal curvature summation obtained through 3rd polynomial fitting decreases as the fitting section is increased. The principal curvature summation obtained from the circular or spherical fitting method is more stable compared to the 3rd polynomial fitting. The relative variation of principal curvature summation through 3rd polynomial fitting is more drastic than that through circular or spherical fitting. The principal curvature summation under 2D and 3D fitting are in good agreement.

4.13.3 Effect of fitting scope on the principal curvature

The principal curvature estimated through 10 sections is obtained in the scope of semi-particle, quarter-particle, eighth-particle and sixteenth-particle. The curvature value extracted from the 2D and 3D fitting methods is shown as below. The principal curvature in the scope of semi-particle is excluded since it is the same as the value in Figures 4.32 and 4.33. The principal curvature summation calculated from 2D and 3D polynomial fitting methods in the scope of quarter-particle, eighth-particle and sixteenth-particle is depicted in Figures 4.38, 4.40 and 4.42 respectively. The principal curvature summation calculated from the circular and spherical fitting methods in the scope of quarter-particle, eighth-particle and sixteenth-particle is depicted in Figures 4.39, 4.41 and 4.43 respectively. Note that the principal curvature in 2D state was calculated by non-linear least-square method whilst the principal curvature in 3D state was calculated according to Eq. (4.19).

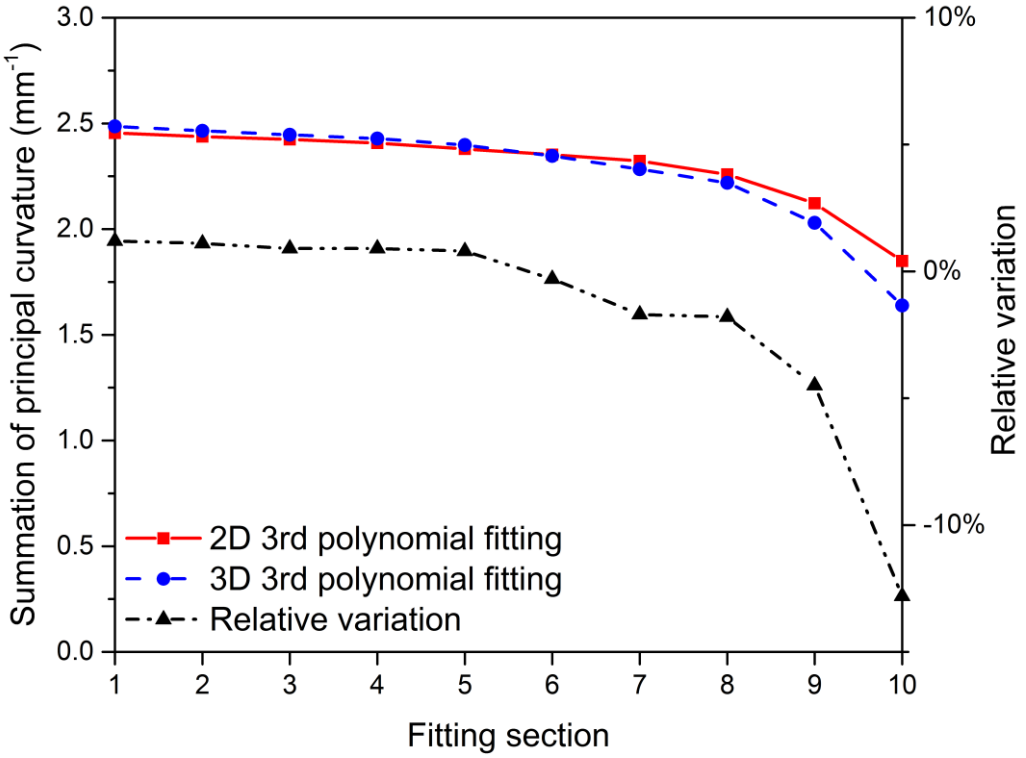

Figure 4.38 Number of fitting sections versus summation of principal curvature from the 2D and 3D polynomial fitting scope of quarter-particle

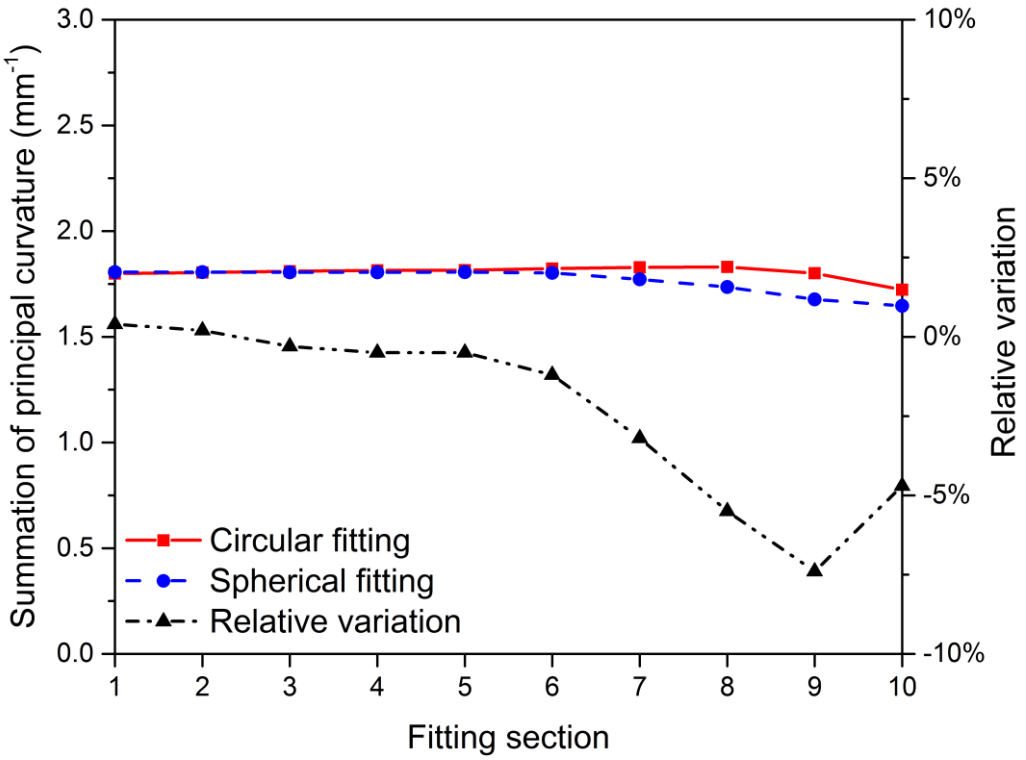

Figure 4.39 Number of fitting section versus summations of principal curvature under circular and spherical fitting scope of quarter particle

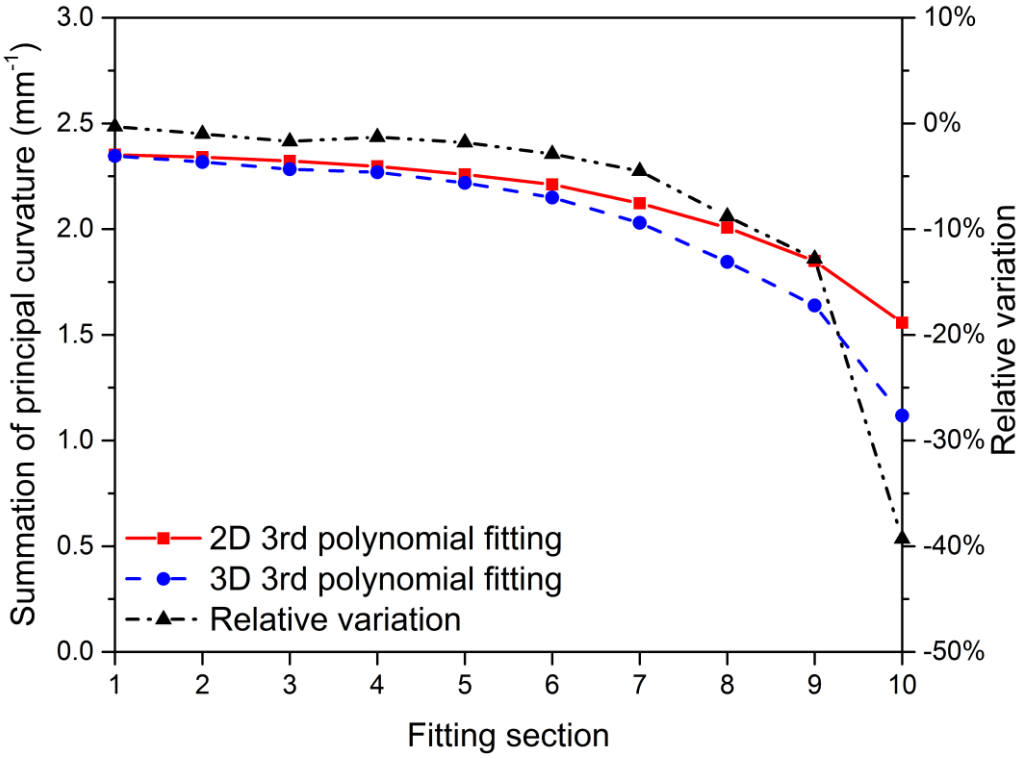

Figure 4.40 Number of fitting section versus summation of principal curvature under 2D and 3D polynomial fitting scope of one-eighth particle

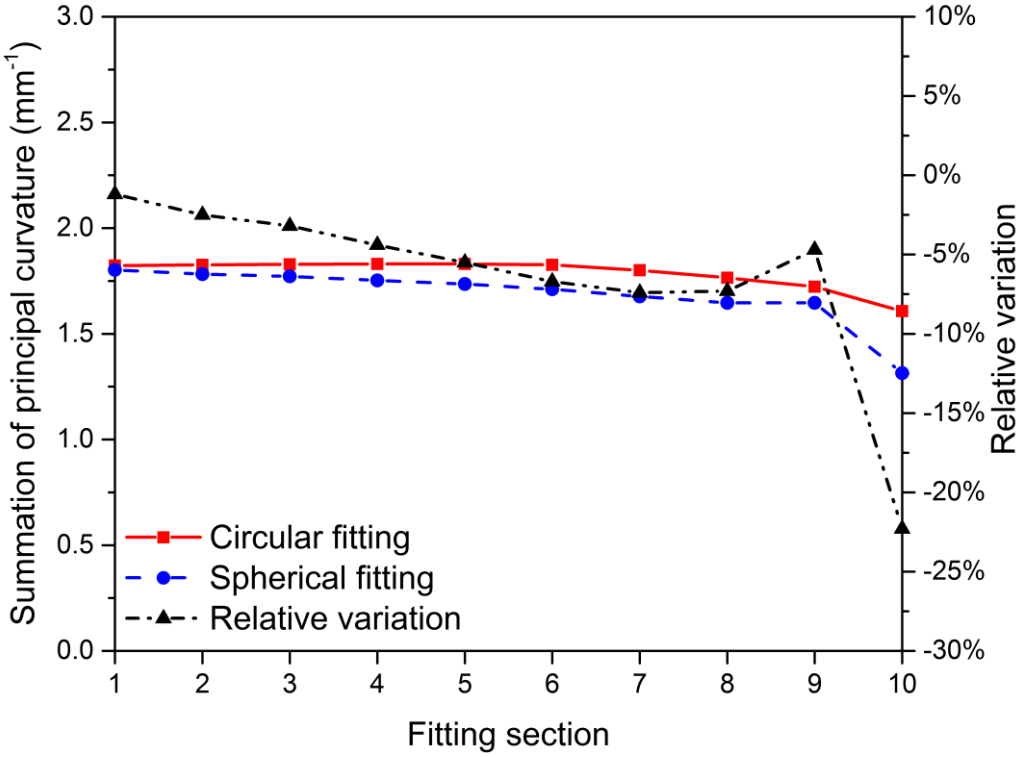

Figure 4.41 Number of fitting section versus summation of principal curvature under circular and spherical fitting scope of one-eighth particle

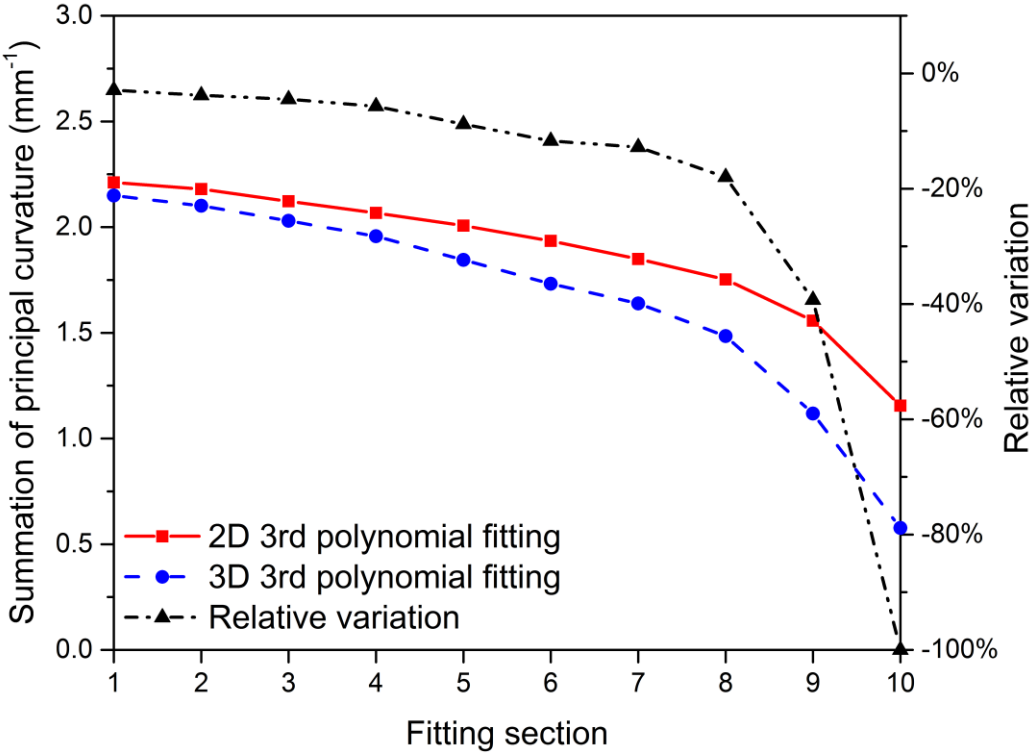

Figure 4.42 Number of fitting section versus summation of principal curvature under 2D and 3D polynomial fitting scope of one-sixteenth particle

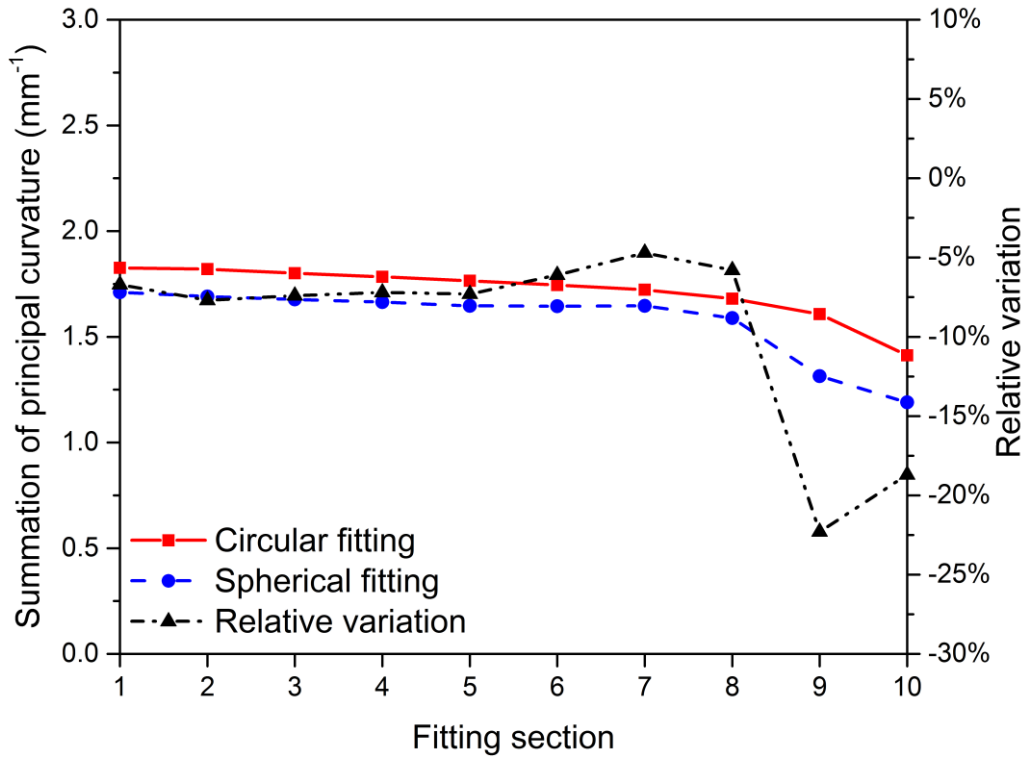

Figure 4.43 Number of fitting section versus summation of principal curvature under circular and spherical fitting scope of one-sixteenth particle

In terms of the 3rd polynomial fitting, the principal curvature summation decreases as the fitting scope is reduced. The difference of principal curvature summation between 2D and 3D condition is larger when the fitting scope is narrower. As for the circular or spherical fitting, the principal curvature summation is lower than that of 3rd polynomial fitting and the relative variation is smaller than that of 3rd polynomial fitting. This indicates that the principal curvature summation obtained by 3rd polynomial fitting is more sensitive to that by circular or spherical fitting.

4.13.4 Influence of contact curvature on Young's modulus

4.13.4.1 Effect of fitting section on Young's modulus

The Young's modulus is a measure of the stiffness of materials during elastic deformation. As indicated from Eq. (4.10), the value of the Young's modulus is associated with the principal curvature summation of the upper and lower contact point during parallel platen compression. The same fitting method is used to estimate the principal curvature of bottom contacting point and the Young's modulus is calculated based on Eq. (4.10) considering the calculated values of principal curvature summation in the previous sections. Note that the traditional way of measuring the contact curvature is to use the average of particle size. For example, the particles tested were 1.135 mm in radius and thus the contact curvature was 1/1.135 mm^{-1}. The Young's modulus through the fitting methods and averaging method is summarized as below. The computed Young's modulus in 10, 20 and 50 sections in terms of semi-particle are shown in Figures. 4.44, 4.45 and 4.46 respectively.

4.13.4.2 Effect of fitting scope on Young's modulus

Similarly, the Young's modulus determined from different fitting methods is presented with different fitting scopes. The Young's modulus determined from a quarter particle scope, one-eighth particle, one-sixteenth particle are shown in Figs. 4.47, 4.48 and 4.49 respectively.

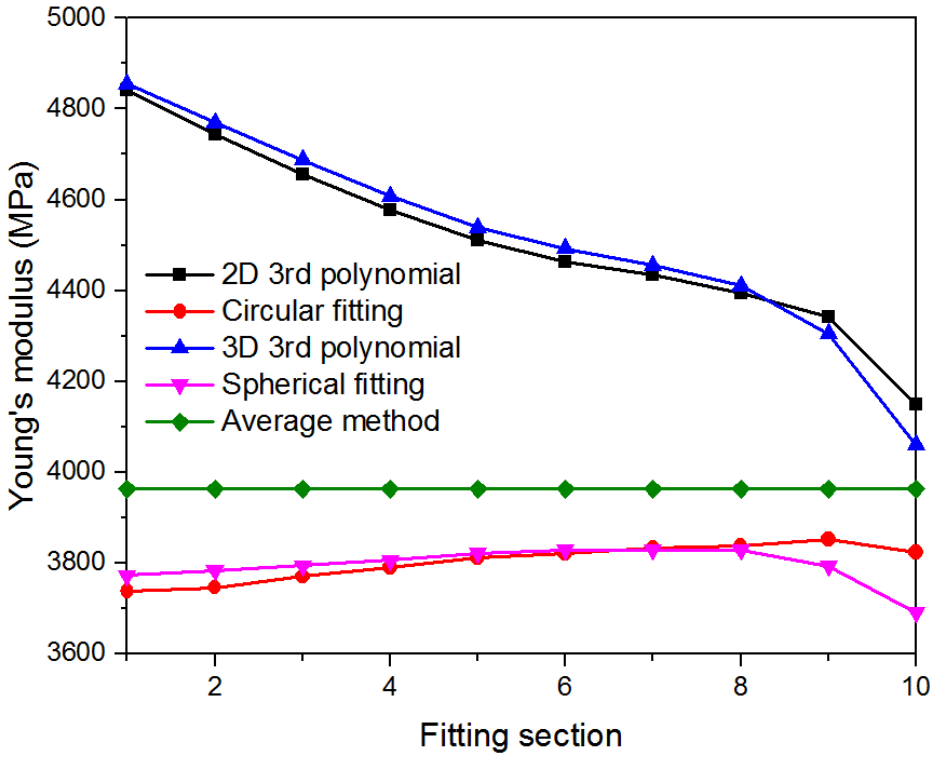

Figure 4.44 The Young's modulus determined from different fitting methods with a semi-particle scope

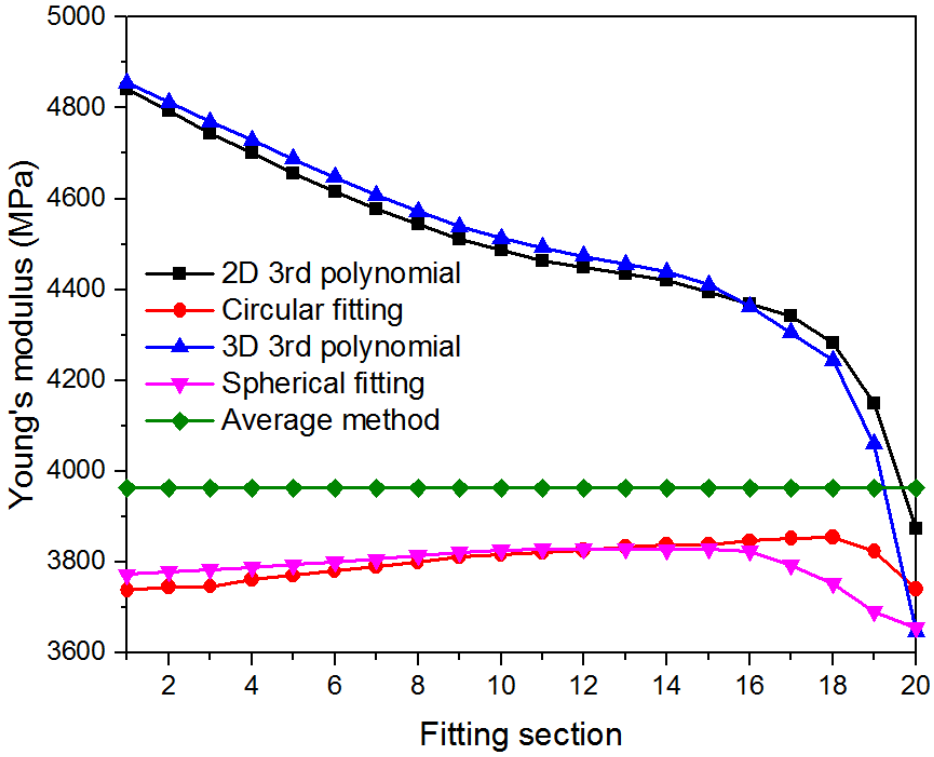

Figure 4.45 The Young's modulus determined by different fitting methods with a semi-particle scope of 20 sections

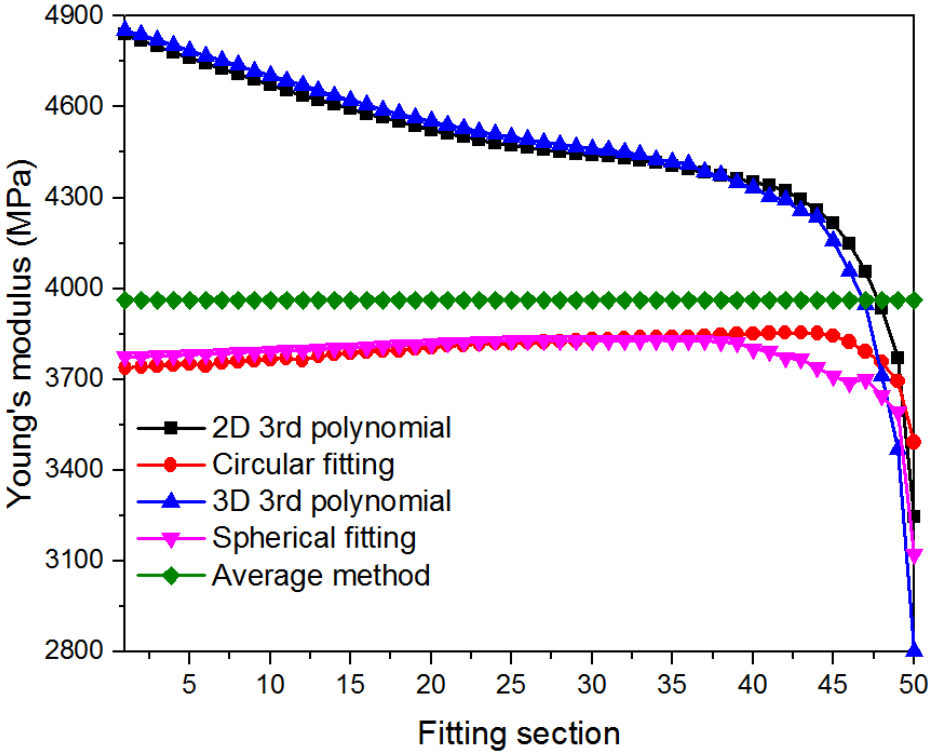

Figure 4.46 The Young's modulus determined by different fitting methods in semi-particle scope of 50 sections

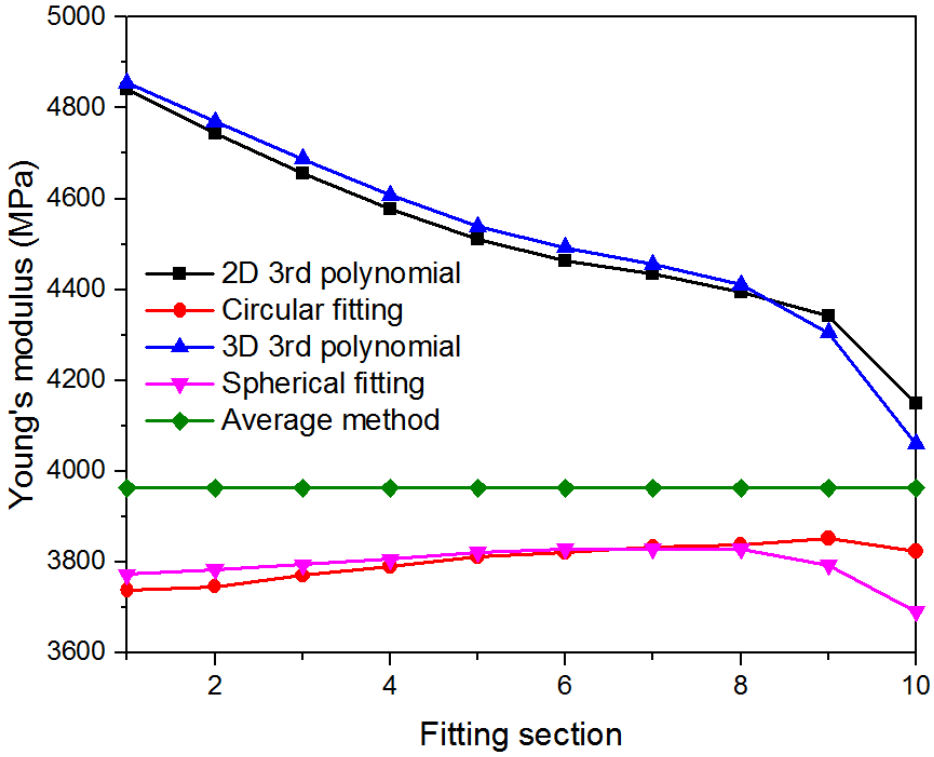

Figure 4.47 The Young's modulus determined from different fitting methods with a quarter particle scope

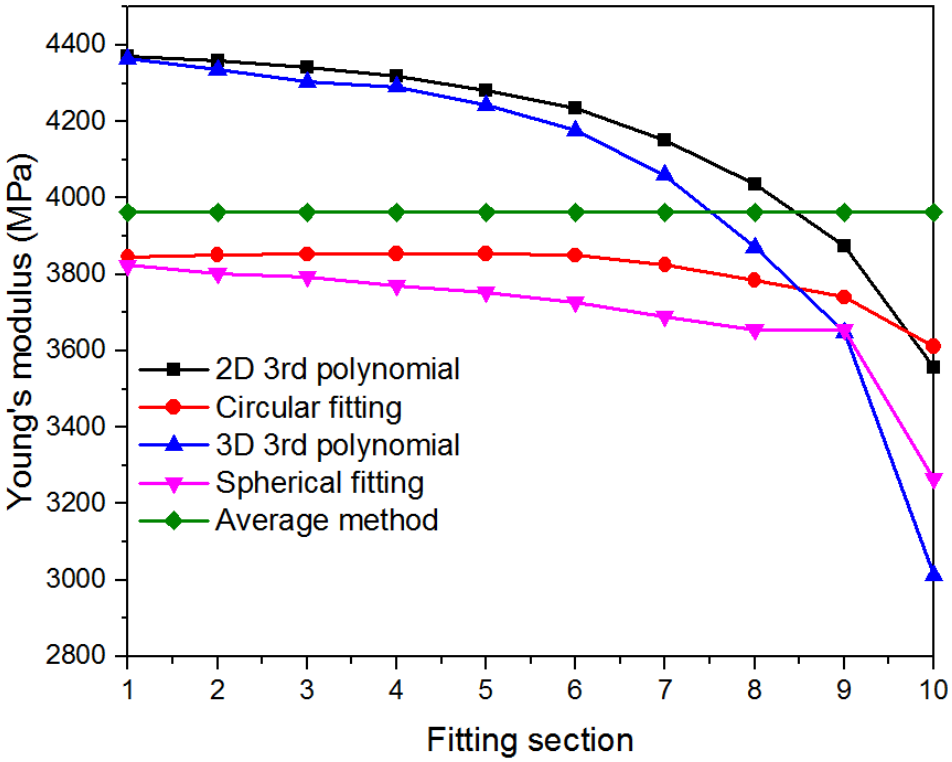

Figure 4.48 The Young's modulus determined from different fitting methods with one-eighth particle scope

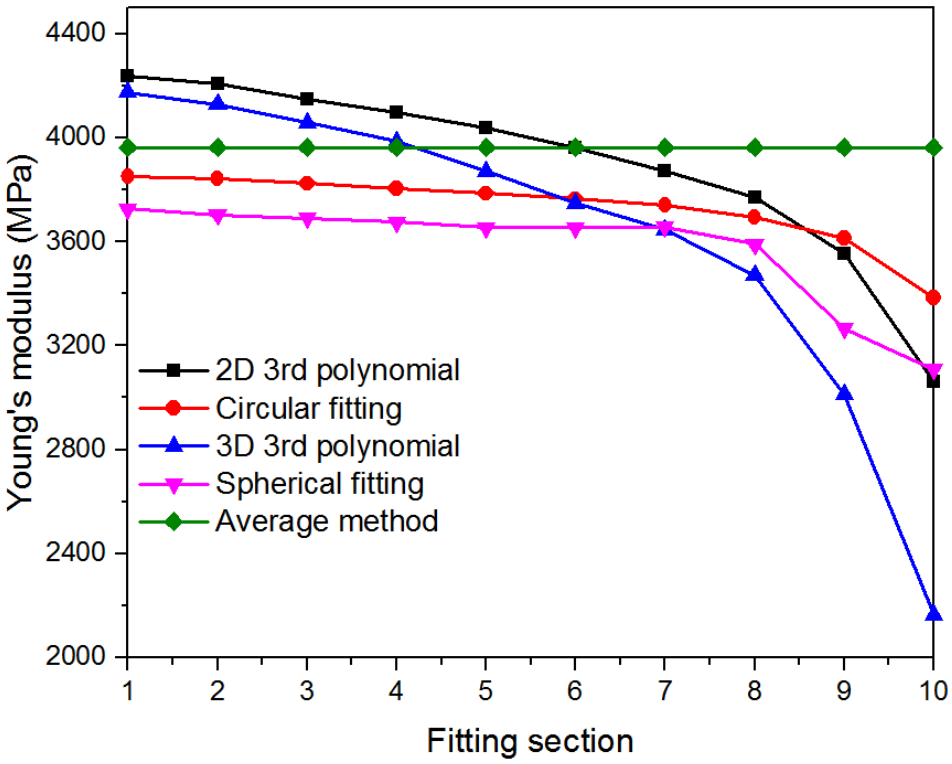

Figure 4.49 The Young's modulus determined from different fitting methods with an one-sixteenth particle scope

4.14 Discussions

1. The Young's modulus reduces with the increase of the number of fitting sections when the 3rd polynomial fitting method is used. The Young's modulus obtained in 10 fitting sections with semi-particle is larger than that by the traditional averaging method. The majority of the Young's modulus obtained in 20 and 50 fitting sections of semi-particle is larger than that by traditional averaging method (3963 MPa) with some lower than 3963 MPa in higher fitting sections. The Young's modulus obtained using the circular and spherical fitting is constantly lower than 3963 MPa for the three fitting sections with a semi-particle.

2. As for the fitting scope, the Young's modulus determined from using the 3rd polynomial fitting method reduces when the fitting scope is reduced from one quarter-particle to one-sixteenth particle. For the same fitting scope, the Young's modulus reduces as the number of fitting sections increases. The summation of the principal curvatures changes dramatically under narrower fitting scope. The Young's modulus from the 3rd polynomial fitting is higher than 3963 MPa in the first fitting section before becoming lower than 3963 MPa in the tenth fitting section. The Young's modulus from the circular and spherical fitting methods is constantly lower than 3963 MPa. The value of the Young's modulus reduces significantly in higher fitting sections and smaller fitting scope, which indicates that the Young's modulus resulting from principal curvature is more sensitive to local fitting regions.

3. The largest value of the Young's modulus calculated from polynomial and spherical fitting is respectively 4855MPa and 3773MPa within section 1 of the semi-particle scope whereas the smallest value of the corresponding Young's modulus is 2165MPa and 3108MPa in section 10 with one-sixteenth particle scope. This indicates that a drastic change of the Young's modulus when fitting from globally to locally, which results from a drastic change of contact curvature.

4. The preceding study has shown that the calculated Young's modulus of a particle exhibits a non-negligible variability, and is highly associated with its profile. The contact curvature becomes significant in determining the Young's modulus when taking particle shape into account. As noted by Miller et al. (2008), an accurate and repeatable

topological characterization measurement is still an enigma. However, a criterion for the determination of the Young's modulus should consider the effect of contact curvature in which the particle shape is an important factor.

4.15 Summary

An in-situ loading X-ray μCT investigation had been carried out to evaluate the progressive failure of particles under compression. A detailed procedure of image processing has been presented in which the raw data are converted into images readable for analysis. In particular, a linear interpolation method has been proposed to alleviate the spatial drift during data collection process. The breakage pattern of six zeolite particles under in-situ loading has been discussed and it has been found that the splitting failure is the dominant failure type. It has also been observed that the cracks first initiate from the contact area then propagate parallel to the loading direction resulting in radial cracks, consistent with the observations of previous work (Shipway and Hutchings, 1993; Cil and Alshibli, 2012).

The digital image correlation (DIC) technique has been used to shed more light on the progressive failure in a quantitative way. With the help of DIC, the displacement field has been produced by correlating subsets in a reference image (undeformed tomography) to subsets in a deformed image (deformed tomography). These images were analysed using 3D DIC to provide full field displacement and strain field mapping, allowing for the evaluation of strain localisation under incremental loading. The strain fields obtained via 3D DIC indicate that localized strain field in the particle has already formed prior to the peak force. The finding from this work reveals that the localized zone forms before the peak force and the localized zone is not uniform. Further application of DIC is shown by the crack growth evaluation inside a particle under compression, which provides a means to study crack propagation and helps to identify the role of crack opening in the failure mechanism. The information obtained from the DIC also serves to validate the bonded contact models which may be used to predict the crack opening in numerical simulation. The combined use of X-ray μCT and DIC is proved useful to show some important information which are difficult to detect in the tomographic images alone.

Finally, the principal curvature at the contact point has been investigated taking the particle shape into account. X-ray μCT tests have been carried out to obtain the profile of a single particle. The orthogonal slices of the particle were binarized to obtain the profile of the particle. Two fitting methods were chosen, the 3rd polynomial fitting and the circular fitting (spherical in 3D). The principal curvature in 2D fitting is optimised by a non-linear least square method. A good agreement of the principal curvature was reached under 2D and 3D condition irrespective of the fitting method. The effect of contact curvature on the Young's modulus determination was then studied and it was found that the Young's modulus changes drastically from global fitting to local fitting, which demonstrates a non-negligible variation when particle shape is considered. It was shown that contact curvature exerts an important role on the determination of Young's modulus when particle shape is taken into account. It is advocated that a criterion for the Young's modulus should consider the effect of contact curvature in which the particle shape is an important factor. However, the sensitivity analysis of the Young's modulus to contact curvature is considered for one particle only. A robust and accurate criterion to determine Young's modulus considering the effect of contact curvature will be the subject of research via a systematic analysis of multiple particles.

Chapter 5

Development of a rigorous particle breakage model

5.1 Introduction

Based on the measured mechanical properties of particles and experimental finding from particle breakage subject to impact loading in Chapter 3, this chapter aims to develop a new particle breakage model from a fundamental level and present a systematic assessment of the new and existing particle breakage models under both normal and oblique impacts. Section 5.2 describes two distinctive breakage patterns of particles under impact loading and Section 5.3 presents the indentation failure process which provides the physical basis for the development of the new breakage model. A detailed review of existing fracture based breakage models is given in Section 5.4. In section 5.5, the reviewed models are assessed with the experimental data from single particle impact test with deficiencies identified, highlighting the need for a more general breakage model. A new breakage model for particulate solids is proposed based on a mechanics approach in Section 5.6. Section 5.7 assess the suitability of the proposed as well as existing particle breakage models against test data under both normal and oblique impact loading collected from the literature. Some key issues with regard to the breakage models are discussed in Section 5.8, before concluding remarks are drawn in Section 5.9.

5.2 Breakage pattern

Particles under impact loading have two breakage patterns: chipping and fragmentation. Chipping is recognized as subsurface material removal from the particle due to local damage such as edge or corner detachment. It is inferred that the size of the original particle is not greatly reduced since the size of the chips is usually very small as compared with the parent particle. Fragmentation refers to the splitting of the original particle into many pieces. Fragmentation results in a wide size distribution of progeny particles and whereby the original particle loses the intactness. From the impact loading perspective, chipping is relevant to small-scale particle fracture under low impact loading whilst fragmentation is related to large-scale particle fracture under high impact loading. The schematic illustration of the two breakage patterns is shown in Figure 5.1,

in which they are distinguished by the particle size distribution after impact (Scala et al. 2007). Note that the solid line and dashed line in Figure 5.1 represent the particle distribution function (PDF) before and after impact respectively. For chipping, the original particles still account for the majority of size proportion though the proportion of fine progeny particle is increased. For fragmentation, the peak in the particle size distribution is shifted to progeny particles with the proportion of original particle size dramatically decreased.

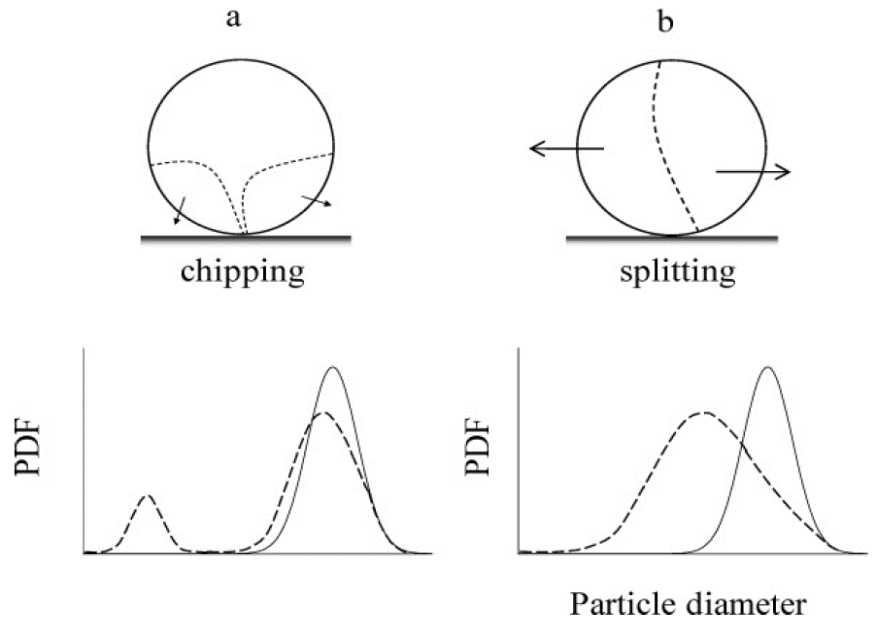

Figure 5.1 Schematic of two breakage patterns: (a) chipping and (b) fragmentation (Adapted from Scala et al. 2007)

In order to characterize the breakage extent of particle in comminution such as impact loading, the selection function and breakage function are widely used in the literature (Rozenblat et al. 2012). The selection function, namely breakage probability, is usually described by the mass loss of the original particle whilst the breakage function is reflected by the size distribution of fragments.

5.3 Failure process in indentation tests

Indentation fracture mechanics has shown significant promise in a micro-scale for studying the grinding mechanisms of particles due to the likeness of the abrasive process between the grinding and the indentation (Malkin and Hwang, 1996). A general failure process of brittle solids under indentation describing the essential feature has

been widely reported in the literature (Lawn and Swain, 1975; Lawn et al. 1975; Swain and Lawn, 1976). The sequence of a complete loading and unloading cycle is as follows (Figure 5.2): (a) Initial loading: A damage zone is induced around the contact point. The size of the compression zone increases with the loading. (b) Formation of the critical zone: A crack initiates below the contact point until a critical loading stage. This crack is termed as the median/radial crack. (c) Stable crack growth: stable extension of the median crack occurs as the loading is further increased. (d) Initial unloading: The median crack begins to close. (e) Residual-stress cracking: Relaxation of deformed material within the contact zone prior to the removal of indenter superimposes intense residual tensile stresses upon the applied field. Sideward cracks termed as lateral cracks begin to appear. (f) Complete unloading: Subsurface lateral cracks continue to extend upwards, which may cause chipping.

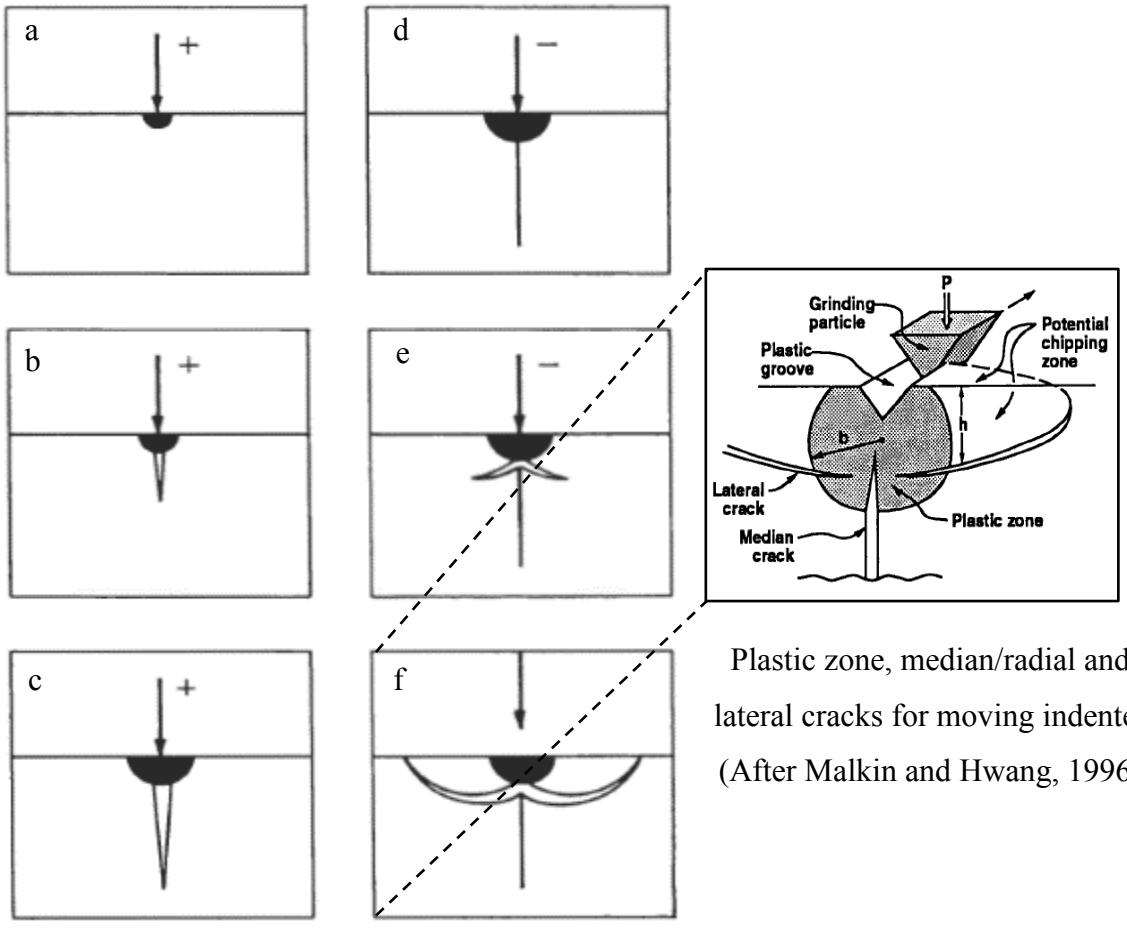

Plastic zone, median/radial and lateral cracks for moving indenter (After Malkin and Hwang, 1996)

Figure 5.2 Schematic of crack formation under point indentation; + denotes loading, - denotes unloading (Adapted from Lawn and Swain 1975)

Figure 5.2 shows that there are four important parameters in the indentation failure process, i.e., contact radius, radial crack length, lateral crack length and the indentation depth. It should also be noted that the radial crack is generated during loading stage whilst lateral crack is generated during the unloading stage.

Individual chipping events in the grinding of brittle materials are resulted from the lateral crack growth whilst fragmentation events in the grinding process are attributed to median/radial crack growth. Yuregir et al. (1986) demonstrated that the crack morphology of a particle under impact is similar to that generated by indentation of a flat surface by an indenter. The indentation failure process from micro-scale thus serves as a physical basis to develop breakage models from a fundamental level. The review of existing particle breakage models based on indentation fracture mechanism is described in the following section.

5.4 Review of fracture based models

5.4.1 Evans and Wilshaw's (1976) model

Evans and Wilshaw (1976) studied the surficial fracture by plastic indentation for a range of brittle materials in the quasi-static regime. A material removal expression was proposed by approximate stress analysis on the assumption that material removal occurs when lateral cracks from adjacent impacts interact.

The hardness (H) of a material determined by indentation is given by

$$H = P/(2a)^2 sin\theta \tag{5.1}$$

where θ is the angle between the indenter face and the direction of applied load (P); $2a$ is the indent diagonal.

The radial and lateral crack length in terms of the applied load and material properties are given following approximate proportionalities:

$$c_r \propto P^{1/2}/(H^{1/4}{K_c}^{1/3}) \tag{5.2a}$$

$$c_l \propto (P/K_c)^{3/4} \tag{5.2b}$$

where c_r and c_l are the radial and lateral crack length respectively; K_c is the fracture toughness. Ghadiri and Zhang (2002) made a comment about the relationship between the normalised crack length, c/a and the normalised critical stress intensity factor, $K_c\phi/(H\sqrt{a})$; where $\emptyset$ is a constraint factor. The main critique for Eq. (5.2b) is that the power of 3/4 cannot be right for the dimensional reason.

It was observed that lateral crack extension can be enhanced by indent interactions and there seems to be a critical separation (r_c) between the sliding indenters. Material removal arising from lateral crack is assumed to occur when the lateral crack from adjacent indenters intersect. The maximum volume of material removal for each particle, V_{det}, is given by

$$V_{det} = \pi(r_c)^2 h \tag{5.3}$$

where h is the depth of the lateral crack.

Considering that $r_c \approx 2c_l$ and the lateral crack depth is proportional to the impression radius a, substituting Eqs. (5.1) and (5.2b) into Eq. (5.3) gives

$$V_{det} \propto \frac{P^2}{{K_c}^{3/2} H^{1/2}} \tag{5.4}$$

It is required to replace P with functional dependence on the impact velocity v. Unfortunately, there is no complete analytical function to describe P over the entire velocity range. However, Evans and Wilshaw (1976) proposed an approximate functional expression for non-work hardening materials as

$$P \propto v^{6/5} R^2 \tag{5.5}$$

The fraction of material loss due to the impact, ε, for a sphere of volume V, is given by

$$\varepsilon = \frac{V_{det}}{V} = \frac{V_{det}}{\frac{4}{3}\pi R^3} \tag{5.6}$$

Substituting Eqs. (5.4) and (5.5) into Eq. (5.6) gives

$$\varepsilon \propto \frac{\rho^{6/5} R}{K_c^{3/2} H^{1/2}} v^{12/5} \tag{5.7}$$

Although the velocity exponent is 2.4 in Eq. (5.7), it was stated that there is an interrelated effect of velocity and hardness on the material removal rate. For example, the velocity exponent increases as the impact velocity or the hardness increases.

5.4.2 Evans et al.'s (1978) model

Evans et al. (1978) investigated the impact fracture in the elastic-plastic response regime, in terms of surface extension and penetration. The impact damage was analysed by using simplified assumptions based on impact dynamics and basic fracture mechanics. Note that the underlying approach adopted for impact damage is analogous to that previously used to characterise the quasi-static indentation (Evans and Wilshaw, 1976) because of the complexity of the impact condition. The contact radius a under impact is expressed as

$$a \propto R v^{1/2} \tag{5.8}$$

The radial crack extension c_r is derived from the best fit of test data incorporating the material properties and projectile parameters

$$c_r \propto R^{4/3} v^{4/3} K_c^{-2/3} \tag{5.9}$$

where R and k_c are the radius and fracture toughness of impact material; v is the impact velocity.

An empirical relation for the damage penetration is expressed as

$$h \propto R v^{1/2} \rho^{1/4} H^{-1/4} \tag{5.10}$$

where ρ is the density of the material.

An expression for the material removal was proposed based on the assumption that material removal is the volume encompassed by the lateral cracks:

$$V_{det} = \pi(c_r)^2 h \tag{5.11}$$

Considering the breakage propensity $\varepsilon = \mathrm{V_{det}}/V$, substituting for c_r and h from Eqs. (5.9) and (5.10) thus gives

$$\varepsilon \propto \frac{\rho^{1/4} R^{2/3}}{K_c^{4/3} H^{1/4}} v^{19/6} \tag{5.12}$$

5.4.3 Hutchings' (1994) model

Hutchings (1994) derived an expression to estimate the impact force on a corner of a cube, and thus calculate the dimension of impression and fractional loss resulting from the impact. It is assumed that the kinetic energy of the particle is dissipated in the plastic deformation of the particle. This gives

$$\frac{1}{2} m v^2 = p\, V_c \tag{5.13}$$

where p is the contact pressure and V_c is the volume of deformed corner of a particle.

Assuming that the linear dimension of the flattened area of corner is proportional to the distance of the particle approaching the target, x, Eq. (5.13) evolves when the contact pressure is substituted by the hardness of a particle:

$$\frac{1}{2} m v^2 \propto H\, x^3 \tag{5.14}$$

The contact force P is given under the quasi-static condition:

$$P \propto H\, x^2 \tag{5.15}$$

Substituting Eq. (5.14) into Eq. (5.15), yields

$$P \propto H^{1/2} \rho^{2/3} R^2 v \tag{5.16}$$

The mean contact pressure is approximated by the hardness (Zhang, 1994). It then follows that the size of the contact impression can be simply expressed in terms of hardness as

$$a \propto \sqrt{\frac{P}{H}} \tag{5.17}$$

Substituting Eq. (5.16) into Eq. (5.17), the compression size is given by

$$a \propto R v^{\frac{2}{3}} \left(\frac{\rho}{H}\right)^{1/3} \tag{5.18}$$

The size of impression radius is expressed as a function of contact force and then the relationship between the impression radius and material property is established.

As the relationship between the contact radius and lateral crack length and depth is the same as that in the model of Ghadiri and Zhang (2002) (see more details in Section 5.4.4), the fractional loss of particle by impact is obtained as follow:

$$\varepsilon \propto \frac{\rho^{4/3} R H^{2/3}}{K_c^2} v^{8/3} \tag{5.19}$$

5.4.4 Ghadiri and Zhang's (2002) model

Ghadiri and Zhang (2002) proposed a breakage model based on the assumption that the formation of subsurface lateral crack results in chipping by impacting a particle against a rigid plate. The lateral crack length is estimated using a linear approximation to the normalised crack length versus the normalised fracture toughness curve; the depth of lateral crack is assumed to be proportional to the contact radius.

5.4.4.1 Lateral crack length and depth

When the particle surface is indented by a sharp indenter, micro-cracks are formed as the dislocation density reaches a critical limit. Evans and Wilshaw (1976) proposed that the length of the radial and lateral subsurface cracks may be calculated from:

$$\frac{c}{a} = fn\left(\frac{K_c}{Y\sqrt{a}}\right) = fn\left(\frac{K_c\emptyset}{H\sqrt{a}}\right) \tag{5.20}$$

where K_c is the critical stress intensity factor and a is the radius of impression. The relationship between the normalised crack length, *c*/*a*, and the normalised critical stress intensity factor $K_c\emptyset$ / $H\sqrt{a}$ have been experimentally determined for a range of materials as shown in Figure 5.3. Note that fn is a function to relate *c*/*a* with $K_c\emptyset$/ $H\sqrt{a}$. The yield stress *Y* can be expressed in terms of the hardness *H*, *Y*=*H*/∅, where ∅ is a constraint factor.

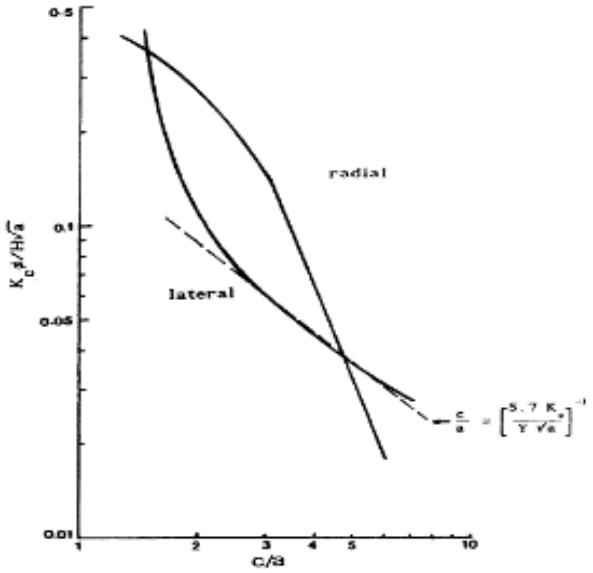

Figure 5.3 Normalised crack length as a function of the normalised k_c for radial and lateral subsurface cracks (After Evans & Wilshaw, 1976)

The lateral crack length c_l is estimated based on Figure 5.3 using a linear approximation to the curve,

$$\frac{c_l}{a} = \left[\frac{5.7K_c}{Y\sqrt{a}}\right]^{-1} = \left[\frac{5.7\emptyset K_c}{H\sqrt{a}}\right]^{-1} \tag{5.21}$$

It has been found that the radius of the plastic zone is proportional to the radius of impression (Evans & Wilshaw, 1976). Thus, the depth of lateral cracks is

$$h \propto a \tag{5.22}$$

5.4.4.2 Size of impression

For a quasi-static approximation, the mean contact pressure, p, at any stage of contact may be expressed in terms of the load, P, and the size of contact impression, a, as

$$p \propto \frac{P}{a^2} \tag{5.23}$$

The mean contact pressure is approximated by the hardness (Zhang, 1994; Wiederhorn & Lawn, 1979). Therefore, the size of the contact impression can simply be expressed in terms of hardness as

$$a \propto \sqrt{\frac{F}{H}} \tag{5.24}$$

5.4.4.3 Contact force

The contact force under impact conditions is given by the Newton's law. For a sphere having radius R and density ρ, impacting at velocity v, it then follows that

$$F = M\frac{d_v}{d_t} = \frac{4}{3}\pi R^3 \frac{d_v}{d_t} \tag{5.25}$$

Here, an approximation based on a two-point difference method may be made:

$$\frac{d_v}{d_t} = \frac{v}{t_p} \tag{5.26}$$

where t_p is the peak contact time, i.e. the time taken from the initial contact until the contact force reaches the peak value. Substituting Eq. (5.26) into Eq. (5.25), the impact force is expressed as

$$F = \frac{4}{3}\pi R^3 \frac{v}{t_p} \tag{5.27}$$

Substituting Eq. (5.27) into Eq. (5.24) gives

$$a \propto \sqrt{\frac{\rho R^3 v}{H t_p}} \tag{5.28}$$

5.4.4.4 Elastic-plastic contact time

The peak contact time dominated by the plastic flow has been given by Andrew (1930) and Tabor (1951) as

$$t_p = \frac{1}{2}\sqrt{\frac{\pi M}{pD}} \tag{5.29}$$

where p is the mean contact pressure, and D and M are the diameter and mass of a spherical projectile, respectively. If the mean contact pressure is replaced by the hardness, Eq. (5.29) can be expressed as

$$t_p = \frac{1}{2}\sqrt{\frac{\pi M}{HD}} \propto \sqrt{\frac{\rho}{H}} R \tag{5.30}$$

Substituting Eq. (5.30) into Eq. (5.28) gives the impression size:

$$a \propto R\sqrt{v}^4 \sqrt{\frac{\rho}{H}} \tag{5.31}$$

5.4.4.5 Fractional mass loss

The material loss is assumed to be the detachment of the lateral subsurface crack induced by the impacting particle against a rigid plate:

$$V_{det} = \frac{1}{3}\pi {c_l}^2 h \tag{5.32}$$

The fraction of material loss removed due to the impact, ε, for a sphere of volume V, is thus

$$\varepsilon = \frac{V_{det}}{V} = \frac{\frac{1}{3}\pi {c_l}^2 h}{\frac{4}{3}\pi R^3} \propto \frac{{c_l}^2 h}{R^3} \tag{5.33}$$

The fractional loss per impact can be elucidated in terms of the particle mechanical properties by substituting the length and depth of a crack in Eqs. (5.21), (5.28) into Eq. (5.33):

$$\varepsilon \propto \frac{\rho v^2 RH}{{K_c}^2} \tag{5.34}$$

Thus far, four breakage models based on indentation fracture mechanism have been summarised. All these models have been proposed by establishing the predictive capacity with material properties and loading conditions. The distinctive advantage of these models is that they contribute to the understanding of the underlying mechanism of particle breakage from a fundamental level. However, it should be noted that only the normal component of the impact velocity is considered in these models even if particle breakage occurs under oblique impact. The key features of the models are summarised in Tables 5.1, 5.2 and 5.3 respectively.

Table 5.1 Key parameters of fracture mechanics based models

Key parameters of breakage models						
Model	**Volume loss**	**Breakage propensity**	**Crack length (c)**	**Depth (h)**	**Contact radius (a)**	**Peak force (P)**
Evans and Wilshaw (1976)	$\pi {r_c}^2 h$	$\varepsilon \propto \frac{\rho^{6/5} R}{K_c^{3/2} H^{1/2}} v^{12/5}$	$r_c \propto P^{3/4} K_c^{-3/4}$	$h \propto a$	$a \propto P^{1/2} H^{1/2}$	$P \propto v^{6/5} R^2$
Evans et al. (1978)	$\pi {C_r}^2 h$	$\varepsilon \propto \frac{\rho^{1/4} R}{K_c^{4/3} H^{1/4}} v^{19/6}$	$c_r \propto R^{4/3} v^{4/3} K_c^{-2/3}$	$h \propto R v^{1/2} \rho^{1/4} H^{-1/4}$	$a \propto R v^{1/2}$	$P \propto H^{-1/2} \rho^{1/2} v$
Hutchings (1994)	${C_l}^2 h$	$\varepsilon \propto \frac{\rho^{4/3} R H^{2/3}}{K_c^2} v^{8/3}$	$\frac{c_l}{a} \propto \left[\frac{K_c}{H\sqrt{a}}\right]^{-1}$	$h \propto a$	$a \propto H^{-1/3} \rho^{1/3} R v^{2/3}$	$P \propto H^{1/3} \rho^{2/3} R^2 v^{4/3}$
Ghadiri and Zhang (2002)	${C_l}^2 h$	$\varepsilon \propto \frac{\rho R H}{K_c^2} v^2$	$\frac{c_l}{a} \propto \left[\frac{K_c}{H\sqrt{a}}\right]^{-1}$	$h \propto a$	$a \propto H^{-1/4} \rho^{1/4} R v^{1/2}$	$P \propto H^{1/2} \rho^{1/2} R^2 v$

Table 5.2 Summary of fracture mechanics based models

Model	Equation	Category	Assumption	Application	Remarks
Evans and Wilshaw (1976)	$\varepsilon \propto \frac{\rho D}{K_D^{3/2} {H_D}^{1/2}} v^{12/5}$	Theoretical	A	Quasi-static	Chipping based
Evans et al. (1978)	$\varepsilon \propto \frac{\rho^{1/4} R}{K_c^{4/3} H^{1/4}} v^{19/6}$	Theoretical	B	Impact loading	Chipping based
Hutchings (1994)	$\varepsilon \propto \frac{\rho^{4/3} D H^{2/3}}{K_c^2} v^{8/3}$	Theoretical	C	Quasi-static	Chipping based
Ghadiri and Zhang (2002)	$\varepsilon \propto \frac{\rho D H}{K_c^2} v^2$	Theoretical	D	Quasi-static	Chipping based

A: Removal of material from adjacent sub-surface lateral cracks

B: Removal of material due to lateral crack extension under impact damage

C: Kinetic energy of particle is converted into plastic deformation

D: Material removal owing to sub-surface lateral cracks and linearity of acceleration

Table 5.3 Schematic diagram of fracture mechanics based models

Model	Schematic	Notation
Evans and Wilshaw (1976)	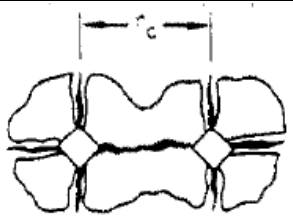	r_c adjacent indent separation
Evans et al. (1978)	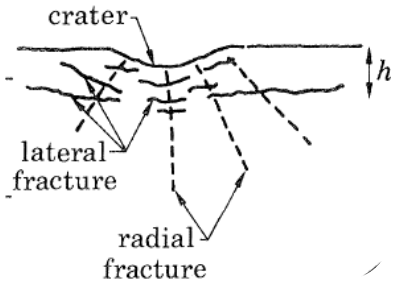	h: lateral crack depth
Hutchings (1994) Ghadiri and Zhang (2002)	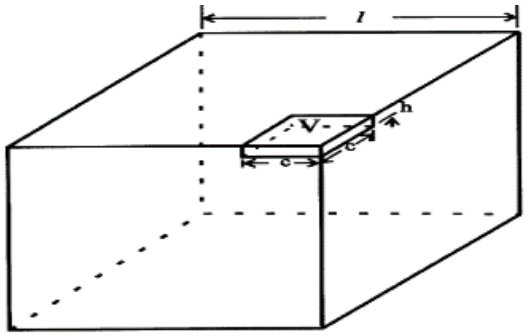	c: lateral crack length h: lateral crack depth l: cubic length V: removal material volume

5.5 Comparison with experimental observations

Experimental results from impact tests in Chapter 3 are fitted with the aforementioned fracture mechanics based breakage models. The mechanical properties including the Young's modulus, hardness and fracture toughness used to fit these breakage models are determined from nanoindentation test in Chapter 3. The fitting results for the reviewed models are shown in Figure 5.4 for the zeolite with diameters ranging from 1.4-1.7 mm.

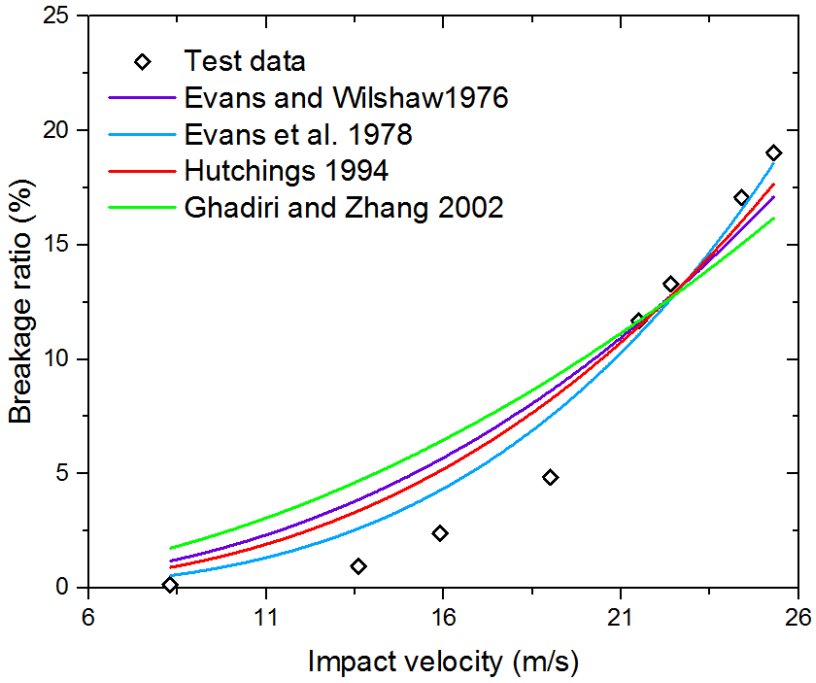

Figure 5.4 Comparison between breakage models and impact test results

Figure 5.4 shows that Ghadiri and Zhang (2002) fitting achieves the highest breakage ratio whilst Evans et al. (1978) fitting witnesses the lowest breakage ratio below the impact velocity 22.4 m/s. In contrast, Evans et al. (1978) fitting gives the highest breakage ratio whilst Ghadiri and Zhang (2002) fitting presents the lowest breakage ratio beyond the impact velocity 22.4 m/s. This is attributed to the variation of the exponent of velocity and the mechanical properties in these breakage models. It should be noted that only normal impact data has been included here. The reason for the fitting of models crossing about 22.4m/s is under investigation. Although the dominant event is chipping over the impact regime, it should also be noted that the breakage under high impact velocity such as 25.4 m/s may be occasionally interfered with fragmentation. The main objective of this section is to investigate the feasibility of the existing

breakage models as compared to experimental results. Clearly, the test breakage ratio of zeolite deviates significantly from all the models, so a new predictive model is necessitated. The discrepancy of velocity exponents in the breakage models and the transition from chipping to fragmentation will be discussed in Section 5.8 with details.

5.6 A new particle breakage model

5.6.1 Under normal impact: dynamic analysis of indentation fracture

Evans et al. (1978) gave the contact radius based on a dynamic analysis:

$$a^2 \propto R^2 v \tag{5.35}$$

and the radial crack length under the impact damage is given

$$c_r \propto v^{4/3} R^{4/3} K_c^{-2/3} \tag{5.36}$$

The crack length obtained is given by approximate proportionalities as shown in Eq. (5.2).

Substituting Eq. (5.2.a) into Eq. (5.36), P is obtained as

$$P \propto H^{1/2} R^{8/3} v^{8/3} K_c^{-2/3} \tag{5.37}$$

Thus, the lateral crack length under impact damage regime in Eq. (5.2 b) evolves as

$$c_l \propto R^2 v^2 K_c^{-5/4} H^{3/8} \tag{5.38}$$

It has been found the depth of lateral cracks h may be expressed as (Evans et al. 1978)

$$h \propto R v^{1/2} \rho^{1/4} H^{-1/4} \tag{5.39}$$

The material loss is assumed to be the formation of the lateral subsurface crack induced by impacting a particle against a rigid plate. The detached volume is given by

$$V_{det} = \pi {c_l}^2 h \tag{5.40}$$

The fraction of material loss due to the impact, ε, for a sphere of volume V, is given by

$$\varepsilon = \frac{\mathrm{V_{det}}}{\mathrm{V}} = \frac{\frac{1}{3}\pi \mathrm{c^2 h}}{\frac{4}{3}\pi \mathrm{R^3}} \propto \frac{\mathrm{c^2 h}}{\mathrm{R^3}} \tag{5.41}$$

The fractional loss per impact can be expressed in terms of the mechanical properties by substituting the length and depth of a crack in Eqs (37), (38) into Eq. (40):

$$\varepsilon \propto \frac{\rho^{1/4} R^2 H^{1/2}}{K_c^{5/2}} v^{9/2} \tag{5.42}$$

The predictions of this new model as well as those of the existing models under normal impact are compared with the impact test data as shown in Figure 5.5. Clearly, the proposed model agrees well with the impact test data.

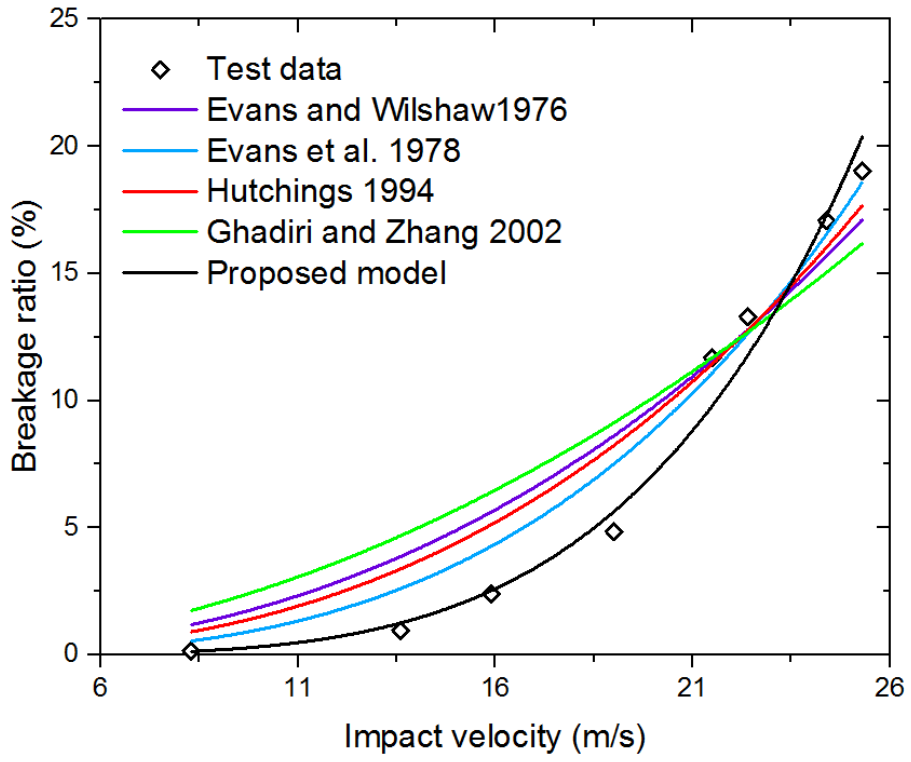

Figure 5.5 Models fitting with impact test data under normal impact

5.6.2 A model considering the impact angle

It is noted that the existing breakage models are only applicable to normal impact, so in general, the tangential velocity component under oblique impact is ignored. The single impact test has shown that tangential velocity exerts a significant influence on the breakage propensity. As a result, understanding the contribution of the tangential component velocity under impact incident is deemed necessary to produce an improved particle breakage model. Note that the effect of the rotational velocity is not considered in the model to be developed below.

When particle is impacted at an angle θ, the normal component of the impact velocity is

$$v_n = vsin\theta \tag{5.43}$$

A normal impact force F_n is resulted from the normal velocity. The tangential component of velocity gives

$$v_t = vcos\theta \tag{5.44}$$

which results in a tangential impact force F_t, but the relationship between v_t and F_t, and that betwee v_n and F_n, are not necessarily the same. F_t is also limited by the dynamic friction between the particle and the impact surface, namely μF_n which is in turn related to $\mu vsin\theta$. A large tangential velocity which does not cause sufficient frictional force may not result in any damage. An 'effective' tangential velocity which can result in particle damage may be expressed approximately in the form of:

$$v_{te} = \mu vsin\theta cos\theta \tag{5.45}$$

This means that the contribution of the tangential component to damage is zero for both normal impact (as there is no tangential velocity in this case), and total tangential 'impact' (as it travels parallel to the impact surface without any interaction force between them).

The resultant of the normal and tangential forces is

$$F = \sqrt{F_n^2 + F_t^2} \tag{5.46}$$

However, as damages caused by F_n and F_t are different even if their value and time characteristics are the same, so the use of the total force could be misleading. Furthermore, damages cannot be summed as vectors anyway. As a simple treatment before further understanding is achieved, it may be assumed that the combined effect of F_n and F_t on damage is the same as that caused by an 'equivalent' normal force F_e in the form of

$$F_e = \sqrt{F_n^2 + \alpha^2 F_t^2} \tag{5.47}$$

where α is a parameter incorporating the contribution of the tangential force F_t.

Considering Eqs. (5.43) and (5.45) and following the force analogy, an 'equivalent' normal impact velocity may be defined as Eq. (5.48), which may be further simplified by merging α and μ as ξ

$$v_{en} = v\sqrt{sin^2\theta + \xi^2 sin^2\theta cos^2\theta} \tag{5.48}$$

in which $\xi = \alpha\mu$ reflects the combined effects of frictional behaviour and various complicated relationships discussed above.

Substituting Eq. (5.48) into Eq. (5.42) gives a model under oblique impact:

$$\varepsilon \propto \frac{\rho^{1/4} R^2 H^{1/2}}{K_c^{5/2}} v^{9/2} \left(sin^2\theta + \xi^2 sin^2\theta cos^2\theta\right)^{9/4} \tag{5.49}$$

The value of ξ may be obtained from best fit of test results. For the set of experiments conducted in this study, $\xi = 1$ represents a very good fit (Figure 5.6).

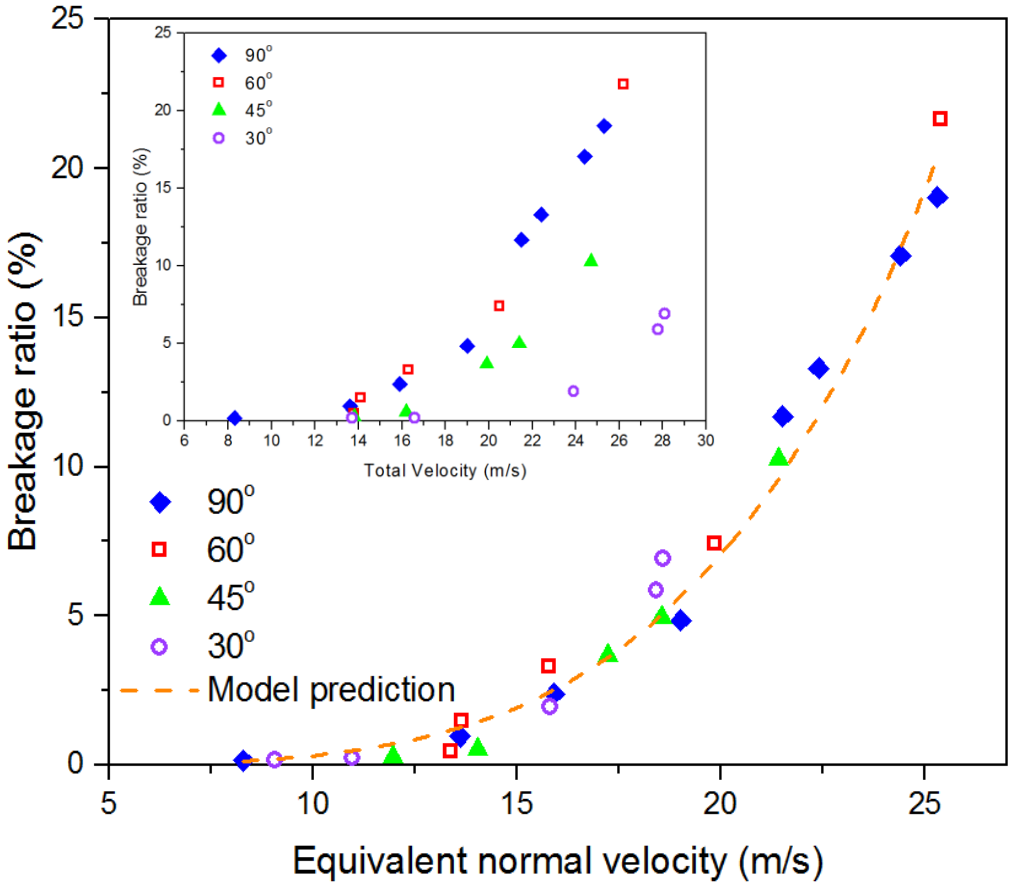

Figure 5.6 Breakage model fitting of impact test results

As shown in Figure 5.6, the breakage percentage including the normal and oblique impact tests falls onto the unification curve of the prediction model. To the best knowledge of the author, this is the first time for a breakage model to enable the contribution of tangential component velocity, which results in a unified curve of breakage propensity prediction under varying impact angles. The developed model based on impact damage analysis is confirmed to be applicable in both normal impact and oblique impact. It is important to note that ξ is a combined action of friction behaviour and the parameter α. A comprehensive assessment of particle breakage models including the proposed model is presented in the following section.

5.7 Assessment of particle breakage models

In Section 5.6, a new breakage model for particulate solids is proposed based on indentation fracture mechanics, which enables the contributions of both the normal and tangential impact velocity to be rationalized. In terms of the application of these models in breakage propensity prediction, three issues are yet to be addressed. First, each model

has only been tested against limited test database though all these models have been proposed based on the same indentation fracture mechanics. Their wider applicability is not clear. Second, a comprehensive comparative assessment of these models is not available. The predictive accuracy and statistical performance of these models are thus unavailable. Third, traditional models for particle breakage merely focus on the normal velocity and consequently fall short in predicting the contribution of tangential component velocity. The equivalent normal velocity proposed here has not been tested against test database from the oblique impact.

This section presents a comprehensive assessment of the particle breakage models under both normal and oblique impact and to examine the suitability of the equivalent normal velocity proposed in Section 5.6. For clarity, the definition of impact breakage ratio in the literature is discussed first. A test database was carefully collected from an extensive literature survey. The database is compared with the particle breakage models under the normal and oblique impact, respectively.

5.7.1 Definition of breakage ratio

Breakage ratio, also known as probability function or selection function, denotes the fraction loss of particle under stressing event pertinent to comminution. The breakage ratio is usually determined experimentally to describe the process of particle size reduction (Petukhov and Kalman, 2004). The breakage function is typically expressed as a function of impact velocity or impact kinetic energy or even the number of impacts. There are three methods to characterise the breakage ratio in experiment. First, the breakage ratio is characterised by the mass loss of original particle. For example, Ghadiri and co-workers (1986, 1995, 2002) define particle as breakage once the size of impacted particles is two sizes below the lower feed size according to British Standard Sieves 410. Second, the breakage ratio is denoted by the number of unbroken particles, which is expressed by Weibull distribution. This method is widely adopted by Salman and co-workers (1995, 2002, 2003) to investigate particle fragmentation subject to impact loading. Third, Tavares et al. (2009) defines the particle breakage as more than 10% mass loss of its original particle. Surface breakage (chipping) occurs with less than 10% mass loss whilst body breakage (fragmentation) takes place with more than 10% mass loss under single particle drop test.

For the breakage models applicable to chipping, the breakage ratio of particles can be expressed by the impact velocity as well as other governing parameters. A general form of particle breakage model may be expressed as:

$$\varepsilon \propto \frac{\rho^a R^b}{K_c^d H^e} v^n \tag{5.50}$$

Inserting C into Eq. (5.50), it follows as a simplified version

$$\varepsilon \propto C v^n \tag{5.51}$$

where C is regarded as a combined effect of physical and mechanical parameters. The velocity parameters for the breakage models are tabulated in Table 5.4.

Table 5.4 Velocity parameters for particle breakage models

Model	Evans and Wilshaw (1976)	Evans et al. (1978)	Hutchings (1994)	Ghadiri and Zhang (2002)	Wang (2016)
Exponent	2.4	3.17	2.67	2.0	4.5

As for the breakage pattern including both chipping and fragmentation, the Weibull distribution is adopted to characterise breakage by counting the number of unbroken particles.

5.7.2 Experimental database

A great number of tests have been reported in the literature on the particle breakage propensity under impact loading. The impact test of particle chipping has been carried out by Zhang and Ghadiri (2002), Kwan et al. (2004) and Couroyer et al. (2005). The impact test of particle fragmentation has been extensively studied by Salman et al. (1995), Salman et al. (2002), Cheong et al. (2003) and Salman et al. (2003). The effect of impact angle was examined by Papadopoulos (1998), Salman et al. (1995), Salman et al. (2002, 2003). In this study, only impact tests of brittle or semi-brittle materials are considered. Tests which were not sufficiently documented or well specified (e.g. the

definition of breakage ratio was not clearly noted) are excluded. With these exclusions, over 300 test results have been collected from the literature. Dataset 1 (Table 5.5) is relevant to chipping for the assessment of breakage models under normal impact., In terms of oblique impact, Dataset 2 and 3 for chipping and fragmentation are listed Considering two breakage patterns under impact under oblique impact in Table 5.6 and 5.7 respectively.

Table 5.5 Dataset 1 of chipping under normal impact

Number	Data source	Particle type	Shape and size	Impact number	Impact velocity (m/s)	Breakage ratio (%)
1	Zhang and Ghadiri 2002	MgO	Cube, 2mm	5	4.50	0.0117
2	Zhang and Ghadiri 2002	MgO	Cube, 2mm	5	5.53	0.0188
3	Zhang and Ghadiri 2002	MgO	Cube, 2mm	5	8.46	0.0414
4	Zhang and Ghadiri 2002	MgO	Cube, 2mm	5	11.10	0.0779
5	Zhang and Ghadiri 2002	MgO	Cube, 2mm	5	14.82	0.1413
6	Zhang and Ghadiri 2002	MgO	Cube, 2mm	5	17.84	0.2021
7	Zhang and Ghadiri 2002	MgO	Cube, 2mm	10	4.50	0.0132
8	Zhang and Ghadiri 2002	MgO	Cube, 2mm	10	5.55	0.0215
9	Zhang and Ghadiri 2002	MgO	Cube, 2mm	10	8.31	0.0472
10	Zhang and Ghadiri 2002	MgO	Cube, 2mm	10	10.87	0.0988
11	Zhang and Ghadiri 2002	MgO	Cube, 2mm	10	14.98	0.1815
12	Zhang and Ghadiri 2002	MgO	Cube, 2mm	15	4.51	0.0142
13	Zhang and Ghadiri 2002	MgO	Cube, 2mm	15	5.53	0.0254
14	Zhang and Ghadiri 2002	MgO	Cube, 2mm	15	8.37	0.0538
15	Zhang and Ghadiri 2002	MgO	Cube, 2mm	15	14.89	0.2304
16	Zhang and Ghadiri 2002	NaCl	Cube, 2mm	5	4.30	0.0036
17	Zhang and Ghadiri 2002	NaCl	Cube, 2mm	5	5.51	0.0059
18	Zhang and Ghadiri 2002	NaCl	Cube, 2mm	5	7.01	0.0133
19	Zhang and Ghadiri 2002	NaCl	Cube, 2mm	5	8.40	0.0165
20	Zhang and Ghadiri 2002	NaCl	Cube, 2mm	5	10.04	0.0206
21	Zhang and Ghadiri 2002	NaCl	Cube, 2mm	10	4.30	0.0099
22	Zhang and Ghadiri 2002	NaCl	Cube, 2mm	10	5.52	0.0113

23	Zhang and Ghadiri 2002	NaCl	Cube, 2mm	10	7.07	0.0276
24	Zhang and Ghadiri 2002	NaCl	Cube, 2mm	10	8.46	0.0330
25	Zhang and Ghadiri 2002	NaCl	Cube, 2mm	10	10.02	0.0437
26	Zhang and Ghadiri 2002	NaCl	Cube, 2mm	15	4.31	0.0112
27	Zhang and Ghadiri 2002	NaCl	Cube, 2mm	15	5.51	0.0151
28	Zhang and Ghadiri 2002	NaCl	Cube, 2mm	15	7.03	0.0370
29	Zhang and Ghadiri 2002	NaCl	Cube, 2mm	15	8.46	0.0604
30	Zhang and Ghadiri 2002	KCl	Cube, 2mm	5	4.31	0.0199
31	Zhang and Ghadiri 2002	KCl	Cube, 2mm	5	5.50	0.0329
32	Zhang and Ghadiri 2002	KCl	Cube, 2mm	5	6.99	0.0644
33	Zhang and Ghadiri 2002	KCl	Cube, 2mm	5	8.38	0.0809
34	Zhang and Ghadiri 2002	KCl	Cube, 2mm	5	11.93	0.1713
35	Zhang and Ghadiri 2002	KCl	Cube, 2mm	10	4.28	0.0244
36	Zhang and Ghadiri 2002	KCl	Cube, 2mm	10	5.51	0.0386
37	Zhang and Ghadiri 2002	KCl	Cube, 2mm	10	6.97	0.0846
38	Zhang and Ghadiri 2002	KCl	Cube, 2mm	10	8.37	0.1180
39	Zhang and Ghadiri 2002	KCl	Cube, 2mm	10	11.89	0.2316
40	Zhang and Ghadiri 2002	KCl	Cube, 2mm	15	4.28	0.0290
41	Zhang and Ghadiri 2002	KCl	Cube, 2mm	15	5.51	0.0444
42	Zhang and Ghadiri 2002	KCl	Cube, 2mm	15	6.97	0.1022
43	Zhang and Ghadiri 2002	KCl	Cube, 2mm	15	8.40	0.1466
44	Kwan et al. 2004	LM	212-250μm	1	35.50	1.2390
45	Kwan et al. 2004	LM	212-250μm	1	45.04	2.9408
46	Kwan et al. 2004	LM	212-250μm	1	52.62	4.9744
47	Kwan et al. 2004	LM	212-250μm	1	60.46	7.2944

48	Kwan et al. 2004	LM	250-300μm	1	34.30	2.1431
49	Kwan et al. 2004	LM	250-300μm	1	41.14	2.9897
50	Kwan et al. 2004	LM	250-300μm	1	49.46	5.3497
51	Kwan et al. 2004	LM	250-300μm	1	58.51	7.4213
52	Kwan et al. 2004	LM	250-300μm	1	61.34	9.7106
53	Kwan et al. 2004	LM	355-425 μm	1	20.50	1.2697
54	Kwan et al. 2004	LM	355-425 μm	1	30.40	2.4380
55	Kwan et al. 2004	LM	355-425 μm	1	38.24	5.2498
56	Kwan et al. 2004	LM	355-425 μm	1	44.84	6.9985
57	Kwan et al. 2004	LM	355-425 μm	1	50.48	9.2411
58	Kwan et al. 2004	LM	355-425 μm	1	55.15	12.5102
59	Kwan et al. 2004	LM	425-500 μm	1	17.82	1.0703
60	Kwan et al. 2004	LM	425-500 μm	1	26.86	2.4862
61	Kwan et al. 2004	LM	425-500 μm	1	32.73	3.8676
62	Kwan et al. 2004	LM	425-500 μm	1	34.81	4.4371
63	Kwan et al. 2004	LM	425-500 μm	1	37.62	4.9232
64	Kwan et al. 2004	LM	425-500 μm	1	40.33	7.2537
65	Kwan et al. 2004	LM	425-500 μm	1	42.66	8.3554
66	Kwan et al. 2004	LM	425-500 μm	1	45.37	9.9893
67	Kwan et al. 2004	LM	425-500 μm	1	50.76	12.5602
68	Couroyer et al. 2005	Alumina	Bead, 1.7-2.0 mm	1	4.62	0.4481
69	Couroyer et al. 2005	Alumina	Bead, 1.7-2.0 mm	1	8.00	1.1860
70	Couroyer et al. 2005	Alumina	Bead, 1.7-2.0 mm	1	10.09	1.5286
71	Couroyer et al. 2005	Alumina	Bead, 1.7-2.0 mm	1	11.80	2.4225
72	Couroyer et al. 2005	Alumina	Bead, 1.7-2.0 mm	1	14.16	4.6640

73	Couroyer et al. 2005	Alumina	Bead, 1.7-2.0 mm	1	16.26	6.4565
74	Couroyer et al. 2005	Alumina	Bead, 1.7-2.0 mm	1	18.14	8.3498
75	Couroyer et al. 2005	Alumina	Bead, 1.7-2.0 mm	1	19.66	10.1944
76	Couroyer et al. 2005	Alumina	Bead, 1.7-2.0 mm	1	20.13	12.3927
77	Couroyer et al. 2005	Alumina	Bead, 1.7-2.0 mm	1	23.15	16.6319
78	Couroyer et al. 2005	Alumina	Bead, 1.7-2.0 mm	1	4.59	0.1095
79	Couroyer et al. 2005	Alumina	Bead, 1.7-2.0 mm	1	7.98	0.1095
80	Couroyer et al. 2005	Alumina	Bead, 1.7-2.0 mm	1	10.06	0.3085
81	Couroyer et al. 2005	Alumina	Bead, 1.7-2.0 mm	1	11.80	0.4577
82	Couroyer et al. 2005	Alumina	Bead, 1.7-2.0 mm	1	11.95	0.8557
83	Couroyer et al. 2005	Alumina	Bead, 1.7-2.0 mm	1	13.97	1.0547
84	Couroyer et al. 2005	Alumina	Bead, 1.7-2.0 mm	1	16.18	1.7015
85	Couroyer et al. 2005	Alumina	Bead, 1.7-2.0 mm	1	17.95	2.3483
86	Couroyer et al. 2005	Alumina	Bead, 1.7-2.0 mm	1	19.60	2.9950
87	Couroyer et al. 2005	Alumina	Bead, 1.7-2.0 mm	1	19.91	3.7413
88	Couroyer et al. 2005	Alumina	Bead, 1.7-2.0 mm	1	22.95	6.0299
89	Wang 2016	Zeolite	Sphere, 1.4-1.7mm	1	8.30	0.1530
90	Wang 2016	Zeolite	Sphere, 1.4-1.7mm	1	13.60	0.9573
91	Wang 2016	Zeolite	Sphere, 1.4-1.7mm	1	15.90	2.3943
92	Wang 2016	Zeolite	Sphere, 1.4-1.7mm	1	19.00	4.8468
93	Wang 2016	Zeolite	Sphere, 1.4-1.7mm	1	21.50	12.2789
94	Wang 2016	Zeolite	Sphere, 1.4-1.7mm	1	22.40	13.3000
95	Wang 2016	Zeolite	Sphere, 1.4-1.7mm	1	24.40	17.0728
96	Wang 2016	Zeolite	Sphere, 1.4-1.7mm	1	25.30	19.0425

Table 5.6 Dataset 2 of chipping under oblique impact

Number	Data source	Particle type and size (mm)	Impact angle (°)	Impact velocity (m/s)	Breakage ratio (%)	Coefficient for equivalent velocity	Normal velocity (m/s)	Equivalent velocity (m/s)
1	Papadopoulos 1998	Porous silica 1, 3.35-4.0	90	4.84	0.92	1.00	4.84	4.8
2	Papadopoulos 1998	Porous silica 1, 3.35-4.0	90	9.21	4.23	1.00	9.21	9.2
3	Papadopoulos 1998	Porous silica 1, 3.35-4.0	90	11.36	7.19	1.00	11.36	11.4
4	Papadopoulos 1998	Porous silica 1, 3.35-4.0	90	15.54	18.23	1.00	15.54	15.5
5	Papadopoulos 1998	Porous silica 1, 3.35-4.0	65	4.24	0.34	1.08	3.84	4.6
6	Papadopoulos 1998	Porous silica 1, 3.35-4.0	65	9.99	6.84	1.08	9.06	10.8
7	Papadopoulos 1998	Porous silica 1, 3.35-4.0	65	11.59	8.76	1.08	10.50	12.5
8	Papadopoulos 1998	Porous silica 1, 3.35-4.0	65	15.47	20.55	1.08	14.02	16.7
9	Papadopoulos 1998	Porous silica 1, 3.35-4.0	45	4.02	0.35	1.02	2.85	4.1
10	Papadopoulos 1998	Porous silica 1, 3.35-4.0	45	9.83	6.56	1.02	6.95	10.0
11	Papadopoulos 1998	Porous silica 1, 3.35-4.0	45	11.63	9.22	1.02	8.22	11.9
12	Papadopoulos 1998	Porous silica 1, 3.35-4.0	45	16.13	18.87	1.02	11.41	16.5
13	Papadopoulos 1998	Porous silica 1, 3.35-4.0	25	4.11	0.21	0.97	1.74	4.0
14	Papadopoulos 1998	Porous silica 1, 3.35-4.0	25	9.99	5.47	0.97	4.22	9.7
15	Papadopoulos 1998	Porous silica 1, 3.35-4.0	25	11.93	7.84	0.97	5.04	11.6
16	Papadopoulos 1998	Porous silica 1, 3.35-4.0	25	15.64	15.86	0.97	6.61	15.2
17	Papadopoulos 1998	Porous silica 2, 1.0-1.18	90	4.72	1.00	1.00	4.72	4.72
18	Papadopoulos 1998	Porous silica 2, 1.0-1.18	90	7.84	0.75	1.00	7.84	7.84
19	Papadopoulos 1998	Porous silica 2, 1.0-1.18	90	11.17	1.39	1.00	11.17	11.17
20	Papadopoulos 1998	Porous silica 2, 1.0-1.18	90	12.66	1.69	1.00	12.66	12.66
21	Papadopoulos 1998	Porous silica 2, 1.0-1.18	90	16.72	4.85	1.00	16.72	16.72
22	Papadopoulos 1998	Porous silica 2, 1.0-1.18	90	20.95	9.52	1.00	20.95	20.95
23	Papadopoulos 1998	Porous silica 2, 1.0-1.18	65	3.73	0.58	0.99	3.38	3.7
24	Papadopoulos 1998	Porous silica 2, 1.0-1.18	65	7.01	0.82	0.99	6.35	6.9
25	Papadopoulos 1998	Porous silica 2, 1.0-1.18	65	10.14	1.09	0.99	9.19	10.0
26	Papadopoulos 1998	Porous silica 2, 1.0-1.18	65	12.02	1.94	0.99	10.89	11.9
27	Papadopoulos 1998	Porous silica 2, 1.0-1.18	65	15.83	3.81	0.99	14.34	15.7

28	Papadopoulos 1998	Porous silica 2, 1.0-1.18	65	20.09	8.08	0.99	18.21	19.9
29	Papadopoulos 1998	Porous silica 2, 1.0-1.18	45	4.02	0.15	0.93	2.84	3.7
30	Papadopoulos 1998	Porous silica 2, 1.0-1.18	45	7.20	0.51	0.93	5.09	6.7
31	Papadopoulos 1998	Porous silica 2, 1.0-1.18	45	10.32	1.09	0.93	7.30	9.6
32	Papadopoulos 1998	Porous silica 2, 1.0-1.18	45	11.97	1.24	0.93	8.47	11.1
33	Papadopoulos 1998	Porous silica 2, 1.0-1.18	45	16.02	3.48	0.93	11.32	14.8
34	Papadopoulos 1998	Porous silica 2, 1.0-1.18	45	20.23	6.67	0.93	14.30	18.8
35	Papadopoulos 1998	Porous silica 2, 1.0-1.18	25	4.37	0.27	0.89	1.85	3.9
36	Papadopoulos 1998	Porous silica 2, 1.0-1.18	25	7.24	0.55	0.89	3.06	6.5
37	Papadopoulos 1998	Porous silica 2, 1.0-1.18	25	10.22	0.88	0.89	4.32	9.1
38	Papadopoulos 1998	Porous silica 2, 1.0-1.18	25	12.03	1.25	0.89	5.08	10.7
39	Papadopoulos 1998	Porous silica 2, 1.0-1.18	25	16.12	3.31	0.89	6.81	14.4
40	Papadopoulos 1998	Porous silica 2, 1.0-1.18	25	20.31	5.89	0.89	8.58	18.1
41	Papadopoulos 1998	Porous silica 3, 2.0-2.36	90	4.65	0.24	1.00	4.65	4.65
42	Papadopoulos 1998	Porous silica 3, 2.0-2.36	90	6.90	1.25	1.00	6.90	6.90
43	Papadopoulos 1998	Porous silica 3, 2.0-2.36	90	10.21	1.62	1.00	10.21	10.21
44	Papadopoulos 1998	Porous silica 3, 2.0-2.36	90	12.29	2.18	1.00	12.29	12.29
45	Papadopoulos 1998	Porous silica 3, 2.0-2.36	90	16.02	3.28	1.00	16.02	16.02
46	Papadopoulos 1998	Porous silica 3, 2.0-2.36	90	18.89	4.31	1.00	18.89	18.89
47	Papadopoulos 1998	Porous silica 3, 2.0-2.36	65	4.34	0.06	0.91	3.93	3.9
48	Papadopoulos 1998	Porous silica 3, 2.0-2.36	65	6.96	0.58	0.91	6.30	6.3
49	Papadopoulos 1998	Porous silica 3, 2.0-2.36	65	10.01	1.23	0.91	9.07	9.1
50	Papadopoulos 1998	Porous silica 3, 2.0-2.36	65	12.10	1.98	0.91	10.96	11.0
51	Papadopoulos 1998	Porous silica 3, 2.0-2.36	65	16.20	2.12	0.91	14.68	14.7
52	Papadopoulos 1998	Porous silica 3, 2.0-2.36	65	20.37	4.08	0.91	18.46	18.5
53	Papadopoulos 1998	Porous silica 3, 2.0-2.36	45	4.39	0.16	0.84	3.10	3.7
54	Papadopoulos 1998	Porous silica 3, 2.0-2.36	45	6.93	0.40	0.84	4.90	5.8
55	Papadopoulos 1998	Porous silica 3, 2.0-2.36	45	10.02	1.00	0.84	7.09	8.4
56	Papadopoulos 1998	Porous silica 3, 2.0-2.36	45	12.10	1.61	0.84	8.55	10.1
57	Papadopoulos 1998	Porous silica 3, 2.0-2.36	45	15.91	2.18	0.84	11.25	13.3
58	Papadopoulos 1998	Porous silica 3, 2.0-2.36	45	19.77	4.14	0.84	13.98	16.6

59	Papadopoulos 1998	Porous silica 3, 2.0-2.36	25	4.44	0.02	0.78	1.88	3.5
60	Papadopoulos 1998	Porous silica 3, 2.0-2.36	25	6.91	0.11	0.78	2.92	5.4
61	Papadopoulos 1998	Porous silica 3, 2.0-2.36	25	10.19	1.04	0.78	4.31	7.9
62	Papadopoulos 1998	Porous silica 3, 2.0-2.36	25	12.46	1.71	0.78	5.27	9.7
63	Papadopoulos 1998	Porous silica 3, 2.0-2.36	25	16.20	1.98	0.78	6.85	12.6
64	Papadopoulos 1998	Porous silica 3, 2.0-2.36	25	20.05	3.48	0.78	8.47	15.6
65	Wang 2016	Zeolite, 1.4-1.7mm	90	8.3	0.15	1.00	8.30	8.3
66	Wang 2016	Zeolite, 1.4-1.7mm	90	13.6	0.96	1.00	13.60	13.6
67	Wang 2016	Zeolite, 1.4-1.7mm	90	15.9	2.39	1.00	15.90	15.9
68	Wang 2016	Zeolite, 1.4-1.7mm	90	19	4.85	1.00	19.00	19.0
69	Wang 2016	Zeolite, 1.4-1.7mm	90	21.5	11.69	1.00	21.50	21.5
70	Wang 2016	Zeolite, 1.4-1.7mm	90	22.4	13.30	1.00	22.40	22.4
71	Wang 2016	Zeolite, 1.4-1.7mm	90	24.4	17.07	1.00	24.40	24.4
72	Wang 2016	Zeolite, 1.4-1.7mm	90	25.3	19.04	1.00	25.30	25.3
73	Wang 2016	Zeolite, 1.4-1.7mm	60	13.8	0.48	0.97	11.95	13.4
74	Wang 2016	Zeolite, 1.4-1.7mm	60	14.1	1.49	0.97	12.21	13.7
75	Wang 2016	Zeolite, 1.4-1.7mm	60	16.3	3.31	0.97	14.12	15.8
76	Wang 2016	Zeolite, 1.4-1.7mm	60	20.5	7.41	0.97	17.75	19.8
77	Wang 2016	Zeolite, 1.4-1.7mm	60	26.2	21.67	0.97	22.71	25.4
78	Wang 2016	Zeolite, 1.4-1.7mm	45	13.8	0.29	0.87	9.76	12.0
79	Wang 2016	Zeolite, 1.4-1.7mm	45	16.2	0.55	0.87	11.46	14.0
80	Wang 2016	Zeolite, 1.4-1.7mm	45	19.9	3.68	0.87	14.07	17.2
81	Wang 2016	Zeolite, 1.4-1.7mm	45	21.4	4.96	0.87	15.13	18.5
82	Wang 2016	Zeolite, 1.4-1.7mm	45	24.7	10.28	0.87	17.49	21.4
83	Wang 2016	Zeolite, 1.4-1.7mm	30	13.7	0.16	0.66	6.85	9.1
84	Wang 2016	Zeolite, 1.4-1.7mm	30	16.6	0.23	0.66	8.29	11.0
85	Wang 2016	Zeolite, 1.4-1.7mm	30	23.9	1.94	0.66	11.95	15.8
86	Wang 2016	Zeolite, 1.4-1.7mm	30	27.8	5.87	0.66	13.92	18.4
87	Wang 2016	Zeolite, 1.4-1.7mm	30	28.1	6.93	0.66	14.05	18.6

Table 5.7 Dataset 3 from chipping to fragmentation under oblique impact

Number	Data source	Particle type and size (mm)	Impact velocity (m/s)	Impact angle (º)	No. of unbroken particles	Coefficient for equivalent velocity	Normal velocity (m/s)	Equivalent velocity (m/s)
1	Salman et al. 1995	Alumina, 5.15	9.02	90	100	1	9.02	9.02
2	Salman et al. 1995	Alumina, 5.15	10.31	90	98	1	10.31	10.31
3	Salman et al. 1995	Alumina, 5.15	12.29	90	97	1	12.29	12.29
4	Salman et al. 1995	Alumina, 5.15	13.77	90	95	1	13.77	13.77
5	Salman et al. 1995	Alumina, 5.15	14.16	90	90	1	14.16	14.16
6	Salman et al. 1995	Alumina, 5.15	15.54	90	86	1	15.54	15.54
7	Salman et al. 1995	Alumina, 5.15	15.82	90	80	1	15.82	15.82
8	Salman et al. 1995	Alumina, 5.15	17.40	90	75	1	17.40	17.40
9	Salman et al. 1995	Alumina, 5.15	17.59	90	70	1	17.59	17.59
10	Salman et al. 1995	Alumina, 5.15	17.28	90	67	1	17.28	17.28
11	Salman et al. 1995	Alumina, 5.15	17.57	90	60	1	17.57	17.57
12	Salman et al. 1995	Alumina, 5.15	18.64	90	49	1	18.64	18.64
13	Salman et al. 1995	Alumina, 5.15	18.63	90	45	1	18.63	18.63
14	Salman et al. 1995	Alumina, 5.15	19.32	90	41	1	19.32	19.32
15	Salman et al. 1995	Alumina, 5.15	19.80	90	36	1	19.80	19.80
16	Salman et al. 1995	Alumina, 5.15	20.09	90	30	1	20.09	20.09
17	Salman et al. 1995	Alumina, 5.15	20.18	90	24	1	20.18	20.18
18	Salman et al. 1995	Alumina, 5.15	20.86	90	18	1	20.86	20.86
19	Salman et al. 1995	Alumina, 5.15	21.44	90	14	1	21.44	21.44
20	Salman et al. 1995	Alumina, 5.15	21.73	90	9	1	21.73	21.73

21	Salman et al. 1995	Alumina, 5.15	23.01	90	5	1	23.01	23.01
22	Salman et al. 1995	Alumina, 5.15	24.30	90	2	1	24.30	24.30
23	Salman et al. 1995	Alumina, 5.15	24.89	90	0	1	24.89	24.89
24	Salman et al. 1995	Alumina, 5.15	8.47	80	100	0.999	8.34	8.46
25	Salman et al. 1995	Alumina, 5.15	11.13	80	99	0.999	10.96	11.12
26	Salman et al. 1995	Alumina, 5.15	13.22	80	98	0.999	13.02	13.21
27	Salman et al. 1995	Alumina, 5.15	13.68	80	93	0.999	13.48	13.67
28	Salman et al. 1995	Alumina, 5.15	15.01	80	89	0.999	14.78	15.00
29	Salman et al. 1995	Alumina, 5.15	15.85	80	85	0.999	15.61	15.84
30	Salman et al. 1995	Alumina, 5.15	16.41	80	76	0.999	16.16	16.40
31	Salman et al. 1995	Alumina, 5.15	17.07	80	73	0.999	16.81	17.06
32	Salman et al. 1995	Alumina, 5.15	16.58	80	68	0.999	16.33	16.57
33	Salman et al. 1995	Alumina, 5.15	17.23	80	59	0.999	16.97	17.22
34	Salman et al. 1995	Alumina, 5.15	19.02	80	49	0.999	18.73	19.01
35	Salman et al. 1995	Alumina, 5.15	19.39	80	42	0.999	19.09	19.38
36	Salman et al. 1995	Alumina, 5.15	19.57	80	38	0.999	19.27	19.56
37	Salman et al. 1995	Alumina, 5.15	19.28	80	33	0.999	18.98	19.26
38	Salman et al. 1995	Alumina, 5.15	19.93	80	28	0.999	19.63	19.92
39	Salman et al. 1995	Alumina, 5.15	20.87	80	23	0.999	20.56	20.86
40	Salman et al. 1995	Alumina, 5.15	20.96	80	17	0.999	20.64	20.94
41	Salman et al. 1995	Alumina, 5.15	21.81	80	13	0.999	21.47	21.79
42	Salman et al. 1995	Alumina, 5.15	22.36	80	5	0.999	22.02	22.35
43	Salman et al. 1995	Alumina, 5.15	23.97	80	2	0.999	23.61	23.96
44	Salman et al. 1995	Alumina, 5.15	25.58	80	0	0.999	25.20	25.57

45	Salman et al. 1995	Alumina, 5.15	7.00	70	100	0.993	6.58	6.95
46	Salman et al. 1995	Alumina, 5.15	9.88	70	100	0.993	9.28	9.80
47	Salman et al. 1995	Alumina, 5.15	11.89	70	97	0.993	11.18	11.81
48	Salman et al. 1995	Alumina, 5.15	13.05	70	95	0.993	12.26	12.95
49	Salman et al. 1995	Alumina, 5.15	14.78	70	86	0.993	13.89	14.67
50	Salman et al. 1995	Alumina, 5.15	15.84	70	79	0.993	14.89	15.72
51	Salman et al. 1995	Alumina, 5.15	17.00	70	74	0.993	15.97	16.87
52	Salman et al. 1995	Alumina, 5.15	16.53	70	63	0.993	15.53	16.41
53	Salman et al. 1995	Alumina, 5.15	18.17	70	54	0.993	17.07	18.03
54	Salman et al. 1995	Alumina, 5.15	19.04	70	46	0.993	17.89	18.90
55	Salman et al. 1995	Alumina, 5.15	18.75	70	42	0.993	17.62	18.61
56	Salman et al. 1995	Alumina, 5.15	19.43	70	36	0.993	18.26	19.29
57	Salman et al. 1995	Alumina, 5.15	18.38	70	33	0.993	17.27	18.24
58	Salman et al. 1995	Alumina, 5.15	20.03	70	16	0.993	18.82	19.88
59	Salman et al. 1995	Alumina, 5.15	21.56	70	15	0.993	20.26	21.40
60	Salman et al. 1995	Alumina, 5.15	22.24	70	6	0.993	20.90	22.07
61	Salman et al. 1995	Alumina, 5.15	22.72	70	4	0.993	21.35	22.55
62	Salman et al. 1995	Alumina, 5.15	23.30	70	1	0.993	21.90	23.13
63	Salman et al. 1995	Alumina, 5.15	25.03	70	1	0.993	23.52	24.84
64	Salman et al. 1995	Alumina, 5.15	7.19	60	100	0.967	6.23	6.96
65	Salman et al. 1995	Alumina, 5.15	9.72	60	99	0.967	8.42	9.40
66	Salman et al. 1995	Alumina, 5.15	13.02	60	95	0.967	11.28	12.59
67	Salman et al. 1995	Alumina, 5.15	14.28	60	90	0.967	12.37	13.81

68	Salman et al. 1995	Alumina, 5.15	15.44	60	83	0.967	13.37	14.93
69	Salman et al. 1995	Alumina, 5.15	16.41	60	77	0.967	14.21	15.87
70	Salman et al. 1995	Alumina, 5.15	15.82	60	73	0.967	13.70	15.30
71	Salman et al. 1995	Alumina, 5.15	16.20	60	67	0.967	14.03	15.67
72	Salman et al. 1995	Alumina, 5.15	17.27	60	64	0.967	14.96	16.70
73	Salman et al. 1995	Alumina, 5.15	17.36	60	61	0.967	15.04	16.79
74	Salman et al. 1995	Alumina, 5.15	18.62	60	54	0.967	16.13	18.01
75	Salman et al. 1995	Alumina, 5.15	19.39	60	42	0.967	16.79	18.75
76	Salman et al. 1995	Alumina, 5.15	18.80	60	37	0.967	16.28	18.18
77	Salman et al. 1995	Alumina, 5.15	19.48	60	35	0.967	16.87	18.84
78	Salman et al. 1995	Alumina, 5.15	19.96	60	27	0.967	17.28	19.30
79	Salman et al. 1995	Alumina, 5.15	21.02	60	16	0.967	18.20	20.32
80	Salman et al. 1995	Alumina, 5.15	22.18	60	12	0.967	19.21	21.45
81	Salman et al. 1995	Alumina, 5.15	22.56	60	8	0.967	19.54	21.82
82	Salman et al. 1995	Alumina, 5.15	24.02	60	2	0.967	20.80	23.23
83	Salman et al. 1995	Alumina, 5.15	29.07	60	2	0.967	25.18	28.12
84	Salman et al. 1995	Alumina, 5.15	7.19	50	100	0.980	5.51	7.05
85	Salman et al. 1995	Alumina, 5.15	9.72	50	99	0.980	7.45	9.52
86	Salman et al. 1995	Alumina, 5.15	13.02	50	95	0.980	9.98	12.76
87	Salman et al. 1995	Alumina, 5.15	14.28	50	90	0.980	10.94	13.99
88	Salman et al. 1995	Alumina, 5.15	15.44	50	83	0.980	11.83	15.13
89	Salman et al. 1995	Alumina, 5.15	16.41	50	77	0.980	12.57	16.07
90	Salman et al. 1995	Alumina, 5.15	15.82	50	73	0.980	12.12	15.50
91	Salman et al. 1995	Alumina, 5.15	16.20	50	67	0.980	12.41	15.87

92	Salman et al. 1995	Alumina, 5.15	17.27	50	64	0.980	13.23	16.92
93	Salman et al. 1995	Alumina, 5.15	17.36	50	61	0.980	13.30	17.01
94	Salman et al. 1995	Alumina, 5.15	18.62	50	54	0.980	14.26	18.24
95	Salman et al. 1995	Alumina, 5.15	19.39	50	42	0.980	14.85	18.99
96	Salman et al. 1995	Alumina, 5.15	18.80	50	37	0.980	14.40	18.42
97	Salman et al. 1995	Alumina, 5.15	19.48	50	35	0.980	14.92	19.08
98	Salman et al. 1995	Alumina, 5.15	19.96	50	27	0.980	15.29	19.55
99	Salman et al. 1995	Alumina, 5.15	21.02	50	16	0.980	16.10	20.59
100	Salman et al. 1995	Alumina, 5.15	22.18	50	12	0.980	16.99	21.73
101	Salman et al. 1995	Alumina, 5.15	22.56	50	8	0.980	17.28	22.10
102	Salman et al. 1995	Alumina, 5.15	24.02	50	2	0.980	18.40	23.53
103	Salman et al. 1995	Alumina, 5.15	29.07	50	2	0.980	22.27	28.48
104	Salman et al. 1995	Alumina, 5.15	11.34	40	97	0.911	7.29	10.34
105	Salman et al. 1995	Alumina, 5.15	13.76	40	93	0.911	8.84	12.54
106	Salman et al. 1995	Alumina, 5.15	14.82	40	84	0.911	9.52	13.51
107	Salman et al. 1995	Alumina, 5.15	16.46	40	78	0.911	10.58	15.00
108	Salman et al. 1995	Alumina, 5.15	17.14	40	75	0.911	11.01	15.62
109	Salman et al. 1995	Alumina, 5.15	17.42	40	69	0.911	11.20	15.88
110	Salman et al. 1995	Alumina, 5.15	19.16	40	65	0.911	12.32	17.47
111	Salman et al. 1995	Alumina, 5.15	19.16	40	61	0.911	12.31	17.46
112	Salman et al. 1995	Alumina, 5.15	19.64	40	58	0.911	12.62	17.90
113	Salman et al. 1995	Alumina, 5.15	20.22	40	55	0.911	13.00	18.43
114	Salman et al. 1995	Alumina, 5.15	20.50	40	42	0.911	13.18	18.68
115	Salman et al. 1995	Alumina, 5.15	22.23	40	32	0.911	14.29	20.26

106	Salman et al. 1995	Alumina, 5.15	23.10	40	22	0.911	14.85	21.05
107	Salman et al. 1995	Alumina, 5.15	24.06	40	18	0.911	15.47	21.93
108	Salman et al. 1995	Alumina, 5.15	24.83	40	13	0.911	15.96	22.63
109	Salman et al. 1995	Alumina, 5.15	26.67	40	9	0.911	17.14	24.31
110	Salman et al. 1995	Alumina, 5.15	29.09	40	0	0.911	18.70	26.51
111	Salman et al. 1995	Alumina, 5.15	30.83	40	0	0.911	19.82	28.10
112	Salman et al. 1995	Alumina, 5.15	13.54	35	97	0.793	7.77	10.73
113	Salman et al. 1995	Alumina, 5.15	14.71	35	97	0.793	8.44	11.66
114	Salman et al. 1995	Alumina, 5.15	16.07	35	96	0.793	9.22	12.74
115	Salman et al. 1995	Alumina, 5.15	16.94	35	91	0.793	9.71	13.42
116	Salman et al. 1995	Alumina, 5.15	19.07	35	86	0.793	10.94	15.11
117	Salman et al. 1995	Alumina, 5.15	18.66	35	81	0.793	10.71	14.79
118	Salman et al. 1995	Alumina, 5.15	18.95	35	80	0.793	10.87	15.02
119	Salman et al. 1995	Alumina, 5.15	20.39	35	72	0.793	11.70	16.16
120	Salman et al. 1995	Alumina, 5.15	21.15	35	65	0.793	12.13	16.76
121	Salman et al. 1995	Alumina, 5.15	21.34	35	62	0.793	12.24	16.91
122	Salman et al. 1995	Alumina, 5.15	21.91	35	56	0.793	12.56	17.36
123	Salman et al. 1995	Alumina, 5.15	23.68	35	63	0.793	13.58	18.77
124	Salman et al. 1995	Alumina, 5.15	24.04	35	54	0.793	13.79	19.06
125	Salman et al. 1995	Alumina, 5.15	10.10	30	99	0.671	5.05	6.77
126	Salman et al. 1995	Alumina, 5.15	11.92	30	99	0.671	5.96	8.00
127	Salman et al. 1995	Alumina, 5.15	13.75	30	98	0.671	6.88	9.22
128	Salman et al. 1995	Alumina, 5.15	15.00	30	97	0.671	7.50	10.06
129	Salman et al. 1995	Alumina, 5.15	15.48	30	93	0.671	7.74	10.38

130	Salman et al. 1995	Alumina, 5.15	16.83	30	94	0.671	8.41	11.29
131	Salman et al. 1995	Alumina, 5.15	18.37	30	92	0.671	9.18	12.32
132	Salman et al. 1995	Alumina, 5.15	18.56	30	87	0.671	9.28	12.45
133	Salman et al. 1995	Alumina, 5.15	19.71	30	84	0.671	9.86	13.22
134	Salman et al. 1995	Alumina, 5.15	21.54	30	80	0.671	10.77	14.45
135	Salman et al. 1995	Alumina, 5.15	22.79	30	78	0.671	11.39	15.29
136	Salman et al. 1995	Alumina, 5.15	25.00	30	68	0.671	12.50	16.77
137	Salman et al. 1995	Alumina, 5.15	28.08	30	57	0.671	14.04	18.83
138	Salman et al. 1995	Alumina, 5.15	15.13	20	100	0.415	5.17	6.27
139	Salman et al. 1995	Alumina, 5.15	18.25	20	99	0.415	6.24	7.57
140	Salman et al. 1995	Alumina, 5.15	19.36	20	98	0.415	6.62	8.03
141	Salman et al. 1995	Alumina, 5.15	22.39	20	97	0.415	7.66	9.28
142	Salman et al. 1995	Alumina, 5.15	23.60	20	100	0.415	8.07	9.79
143	Salman et al. 1995	Alumina, 5.15	25.21	20	98	0.415	8.62	10.46
144	Salman et al. 1995	Alumina, 5.15	26.82	20	98	0.415	9.17	11.12
145	Salman et al. 1995	Alumina, 5.15	27.93	20	97	0.415	9.55	11.58
146	Salman et al. 1995	Alumina, 5.15	31.16	20	96	0.415	10.66	12.92
147	Salman et al. 2002	Alumina, 5.15	x	x	x	x	x	x
148	Salman et al. 2003	Fertiliser, 3.2	x	x	x	x	x	x
149	Salman et al. 2003	Fertiliser, 5.3	x	x	x	x	x	x
150	Salman et al. 2003	Fertiliser, 7.2	x	x	x	x	x	x

5.7.3 Assessment of particle breakage models under normal impact

The dataset 1 in Table 5.5 covers test particles with size ranging from 0.2 to 2.0 mm, the impact number from 1 to 15, the impact velocity from 4 to 60 m/s, the breakage ratio from 0.01 to 19 %. The breakage ratio is defined with the same criterion, i.e. debris defined as two sizes below the lower feed size of the original particle. Table 5.5 shows that the breakage ratio increases as the number of impact increases for the same kind of particles. It may be concluded that the stressing event exerts influence on the velocity exponent. As for the assessment of the five breakage models, Eq. (5.51) is fitted against the data set in Table 5.5 with corresponding velocity exponent using the nonlinear least square method. Consequently, the parameter C as the combined effect of physical and mechanical properties is obtained and the predictive breakage ratio of each model R_p is achieved by the multiplying C with v^n.

5.7.3.1 Statistics of fitting of the breakage models

The value of C for each fitting breakage model and the best fitting equation for Dataset 1 (Table 5.5) are tabulated in Table 5.8. For the best fitting of the subset in Dataset 1, the velocity exponent is varied from 1.8 to 4.0, which is lower than the exponent of 4.5 proposed in the new breakage model. This is presumably because that the velocity exponent of proposed model is not universal to all the chipping data. Note that the R-square is larger if the velocity exponent in the breakage models is closer to that of the best fit equation, i.e. a better fit. The velocity exponent appears to be small when test data are fitted with relatively small breakage ratio. The velocity exponent becomes increasingly large when the breakage ratio is varied in a wider range. This infers that the velocity exponent may increase with the increasing impact velocity and breakage ratio. It should also be noted that only 3 subset data fitting gives the same velocity exponent in the breakage models. The majority of velocity exponents obtained from the best fitting are different from that in the particle breakage models.

5.7.3.2 Graphical comparison of dataset 1

The predicted breakage ratio (R_p) in these breakage models is compared with the reported breakage ratio (R) in dataset 1. The ratio of R_p/R is plotted against the impact velocity in Dataset 1 (Figure 5.7). It is seen that the majority of the data points fall in the range between 0 and 2 irrespective of the breakage models. When the impact

Table 5.8 Fitting goodness of breakage models in dataset 1

Model	Evans et al. 1976		Evans et al. 1978		Hutchings 1994		Ghadiri et al. 2002		Wang 2016		Best fitting		
Exponent	2.4		3.17		2.67		2.0		4.5				
	C	RS	C	RS	C	RS	C	RS	C	RS	C	n	RS
Mgo 5	0.02093	0.9889	0.002386	0.9222	0.009814	0.9702	0.06352	0.9992	5.324e-05	0.7678	0.06352	2.0	0.999
Mgo 10	0.02834	0.9892	0.00366	0.9208	0.01389	0.9711	0.08.31	0.9945	0.0001007	0.7613	0.0579	2.1	0.996
Mgo 15	0.03521	0.9989	0.004479	0.981	0.01715	0.9962	0.1009	0.9868	0.0001232	0.9343	0.03521	2.4	0.998
NaCl 5	0.009118	0.8936	0.001622	0.7007	0.004998	0.8356	0.02196	0.9483	7.736e-05	0.2872	0.9564	1.8	0.956
NaCl 10	0.01894	0.9047	0.00338	0.7222	0.01039	0.85	0.04559	0.9554	0.0001626	0.3266	0.06876	1.8	0.962
NaCl 15	0.03454	0.9756	0.007117	0.9833	0.01993	0.9882	0.07714	0.9307	0.0004376	0.872	0.01417	2.84	0.990
Kcl 5	0.04652	0.9763	0.007165	0.8611	0.02428	0.9437	0.1199	0.9956	0.0002649	0.6216	0.1199	2.0	0.995
Kcl 10	0.06372	0.9774	0.009843	0.8681	0.03329	0.9471	0.1639	0.993	0.0003653	0.6334	0.1639	2.0	0.993
Kcl 15	0.08953	0.983	0.01845	0.9464	0.05167	0.9808	0.2	0.9571	0.001136	0.7556	0.07457	2.49	0.984
LM 212	0.0003658	0.9591	1.67e-05	0.9965	0.0001244	0.9827	0.001794	0.8987	7.651e-08	0.9077	2.02e-05	3.12	0.997
LM 250	0.00046	0.9718	2.047e-05	0.9635	0.0001549	0.9787	0.002288	0.9354	9.064e-08	0.828	0.000143	2.69	0.979
LM 355	0.0007925	0.9905	3.869e-05	0.9697	0.0002758	0.9908	0.003752	0.9684	2.001e-07	0.8394	0.000457	2.541	0.992
LM 425	0.0009938	0.9804	5.352e-05	0.9703	0.0003582	0.9876	0.004464	0.944	3.219e-07	0.7894	0.000332	2.69	0.988
Alumina 1	0.008514	0.9878	0.0008354	0.9836	0.003789	0.9939	0.02793	0.9584	1.415e-05	0.8734	0.003284	2.718	0.994
Alumina 2	0.002725	0.9291	0.0002744	0.9843	0.001225	0.9559	0.008789	0.8701	4.807e-06	0.9726	6.70e-05	3.637	0.992
Zeolite	0.007394	0.8989	0.0006667	0.9608	0.003191	0.9271	0.02546	0.8405	9.946e-06	0.9725	5.26e-05	3.975	0.978

velocity is less than 20 m/s, all the breakage models predict some higher values of R_p/R more than 2 except for Wang (2016). This implies that the predicted breakage ratio by Wang is underestimated compared to the reported values in Dataset 1 under low impact velocity. However, when the impact velocity is beyond 20 m/s, all R_p/R values are smaller than 2. The majority of R_p/R values are lower than 1.5, indicating a better prediction for these breakage models. The vast majority of R_p/R for Evans and Wilshaw 1976, Hutchings 1994 and Ghadiri and Zhang 2002 are larger than 1 whilst the majority of R_p/R for Evans et al. 1978 and Wang 2016 are smaller than 1. This implies that the models of Evans and Wilshaw 1976, Hutchings 1994 and Ghadiri and Zhang 2002 tend to overestimate the breakage ratio whilst the models of Evans et al. 1978 and Wang 2016 tend to underestimate the breakage ratio throughout the model fitting of dataset 1.

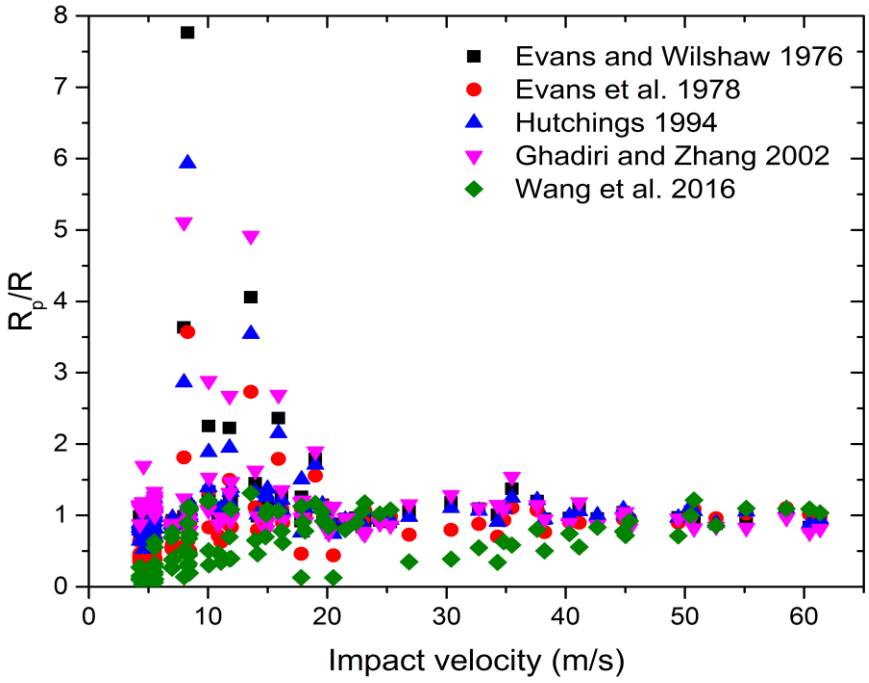

Figure 5.7 R_p/R vs. impact velocity: Dataset 1

5.7.3.3 Statistics of model prediction to test ratios (R_p/R)

The statistics of the model prediction to the test data ratios is summarized in Table 5.9. Note that a good predictive model would feature an average of R_p/R close to 1.0 with a small coefficient of variation. Table 5.9 shows that Evans et al.'s (1978) model gives the average value of R_p/R closest to 1.0. However, all models exhibit relatively large

values of coefficient of variation, demonstrating large scatters of the predicted value compared with test data. Comparatively, Evans et al.'s (1978) represents the best one among these breakage models since it has the closest average value of R_p/R with 0.89 as well as the smallest coefficient of variation 0.51.

Table 5.9 Statistics of predictive competence for breakage models

Model		Evans and Wilshaw (1976)	Evans et al. (1978)	Hutchings (1994)	Ghadiri and Zhang (2002)	Wang (2016)
Exponent		2.4	3.17	2.67	2.0	4.5
R_p/R	Average	1.19	0.89	1.15	1.29	0.62
	Stdv	0.83	0.46	0.64	1.25	0.37
	CoV	0.70	0.51	0.55	0.97	0.59

Figure 5.8 shows the relationship between velocity exponent and the average of R_p/R. It shows that the average R_p/R decreases as the velocity exponent increases. In general, it suggests that a larger velocity exponent is more likely to underestimate the breakage ratio, which agrees well with the finding from the graphical comparison.

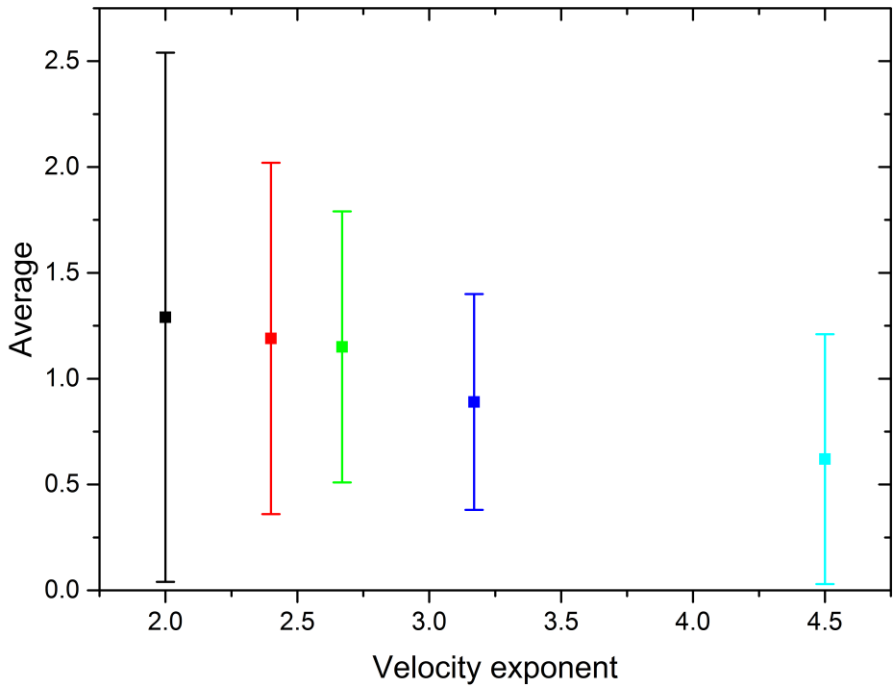

Figure 5.8 Plot of velocity exponent vs. Rp/R

5.7.4 Assessment of particle breakage models under oblique impact

As noted before, existing models for particle breakage merely consider the normal component velocity under oblique impact and consequently fall short of predicting the contribution of tangential component velocity on breakage propensity. The equivalent normal velocity is thus proposed to address the deficiency of existing models. In terms of the dataset from oblique impact, dataset 2 in Table 5.7 is collected in the regime of chipping and dataset 3 in Table 5.8 is collected in the regime covering both chipping and fragmentation. Considering the scope of model application, a power trend model is applied to fit dataset 2 whereas Weibull distribution is applied to fit dataset 3. In terms of the assessment of breakage models under oblique impact, the best fitting parameters in dataset 2 and 3 are first obtained in the case of normal impact. Then the equivalent normal velocity is inserted into the breakage models under different impact angles to examine its serviceability. To the best knowledge of the author, there is no other breakage models considering the effect of impact angle. Traditional way of predicting particle breakage propensity under oblique impact is to insert the normal component velocity into the breakage models which is applicable under normal impact. The breakage propensity estimated by normal component velocity and equivalent normal velocity are compared and the ratio of R_p/R is summarized respectively.

5.7.4.1 Graphical comparison of dataset 2

As an example, Figure 5.9 is the combined plot of reported breakage ratio of PS2 in dataset 2 and the predicted breakage ratio by equivalent normal velocity under four impact angles, 90^o, 65^o, 45^o, 25^o. In the upper left of Figure 5.9, the reported breakage ratios at four impact angles are nearly the same at low normal component velocity (> 5 m/s). When the normal component velocity is larger than 5 m/s, the breakage ratio under oblique impact becomes more deviated from that under normal impact. In particular, the breakage ratio under 25^o presents the highest breakage ratio among the four impact angles. A conclusion may be drawn that the breakage ratio increases as the impact angle decreases given the same normal component velocity. In other words, the tangential component velocity becomes increasingly important with the increase of impact velocity. This is in good accordance with the experimental finding by single particle impact test in Chapter 3. As mentioned above, the chipping data is assumed to follow a power trend. For the breakage data of PS2 under normal impact, the velocity exponent

is determined as 3.06 using nonlinear least square method. As for breakage prediction of oblique impact, the breakage ratios under impact angles are assumed to follow the same power trend. However, the normal component impact velocity (v_n) is replaced with the equivalent normal velocity (v_{eq}).

In the centre of Figure 5.9, the predictive breakage ratio by equivalent normal velocity is compared with that reported in the dataset 2. It is found that the breakage ratios under four impact angles simultaneously arrive at the predictive curve when the equivalent normal velocity is introduced in the breakage model.

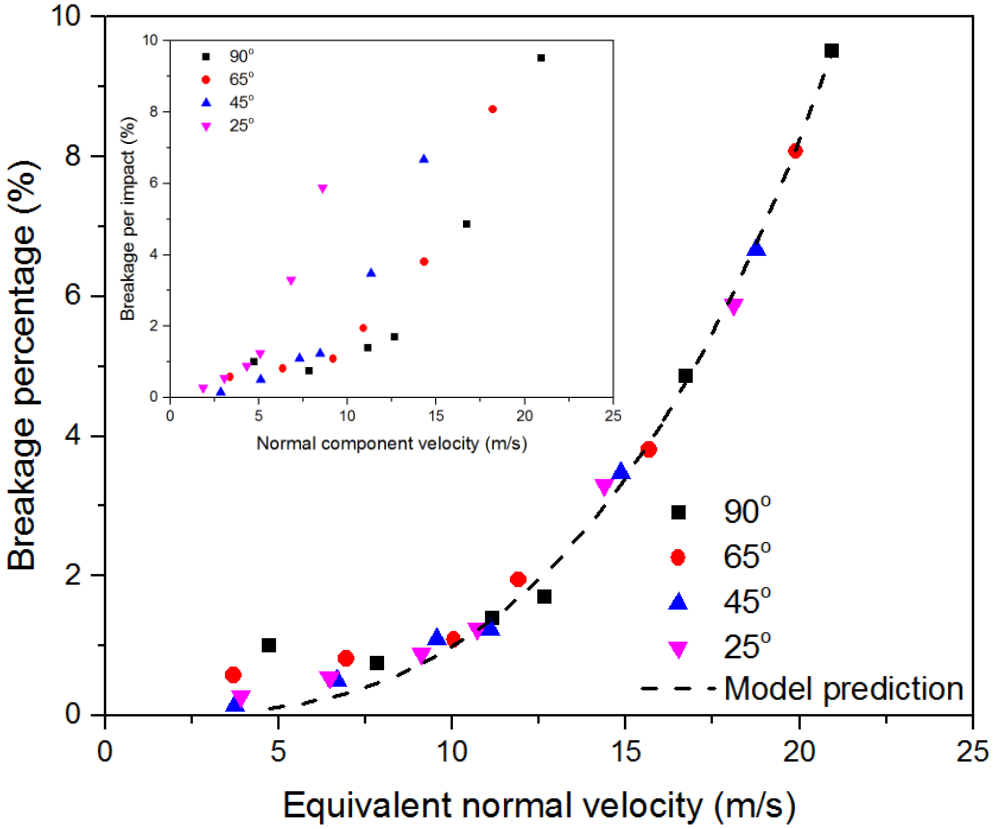

Figure 5.9 Breakage model fitting of PS2 impact test data

(Data source from Papadopoulos 1998)

The predictive curve based on the equivalent normal velocity demonstrates a remarkable unification of breakage test data despite some scatter of breakage ratio under the impact velocity of 5 m/s. The same unification trend is also observed in the breakage model fitting by means of equivalent normal velocity. The model fitting results of other particles in dataset 2 should be referred to Appendix C.

For a direct comparison, the predictive value of breakage ratio by means of normal component velocity and equivalent normal velocity is calculated based on dataset 2. The ratio of R_p/R under normal component velocity and equivalent normal velocity is shown in Figure 5.10. It indicates from Figure 5.10 that the ratio of R_p/R by means of equivalent normal velocity fitting is less scattered than that by means of normal component velocity fitting. Moreover, the ratio of R_p/R by means of equivalent normal velocity fitting converges to 1 more than that by means of normal component velocity.

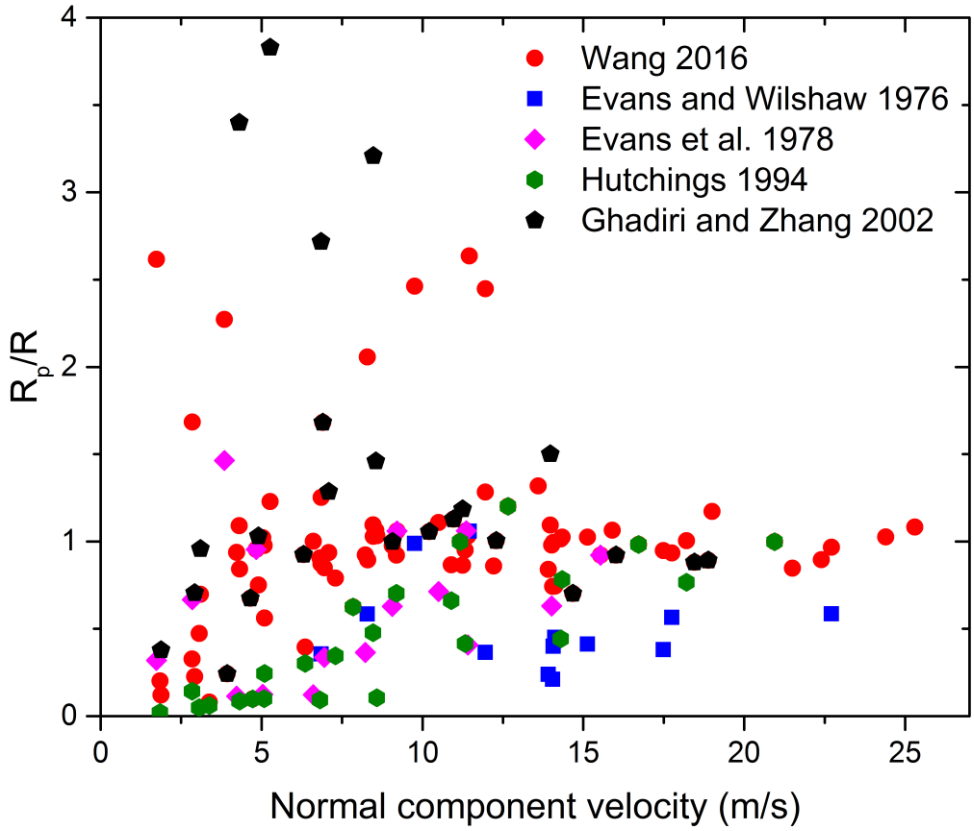

Figure 5.10 R_p/R vs. impact velocity in terms of model assessment in dataset 2

5.7.4.2 Statistics of model fitting results of dataset 2

Table 5.10 summarizes the statistics of R_p/R under two fitting methods, namely normal component velocity from existing breakage models and equivalent normal velocity from the newly proposed model in this work. The average of R_p/R achieved by equivalent normal velocity is 1 as compared to the average of R_p/R obtained by normal component velocity. This implies that the breakage model based on normal component velocity tends to underestimate the breakage ratio under oblique impact. It could be accounted by the lack of tangential component velocity contribution. The coefficient of

variation based on equivalent normal velocity is smaller than that based on normal component velocity. It is manifest that the equivalent normal velocity is superior to the normal component velocity in terms of oblique impact fitting.

Table 5.10 Statistics of R_p/R by normal component velocity and equivalent normal velocity

Model	R_p/R		
	Average	Stdv	CoV
Evans and Wilshaw 1976	0.73	0.37	0.50
Evans et al. 1978	0.62	0.40	0.64
Hutchings 1994	0.46	0.37	0.82
Ghadiri and Zhang 2002	1.37	0.95	0.70
Wang 2016	1.0	0.48	0.48

5.7.4.3 Graphical comparison of dataset 3

Dataset 3 includes the breakage data covering both chipping and fragmentation under oblique impact. As a typical example from dataset 3, Figure 5.11 presents the impact results of 5.15 mm alumina over a range of impact velocity from 5 to 30 m/s with impact angle from 90^o (normal) down to 20^o. It illustrates that particles remain unbroken at low impact velocities and above the velocity of 10 m/s particles begin to break. The number of unbroken particles diminishes as the impact velocity is further increased. As the impact angle is decreased, the number of unbroken particles increases given the same impact velocity. The number of unbroken particles under 20^o reach as high as 96 under 31 m/s whereas all the particles have been broken from 90^o to 50^o under 31 m/s. It should also be noted that the breakage curve under the impact angle from 90^o to 50^o is very close. However, below the impact angle of 50^o, the breakage propensity becomes substantially lower as compared to that from 90^o to 50^o. This indicates that tangential component velocity is increasingly important with the decrease of impact angle.

As for the assessment of breakage models in dataset 3, Weibull distribution is chosen because of its simple function and close prediction with the experimental data. This gives

$$N_0 = 100exp^{\left(-\left(\frac{v}{c}\right)^m\right)} \tag{5.52}$$

where v is the impact velocity; c is a parameter and m is called Weibull modulus. The fitting value of c and m could be determined by least square method at different impact angles. The fitting parameters c and m are typically changing under different impact angles. The emerging challenge is whether it is possible to predict the breakage propensity in the range of fragmentation by the same set value of c and m. Another challenge is whether the equivalent normal velocity is able to enable a unification of breakage curve in the case of fragmentation.

To answer these two questions, the following actions are taken, which are similar to the assessing procedure in dataset 2. First, it is assumed that the number of unbroken particles follows the Weibull distribution and hereby the fitting parameters c and m could be determined by the least square method. Second, it is assumed that the breakage propensity (the number of unbroken particles) follows the Weibull distribution with the same fitting parameters c and m, which are achieved under normal impact. Then, the only variation in Eq. (5.52) is the impact velocity. However, as stated previously, there are no existing models accounting for the contribution of tangential component velocity under oblique impact. Figure 5.12 displays the predictive number of unbroken particles via equivalent normal velocity. It clearly shows that the number of unbroken particle invariably follow the trend line of predictive function. The unification curve is also observed in the modelling fitting of remaining data in database 3 (See Appendix C as well as fitting parameters of the equivalent normal velocity).

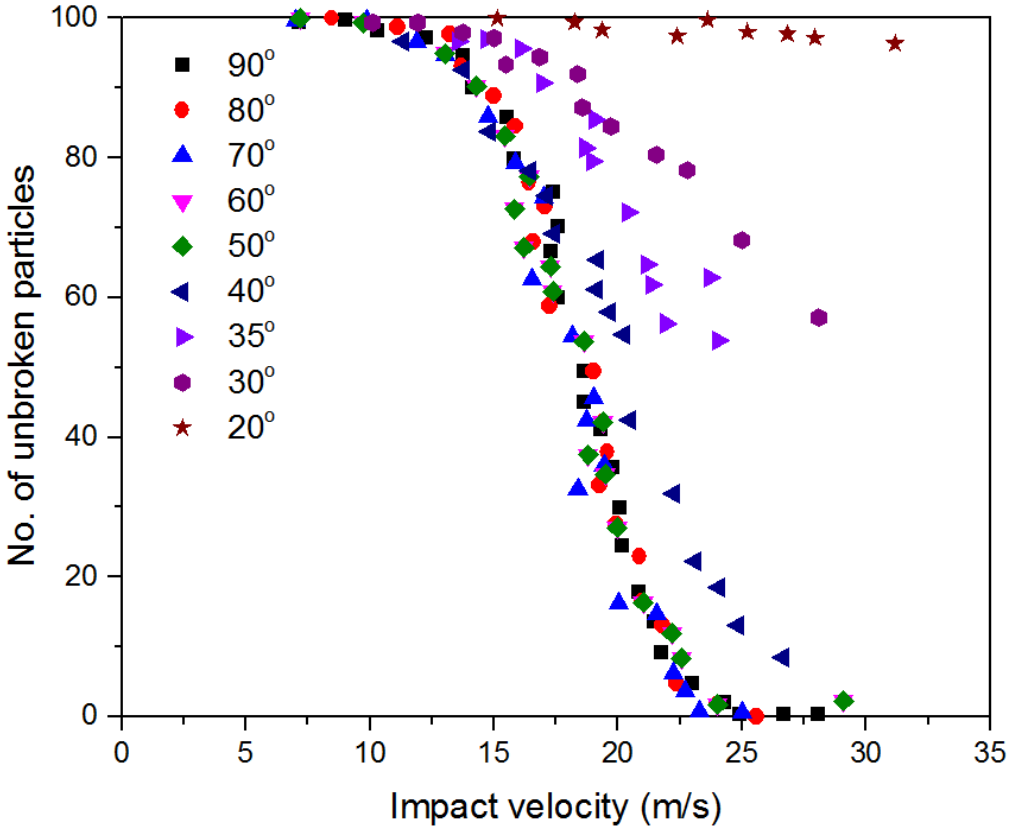

Figure 5.11 Breakage data of alumina 5.15 mm (Data from Salman et al., 1995)

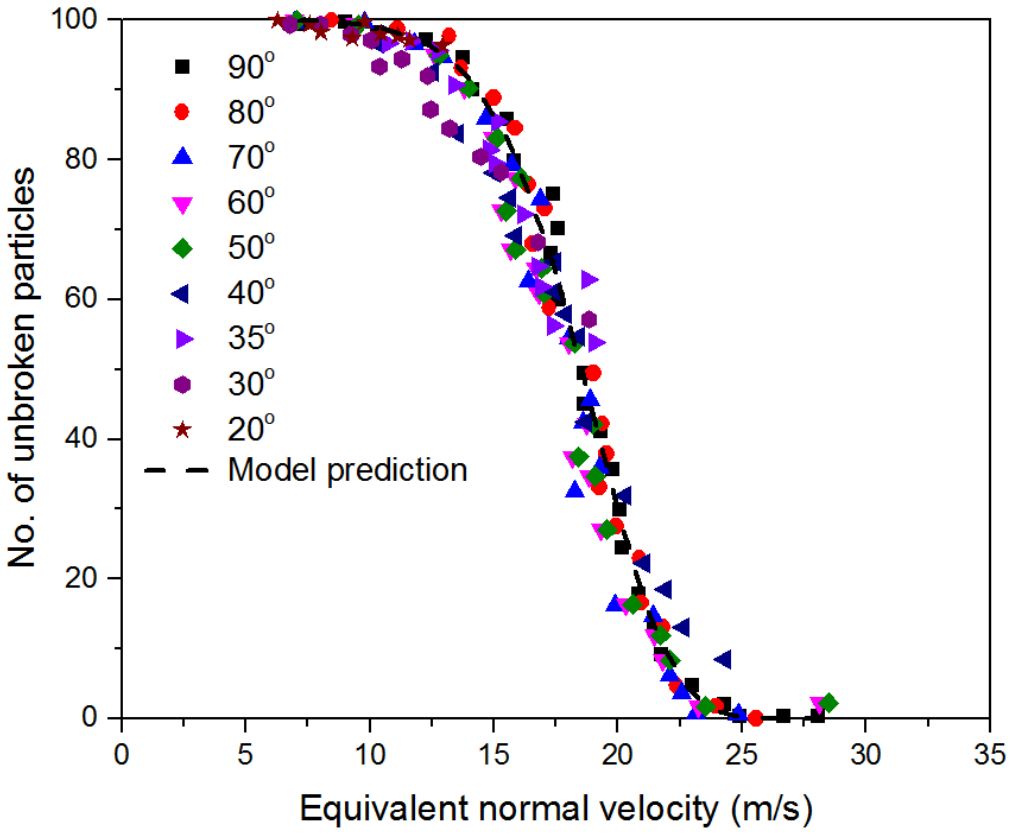

Figure 5.12 Model prediction vs. breakage data collection

For a comparative analysis, the impact velocity in Eq. (5.52) is replaced by normal component velocity and equivalent normal velocity for the sake of breakage model assessment. Thus, the ratio of predictive breakage propensity N_p vs. the reported breakage propensity N is summarized in Figure 5.13. Figure 5.13 (a) shows the N_p/N through normal component velocity fitting whereas Figure 5.13 (b) shows the N_p/N through equivalent normal velocity.

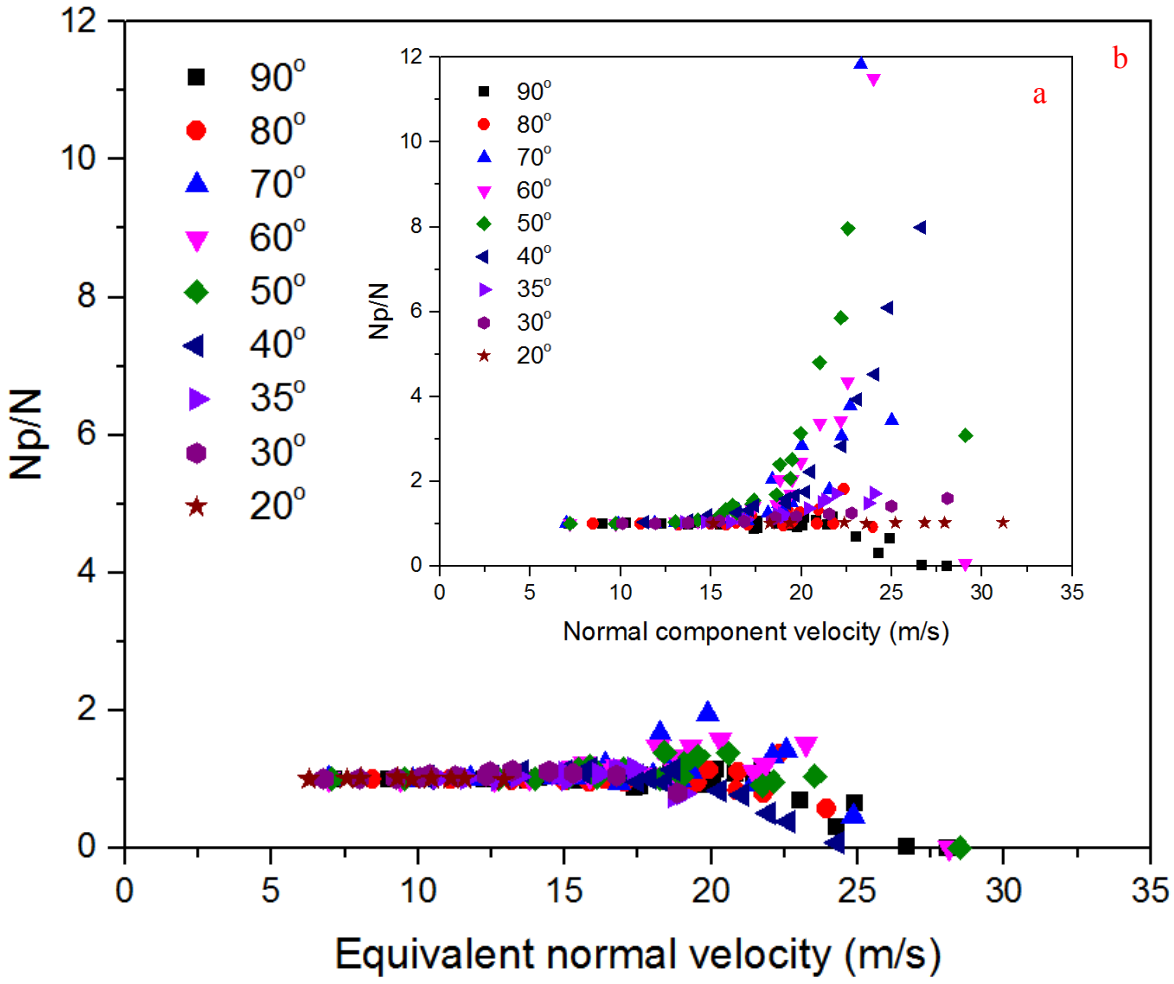

Figure 5.13 Comparison of Np/N by normal component velocity and equivalent normal velocity fitting

Figure 5.13a indicates that the ratio of N_p/N through normal component velocity fitting is close to 1 below 17m/s. Then the ratio of N_p/N becomes scattered beyond 17m/s. For example, some values of N_p/N reach higher than 2 with the highest value topping at 12. In general, the number of unbroken particles is overestimated through normal component velocity fitting. As compared to Figure 5.13a, Figure 5.13b exhibits a stable

trend of N_p/N converging to 1 despite some underestimated value at higher impact velocity (beyond 25 m/s). All the values of N_p/N stay in the range between 0 and 2. This infers that the equivalent normal velocity fitting is more likely to give reliable prediction of breakage propensity as compared to normal component velocity fitting.

5.7.4.4 Statistics of model fitting results of data set 3

Table 5.11 summarizes the statistics of N_p/N using normal component velocity fitting and equivalent normal velocity fitting. It shows that the fitting method using equivalent normal velocity presents a very good prediction with the average of N_p/N close to 1 and relatively small coefficient of variation. However, the normal component velocity shows a relatively poor statistical performance in terms of breakage propensity prediction. This is evidenced by the average value of N_p/N as 2.06 and the relatively high coefficient of variation as 1.47.

Table 5.11 Statistics of Np/N by normal velocity and equivalent normal velocity fitting

Model	N_p/N		
	Average	Stdv	CoV
Normal component velocity	2.06	3.03	1.47
Equivalent normal velocity	1.06	0.34	0.32

It would be interesting to compare the statistical performance between dataset 2 and 3 so as to evaluate the model application of chipping and fragmentation respectively. Similarly, the equivalent normal velocity is superior to give closer prediction of breakage propensity including both chipping and fragmentation as compared to normal component velocity. However, it appears that model fitting of fragmentation in dataset 3 exhibits more scatter than model fitting of chipping in dataset 2. In other words, the influence of tangential component velocity under fragmentation is more pronounced than that under chipping. Besides, the experimental test has confirmed that the tangential component velocity plays an increasingly role in particle breakage. The

comparative analysis under oblique model assessment suggests that equivalent normal velocity is able to address the deficiency in existing breakage models and to provide close prediction in both chipping and fragmentation regime.

As for now, the assessment of particle breakage models against three datasets has been completed under both normal and oblique impact. The dataset 1 covers the dataset of chipping under normal impact and is evaluated against five particle breakage models. The assessment of respective velocity exponent in five models has shown that none of these models is competent in the complete fitting of dataset 1 despite some models prevailing in some limited data range. It is worth noting that the velocity exponent increases with a wider range of impact velocity and a larger breadth of breakage ratio. The dataset 2 and 3 includes the data of chipping and fragmentation under oblique impact respectively. The power law is assumed to apply in chipping and Weibull distribution is assumed to apply in fragmentation. The assessment of breakage models for dataset 2 and 3 has shown that the equivalent normal velocity is not only applicable to chipping regime but also applicable to fragmentation regime. In particular, the equivalent normal velocity gives more stable prediction of breakage propensity in fragmentation than chipping. Some relevant discussions are further detailed as below.

5.8 Discussion

5.8.1 Mechanical property

Previous studies indicated that the breakage behaviour of particulate solids is influenced by mechanical property. The brittleness index (BI), proposed by Lawn and Marshall (1979), is commonly used to characterize the degree of size reduction during milling operation:

$$BI = \frac{H}{K_c} \tag{5.53}$$

A higher value of BI indicates a more brittle material, of which the hardness and fracture toughness were calculated by nanoindentation (Taylor et al. 2004); Meier et al. (2009) obtained a relationship between the brittleness index and two adjusted breakage parameters from the model of Peukert and Vogel (2003). However, the importance of other possibly important factors has not been yet identified in this study. Apart from the

indentation technique, the scratch test provides another means to measure the fracture toughness (Akono et al., 2011). It is worth noting that the variability of the mechanical properties may play a role in the breakage phenomena of particulates. Miller et al. (2008) investigated surface roughness of the particle, which should be reduced to a tolerable level in order to achieve a reliable result from nanoindentation. The tests of roughness at various locations on the same sample show a large variability of the roughness measurement. Increased scatter in mechanical properties such as Young's modulus and hardness was observed due to the existence of significant surface roughness (Kim et al. 2006). Despite a criterion proposed for roughness of surfaces for nanoidentation, it is suggested to adopt alternative quantification of roughness and investigate the variation of mechanical property considering the intrinsic difficulty of topological characterization.

5.8.2 Velocity exponent

The breakage susceptibility of particle is related to the impact velocity as well as other governing parameters. A general form of particle breakage model is

$$\varepsilon \propto \frac{\rho^a R^b}{k_c^d H^e} v^n \tag{5.54}$$

As noted by Finnie (1972), an exponent of n=2 was observed experimentally as the first approximation. However, the actual value was found to be 2.4 in many cases for brittle materials. Amongst fracture-based models, Evans and Wilshaw (1976), Hutchings (1978), and Ghadiri and Zhang (2002) give velocity exponents 2.4, 2.67 and 2 in the static or quasi-static range respectively, compared with the predicted value of 3.17 (Evans et al. 1978) and 4.5 for this work in dynamic range. Thus far there are no explicit explanations for the discrepancy of impact velocity.

Possible reasons emerge from the preceding analysis as follows: (1) The mechanism of load transfer from impact velocity to the applying force is lacking. Hence, semi-empirical approach has to be adopted to determine the role of major material properties on indentation fracture such as the estimate of the final crack size due to impact. The problem of load transfer arises because a rigorous solution of elastic-plastic response of the indentation process is not available. (2) Subsurface lateral crack is assumed to be

accountable for material fractional loss during impact. However, particle breakage during impact is a combined action of material loss from radial crack, conical crack and lateral crack. Consequently, the breakage model derived from lateral crack tends to underestimate the breakage extent. (3) The variation of mechanical property in different impact loading regimes may alter the breakage performance of particle. For example, the measured value of fracture toughness and hardness under indentation may be different from that under impact loading. (4) Other factors such as particle microstructure and heterogeneity, particle shape and angularity, and thermal properties have not been considered in the models. These factors are out of the scope of this work, which forms an interesting subject for the future research.

5.8.3 Impact angle

The effect of impact angle has been widely studied by previous work with the emphasis on normal component velocity. For example, Salman et al. (2002) examined the effect of impact angle on alumina particle fragmentation and found two types of particle fragmentation, i.e. normal fragmentation and oblique fragmentation. The noticeable difference for oblique impact is the asymmetry of oblique fragmentation as compared to normal fragmentation. Cheong et al. (2003) investigated the effect of impact angle and velocity on the size distribution of glass fragment. More damage was sustained as the increase of impact angle from 15^{o} to 90^{o} at the impact velocity of 26 m/s and it was concluded that normal component of impact velocity is main driving force for breakage, which is in accordance with the work from Samimi et al. (2004) and Subero et al. (2005). In terms of impact energy in grinding system, only the normal component of the velocity is considered (Meier and Peukert, 2007; Meier et al. 2009). Although the key role of the normal component has been recognized during these studies, little attention has been paid to the significance of the tangential component. Hence, little efforts have been committed to rationalize the effect of tangential component velocity in the breakage models. As the significance of tangential component velocity identified in this study as well as some previous work (Papadopoulos 1998, Samimi et al. 2004), it necessitates the incorporation of tangential component velocity in the breakage model. The mobilisation of dynamic friction coefficient is very likely to address this issue. The assessment of dataset 2 and 3 has proved that the equivalent normal velocity mobilised by dynamic friction coefficient is superior not only in the predictive accuracy but also in statistical reliability.

5.8.4 From chipping to fragmentation

The breakage pattern is transformed from chipping to fragmentation alongside the increase of impact velocity. Thus, the threshold of impact velocity may serve as the indicator for breakage pattern transition. Experimental study by Andrews and Kim (1999) indicates that the particle undergoes fragmentation above a threshold velocity, which depends on the particle size and mechanical property. However, it appears that there is no theoretical basis to predict the threshold velocity, which is able to help categorize the breakage pattern upon impact velocity. From the survey of breakage models, it can be seen that there is mechanistic ground in terms of chipping whereas the theoretical models in fragmentation regime are still lacking. In grinding system, particle breakage is a combined effect of chipping and fragmentation as well as damage accumulation by repetitive impacts. Recent work by Ali et al. (2015) seems very promising to analyse particle breakage by linking the change of surface area of different particle sizes with impact velocity and material properties. However, the main concern is whether the serviceability of breakage model from chipping is still tenable in grinding considering the velocity difference in two different stressing events. A fully-fledged theoretical model considering multiple factors, which takes into account both chipping and fragmentation remains challenging due to the complexity of grinding process.

5.9 Summary

This chapter has presented a thorough study of particle breakage subject to impact loading pertinent to comminution. Existing fracture mechanics based models have been reviewed with their similarities and differences highlighted. This literature review lends itself to the development of grinding mechanism and provides detailed information of existing breakage models. The fracture mechanics based models are then assessed with single particle impact data, which enables the deficiencies of the existing models to be identified. The following conclusions can be drawn based on this study:

1. A breakage model for brittle particulate solids has been developed based on a mechanistic approach assuming that the subsurface lateral crack accounts for the chipping mechanism. Considering the limitations of existing models in predicting the breakage under oblique impact and the significance of tangential velocity identified from experiment, the effect of impact angle is considered in the developed breakage

model, which enables the contributions of normal and tangential components of the impact velocity to be rationalized.

2. The assessment of existing breakage (chipping) models as well as the new model shows a large scatter in terms of the predictive breakage ratio. This implies that one breakage model based on limited test data is unlikely to be reliable in another breakage model. As a whole, the models by Evans et al. (1978) and Wang (2016) tend to underestimate the breakage ratio whilst the models by Evans and Wilshaw (1976), Hutchings (1994) and Ghadiri and Zhang (2002) tend to overestimate the breakage ratio. The lack of velocity exponent generality could be attributed to the complicated load transfer mechanism, simplified assumption of chipping, the variability of mechanical property under impact loading and exclusion of other factors such as particle microstructure and thermal property.

3. The assessment of breakage models including both chipping and fragmentation under oblique impact suggests that the proposed equivalent normal velocity is able to give close prediction with experimental results. The breakage propensity based on normal component velocity is likely to be underestimated if the tangential component velocity is ignored. The mobilisation of dynamic friction under oblique impact enables a remarkable unification curve of breakage propensity for the whole impact angles.

Chapter 6

Milling tests in impact pin mill

6.1 Introduction

Milling is an important mechanical unit operation in many industrial sectors such as chemical processing, mineral processing, pharmaceutical and agricultural engineering for the purpose of intentional size reduction of materials. The size reduction is realised by the breakdown of feed particles under various stressing events, which results in a finer size of product particle. Despite many attempts to investigate the mechanical behaviour during a milling process, the grindability of a material in a milling operation is still very difficult to predict. Milling has been known to be extremely inefficient and energy-intensive. Therefore, an improved understanding of a milling operation can lead to the optimisation and refinement in a milling process.

Several comminution theories have been developed in an attempt to determine the energy input required for grinding of a given size reduction ratio. Three classical laws for grinding energy have been detailed in the literature survey of Chapter 2. In general, the three laws, i.e. Kick's law, Rittinger's law and Bond's law are expressed as a function of feed particle size and product particle size. Numerous researchers have investigated the grinding energy requirement based on the three laws. For example, Deniz (2004) presented a comparison of the breakage parameters of six different limestones in a batch laboratory ball mill and their relationship with Bond's grindability. Chen et al. (2004) carried out an energy-based analysis of milling of α-lactose monohydrate using a single-ball-mill. The time evolution of d_{90}, d_{50}, d_{10} of product particle was fitted with Kick, Rittinger and Bond's models. The results showed that Rittinger's model best describes the milling behaviour for low mill loadings at high frequencies whilst Kick's model is more suitable for high mill loadings at low frequencies. Kanda and Kotake (2007) introduced the methods to measure two grindability indices, i.e. Hardgrove index and Bond's index. Ipek and Goktepe (2011) determined the Bond's work index of zeolite particle with diameter 3350 μm. Shashidhar et al. (2013) studied the energy consumption in an impact type hammer mill

and a pin mill. It was found that the energy consumption follows a linear relationship with size reduction ratio.

As pointed out by Leschonski (1981), the behaviour and properties of particulate materials are to a large extent dependent on their size distributions. Hence, the measurement and interpretation of particle size distribution (PSD) is an important way to characterize a milling process. The mathematical modelling of particle size distribution arising from milling has been extensively investigated in the literature, which is known as a breakage function. Examples of the breakage functions include the normal and log-normal distributions, the Rosin-Rammler-Bennett (RRB) and the Gates-Gaudin-Schumann models, which have been summarized in Chapter 2. Yu and Standish (1990) systematically described the commonly used functions for size distribution as well as their applicability and limitation summarized. Manohar and Sridhar (2001) characterized the particle size distribution by Rosin-Rammler-Bennett (RRB) equation. Shashidhar et al. (2013) summarized various mathematical models available in the literature to describe particle size distribution. Apart from PSD, there are other size parameters to characterize the milling degree of product particle, e.g. uniformity index, relative size span, skewness, kurtosis and size guide number. A list of size parameters in the literature is summarized in Table 6.1 based on Shashidhar et al. (2013). As shown in Table 6.1, all the size parameters are expressed as a function of the product particle size. The letter d refers to the diameter and the subscript value denotes the value of percentile on a cumulative curve.

This chapter presents the results of milling test through an impact pin mill. Two types of particles, namely zeolite 4Ak and alumina with three size ranges are chosen for this study. The effects of rotary speed and feed rate on the milling results are studied. Section 6.2 presents the basic information of the selected impact pin mill and its working principle. The layout of the rotary and disc pins is detailed. The experimental setup of milling tests is described in Section 6.3. The grinding variables in the impact pin mill consist of rotary speed and feed rate. Section 6.4 gives the milling results with regard to material grindability. Six parameters are chosen to characterise the milling results due to their popularity and ease of interpretation. These parameters include fineness, median product size, relative size span, grinding energy, size reduction ratio and specific surface energy. The relationships between relevant parameters are

discussed. Finally, a summary emerging from the activity in abovementioned sections is given in Section 6.5.

Table 6.1 Commonly used size parameters for grindability

Parameter	**Formula**	**Reference**
Median particle size	$S_{gn} = d_{50}$	Canadian Fertilizer Institute (1982)
Size reduction ratio	SRR=d50, p/d50, f	Verheezen et al. (2004)
Uniformity index	$U_i = 100 * d_5/d_{95}$	Canadian Fertilizer Institute (1982)
Coefficient of uniformity	$C_u = d_{60}/d_{10}$	Craig (2004)
Coefficient of gradation	$C_g = {d_{30}}^2/(d_{10} \,.\, d_{60})$	Craig (2004)
Effective size	$E_s = d_{10}$	Craig (2004)
Size relative span	$S_{rs} = (d_{90-}d_{10})/d_{50}$	Allais et al. (2006)
Graphic mean	$G_m = (d_{16} + d_{50} + d_{84})/3$	Folk and Ward (1957)
Inclusive graphic skewness	I_{gs} =$((d_{16} + d_{84} - 2 * d_{50}))$/(2*$(d_{84} - d_{16})$)+ $((d_5 + d_{95} - 2 * d_{50}))$/(2*$(d_{95} - d_5)$)	Folk and Ward (1957)
Inclusive graphic standard deviation	$I_{gsd} = (d_{84-}d_{16})/4 + (d_{95} - d_5)/6.6$	Folk and Ward (1957)
Graphic kurtosis	$G_k = (d_{95}-d_5)/(2.44 * (d_{75} - d_{25}))$	Folk and Ward (1957)

6.2 Fine impact pin mill UPZ100

Impact mills are usually chosen as the types of mills for fine and intermediate grinding. Typical impact mills include high-speed rotating disk, hammer, axial flow and annular. A high-speed rotating disk pin mill generates considerable impact between the particulate solids and pins. The study is based on the UPZ100 pin mill which is a centrifugal impact pin mill from Hosokawa (Figure 6.1).

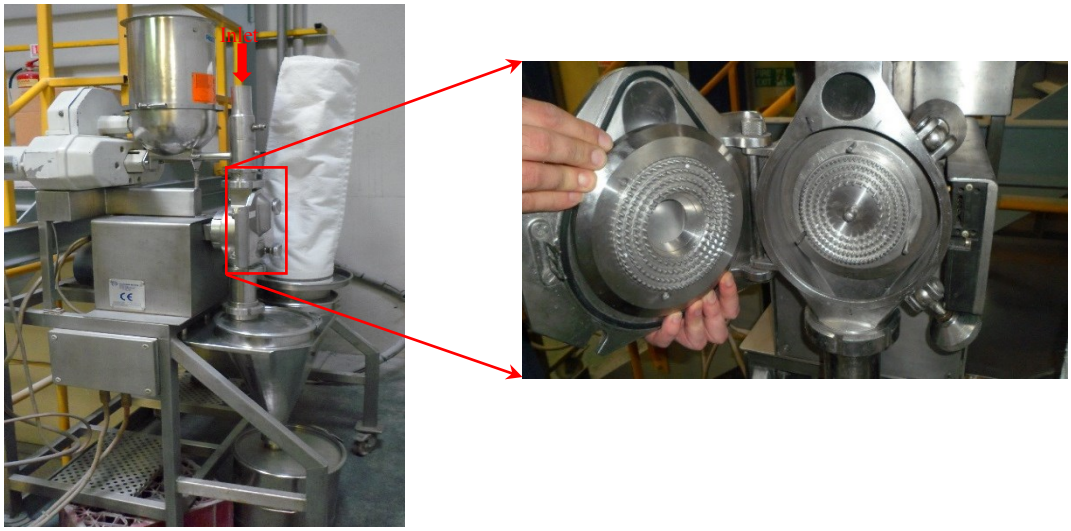

Figure 6.1 Impact pin mill UPZ 100

As can be seen in Figure 6.1, the initial particles are fed to the inlet on the top. Then the feed particles transport to the pin milling region mounted with rotary and stationary discs. The product particles after milling are collected from the bucket at the bottom. For clarity, the sketch of stationary and rotary discs with pin mounted is shown in Figure 6.2.

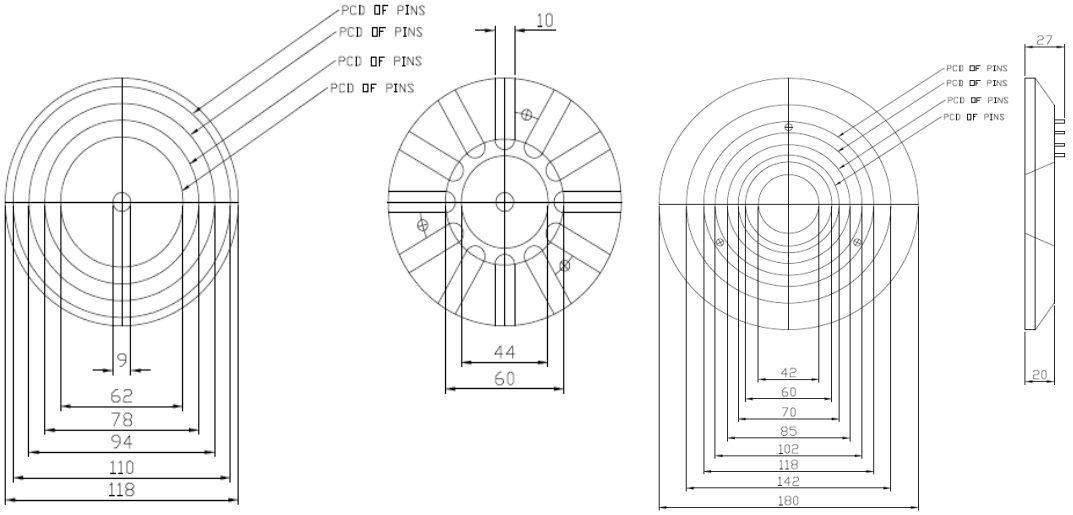

Figure 6.2 Sketch of rotary (left) and stationary (right) discs (unit: cm)

The pin layer in stationary and rotary discs is interlaced. The information of pins layer in rotary and stationary discs is given in Table 6.2 and Table 6.3 respectively.

Table 6.2 Pins layer in rotary discs

Rotary disc	Ring radius (mm)	Pin No.	Pin spacing (mm)	Pin radius (mm)	Net spacing (mm)
R1	31	24	8.11	1.5	5.11
R3	39	40	6.12	1.5	3.12
R5	47	58	5.09	1.5	2.09
R7	55	70	4.93	1.5	1.93

Table 6.3 Pins layer in stationary discs

Stationary disc	Ring radius (mm)	Pin No.	Pin spacing (mm)	Pin radius (mm)	Net spacing (mm)
R2	35	32	6.87	1.5	3.87
R4	43	44	6.14	1.5	3.14
R6	51	54	5.93	1.5	2.93
R8	59	62	5.98	1.5	2.98

It could be seen that the number of pins increases with the increase of ring radius. The radius of pin is the same as 1.5 mm in each layer of disc. The nest spacing (pin spacing minus pin radius) is diminishing outwards for both stationary and rotary discs due to the fact that the size of particle size is reduced radially during the milling operation. However, the pin spacing and net spacing in rotary disc are larger than that in stationary discs because the feed particle first pass through the rotary disc and then the stationary disc in turn.

6.3 Experimental setup

The rotating pin discs at high speed result in particle size reduction due to collision energy input. In the tests herein, a batch of 500 g zeolite particle (1.2-2.0 mm; 2.0-2.5mm) and 500g alumina particle (1.0-1.18 mm) were used for each milling tests.

The rotary speed was varied at 8000, 10000, 12000 and 18000 RPM for both materials. The feed rate was set to 9, 14, 19, 24 kg/h in every rotary speed test. After each milling test, the particle size distribution is analyzed using a Malvern Mastersizer 2000 particle analyzer (Malvern Instruments, UK). The Mastersizer 2000 (Figure 6.3) is based on the technique of laser diffraction to measure the size of product particle. It is achieved by measuring the intensity of light scattered as a laser beam passes through a dispersed particulate sample. This data is analyzed to calculate the size of product size which created the scattering pattern. The packed density of the product particle was measured using Micron Powder Characteristics Tester PT-X (Figure 6.3).

Figure 6.3 Mastersizer 2000 and Micron Powder Characteristics Tester PT-X

6.4 Milling results and discussion

In this section, the milling results are presented to investigate the material grindability in the UPZ100 pin mill. Six parameters are chosen to characterise the grindability because they are widely used and easy to interpret. These include particle size distribution, median particle size, specific surface area, fineness, relative size span, grinding energy, size reduction ratio. The effects of rotary speed and feed rate on these parameters are discussed. The relationship between relevant parameters are discussed as well.

6.4.1 Particle size distribution (PSD)

The goal of impact pin milling is to reduce particle size to a desired specification. As noted in Section 6.1, particle size distribution is an important indicator for the product particle quality and milling performance. Remember that the fundamental size distribution derived by the technique of Mastersizer 2000 is volume based. Figures 6.4,

6.5 and 6.6 present the cumulative particle size distribution of zeolite (1.2-2.0 mm; 2.0-2.5 mm) and alumina (1.0-1.18 mm) under varying rotary speed and feed rate respectively. These figures indicate that the product size are drastically reduced after the impact pin mill as compared to the feed particle size. The product particle size becomes finer with the increase of rotary speed. The product particle size fluctuates with the increase of feed rate. The influence of feed rate is found to be significant at the rotary speed of 10000 RPM whilst the influence of feed rate on the particle size distribution is minimal at the largest rotary speed of 18000 RPM. The majority of finest product size tends to be achieved at the smallest feed rate of 9 kg/h. This implies that a smaller feed rate is more likely to achieve a higher degree of size reduction. For clarity, the characteristic sizes of the product particle d_{10}, d_{50}, d_{80}, d_{90}, d_{99} for zeolite and alumina particle are summarized in Table 6.4. Considering the four options of feed rate and rotary speed for three types of feed particle size, there are 48 runs in total of the impact pin mill tests.

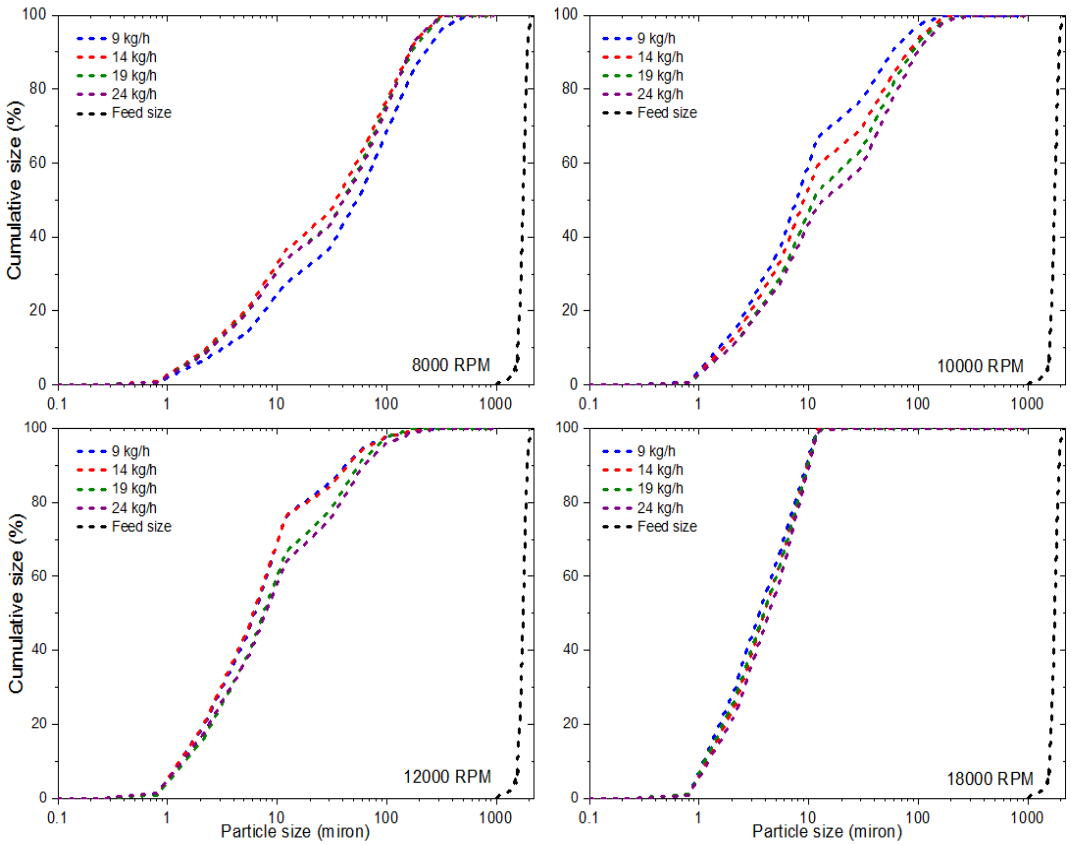

Figure 6.4 Cumulative particle size distribution for zeolite (1.2-2.0 mm)

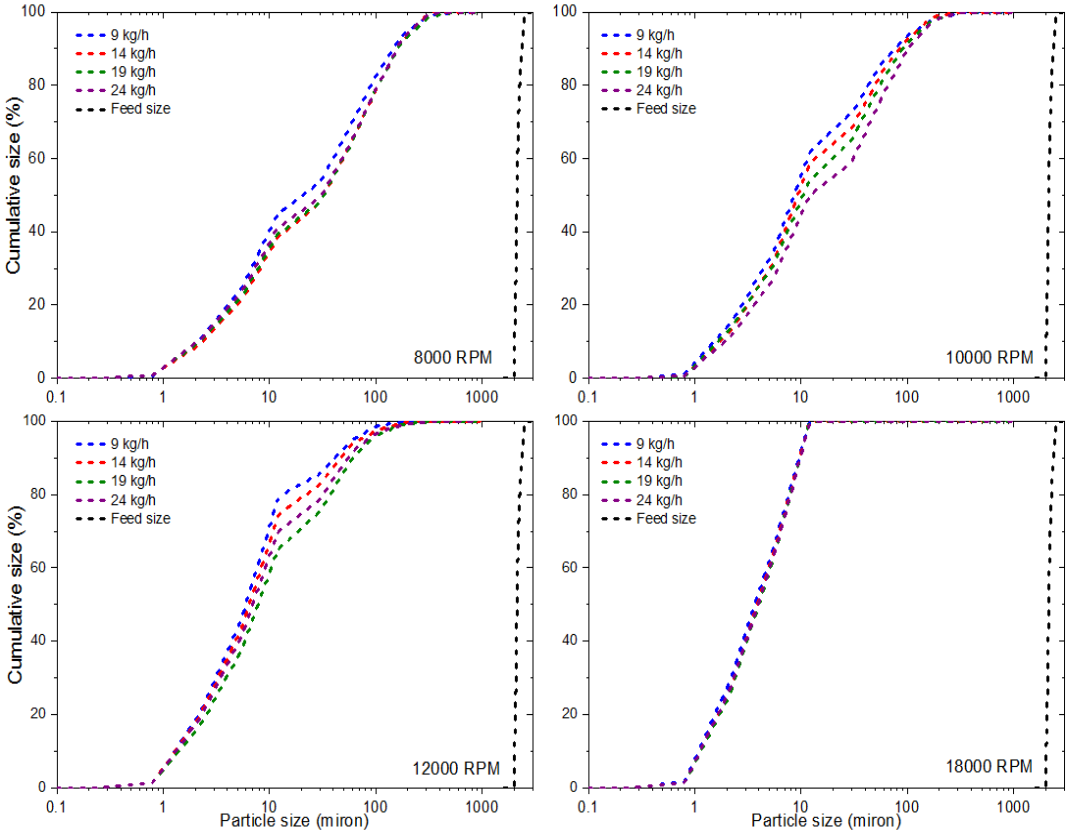

Figure 6.5 Cumulative particle size distribution for zeolite (2.0-2.5 mm)

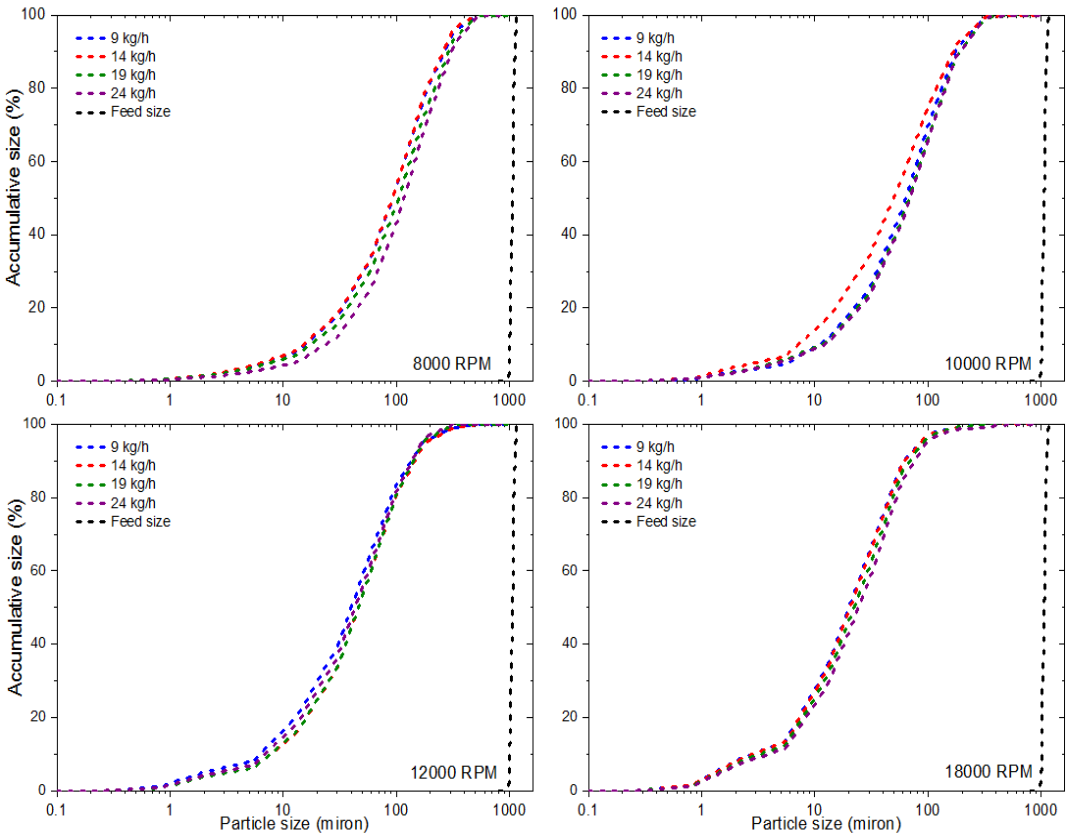

Figure 6.6 Cumulative particle size distribution for alumina (1.0-1.18 mm)

Table 6.4 Characteristic size parameters in PSD

		Particle size distribution of product														
		Zeolite (1.2-2.0 mm)					Zeolite (2.0-2.5 mm)					Alumina (1.0-1.18 mm)				
No.	Rotary speed (RPM)	d_{10} μm	d_{50} μm	d_{80} μm	d_{90} μm	d_{99} μm	d_{10} μm	d_{50} μm	d_{80} μm	d_{90} μm	d_{99} μm	d_{10} μm	d_{50} μm	d_{80} μm	d_{90} μm	d_{99} μm
1	8000	3.50	54.40	145.25	216.50	430.60	2.10	23.60	90.19	143.20	306.40	16.40	93.60	188.10	252.30	409.52
2	8000	2.30	35.50	112.28	161.60	250.00	2.40	33.30	105.60	159.90	276.20	15.90	92.90	185.10	244.90	384.50
3	8000	2.40	41.60	115.90	169.00	285.90	2.20	32.90	104.72	160.00	338.40	19.10	104.50	211.08	280.90	441.40
4	8000	2.50	42.10	118.18	160.70	240.00	2.10	31.20	104.01	156.50	284.10	25.40	117.70	228.65	301.60	474.50
5	10000	1.70	7.30	35.23	57.30	123.80	1.70	8.10	42.85	74.80	221.69	10.80	63.20	128.96	174.60	286.56
6	10000	1.80	8.40	48.56	80.00	153.30	1.80	8.50	49.32	82.70	181.50	7.50	50.30	116.07	163.30	291.60
7	10000	2.00	10.50	55.87	85.70	182.80	1.80	9.70	55.37	89.60	212.10	11.40	68.00	138.32	186.80	306.80
8	10000	2.00	13.90	64.07	95.80	191.60	1.98	12.10	65.21	100.70	213.70	12.20	69.40	139.34	187.40	305.72
9	12000	1.50	6.20	18.72	41.30	159.00	1.50	6.00	13.29	40.40	108.60	6.60	40.60	88.89	127.30	308.70
10	12000	1.52	6.00	20.89	43.50	149.20	1.50	6.30	24.39	45.30	145.00	8.10	47.10	97.99	137.60	301.70
11	12000	1.70	7.20	33.93	55.10	122.50	1.60	7.40	37.34	60.60	167.70	8.10	47.00	97.48	135.00	240.20
12	12000	1.60	7.50	37.89	61.40	180.40	1.50	6.80	31.97	54.20	172.70	7.30	44.10	94.42	130.40	220.60
13	18000	1.30	3.50	7.01	8.40	10.90	1.27	3.80	7.04	8.40	10.70	3.10	20.90	43.56	60.40	158.10
14	18000	1.40	4.10	7.31	8.70	11.40	1.33	4.10	7.21	8.60	11.10	3.30	21.30	44.15	61.10	168.70
15	18000	1.36	4.00	7.42	8.90	11.90	1.36	4.23	7.34	8.70	11.30	4.10	23.20	47.89	66.00	158.90
16	18000	1.50	4.50	7.75	9.20	12.30	1.32	4.15	7.37	8.80	11.70	4.70	25.20	51.72	71.60	270.30

6.4.2 Fineness

The fineness of product in a milling operation may be expressed with a reference value d_{90}, which characterize the product quality of a batch milling. d_{90} refers to the product particle size at 90% of the cumulative PSD. The fineness of zeolite (1.2-2.0 mm; 2.0-2.5 mm) and alumina (1.0-1.18 mm) has been summarized in Table 6.4. The effect of rotary speed and feed rate on the milling fineness is shown in Figures 6.7, 6.8 and 6.9 for three sizes particle respectively. These figures demonstrate that the fineness of product particle increase as the rotary speed is increased. The minimum fineness for three product particle is achieved at the highest rotary speed (18000 RPM) and the lowest feed rate (9 kg/h). The minimum fineness for product zeolite (1.2-2.0 mm), zeolite (2.0-2.5 mm) and alumina (1.0-1.18 mm) is 8.4 microns, 8.4 microns and 60.4 microns respectively. However, the feed rate has different effects on the three sizes particle. With regard to zeolite (1.2-2.0 mm) in Figure 6.7, the fineness of product particle increases alongside the increase of feed rate except for under 8000 RPM. Under rotary speed of 8000 RPM, the fineness of product particle decreases from 216.5 microns to 161.6 microns as the feed rate is increased from 9 kg/h to 14 kg/h. Then the fineness of product particle increases to 169 microns under 19 kg/h before decreasing to 160.7 microns under 24 kg/h.

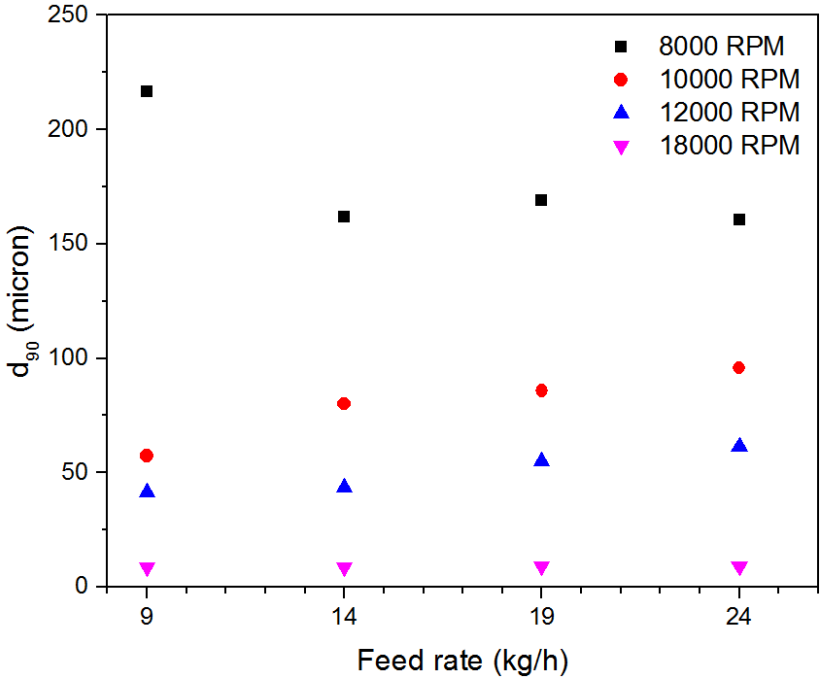

Figure 6.7 The fineness d_{90} of zeolite (1.2-2.0 mm) under varying rotary speed and feed rate

As can be seen from Figure 6.8, the fineness of product particle (2.0-2.5 mm) increases with the growth of feed rate under rotary speed of 10000 and 18000 RPM. However, the fineness of product particle (2.0-2.5 mm) increases gradually from 9 kg/h to 19 kg/h under 8000 and 12000 RPM. Then the fineness of product particle (2.0-2.5 mm) decreases slightly from 19 kg/h to 24 kg/h.

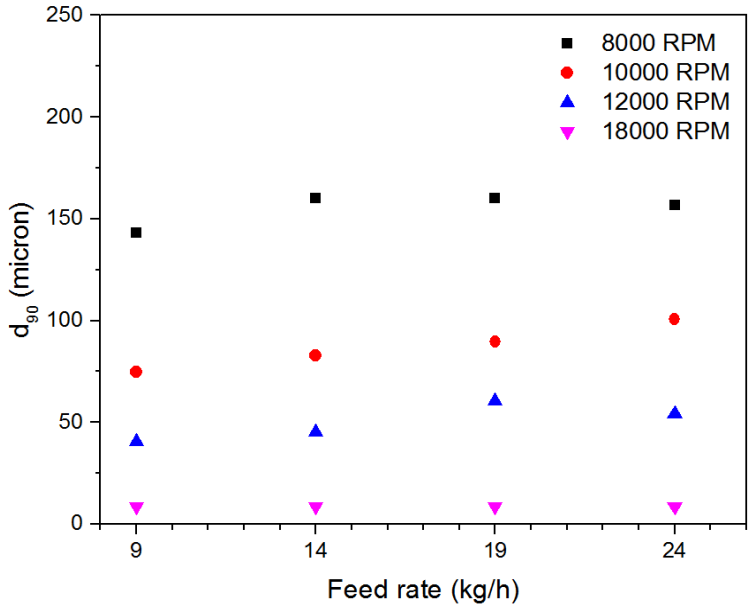

Figure 6.8 The fineness d_{90} of zeolite (2.0-2.5 mm) under varying rotary speed and feed rate

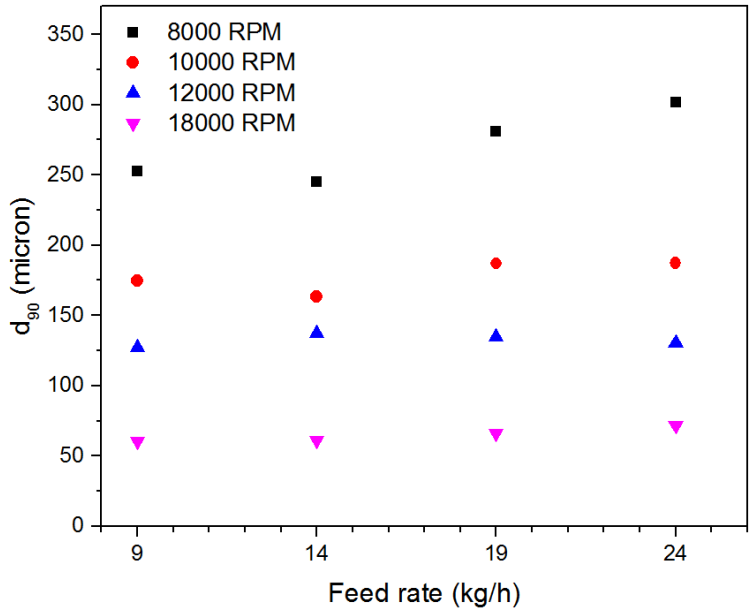

Figure 6.9 The fineness d_{90} of alumina (1.0-1.18 mm) under varying rotary speed and feed rate

In terms of alumina (1.0-1.18 mm), Figure 6.9 illustrates that the feed rate has the same effect on the fineness of product particle (1.0-1.18 mm) under 8000 and 10000 RPM. The fineness of product particle (1.0-1.18 mm) decreases slightly from 9 kg/h to 14 kg/h and then gradually increases until 24 kg/h. The fineness of product particle (1.0-1.18 mm) fluctuates with the feed rate under 12000 RPM whilst the fineness of product particle (1.0-1.18 mm) increases with the growth of feed rate under 18000 RPM.

6.4.3 Median product size

The median size of milled particle samples for both materials were analysed using Mastercurve 2000 particle analyser after each milling. In order to quantify the milling performance and the milling effect at different milling conditions, the median particle diameter d_{50} from the particle size distribution of zeolite particle (1.2-2.0 mm; 2.0-2.5 mm) and alumina particle (1.0-1.18 mm) is depicted in Figure 6.10.

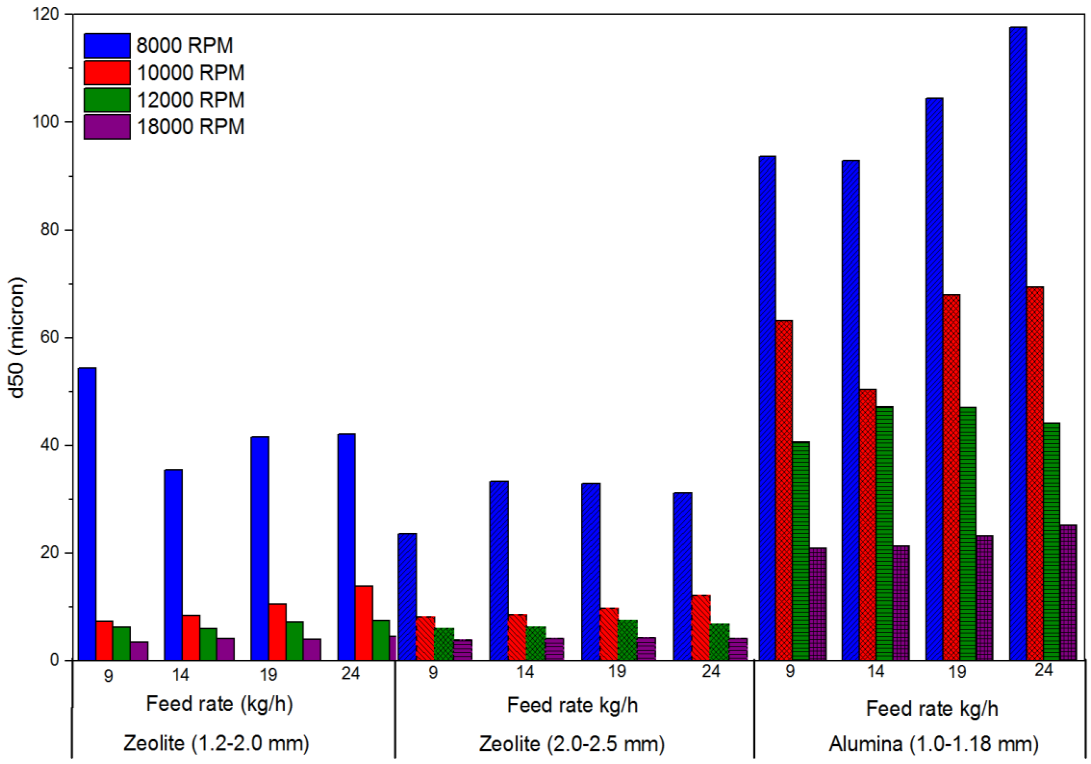

Figure 6.10 Median size d_{50} of milled particles

As observed from Figure 6.10, the median size (d_{50}) decreases along with increasing rotary speed of disc at the same feed rate. Median size decreases sharply with the increase of rotary speed from 8000 RPM to 10000 RPM and thereafter decreases more

gradually with the increase of rotary speed until 18000 RPM. As for two feed sizes of zeolite, feed rate appears to have a big influence in the median size at the low rotary speed (8000 RPM). However, the effect of feed rate becomes less apparent at higher rotary speed.

The median size spans from 3.5 microns to 54.4 microns for zeolite 1.2-2.0 mm; the median size spans from 3.8 microns to 33.3 microns for zeolite 2.0-2.5 mm; the median size spans from 20.9 microns to 117.7 microns for alumina 1.0-1.18 mm. The median size variation indicates that alumina is harder to grind than zeolite.

6.4.4 Relative size span

The relative size span, an indicator of particle size distribution, is used to indicate the breadth of distribution. This is given by:

$$span = \frac{d_{90} - d_{10}}{d_{50}} \tag{6.1}$$

where d_{10}, d_{50} and d_{90} represent the sieve size below which 10%, 50% and 90% of the ground particles reside. The relative size spans of both materials are depicted in Figure 6.11 corresponding to the different operational conditions.

It shows that zeolite has a larger size span than alumina under the rotary speed of 8000, 10000 and 12000 RPM although the median size of zeolite is smaller than that of alumina. However, the size span of zeolite is smaller than that of alumina when the rotary speed is set to 18000 RPM. It is interesting to note that the smallest size span for zeolite is obtained at the rotary speed of 18000 RPM whilst the smallest size span for alumina is achieved at the rotary speed of 8000 RPM under the same feed rate.

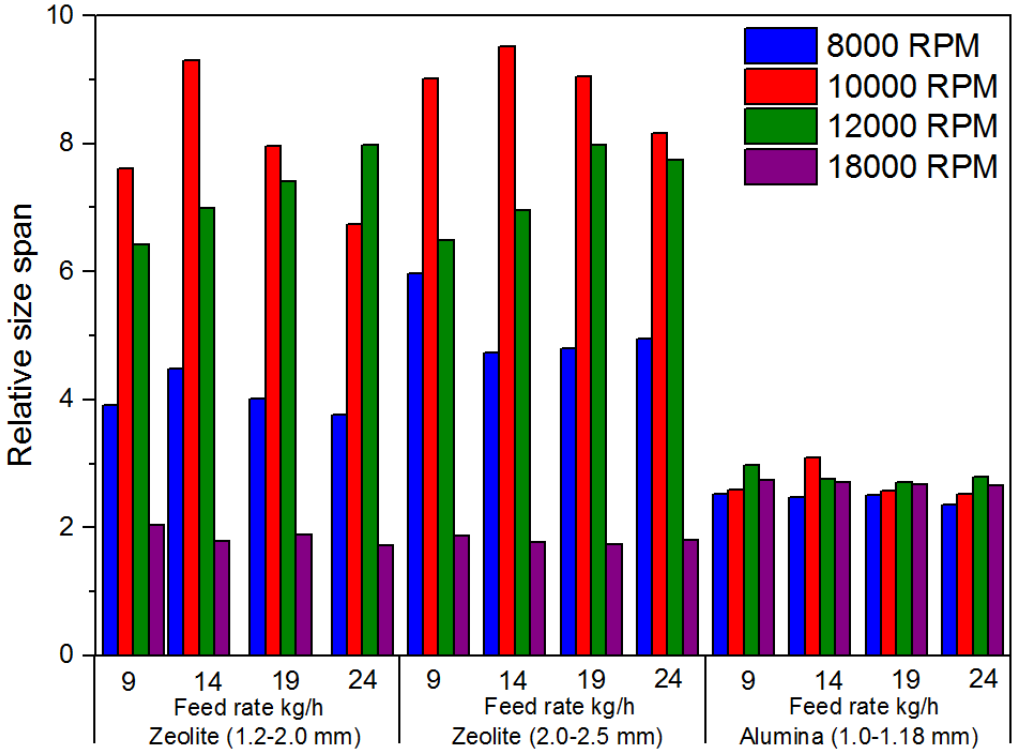

Figure 6.11 Relative size span of milled materials

6.4.5 Comminution energy based on size reduction

The literature review in Chapter 2 has shown that grinding energy consumption could be expressed by three classical laws, namely Rittinger's law, Kick's law and Bond's law. Rittinger's law (1867) assumes that grinding energy is proportional to the newly generated surface area. Kick's law (1885) relates the grinding energy to the sizes of the feed particles and the product particles. Later work by Bond (1952) proposed an equation assuming that the grinding energy is inversely proportional to the square root of the diameter of the product particles. Note that the nominal size of the product particles in Bond's law refers to 80% passing size of the product particles. Considering the applicability of the three laws, Kick's law is considered valid for coarse milling; Bond's law and Rittinger's law are considered valid for intermediate and fine grinding milling respectively. However, Austin (1973) pointed out that Bond's law and Rittinger's law may be applied to the same set of grinding data. Bond's law is adopted herein for the calculation of grinding energy due to its widespread use in most industrial grinding circuits. Thus, the Bond's law is given below:

$$W = 10W_i\left(\frac{1}{\sqrt{x_P}} - \frac{1}{\sqrt{x_F}}\right) \tag{6.2}$$

where W (kWh/t) is the grinding energy per tonne; x_P (micron) and x_F (micron) are the particle size at which 80% of the product and feed particle pass through the sieve respectively. W_i (kWh/t) is known as Bond's work index which can be expressed as

$$W_i = \frac{48.95}{{P_1}^{0.23} G^{0.82} (\frac{10}{\sqrt{x_P}} - \frac{10}{\sqrt{x_F}})} \tag{6.3}$$

where P_1 is the sieve opening for grindability test; G is the mill grindability. The Bond's work index expresses the resistance of a material to a milling operation, which has been widely used to estimate the energy required for many milling operations. The higher value of the Bond's work index indicates a larger difficulty to grind the particle. The Bond's work index is typically determined from a ball milling test. A detailed process to measure the Bond's work index could be found in Ipek and Goktepe (2011). It should be noted that the objective of this chapter is not to determine the Bond's work index from a standard procedure. Instead, the purpose is to estimate the grinding energy required for a given material with a specific grinding size. The Bond's work indexes for zeolite and alumina are adopted as 10.48 kWh/t and 17.90 kWh/t respectively based on Ipek and Goktepe (2011) and the practical guide of mineral processing engineering. The value of Bond's work index indicates that alumina is more difficult to break as compared to zeolite, which is in line with the message from Figure 6.10. The grinding energy in Eq. (6.2) could be obtained with the nominal size of feed particle and product particle in conjunction with the value of Bond's work index.

Figures 6.12-6.14 shows the grinding energy required for zeolite and alumina under varying feed rate and rotary speed respectively. It is found that the grinding energy increases with the increase of rotary speed at a given feed rate. For example, in Figure 6.12, the grinding energy of zeolite (1.2-2.0 mm) at 18000 RPM is seven times the grinding energy at 8000 RPM. However, the effect of feed rate on grinding energy is more complicated. Figures 6.12 shows that the grinding energy of zeolite (1.2-2.0 mm) decreases with the increase of feed rate under the rotary speed of 10000, 12000 and

18000 RPM. The variation of specific surface area under different feed rates and rotary speeds is plotted in Section 6.4.7 and the combined plot of specific surface area divided by the grinding energy is given in Appendix D.

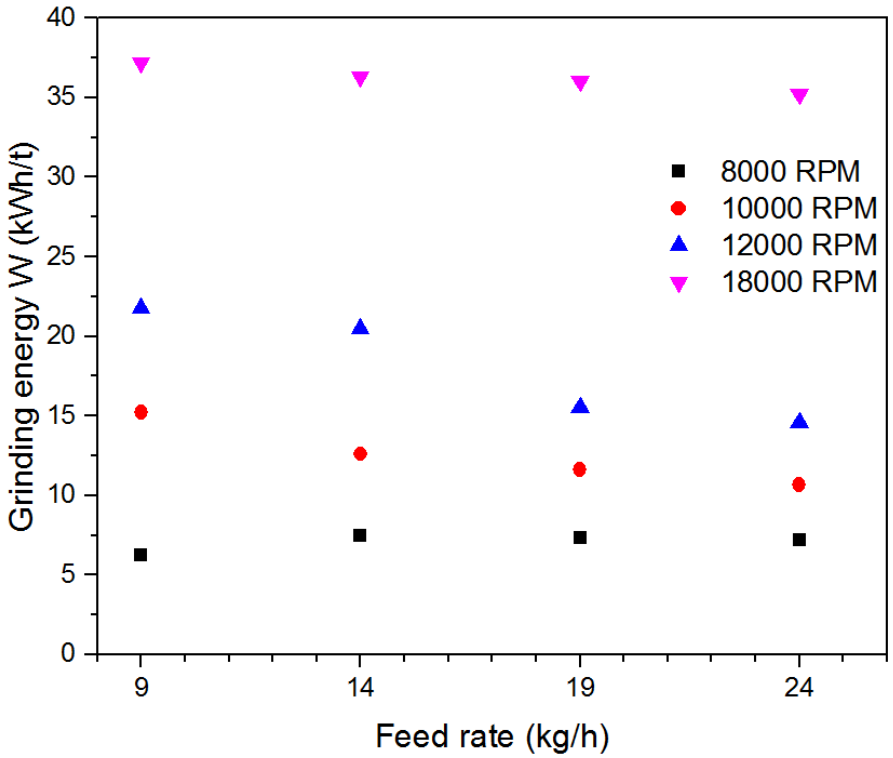

Figure 6.12 Estimated grinding energy of zeolite particle (1.2-2.0 mm) based on Bond's law

Figure 6.13 demonstrates that the grinding energy of zeolite (2.0-2.5 mm) is more sensitive to feed rate under the rotary speed of 12000 RPM as compared to another three rotary speeds. As shown in Figure 6.14, the grinding energy of alumina (1.0-1.18 mm) increases with the growth of rotary speed and the influence of feed rate is less effective than that of rotary speed. It should also be noted that the grinding energy of zeolite (1.2-2.0 mm; 2.0-2.5 mm) is much higher than that of alumina (1.0-1.18 mm) although alumina has more resistance to breakage as compared to zeolite. This is because the zeolite undergoes a much greater size reduction than the alumina, which is analysed in the following section.

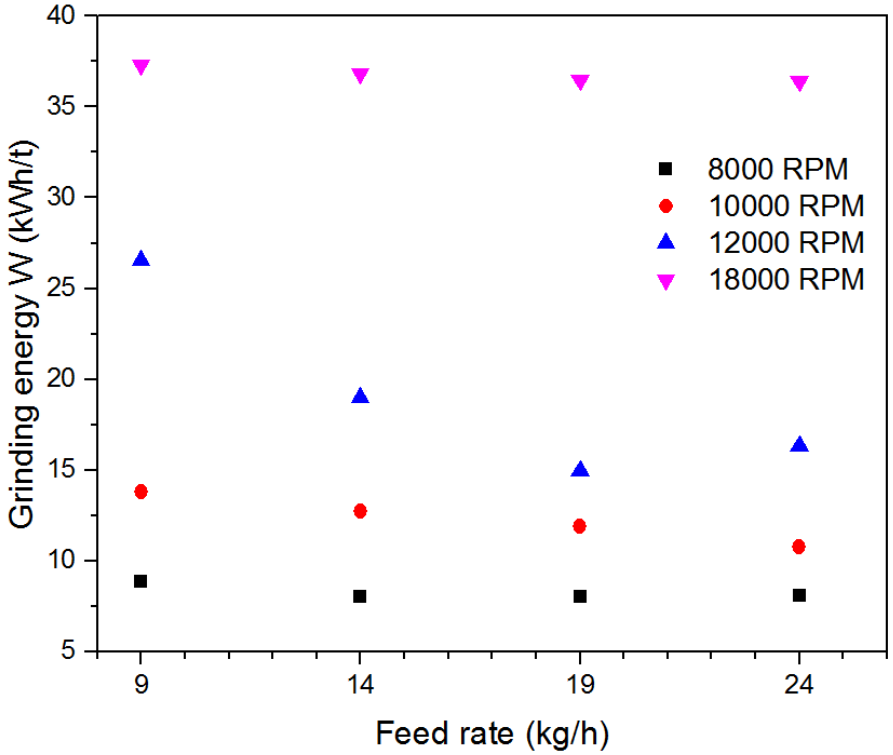

Figure 6.13 Estimated grinding energy of zeolite particle (2.0-2.5 mm) based on Bond's law

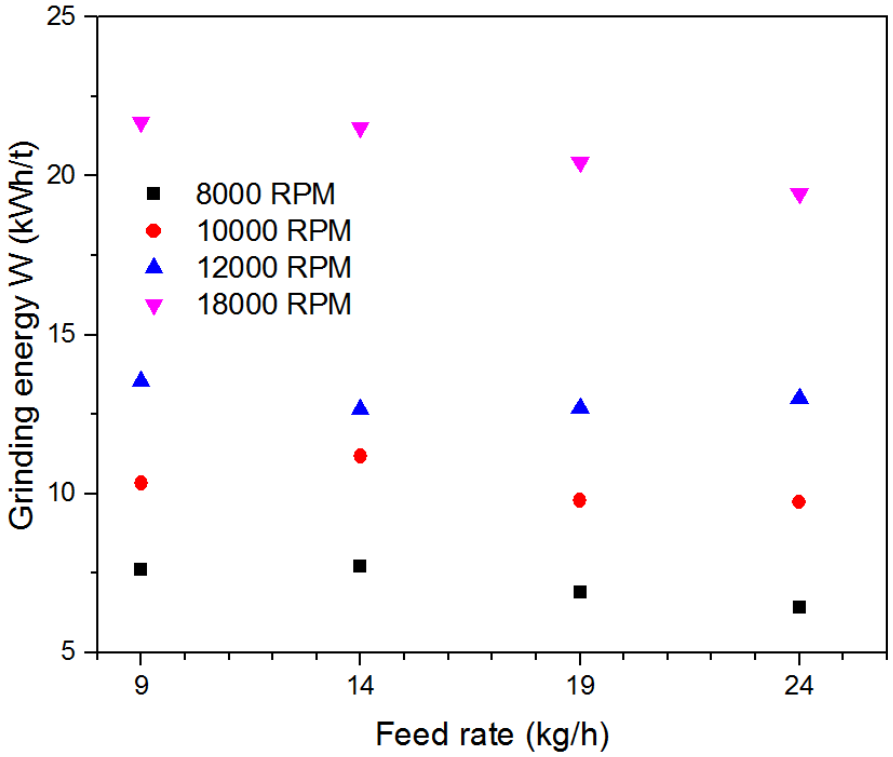

Figure 6.14 Estimated grinding energy of alumina particle (1.0-1.18 mm) based on Bond's law

6.4.6 Size reduction ratio

In order to quantify the extent of milling, a size reduction ratio (*SRR*) was introduced by Verheezen et al. (2004) as follows:

$$SRR = D_{50,F}/D_{50,P} \tag{6.4}$$

where $D_{50,F}$ is the median size of feed particle before milling and $D_{50,P}$ is the median of product particle after milling.

Figures 6.15, 6.16 and 6.17 give the degree of milling for zeolite (1.2-2.0 mm; 2.0-2.5 mm) and alumina (1.0-1.18 mm) under varying rotary speed and feed rate. The results show a significant increase of size reduction ratio when the rotary speed is increased from 8000 RPM to 18000 RPM. For example, the size reduction ratio of zeolite (1.2-2.0 mm) is increased from 32.3 at 8000 RPM to 502.4 at 18000 RPM under feed rate of 9 kg/h. The zeolite (2.0-2.5 mm) has the largest size reduction ratio with the minimum size reduction ratio for alumina (1.0-1.18 mm) under the same milling condition. In contrast to the rotary speed, feed rate is less influential on the size reduction ratio. The difference of size reduction ratio in the four feed rates is not very significant although some fluctuations are observed under the same rotary speed. The effect of feed rate is increasingly pronounced when the rotary speed is increased. The results show that the size reduction ratio is generally larger at smaller feed rate.

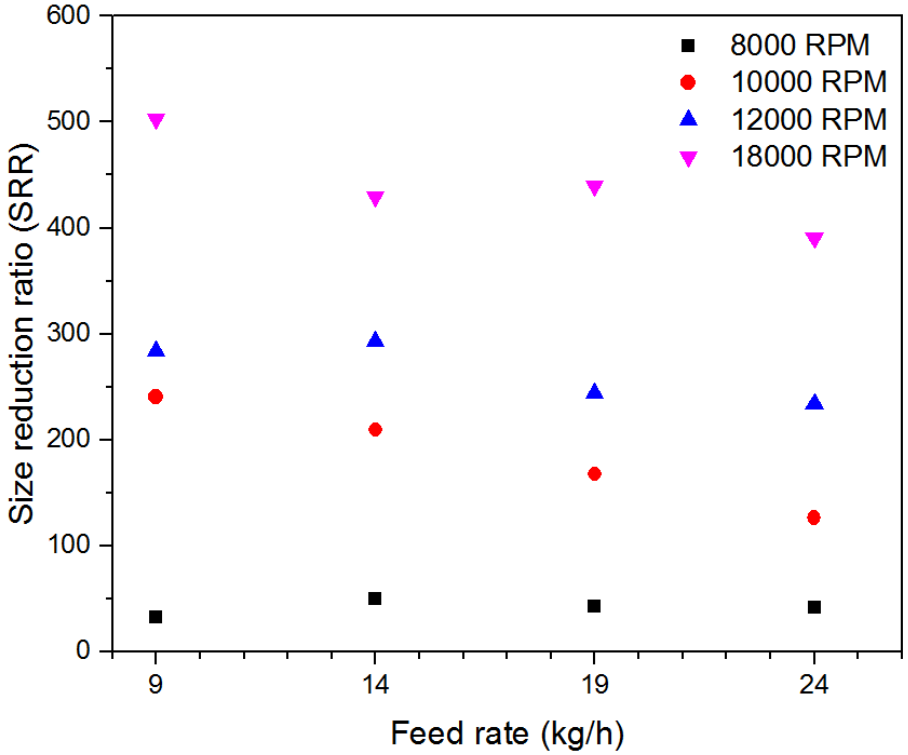

Figure 6.15 Size reduction ratio of zeolite (1.2-2.0 mm) in impact pin mill under varying rotary speed and feed rate

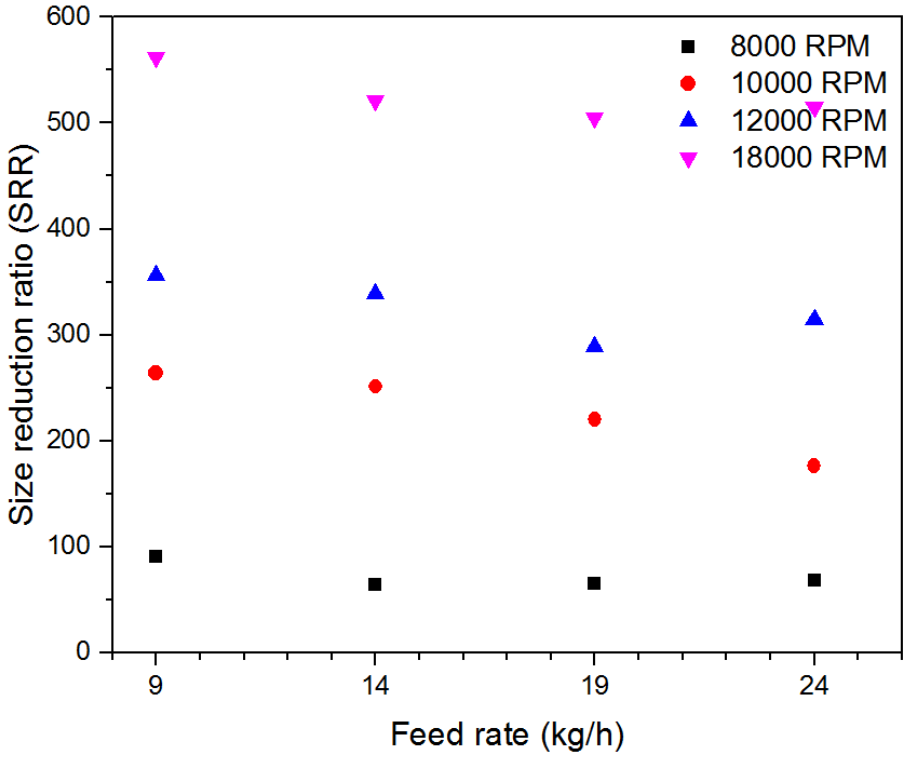

Figure 6.16 Size reduction ratio of zeolite (2.0-2.5 mm) in impact pin mill under varying rotary speed and feed rate

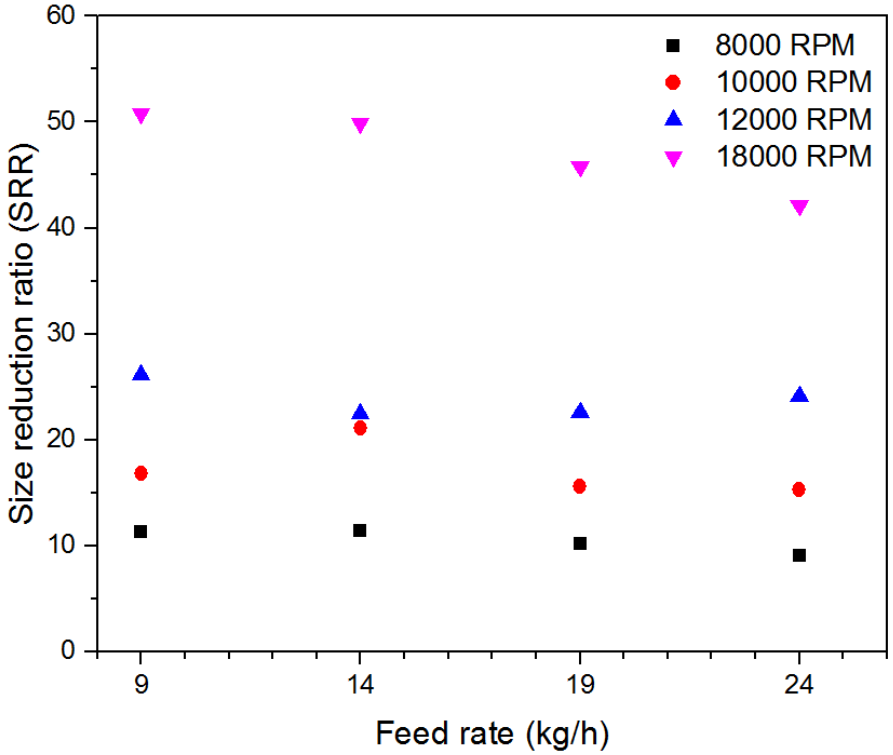

Figure 6.17 Size reduction ratio of alumina (1.0-1.18 mm) in impact pin mill under varying rotary speed and feed rate

It would be interesting to take a look at the relationship between the grinding energy and size reduction ratio. Figure 6.18 presents the energy requirement of grinding as a function of size reduction ratio. It is noted that alumina requires much more grinding energy input than zeolite for the purpose of same degree of size reduction. This is due to the fact that alumina has larger fracture toughness and thereby has more resistance to breakage. Larger zeolite particle appears to need slightly less grinding energy than the smaller zeolite particle. The reason for this is unclear.

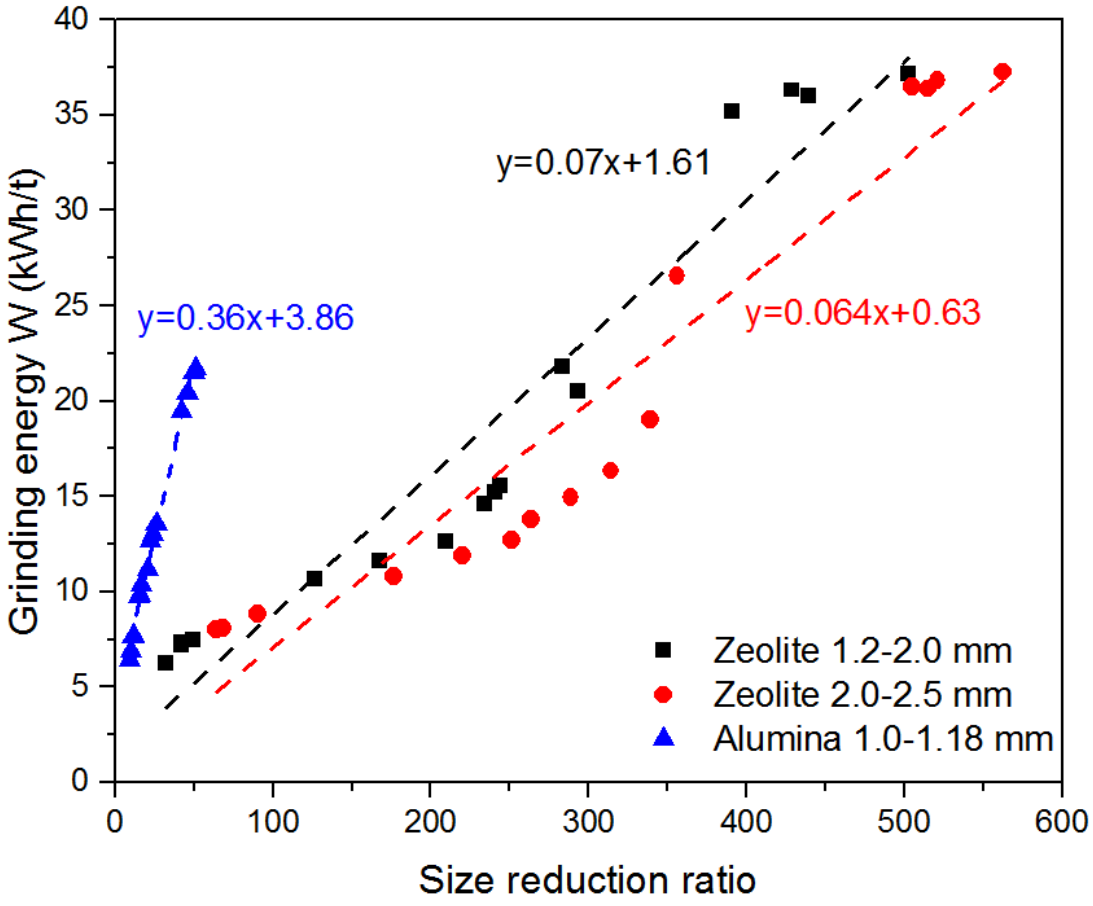

Figure 6.18 Grinding energy as a function of size reduction ratio

Curve fitting in Figure 6.18 indicates that the grinding energy approximately follows a linear relationship with the size reduction ratio, which agrees well with the previous results (Shashidhar et al., 2013). This reveals that a finer size reduction of material requires more energy input. Effective specific energy consumption (ratio of energy consumption to size reduction ratio) is found to be 0.07, 0.064 and 0.36 kWh/t for zeolite (1.2-2.0 mm; 2.0-2.5 mm) and alumina (1.0-1.18) respectively.

6.4.7 Specific surface area

Specific surface area (SSA) is defined as the total area of the product particles divided by the total weight. The specific surface area of the product particle is calculated based on the particle size distribution via laser diffraction using Mastersizer 2000 and density. The particle size is determined by converting the weight of particle into the weight of sphere based on the equivalent sphere theory. Figures 6.19-6.21 demonstrate the specific surface area of zeolite (1.2-2.0; 2.0-2.5 mm) and alumina (1.0-1.18 mm) under varying rotary speed and feed rate respectively.

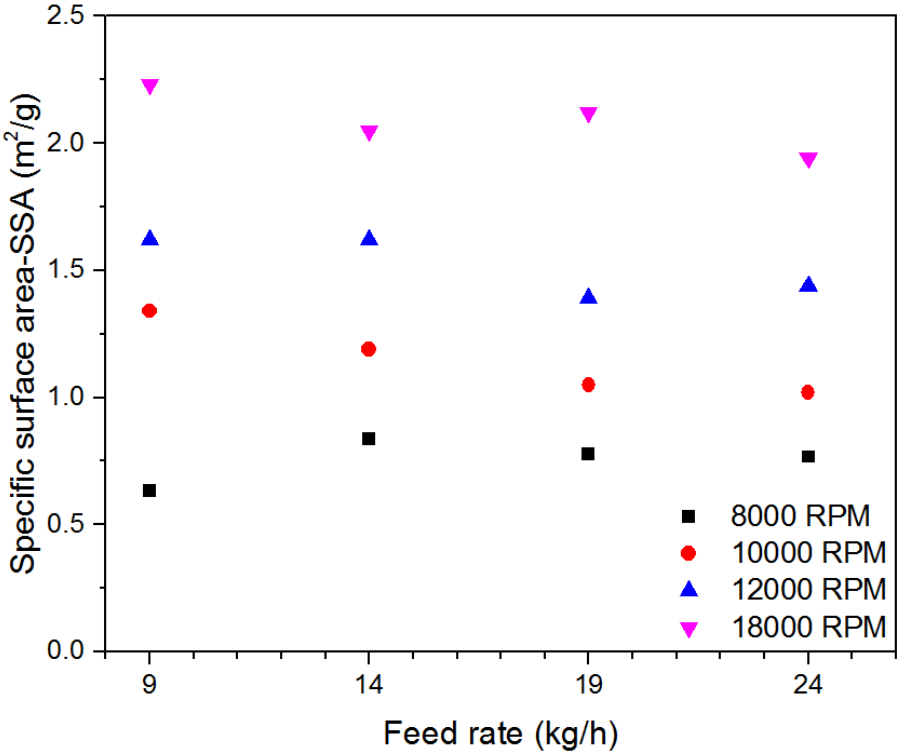

Figure 6.19 Specific surface area of zeolite particles (1.2-2.0 mm) in impact pin mill under varying rotary speed and feed rate

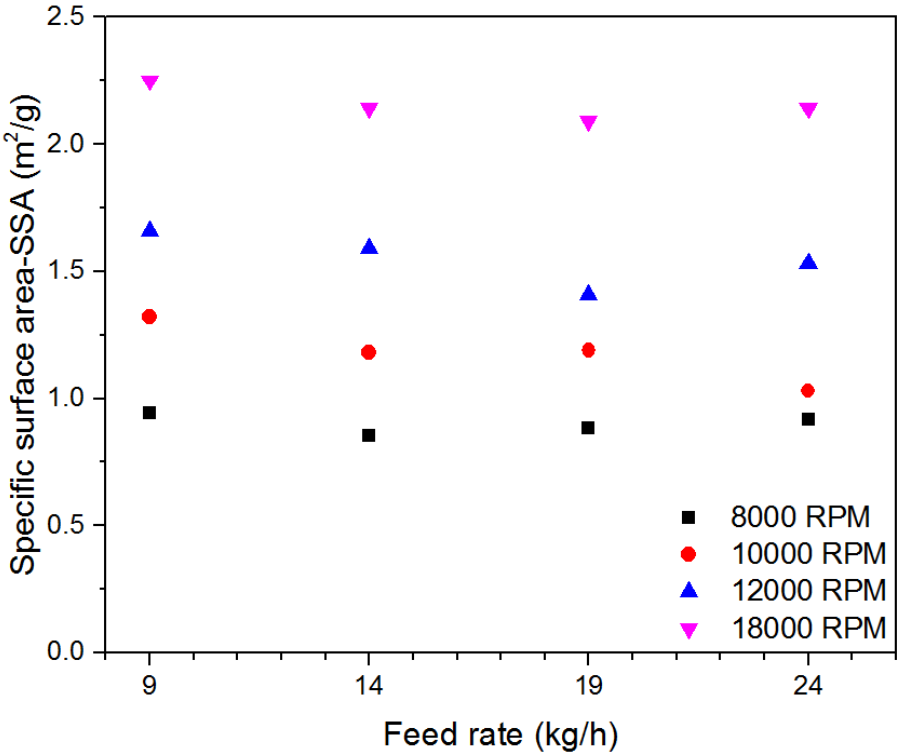

Figure 6.20 Specific surface area of zeolite particles (2.0-2.5 mm) in impact pin mill under varying rotary speed and feed rate

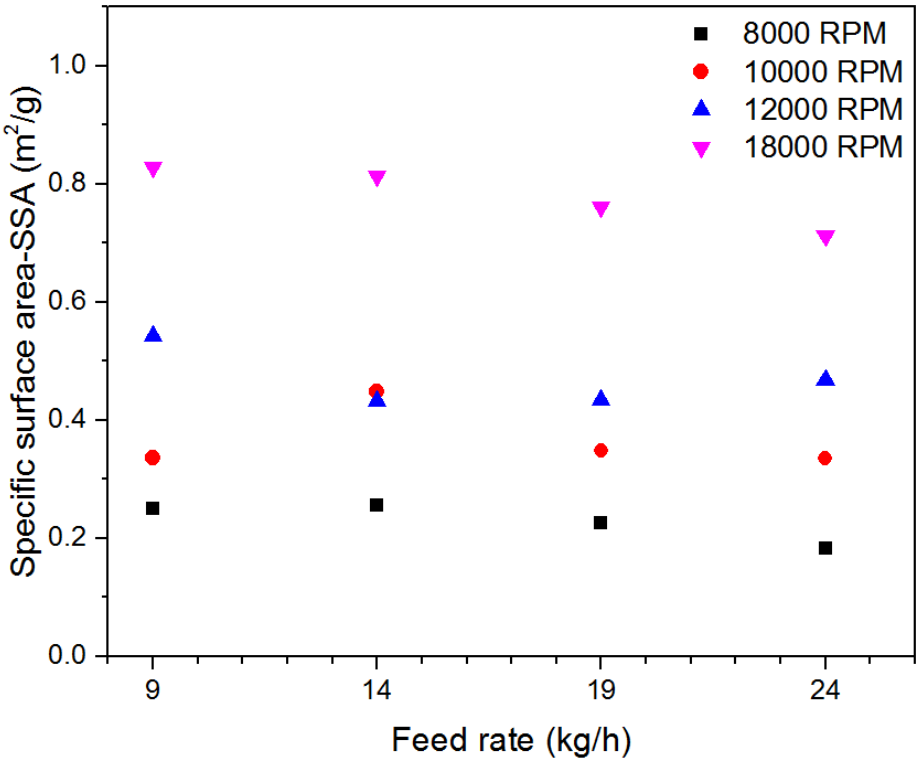

Figure 6.21 Specific surface area of zeolite particles (1.0-1.18 mm) in impact pin mill under varying rotary speed and feed rate

As seen from Figures 6.19, 6.20 and 6.21, the specific surface area of product particle increases with the increase of rotary speed. The specific surface area of product particle fluctuates with the increase of feed rate. However, the specific surface area of product particle tends to be larger at smaller feed rate in most cases, which suggests a finer size of product particle. A closer look at the relationship between the fine product size (d_{10}) and specific surface area is presented in Figure 6.22. As expected, the specific surface area increases with the decrease of d_{10} of product particle. The specific surface area of alumina (1.0-1.18 mm) is smaller than that of zeolite (1.2-2.0 mm; 2.0- 2.5 mm) for the same median size of product particle.

The specific surface area is found to follow a power law with the median size of product size. Particularly, the specific surface area of 1.2-2.0 mm and 2.0-2.5 mm zeolite appears to follow the same power fitting although the specific surface area of 2.0-2.5 mm product particle is relatively large.

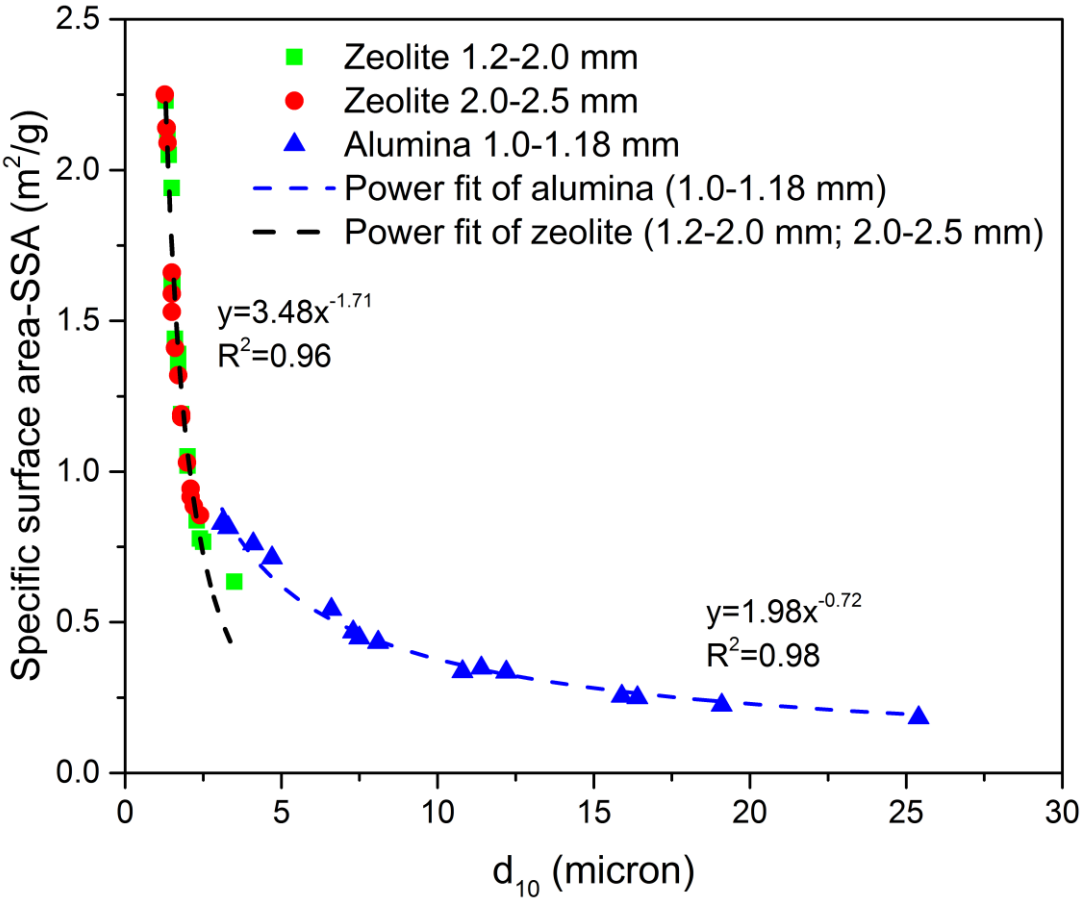

Figure 6.22 Specific surface area as a function of d_{10}

6.5 Summary

Impact pin mill test was carried out to study particle breakage through an impact pin mill UPZ 100. Two types of particles, zeolite (1.2-2.0 mm; 2.0-2.5 mm) and alumina (1.0-1.18 mm) are chosen under impact pin milling operation. The rotary speed was varied at 8000, 10000, 12000 and 18000 RPM whilst the feed rate was varied at 9, 14, 19, 24 kg/h in every rotary speed test.

The effect of rotary speed and feed rate on the milling performance was analyzed. It was found that the rotary speed is more influential on the product particle size distribution than the feed rate. Considering the popularity and ease of interpretation, six parameters, namely fineness, median product size, relative size span, bond's grinding energy, size reduction ratio and specific surface area are selected to characterize the milling results. It shows that the minimum median particle size and fineness of product are achieved at the highest rotary speed 18000 RPM and the lowest feed rate 9 kg/h. The smallest relative size span for zeolite (1.2-2.0 mm and 2.0-2.5 mm) is obtained at

the rotary speed 18000 RPM whilst the smallest relative size span for alumina (1.0-1.18 mm) is obtained at the rotary speed 8000 RPM. The energy consumption for grinding was studied based on Bond's energy law. It was observed that the grinding energy follows approximately a linear relationship with the size reduction ratio. The alumina particle needs more grinding energy as compared to the zeolite particle. The specific surface area was observed to follow a power law with the median size of product size.

The impact milling tests through an impact pin mill shed more insights into the evaluation of milling performance. The collective data presented via impact pin mill provides the basis for the validation of numerical simulation.

Chapter 7

Bonded DEM modelling of particle impact breakage

7.1 Introduction

The Discrete Element Method (DEM) was initially proposed by Cundall (1971) to describe the mechanical behaviour of granular assemblies (Cundall and Strack, 1979). Since its inception, this method has gained increasing popularity to model granular mechanics problems and is extensively used in engineering disciplines involving particulate materials. The application of DEM to particle breakage has been reviewed in Chapter 2. The interactions between the constituent particles are based on contact mechanics. As noted by Moreno et al. (2003) in terms of impact breakage through DEM, for the case without adhesion, the contact behaviour is based on Hertz analysis and Mindlin and Deresiewicz model (1953) for the normal and tangential forces respectively. For the case with adhesion, the model of Johnson et al. (1971) is used for the normal contact while the tangential contact is provided by the models of Thornton and Yin (1991). In this work, the constituent particles are modelled by a new bonded contact model proposed by Brown et al. (2014). A brief review of several bonded contact models is given below.

Numerous bonded contact models have been developed in the context of DEM. Potyondy and Cundall (2004) proposed a bonded particle model for rock where particles are connected by a point of glue with constant normal and shear stiffness acting at a point (Cho et al., 2007). A more complex parallel bond model (Potyondy and Cundall, 2004) was developed which approximates the physical behaviour of a cement-like substance joining the two particles. The bonded contacts in the parallel bond model can be envisaged as a set of elastic springs uniformly distributed over a rectangular cross section with a constant normal and shear bond stiffness lying on the contact plane and centered at the contact point (Cho et al., 2007). A feature of the parallel bond is the ability to transmit moments in addition to normal and shear forces. Ergenzinger et al. (2011) proposed a bonded contact model which connects the centres of neighbouring particles using a spring model. This model was used to investigate the progressive failure of strong rock under uniaxial compression. The bonded model is able to resist

relative displacement due to compression and tension. However, the ability to resist shear, bending or twisting actions is lacking. Recently, Brown et al. (2014) proposed a new bonded contact model based on Timoshenko beam theory which considers axial, shear and bending behaviour of the bond.

The major objective of this chapter is to investigate the breakage behaviour of individual particles subjected to normal impact loading through a bonded contact model (Brown 2013, Brown et al., 2014). A novel bonded contact model based on Timoshenko beam theory considering axial, shear and bending behaviour was utilized. The breakage behaviours of chipping and fragmentation are investigated under varying impact velocities. Section 7.2 describes the bonded contact model in details whilst Section 7.3 introduces the Hertz-Mindlin contact law for non-bonded contacts. Section 7.4 describes the implementation of bonded contact model including the initial particle formation and selection of model input parameters. The breakage results of particles subjected to normal impact loading are presented in Section 7.5. Five factors are chosen to characterise the impact breakage: breakage pattern, contact force, contact evolution, failure mode and damage ratio. The numerical results from bonded DEM are validated against the single zeolite particle impact test in Chapter 3 and the disparity between the numerical and experimental results is discussed when the same breakage criterion is applied to both the physical experiment and the DEM simulation. Section 7.6 conducts a parametric study of the relatively influential model parameters in the bonded contact model.

7.2 Timoshenko beam bond model (TBBM)

A novel bonded contact model based on Timoshenko beam theory, which will be referred to as the Timoshenko Beam Bond Model (TBBM), has been developed by Brown et al. (2014) to study both cementitious granular materials and deformable structures. The cementitious material is represented by an assembly of bonded DEM particles. Because of their spherical nature, only one contact is allowed between any two particles. Apart from resisting compressive and shear forces, the bonded contacts can resist tensile forces as well bending and twisting moments. Material damage may be represented by the breakage of bonds, which enables detailed investigation of the progressive damage of a material subjected to load. The description of this bonded

contact model is briefly given below. More details about TBBM have been given elsewhere (Brown, 2013; Brown et al., 2014).

7.2.1 Bonded contact model description

For a bonded contact, a beam element is assumed to rigidly connect the two particles and each bond element is assumed to be circular and straight in three-dimensional space in terms of formation. The behaviour of the bond is assumed to follow Timoshenko beam theory (Timoshenko 1922). It is assumed that the beam element connects the centres of the two particles (Figure 7.1) and thus each end of the bond shares the same six degrees of freedom as the particle.

As shown in Figure 7.1, the centres of particles A and B are connected by a single bond with two end points α and β. L_b and r_b denote the length and radius of the bond, respectively. The positions of the two particles are denoted by vectors $\{P_A\}$ and $\{P_B\}$ in the global Cartesian coordinate system (X, Y, Z).

$$\{P_i\} = \{X_i\ Y_i\ Z_i\}\ i = A, B \tag{7.1}$$

The length of the bond is given:

$$L_b = \|P_A - P_B\| = \chi_\beta - \chi_\alpha \tag{7.2}$$

where χ_α and χ_β are the x-coordinates of the two ends of the beam in the local coordinate system.

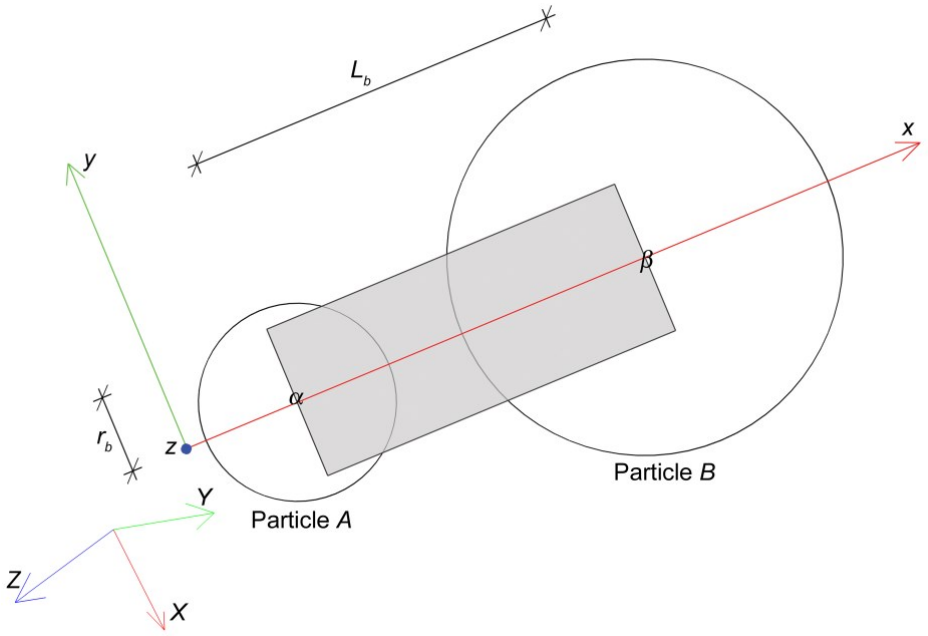

Figure 7.1 Projected view through the central axis of a bond connecting particles A and B (Adapted from Brown et al. 2014)

Timoshenko beam theory is used to relate the internal forces and moments to the particle displacements and rotations. The increments of the internal forces and moments in each time step are determined from the incremental displacements and rotations at the bond ends using Timoshenko beam theory. This gives:

$$\{\Delta F\} = [K] \cdot \{\Delta u\} \tag{7.3}$$

where the incremental force vector $\{\Delta F\}$ and displacement (rotation) vector $\{\Delta u\}$ are

$$\{\Delta F\} = \begin{matrix} \{\Delta F_{\alpha x}\ \Delta F_{\alpha y}\ \Delta F_{\alpha z}\ \ \Delta M_{\alpha x}\ \Delta M_{\alpha y}\ \Delta M_{\alpha z} \\ \Delta F_{\beta x}\ \Delta F_{\beta y}\ \Delta F_{\beta z}\ \ \Delta M_{\beta x}\ \Delta M_{\beta y}\ \Delta M_{\beta z}\ \}^T \end{matrix} \tag{7.4.a}$$

$$\{\Delta u\} = \begin{matrix} \{\Delta d_{\alpha x}\ \Delta d_{\alpha y}\ \Delta d_{\alpha z}\ \ \Delta \theta_{\alpha x}\ \Delta \theta_{\alpha y}\ \Delta \theta_{\alpha z} \\ \Delta d_{\beta x}\ \Delta d_{\beta y}\ \Delta d_{\beta z}\ \ \Delta \theta_{\beta x}\ \Delta \theta_{\beta y}\ \Delta \theta_{\beta z}\ \}^T \end{matrix} \tag{7.4.b}$$

in which $\{\Delta F\}$ contains 12 force (F) and moment (M) increments at the two ends of the bond, $\{\Delta u\}$ contains 12 displacement (d) and rotation (θ) increments at the two ends of the bond; and $[K]$ is a 12x12 tangential stiffness matrix. The internal total force (F) and

moments (M) are depicted in Figure 7.2. α and β denotes the two ends of the bond, and x, y and z denote the direction of the force in the local coordinate system of the bond.

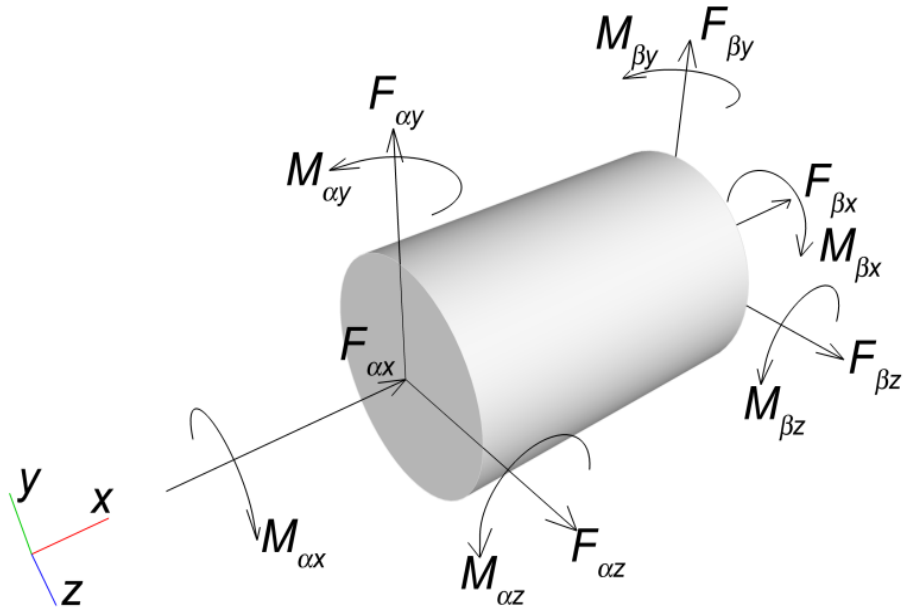

Figure 7.2 Forces and moments acting at the ends of a bond in the local coordinate system (Adapted from Brown et al. 2014)

7.2.2 Stiffness matrix

The tangential stiffness matrix [K] remains constant before failure for small deformation linear elastic bonds and the general form is presented by Przemieniecki (1986):

$$[K] = \begin{bmatrix} K_1 & -K_2 & -K_1 & -K_2 \\ K_2 & K_3 & -K_2 & K_4 \\ -K_1 & K_2 & K_1 & K_2 \\ K_2 & K_4 & -K_2 & K_3 \end{bmatrix} \tag{7.5}$$

where

$$[K_1] = \begin{bmatrix} \frac{E_b A_b}{L_b} & 0 & 0 \\ 0 & \frac{12k}{{L_b}^2(1+\Phi)} & 0 \\ 0 & 0 & \frac{12k}{{L_b}^2(1+\Phi)} \end{bmatrix}$$

$$[K_2] = \begin{bmatrix} 0 & 0 & 0 \\ 0 & 0 & \dfrac{-6k}{L_b(1+\Phi)} \\ 0 & \dfrac{6k}{L_b(1+\Phi)} & 0 \end{bmatrix}$$

$$[K_3] = \begin{bmatrix} \dfrac{k}{1+v_b} & 0 & 0 \\ 0 & \dfrac{k(4+\Phi)}{(1+\Phi)} & 0 \\ 0 & 0 & \dfrac{k(4+\Phi)}{(1+\Phi)} \end{bmatrix}$$

$$[K_4] = \begin{bmatrix} \dfrac{-k}{1+v_b} & 0 & 0 \\ 0 & \dfrac{k(2-\Phi)}{(1+\Phi)} & 0 \\ 0 & 0 & \dfrac{k(2-\Phi)}{(1+\Phi)} \end{bmatrix}$$

where $k = \frac{E_b I_b}{L_b}$, E_b is the Young's modulus, v_b is the Poisson's ratio, A_b is the cross-sectional area, I_b is the second moment of area of the bond and $\Phi = \frac{f_s 12 E_b I_b}{G_b A_b L_b^2}$ is the Timoshenko shear coefficient; where f_s and G_b are the form factor for shear and the bond's shear modulus respectively.

7.2.3 Transformation matrix

The displacement increment of the bond ends is determined by multiplying the global displacement increment vector by the transformation matrix [γ]:

$$\{u\} = \begin{bmatrix} \gamma & . & . & . \\ . & \gamma & . & . \\ . & . & \gamma & . \\ . & . & . & \gamma \end{bmatrix} \{u_g\} \tag{7.6}$$

The transformation matrix [γ] consists of nine directional cosines, which refer to the nine angles between the three vectors defining the axes of the global coordinate system and the three vectors defining the axes of the local coordinate system.

$$[\gamma] = \begin{bmatrix} x_X & x_Y & x_Z \\ y_X & y_Y & y_z \\ z_X & z_Y & z_Z \end{bmatrix} \tag{7.7}$$

The three vectors defining the local coordinate system in the transformation matrix are:

$$\begin{aligned} \{\hat{x}\} &= \{x_X \;\; x_Y \;\; x_Z\}^T \\ \{\hat{y}\} &= \{y_X \;\; y_Y \;\; y_Z\}^T \\ \{\hat{z}\} &= \{z_X \;\; z_Y \;\; z_Z\}^T \end{aligned} \tag{7.8}$$

The determination of $\{\hat{x}\}$, $\{\hat{y}\}$ and $\{\hat{z}\}$ is given elsewhere (Brown et al., 2014).

7.2.4 Bond stress calculations and bond strength distributions

On the assumption of small deformation, the bond stress, including total internal forces and moments at the bond ends at any given time, is given by:

$$\{F\} = \sum \Delta F \tag{7.9}$$

where $\{F\}$ contains 12 total forces and moments, it gives:

$$\{F\} = \{F_{\alpha x} \; F_{\alpha y} \; F_{\alpha z} \;\; M_{\alpha x} \; M_{\alpha y} \; M_{\alpha z} \;\; F_{\beta x} \; F_{\beta y} \; F_{\beta z} \;\; M_{\beta x} \; M_{\beta y} \; M_{\beta z} \;\}^T \tag{7.10}$$

Bonds are assumed to behave in a linear elastic brittle way; a bond is deemed to fail if the maximum value of any calculated stress exceeds the corresponding strength. The failure criteria consist of three parameters, i.e., compressive σ_C , tensile σ_T and shear r. Note that the three strength parameters are independent of each other, which means the compressive stress doesn't exert influence on the shear or tensile failure criteria.

The model incorporates a stochastic variation of the bond strength, with compressive, tensile and shear strength following a Gaussian distribution.

$$\sigma_C = S_C \cdot ((\zeta_C \cdot N) + 1)$$
$$\sigma_T = S_T \cdot ((\zeta_T \cdot N) + 1) \quad (7.11)$$
$$\mathrm{r} = S_S \cdot ((\zeta_S \cdot N) + 1)$$

where S_C is the mean bond compressive strength, S_T is the mean bond tensile strength, S_S is the mean bond shear strength, ζ_C, ζ_T and ζ_S are the coefficients of variation of compressive strength, tensile strength and shear strength, respectively. N is a random number drawn from a standard normal distribution.

7.3 The Hertz-Mindlin contact model

For a non-bonded contact, the Hertz-Mindlin with no slip contact law is used as a spring-dashpot configuration. Based on Hertz theory, Mindlin and Deresiewicz (1953) developed an incremental tangential force-displacement relation for identical spheres subjected to a frictional contact force in the tangential direction. The combined Hertz-Mindlin no slip contact model is commonly used for DEM simulations and in available in EDEM (DEM Solutions, 2015). The schematic illustration of Hertz-Mindlin no slip model is shown in Figure 7.3. As noted before, the normal force is based on Hertz contact theory while the tangential force is based on the work of Mindlin and Deresiewicz (1953). When Particle A and B are in contact, the normal component of the contact force is expressed as the sum of the normal spring force F_{ns} and normal damping force F_{nd}, i.e.,

$$F_n = F_{ns} + F_{nd} \quad (7.12)$$

where

$$F_{ns} = \frac{4}{3} E^* \sqrt{r^*} \delta_n^{1.5} \quad (7.13.a)$$

$$F_{nd} = -2 \sqrt{\frac{5}{6}} b_d \sqrt{S_n m^*} V_{n,relative} \quad (7.13.b)$$

in which

$$\frac{1}{E^*} = \frac{1-\nu_A^2}{E_A} + \frac{1-\nu_B^2}{E_B} \tag{7.14.a}$$

$$r^* = \frac{r_A \cdot r_B}{r_A + r_B} \tag{7.14.b}$$

$$m^* = \frac{m_A \cdot m_B}{m_A + m_B} \tag{7.14.c}$$

$$b_d = \frac{\ln e}{\sqrt{ln^2 e + \pi^2}} \tag{7.14.d}$$

where E^* is the equivalent Young's modulus of the two particles, r^* is the equivalent radius, δ_n is the normal overlap, b_d is a damping ratio related to the coefficient of restitution e, S_n is the normal stiffness, m^* is the equivalent mass, $V_{n,relative}$ is the normal component of the relative velocity.

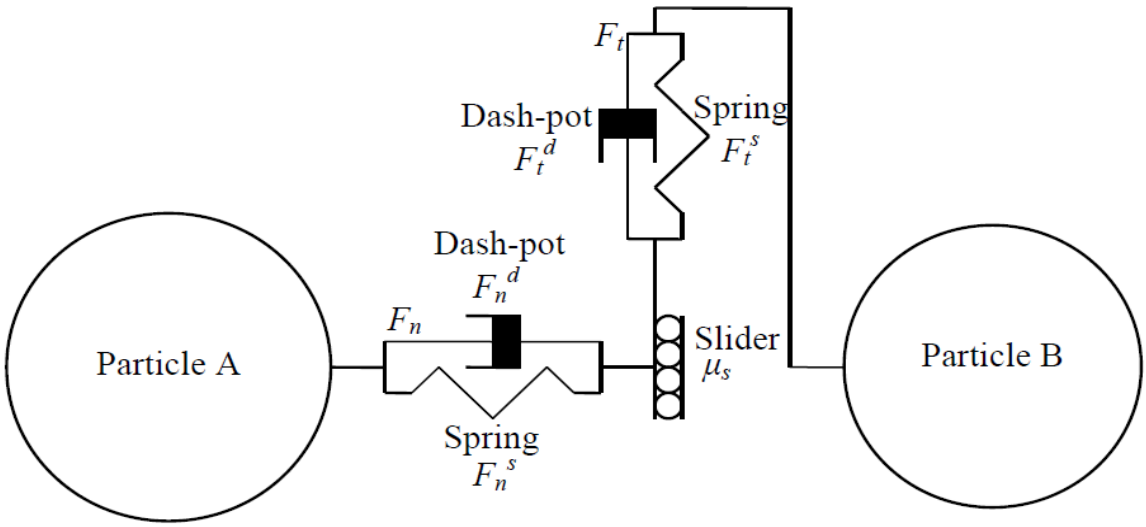

Figure 7.3 A spring-dashpot configuration of two particles A and B (After Brown, 2013)

Likewise, the tangential force F_t is calculated as the sum of the tangential spring force (F_{ts}) and tangential damping force (F_{td}):

$$F_t = F_{ts} + F_{td} \tag{7.15}$$

where

$$F_{ts} = -S_t \delta_t \tag{7.16.a}$$

$$F_{td} = -2\sqrt{\frac{5}{6}} b_d \sqrt{S_t m^*} V_{t,relative} \tag{7.16.b}$$

S_t is the tangential stiffness, δ_t is the normal overlap and $V_{t,relative}$ is the tangential component of relative velocity. The tangential force is limited by the Coulomb friction law $\mu_s F_n$, where μ_s is the coefficient of static friction. The normal stiffness S_n and the tangential stiffness S_t are given as:

$$S_n = 2E^* \sqrt{r^* \delta_n} \tag{7.17.a}$$

$$S_t = 8G^* \sqrt{r^* \delta_t} \tag{7.17.b}$$

$$\frac{1}{G^*} = \frac{1-\nu_A^2}{G_A} + \frac{1-\nu_B^2}{G_B} \tag{7.17.c}$$

where G^* is the equivalent shear modulus. This contact model shows a non-linear relationship between the force and overlap. Applications of the Hertz-Mindlin no slip model can be found in the literature (Tsuji et al., 1992; Misra and Cheung, 1999).

7.4 Implementation of the Timoshenko beam bond model

The TBBM has been implemented in the three-dimensional discrete element software EDEM (DEM Solutions, 2015) through an Application Programming Interface (API). A detailed description of the TBBM implementation and its verification can be found in Brown (2013) and Brown et al. (2014). Herein, the initial particle assembly and parameters selection are introduced as a reference case simulation.

7.4.1 Initial particle assembly

The DEM model of a spherical test particle was generated by bonding together a large number of constituent spheres. A trial-and-error process was followed to seek a packing fraction that would reflect the bulk stiffness and impact characteristics observed in the zeolite experiments. A random particle assembly with 63% solid fraction was generated using a collective rearrangement technique developed by Labra et al. (2010). This generation technique randomly creates particles according to an imposed particle size distribution. A spherical specimen of 1.6 mm in diameter is assembled using this generation technique, following a uniform size distribution with average particle radius (r_{av}) 0.04 mm. A total of 3687 constituent spheres was generated with the minimum (r_{min}) and maximum (r_{max}) radii set equal to 0.016 mm and 0.064 mm, respectively. The initial particle assembly is shown in Figure 7.4 and the generated particle size distribution is shown in Figure 7.5.

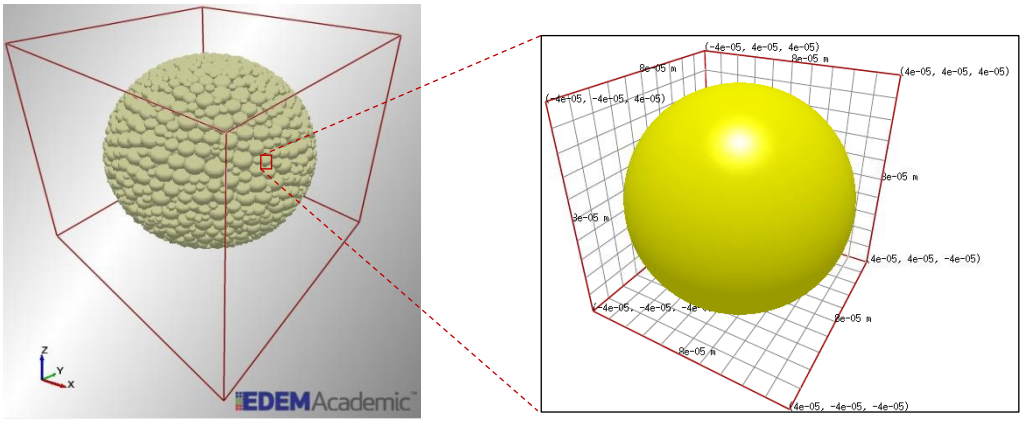

Figure 7.4 Initial particle assembly

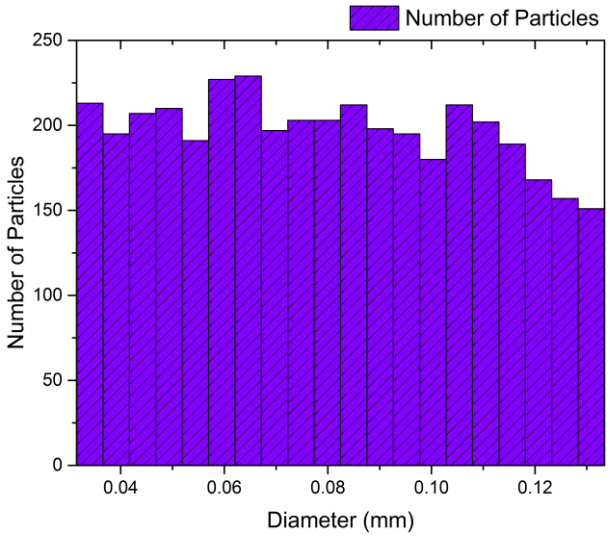

Figure 7.5 Micro-particle size distribution of the initial assembly

André et al. (2012) gave a dispersion factor d_f to indicate the variation in a predefined particle size spectrum.

$$d_f = \frac{r_{max} - r_{min}}{r_{av}} \tag{7.18}$$

The dispersion factor in this case is 1.2 as calculated from Eq. (7.18). The characteristics of the particle assembly are tabulated in Table 7.1.

Table 7.1 Characteristics of particle assembly

Parameter	**Description**	**Value**
R	Radius of multi-sphere particle assembly (mm)	0.8
n_p	Total number of constituent spheres	3687
n	Porosity	0.37
r_{av}	Average radius of constituent sphere (mm)	0.04
r_{min}	Minimum radius of constituent sphere (mm)	0.016
r_{max}	Maximum radius of constituent sphere (mm)	0.064

7.4.2 Simulation parameters of reference case

The input parameters for TBBM modelling can be divided into four categories: bond parameters, non-bonded parameters, bond fabrication parameters and numerical parameters (Brown, 2013). The parameters within each category for a reference case simulation are described below.

7.4.2.1 Bond parameters

The underlying theory to elucidate the bonded contact behaviour has been described in Section 7.2. For simplicity, the coefficient of variation for three strength components is kept the same as 0.2. The mean shear strength is set equal to the mean tensile strength which is $1/9^{th}$ of the mean compressive strength. The characteristics of the bonded contact parameters are shown in Table 7.2.

Table 7.2 Set of particle bond parameters for the reference case

Parameter	Description	Value
E_b	Young's modulus (GPa)	90
V_b	Poisson's ratio	0.2
S_C	Mean compressive strength (MPa)	990
ζ_C	Coefficient of variation of compressive strength	0.2
S_T	Mean tensile strength (MPa)	110
ζ_T	Coefficient of variation of tensile strength	0.2
S_S	Mean shear strength (MPa)	110
ζ_S	Coefficient of variation of shear strength	0.2

7.4.2.2 Non-bonded parameters

The Hertz-Mindlin with no slip contact model was chosen to represent the behaviour for non-bonded contacts. The characteristics of non-bonded parameters are summarized in Table 7.3.

Table 7.3 Particle non-bonded parameters for the reference case

Parameter	**Description**	**Value**
E_p	Particle Young's modulus (GPa)	25
ν_p	Particle Poisson's ratio	0.2
μ_{sp}	Particle-particle static friction	0.5
e_{rp}	Particle-particle restitution	0.5
μ_{rp}	Particle-particle rolling friction	0
E_g	Plate Young's modulus (GPa)	200
ν_g	Plate Poisson's ratio	0.3
e_{pg}	Platen-particle coefficient of restitution	0.5
μ_{sg}	Platen-particle coefficient of static friction	0.5
μ_{rg}	Platen-particle coefficient of rolling friction	0

The subscripts p and g represent the properties of particle and geometry, respectively. The geometry is assumed to be made from steel. The interaction parameters for particle-particle and particle-geometry consist of coefficients of restitution, static friction and rolling friction, all of which are shown in Table 7.3.

7.4.2.3 Bond fabrication parameters

There are two bond fabrication parameters: contact radius multiplier (η) and bond radius multiplier (λ). The contact radius serves to increase the search radius of neighbouring particles, which do not have a physical overlap. As shown by Brown (2013), the contact radius multiplier greatly influences the number of bonds. Increasing the contact radius multiplier increases the number of bonds and normally leads to an increasing failure strength of the assembly. A contact radius multiplier of 1.2 was

chosen for the reference case, leading to an average number of bonds per particle of 8.92.

The bond radius multiplier, λ, defines the radius of each bond (r_b) according to:

$$r_b = \lambda \cdot \min(r_A, r_B) \tag{7.19}$$

where r_A and r_B are the radii of bonded particles A and B respectively. The bond radius multiplier gives flexibility in the way the bond radius is determined. A default value of one is recommended for the bond radius multiplier (Brown, 2013).

7.4.2.4 Numerical parameters

To ensure the numerical stability of a simulation using the TBBM model, a number of input parameters which affect the numerical stability of a simulation should be considered: time step (Δt), loading rate (L_r) and global damping (i_d). The time step used in the TBBM simulation was determined based on the critical time step, which is the largest time step to avoid any force transition beyond the nearest neighbouring particles. As noted by Brown et al. (2014), the critical time step is chosen as the lower of the values of critical time step for both bonded and non-bonded contacts, as shown in Eq. (7.20):

$$\Delta t = \xi \min(\Delta t_{bcrit}, \Delta t_{HMcrit}) \tag{7.20}$$

where ξ is a factor ranging between zero and one. Δt_{bcrit} and Δt_{HMcrit} are the critical time steps for bonded and non-bonded, Hertz-Mindlin contacts, respectively.

The critical time step for a bonded contact is estimated from an assembly of particles using an equivalent single degree of freedom system (O'Sullivan et al., 2004):

$$\Delta t_{bcrit} = 2\sqrt{\frac{m_{pmin}}{K_{bmax}}} \tag{7.21}$$

where m_{pmin} is the minimum mass of a constituent particle and K_{bmax} is the largest bond stiffness component for that contact.

The critical time step for a non-bonded contact is determined based on the Rayleigh time step, which corresponds to the time taken for a shear wave to propagate through a solid particle (EDEM User Guide, 2015):

$$\Delta t_{HMcrit} = \frac{\pi r_p \left(\frac{\rho_p}{G_p}\right)^{0.5}}{\left(0.1631\upsilon_p + 0.8766\right)} \tag{7.22}$$

where r_p is the radius of the smallest constituent particle, ρ_p and G_p are the density and shear modulus of the spherical particles, respectively, and υ_p is the Poisson's ratio. The time step is thus obtained when the lower value in Eqs. (7.21) and (7.22) is chosen. In the reference case of simulation, ξ was selected to be 0.10 and the time step was calculated to be 4.38e-10 s.

The loading rates for the reference case are controlled by varying the impact velocity from 10 m/s to 100 m/s. It is noted that the impact velocities in the physical single particle impact tests are varied from 5 m/s to 30 m/s. In real materials, kinetic energy is dissipated through microscopic actions such as internal friction and wave scattering (Potyondy and Cundall, 2004). Additional artificial damping can be introduced to reduce the kinetic energy as the frictional sliding does not represent the full damping effect. Non-viscous damping is applied in the TBBM through the equations of motion so that energy is dissipated in every particle in the system. In the reference case, the global damping is chosen as 0.05. The damping forces (F_d) and moments (M_d) are applied to each of the six degrees of freedom for each particle.

$$F_{di} = \frac{-l_d|F_i|V_i}{|V_i|} \; i = X, Y, Z \tag{7.23}$$

$$M_{di} = \frac{-l_d|M_i|\omega_i}{|\omega_i|} \; i = X, Y, Z \tag{7.24 }$$

where F and M are the sum of forces and moments exerting on the particle, V and ω are the translational and angular velocity respectively, X, Y and Z are degrees of freedom whilst l_d is a dimensionless constant which defines the magnitude of the damping. More information regarding the loading rate and global damping could be referred to Brown (2013). The numerical parameters are shown in Table 7.4.

Table 7.4 Global parameters for the reference case

Parameter	**Description**	**Value**
Δt	Time step (s)	4.38e-10
ι_d	Global damping coefficient	0.05
L_r	Impact velocity (m.s^{-1})	10, 16, 20, 24, 30, 40, 60, 80, 100

Apart from the parameters selection mentioned above, the selection of gravity in simulations should also be considered. For all the simulations in the present work, the acceleration due to gravity is set to zero so the effect of gravity is excluded.

7.5 Numerical results of particle breakage under normal impact loading

The results of DEM simulations of a single particle under normal impact are presented through a reference case using a wide spectrum of impact velocities. Five factors are used to characterise the impact breakage: breakage pattern, contact force, contact evolution, failure mode and damage ratio.

7.5.1 Breakage pattern characterisation

The breakage patterns of agglomerates reported by Thornton et al. (1999) were divided into three types, namely rebound, fracture and shattering depending on the magnitude of impact velocity. Rebound was characterised by only a small percentage of broken bonds close to the impact zone resulting in a small amount of fine debris. Fracture is reserved for breakage patterns in which clear fracture planes (cracks) are visible (Mishra and Thornton, 2001). This mode leads to two or more large daughter fragments and is typically accompanied by some fines production close to the impact site. Shattering can be viewed as a further evolution of fracture, in which large daughter fragments are

broken into small clusters of primary particles under higher impact velocities than for fracture. Ghadiri et al. (2007) compared the breakage patterns between DEM simulations from Mishra and Thornton (2001) and experimental results from Subero and Ghadiri (2001). Four breakage patterns were summarized depending on the impact velocity as shown in Figure 7.6. A detailed review of other breakage patterns has been shown elsewhere (Ghadiri et al., 2007).

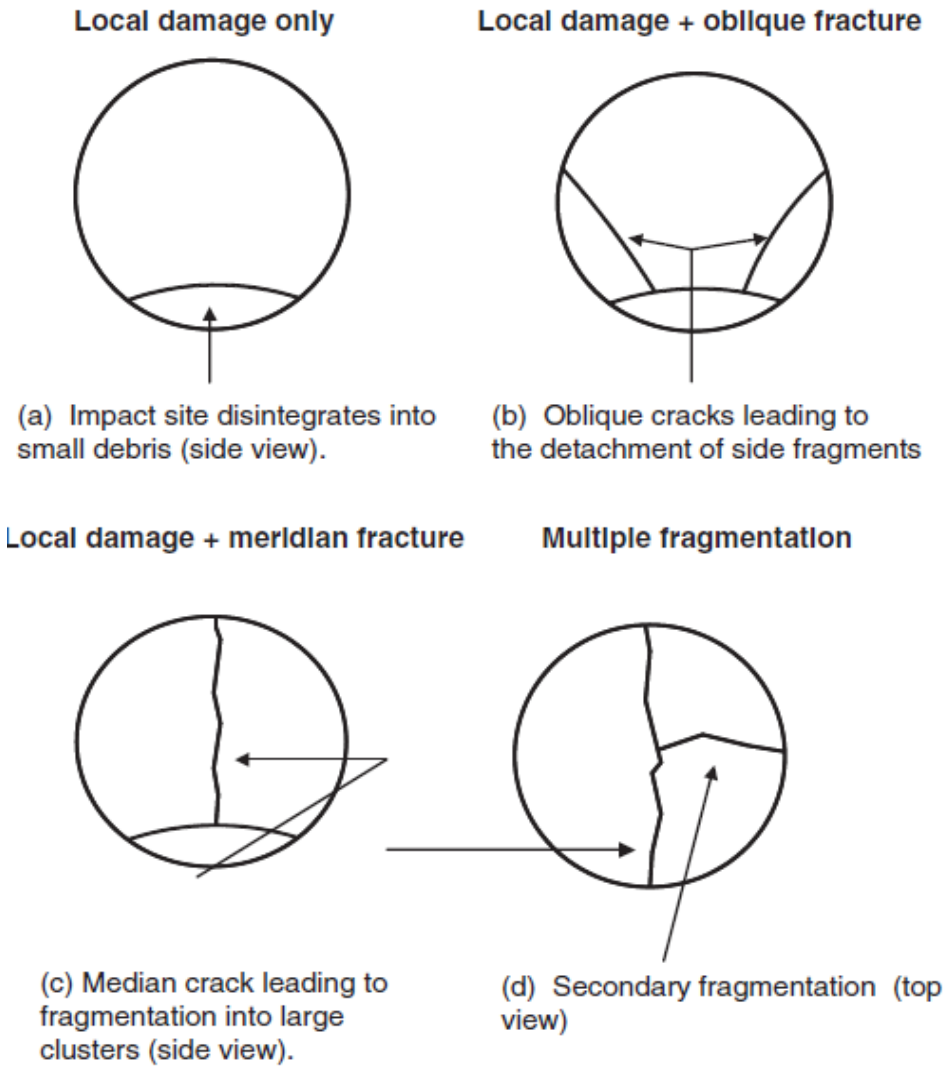

Figure 7.6 Experimental breakage patterns of agglomerate
(After Ghadiri et al., 2007)

To ensure that breakage patterns are defined consistently in these DEM simulations, two breakage patterns are defined based on the preceding literature survey: chipping and fragmentation. Rebound is equivalent to chipping whilst fracture is equivalent to fragmentation. The snapshots depicting impact events at 10 m/s and 30 m/s are shown

in Figures 7.7 and 7.8 respectively. From Figure 7.7, it is observed that only small parts are detached from the original particle, resulting in a small amount of mass loss. By contrast, the particle is broken into several large daughter particles and much debris at 30 m/s as shown in Figure 7.8. The breakage pattern is found to switch from chipping to fragmentation as the impact velocity increases.

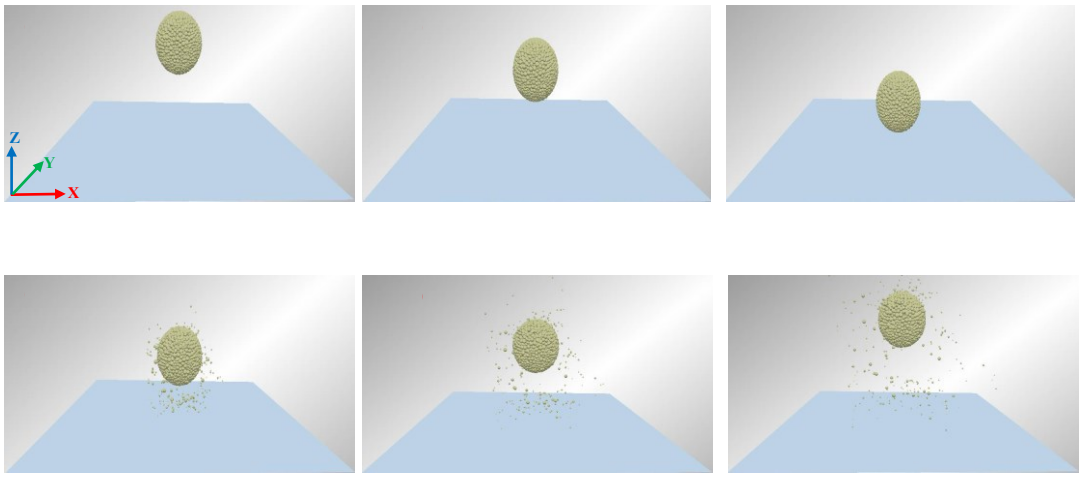

Figure 7.7 Particle breakage at 10 m/s-chipping

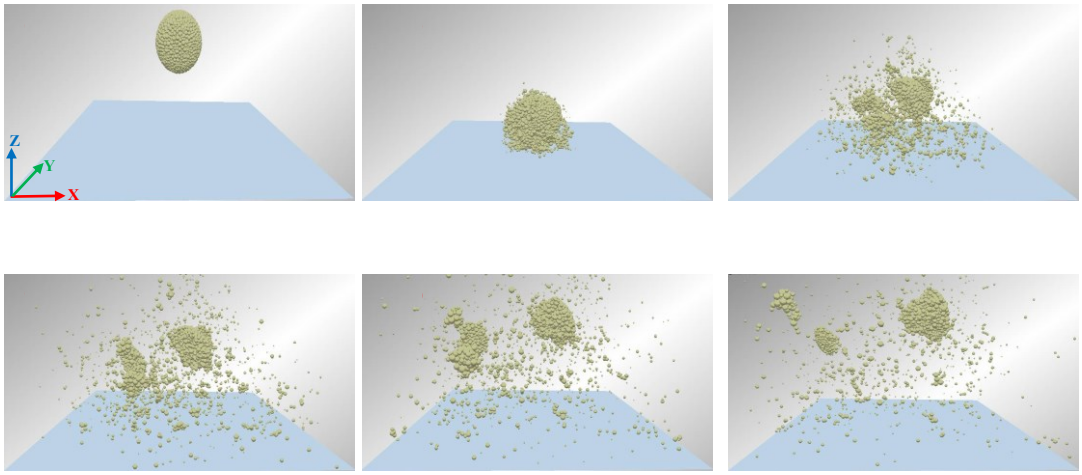

Figure 7.8 Particle breakage at 30 m/s-fragmentation

7.5.2 Contact fabric evolution

7.5.2.1 Contact force evolution

Figure 7.9 shows the evolution of the force exerted on the plate in the z direction for impact velocities of 10 m/s, 16 m/s and 24 m/s. The maximum forces generated at the plate approximately correspond to elapsed times of 0.100007s, 0.100006s or 0.100005s,

respectively. For the impact velocity of 10 m/s, the plate force increases to maximum at about 0.100007s time and then falls to zero at about 0.100013s time. The trends of plate contact force at impact velocities of 16 m/s and 24 m/s are similar to that at 10 m/s. The maximum force on the plate increases with an increase of impact velocity and the duration of the impact event decreases, which agrees well with Mishra and Thornton (2001).

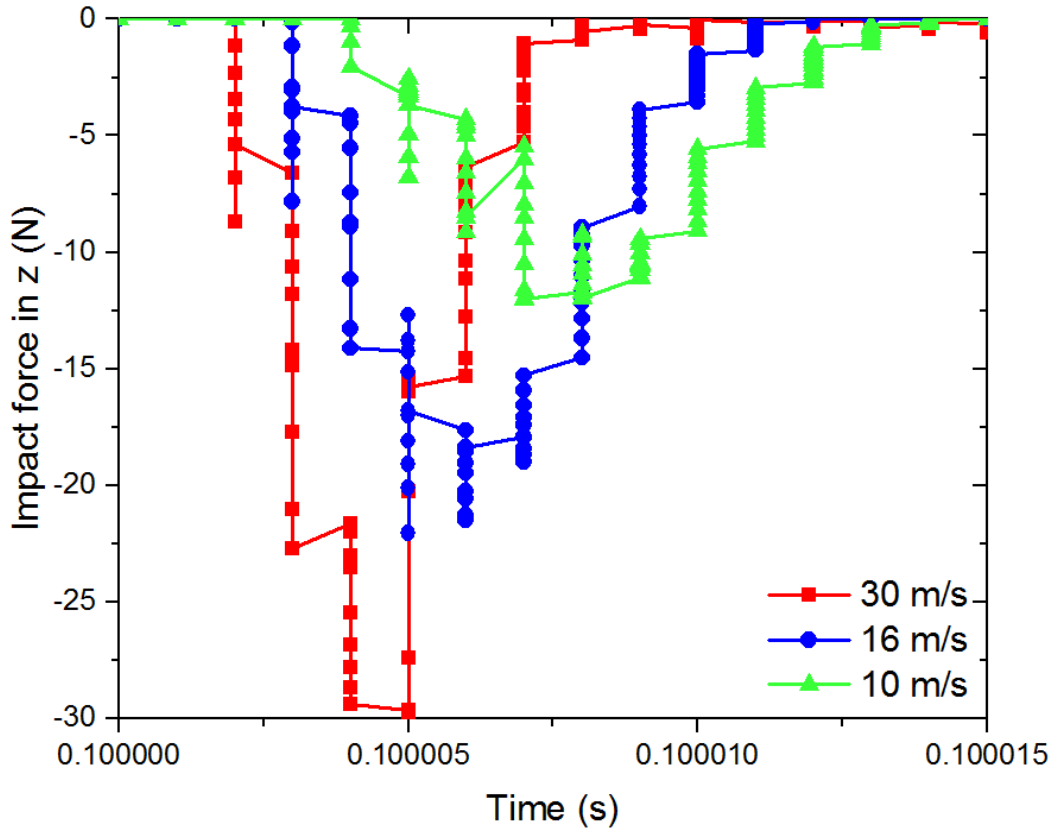

Figure 7.9 Contact force on plate in z direction under varying impact velocities

It should be noted that some fluctuations of the plate contact force are observed, which were also reported elsewhere (Thornton et al., 1999; Mishra and Thornton 2000). This would appear to be due to debris detachment from the particle at the impact zone resulting from force propagation before secondary impact with the plate.

7.5.2.2 Contact network evolution

The transition of breakage pattern is further confirmed by comparing the contact evolution at two impact velocities (Figures 7.10 and 7.11). Figure 7.10 shows that the particle remains largely intact at 10 m/s with some internal broken bonds that do not lead to failure. No cracks are observed but some local detachments of small pieces occur

in the contact zone. Under 30 m/s impact (Figure 7.11), extensive broken bonds (blue) are observed in the contact zone which soon propagate throughout the whole particle. There are many more broken bonds (blue) at 30 m/s with the initiation of a cone shaped crack pattern (Figure 7.11). The secondary crack is then generated as the contact evolves, resulting in several pieces of the fragmented particle. These findings are consistent with those reported in Thornton et al. (1996). The broken bonds are concentrated at the impact zone at 10 m/s while the broken bonds are relatively distributed at 30 m/s.

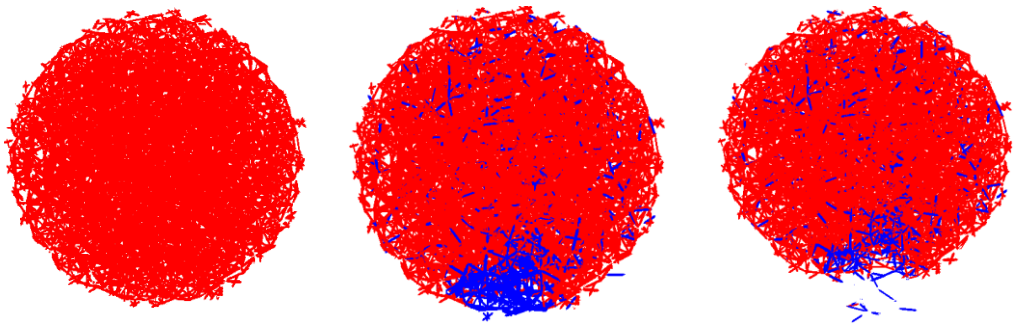

Figure 7.10 Surface damage resulting in chipping at impact velocity of 10 m/s (red=intact bond, blue=broken bond)

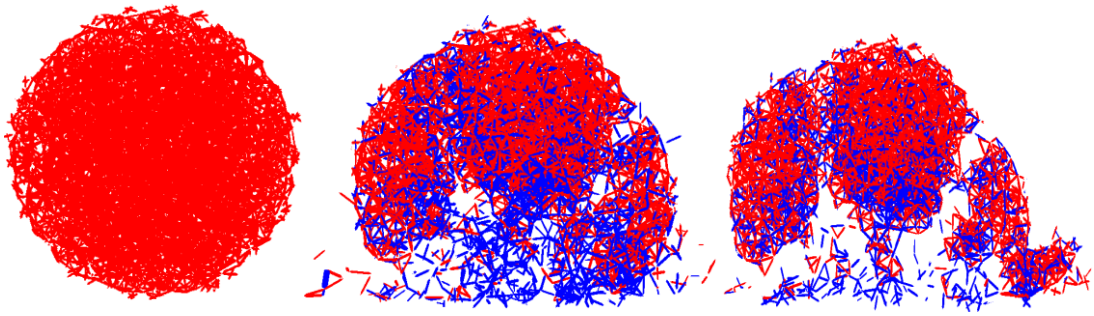

Figure 7.11 Cone crack initiated with secondary crack propagation leading to fragmentation at impact velocity of 30 m/s (red=intact bond, blue=broken bond)

7.5.3 Failure mode

The cumulative distribution of broken bonds resulting from compression, tension and shear during the impact loading is shown in Figure 7.12. This classification sheds more light on the dominant failure mechanism. Tension failure accounts for the majority of

broken bonds; compressive and shear failure are negligible. The proportion of bonds exhibiting tension failure increases as the impact velocity is increased.

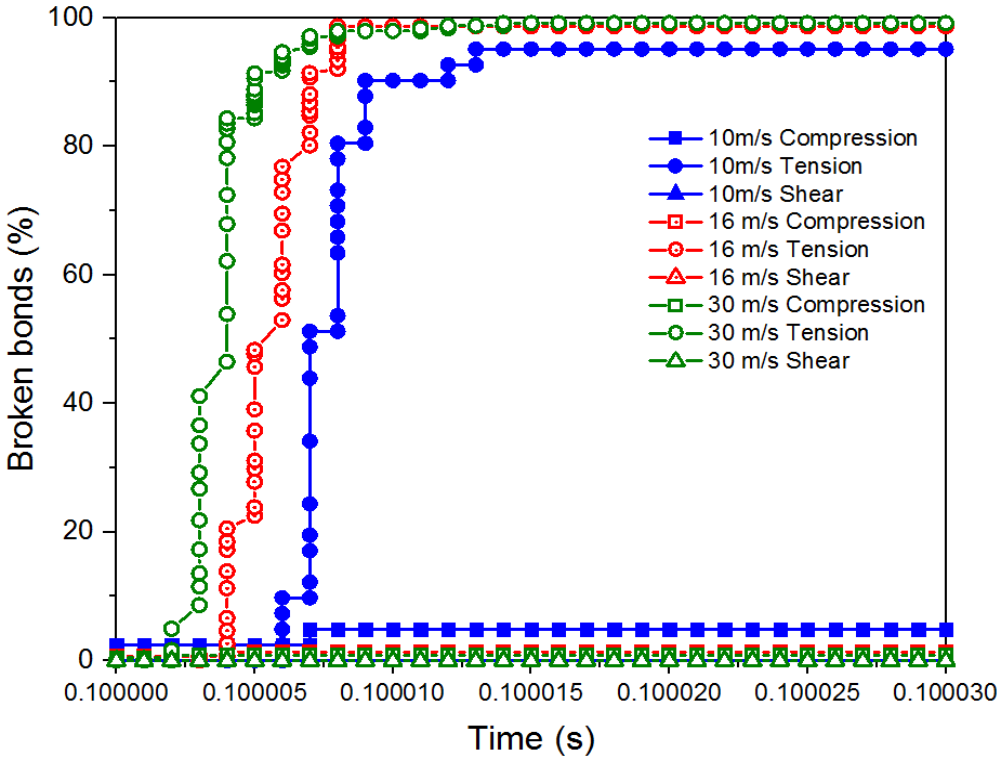

Figure 7.12 Failure modes of bonds subjected to impact loading

Considering the mean value of bond compressive strength is significantly higher than tensile strength, it is unlikely that the bonds fail through compression. The preponderance of tensile failures is in line with the findings of other authors including Thornton et al. (1996), Antonyuk et al. (2006) and Wittel et al. (2008).

7.5.4 Analysis of damage ratio

Damage ratio is typically used to represent the degree of impact breakage in a DEM simulation. This was first proposed by Kafui and Thornton (1993). The damage ratio is defined as a function of broken bonds as:

$$D_r = \frac{B_0 - B}{B_0} \tag{7.25}$$

where D_r is the damage ratio; B_0 and B are the numbers of bonded contacts before and after impact, respectively. The damage ratio is depicted in Figure 7.13 for impact

velocities ranging from 10 m/s to 100 m/s. The damage ratio rises rapidly as the impact velocity increases from 10 m/s to 40 m/s. However, successive increases of damage ratio as the impact velocity is increased from 40 m/s to 100 m/s are not as marked. The damage ratio eventually peaks as 89% at the highest impact velocity of 100 m/s. The dependency of the damage ratio on the impact velocity is in good agreement with the previous results of Thornton et al. (1996), Subero et al. (1999) and Moreno et al. (2006). The damage ratio increases with increasing impact velocity as expected. However, the damage ratio is much higher than the breakage ratio measured for the same impact velocity under single particle impact test. The reason for the difference is due to the fact that the damage ratio is defined by the number of broken bonds while the breakage propensity is defined by the resulting volume loss due to impact based on particle size distribution.

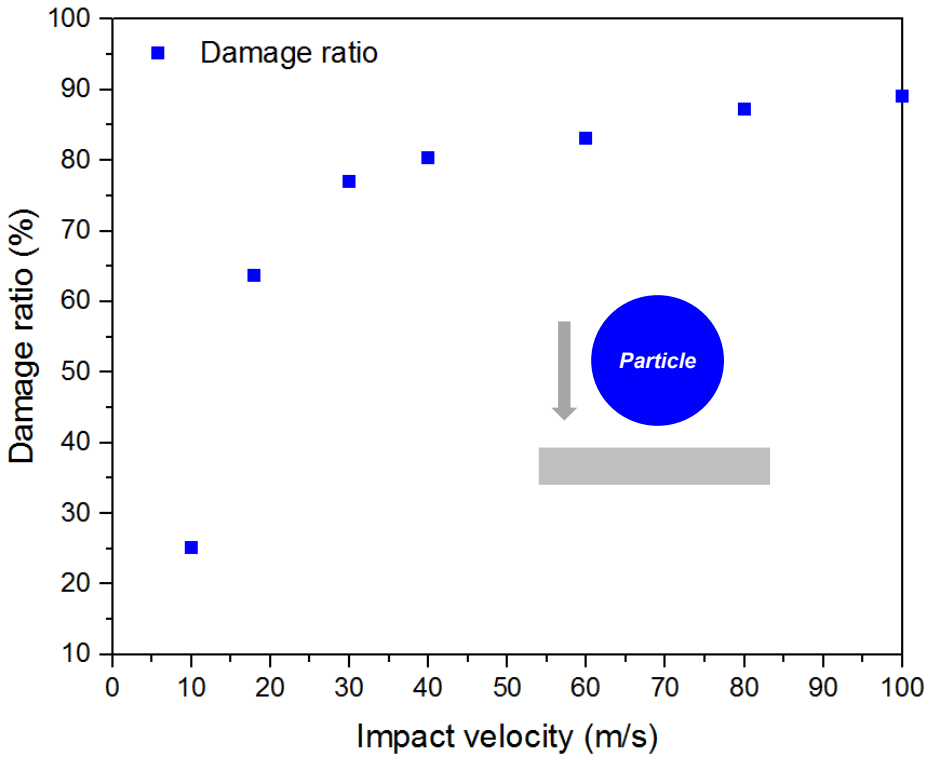

Figure 7.13 Damage ratios for particles at impacts ranging from 10 m/s to 100 m/s

As mentioned by Subero et al. (1999), the damage ratio accounts for the total contact separation rather than the actual size reduction; it is therefore difficult to compare it directly with experimental results based on sieve analysis of particle size distribution. This motivates a unification of the criteria used to characterize breakage probability, which is described in the following section.

7.5.5 Summary of reference case simulation

The DEM simulation of bonded particle breakage when subjected to normal impact loading has been discussed in detail through a reference case using a proposed set of input parameters. Two breakage patterns, chipping and fragmentation, were observed. A transition from chipping to fragmentation was seen with increasing impact velocity. Tension failure accounts for the majority of broken bonds; compressive and shear failures are negligible which provides some micromechanical insight into the impact breakage. The damage ratio based on the proportion of broken bonds shows a rapid growth up to an impact velocity of 40 m/s. The increase in damage ratio with impact velocity is not as marked beyond 40 m/s. The maximum damage ratio of 89% is reached at 100 m/s impact. As a collaborative project with Hosokawa Ltd UK is continued, DEM simulations of bonded particle breakage subject to oblique impact are underway and the relevant results will be reported within a master thesis.

7.6 Validation of bonded DEM simulation against experiment

As described above, particle breakage is quantified by the damage ratio which is defined as the ratio of the number of broken bonds to the total number of bonds before impact (Thornton et al., 1996). In terms of experiment, particle breakage is quantified by the breakage ratio which is defined as the ratio of debris mass to the total mass of mother and debris particles (Refer to Chapter 3). It should be noted that there are very few direct comparisons in the literature with respect to breakage results between the experiment and simulation considering the different definitions of the breakage propensity (breakage ratio in experiment whereas the damage ratio in simulation). Because of that, the particle size distribution after impact in the bonded DEM simulation has been analyzed. The same breakage criterion, i.e., breakage ratio, is adopted, which enables the breakage propensity of the physical experiments and DEM simulations to be compared. A post-processing function to characterize the particle size distribution after the impact simulation was developed, which is described below.

This function firstly identifies the ID of the particles forming each cluster based on a node matrix ID and adjacent matrix. The identification of the particle IDs in each cluster is based on the Breadth-First search algorithm. The effects of different shape fitting such as ellipse, rectangle and circle were discussed by Kumara et al. (2011) and it was

found that the ellipse gave the closest size prediction of that measured by sieve analysis. Therefore, the cluster is assumed to have an ellipsoidal shape and the radii of the ellipsoid can be determined through Matlab based on the function developed by Petrov (2015). Kumara et al. (2012) investigated the effects of grain size definition by two methods as a function of ellipsoid fitting. Figure 7.14 shows the grain size definition for particles passing parallel to sides of a sieve (D_1) or through the diagonal of a sieve (D_2), respectively:

$$D_1 = \sqrt{0.5(b^2 + c^2)} \tag{7.26 a}$$

$$D_2 = b\sqrt{0.5(1 + \alpha^2)} \tag{7.26 b}$$

where b and c are the intermediate diameter and shortest diameter of the cluster based on ellipsoid fitting. α is a constant between the intermediate diameter and shortest diameter of the particle. The particle size defined by D_2 is closer to the sieve analysis than that defined by D_1. Hence, D_2 is used in this work to measure the particle size distribution.

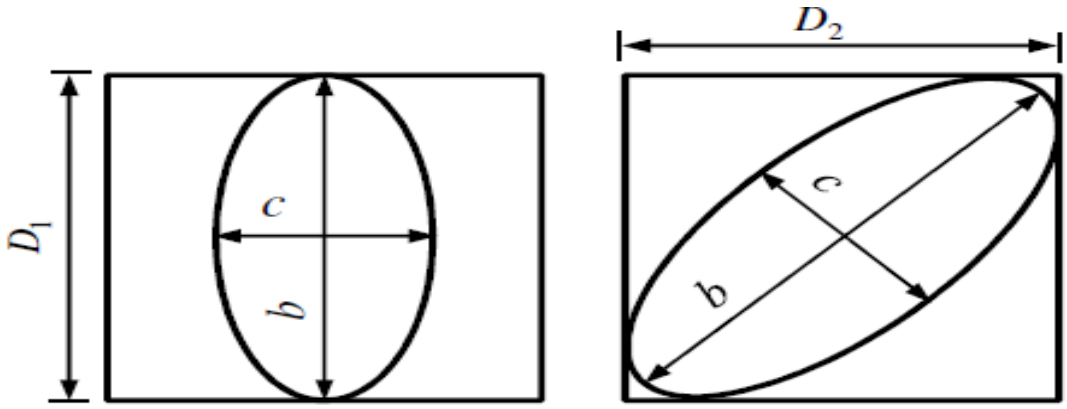

Figure 7.14 Schematic outline of particle size definition (a) parallel to sides and (b) through diagonal of square sieve (After Kumara et al., 2012)

Figure 7.15 depicts the breakage ratio of the bonded DEM simulations after impacts at velocities of 10, 16, 20 and 24 m/s based on the post-processing function, which is compared with the impact test results at impact velocities up to 26 m/s.

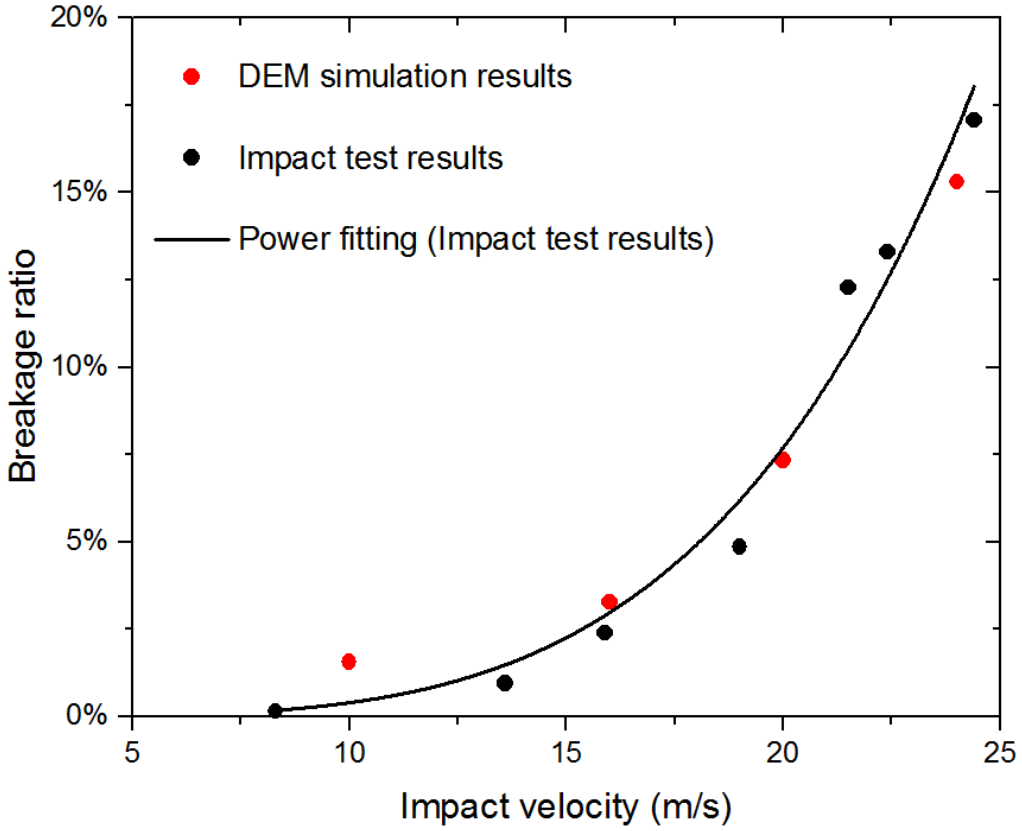

Figure 7.15 Validation of bonded DEM simulation against impact test results

A close agreement is achieved between the DEM simulations and impact test results although the breakage ratio in the DEM simulations is overestimated at the lowest impact velocity (10 m/s) compared to the physical impact test. This indicates that the effect of input parameter variation on the breakage ratio needs to be assessed relative to the reference case, which is discussed in the following section.

7.7 Parametric study

This section presents a parametric study which investigates the effect of the relatively influential input parameters of the Edinburgh Bonded Particle Model (EBPM) on the DEM simulation of particle breakage subject to normal impact loading. The influence of each selected parameter is examined while the other parameters are kept constant at the values set in the reference simulation case. As mentioned above, two contact models are adopted: the Timoshenko Beam Bonded Contact Model (TBBM) for bonded contacts and the Hertz-Mindlin Contact Model (HMCM) for non-bonded contacts. As noted by Brown (2013), the parameters in the context of TBBM and HMCM can be divided into four categories, which has been described in Section 7.4.2.

Brown (2013) scrutinizes the influence of the model input parameters of EBPM on the simulation results from uni-axial compression of a concrete specimen. The predictive capacity of the EBPM was evaluated by inspecting four important bulk responses: the ultimate compressive strength, the secant modulus of elasticity, the axial strain at failure and the Poisson's ratio. By exploring the influence of input parameters on the bulk properties, the relative importance of these parameters was identified. It was concluded that the most influential parameters amongst all input parameters are bond Young's modulus, mean bond tensile and shear strengths, coefficients of variation of tensile and shear strength, and contact radius multiplier. Specifically, bond Young's modulus, contact radius multiplier and bond radius multiplier significantly influence the bulk stiffness while the contact radius multiplier, bond radius multiplier, mean tensile and shear bond strengths, coefficient of variation of bond strength and bond Young's modulus all have a significant influence on bulk strength. The parameters which have a critical influence on the strain at failure, Poisson's ratio, post-peak behavior and failure mode are discussed in Brown (2013). It is noted that a comprehensive parameter optimisation study is not the aim of this work although it is possible to do so such as Johnstone (2010).

Combined with the systematic parametric study from Brown (2013) and the breakage results indicated from the reference case, four critical parameters are chosen for parametric study in this thesis: bond Young's modulus, mean tensile bond strength, coefficient of variation of bond strengths, and restitution coefficient between particles. The breakage ratio of bonded particles is evaluated in the context of normal impact breakage. The method to determinate the breakage ratio is the same as that mentioned in Section 7.6. Note that the number and the size range of the micro-spheres are kept the same as for the reference simulation case. The impact velocity is the only source of load for these simulations in which gravity is excluded. Four impact velocities (10 m/s, 16 m/s, 20 m/s and 24 m/s) were selected falling in the range of impact velocity in Chapter 3. The ranges chosen for the four key input parameters used for the parametric study are shown in Table 7.5.

Table 7.5 Range of key input parameters used in parametric study

Parameters	Description	Reference case	Comparative case I	Comparative case II
E_b	Bond Young's modulus (GPa)	90	60	120
S_t	Mean tensile strength (MPa)	110	100	120
ζ	Coefficient of variation of bond strengths	0.2	0.4	0.8
e_{rp}	Particle & particle coefficient of restitution	0.5	0.1	0.9

7.7.1 Influence of bond Young's modulus

The Young's modulus of the bonds controls the stiffness of each bond. The input Young's modulus was chosen from a range between 60 GPa and 120 GPa. The breakage ratio of particle when using values of 60 GPa and 120 GPa under four impact velocities 10 m/s, 16 m/s, 20 m/s and 24 m/s are compared with the reference simulation case with $E_b = 90\ GPa$ on Figure 7.16.

Amongst the three chosen bond Young's moduli, the difference of breakage ratio becomes more significant as impact velocity increases. The breakage ratio at 10 m/s is almost independent of bond Young's modulus whereas the difference of breakage ratio at 24 m/s is much more substantial. The highest breakage ratio was obtained at 90 GPa and the lowest breakage ratio was found at 60 GPa. This indicates that the bonded Young's modulus has an increasing influence on the breakage ratio with the increase of impact velocity. Compared with the 60 GPa and 120 GPa cases, the reference case with a bond Young's modulus of 90 GPa gives closer predictions of the impact test results. Beyond the impact velocity of 20 m/s, the bond Young's modulus of 60 GPa is apt to give the lowest breakage ratio and the bonded Young's modulus of 90 GPa is apt to give the highest breakage ratio. As noted by Brown (2013), for the case of cylindrical concrete under uniaxial loading, the increase of bond Young's modulus results in the decrease of strain and strength at failure. If this trend is applicable to the events under impact loading, the bond Young's modulus of 120 GPa ought to produce the highest

breakage ratio. However, the increase of bond Young's modulus appears to be disproportionate to the variation in the breakage ratio. The reason for the variation of breakage ratio is still under investigation.

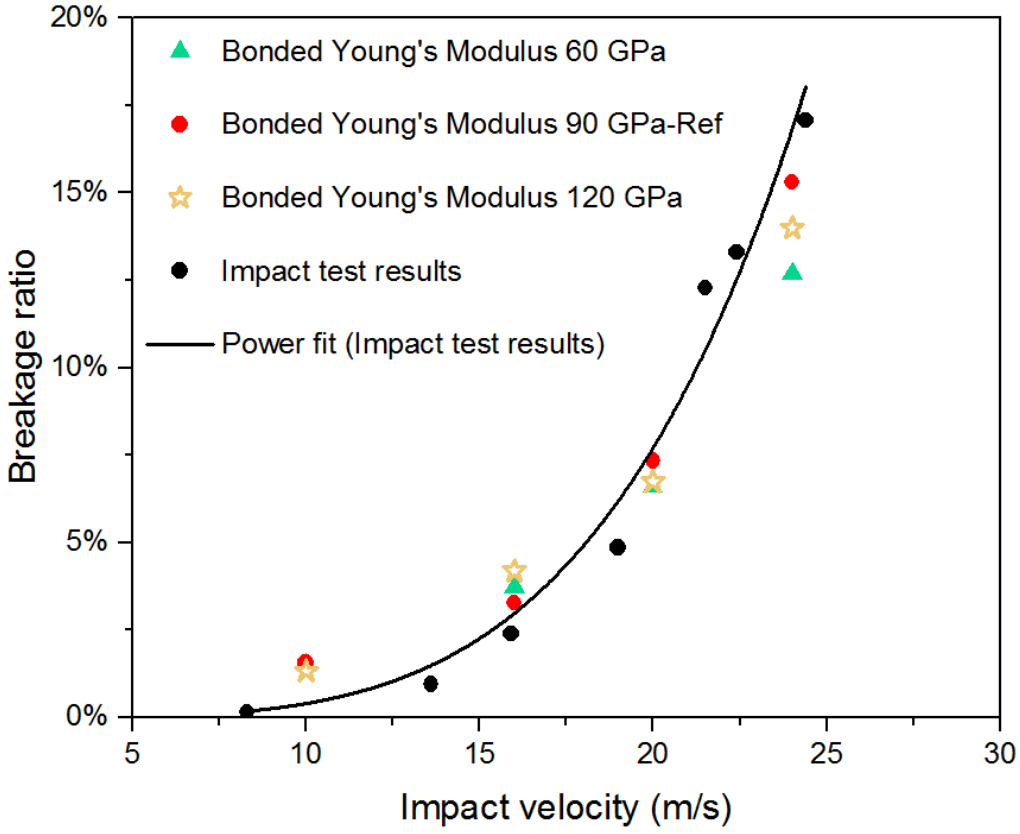

Figure 7.16 Influence of bond Young's modulus on the breakage ratio

7.7.2 Influence of the mean tensile bond strength

The tensile strength is assumed to follow a Gaussian distribution defined by a mean and a standard deviation. The reason for choosing the mean tensile strength of the bond is due to the fact that tensile failure is the dominant failure type in the reference case while the failure through compression and shear is negligible. The mean tensile strength of the bonds in the reference simulation case is assigned as 1.1e8 Pa whereas the mean tensile strength in comparative cases is given as 1.0e8 Pa and 1.2e8 Pa respectively. The influence of mean tensile strength on the breakage ratio is shown in Figure 7.17. The influence of coefficient of variation of bond strength on breakage ratio is discussed in Section 7.7.3.

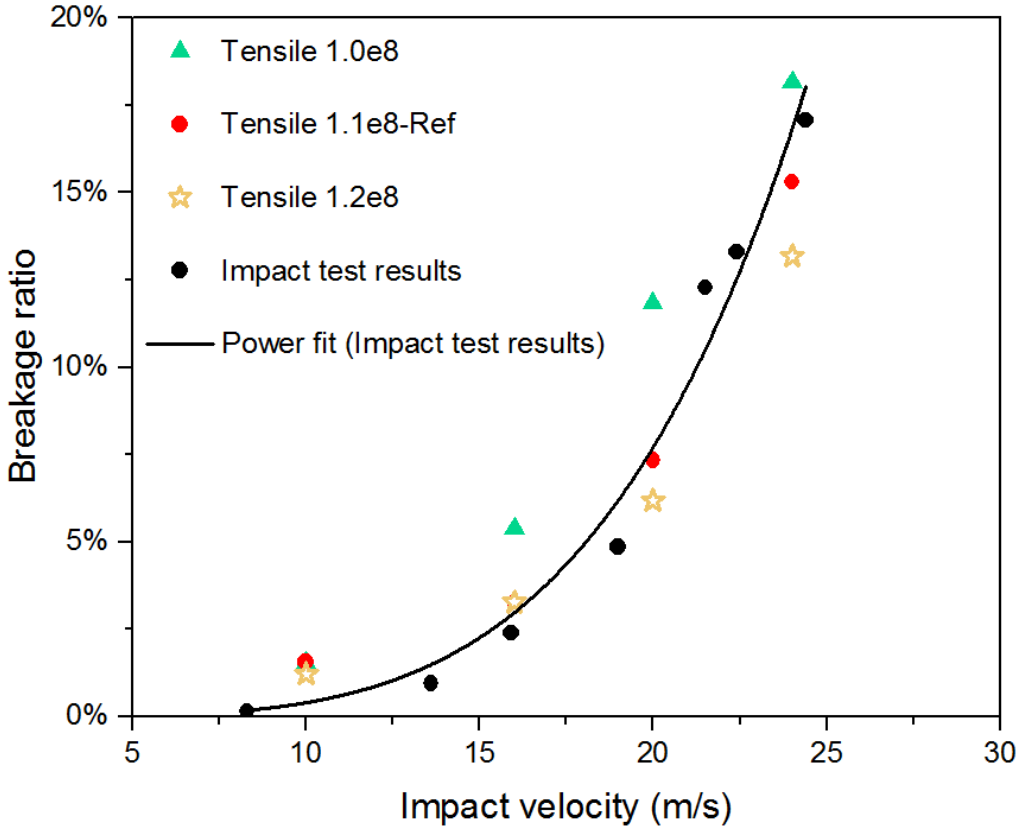

Figure 7.17 Influence of mean tensile bond strength on breakage ratio

Figure 7.17 indicates that the mean bond tensile strength has a critical influence on the breakage ratio. As the mean tensile strength increases, the breakage ratio decreases. This is due to the fact that the average bond strength is augmented when the mean tensile strength is increased. Considering tensile failure as the dominant failure mode, the higher average bond strength has a bigger resistance to impact breakage which results in a lower breakage ratio. The breakage ratio at 10 m/s stays roughly the same for the varying value of the mean tensile strength. However, the difference of breakage ratio becomes relatively large with the increase of impact velocity under varying mean tensile strength. The mean tensile strength has an increasing influence on the breakage ratio as the impact velocity is increased.

7.7.3 Influence of the coefficient of variation of the strength parameters

Following the investigation of the influence of the mean bond tensile strength, the influence of coefficient of variation of the strength parameters is investigated. The coefficient of variation (CoV), also known as relative standard deviation, is defined as the ratio of the standard deviation to the mean. For simplicity, the coefficients of

variation of the three strength components (compression, tension and shear) are assumed to be the same. The strength distribution is typically truncated between zero and double the mean strength. The values of coefficient of variation are chosen as 0.2, 0.4 and 0.8 for this parametric study. The influence of the coefficient of variation on the distribution of tensile strength is shown in Figure 7.18. The distribution for the compressive and shear strength follows the similar trend.

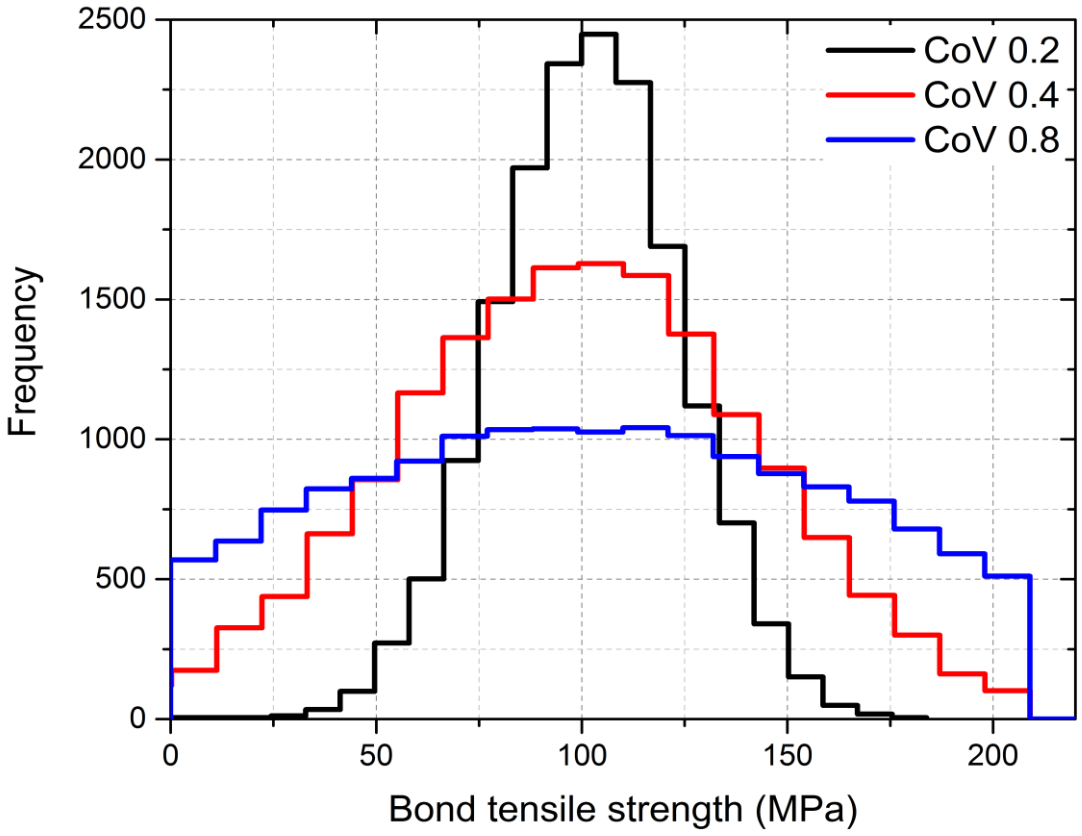

Figure 7.18 Distribution of tensile bond strength for varying coefficient of variation

As seen from Figure 7.18, the distribution of tensile bond strength becomes more flattened as the CoV is increased, i.e., the distribution of bond strength is more concentrated around the mean value under lower CoV. The influence of coefficient of variation on the breakage ratio is presented in Figure 7.19.

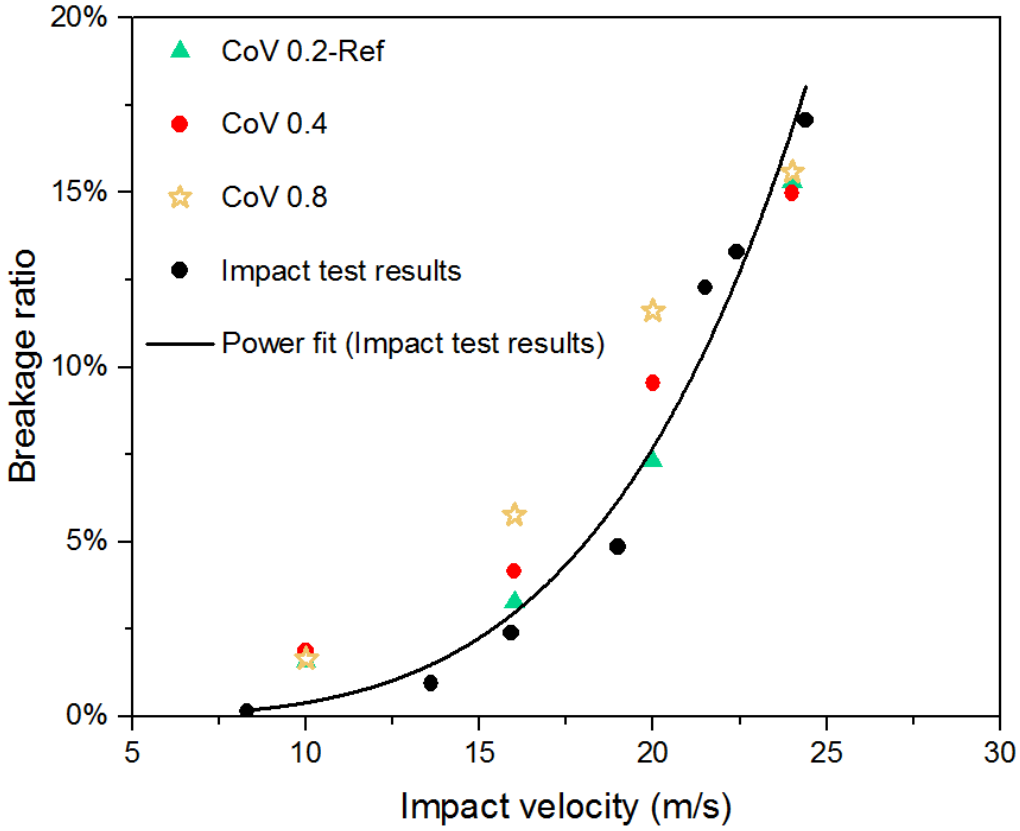

Figure 7.19 Influence of coefficient of variation of strength on breakage ratio

As seen from Figure 7.19, the influence of CoV at medium impact velocities is more significant than at low and high impact velocities. When the coefficient of variation is increased from 0.2 to 0.8, the breakage ratios at 10 m/s and 24 m/s are largely the same whilst the disparity of breakage ratio at 16 m/s and 20 m/s is relatively significant.

7.7.4 Influence of particle & particle restitution coefficient

The coefficient of restitution is defined as the ratio of relative velocity after and before an impact. The range of coefficient of restitution spans from 0 to 1. The coefficient of restitution between particles is assumed to be 0.5 in the reference cases. For comparative analysis, the coefficients of restitution between particles are chosen as 0.1 and 0.9. The influence of coefficient of restitution on the breakage ratio is shown in Figure 7.20.

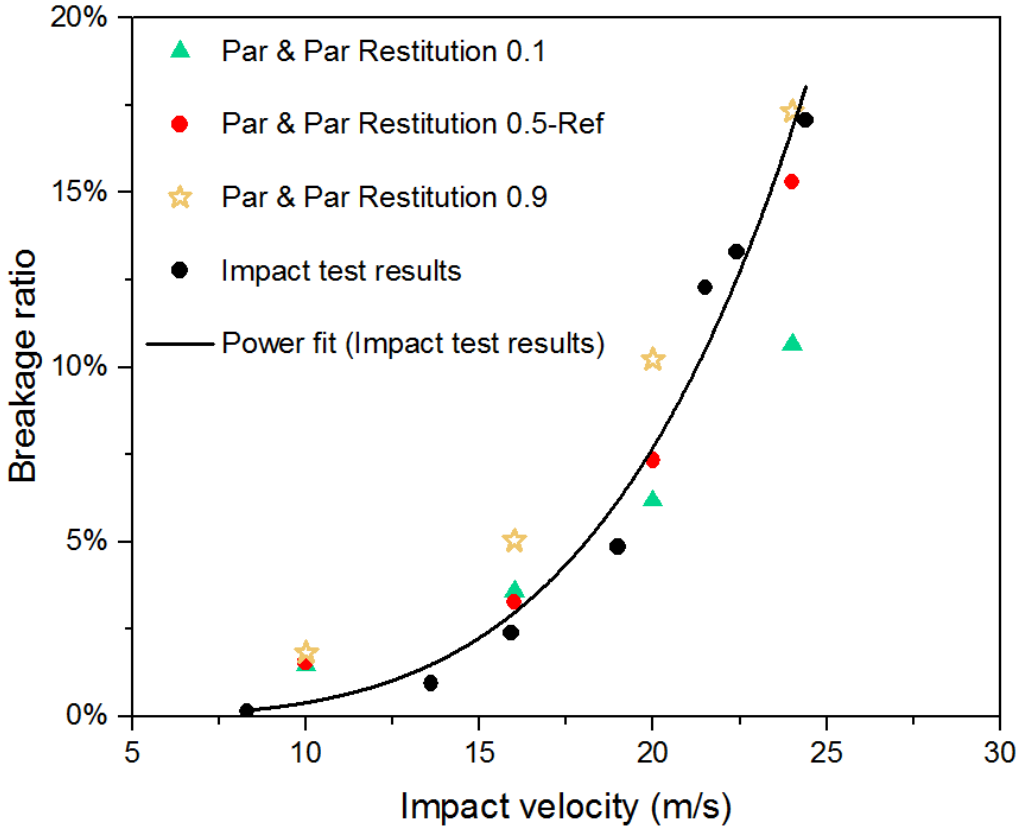

Figure 7.20 Influence of particle & particle restitution coefficient

As seen in Figure 7.20, as the coefficient of restitution increases so does the breakage ratio. This is because particles are more energy active when a higher restitution coefficient is given, which results in a higher breakage ratio. It should be highlighted that the difference of breakage ratio becomes increasingly distinguished as the impact velocity is increased. This demonstrates that the particle & particle restitution coefficient has an increasingly significant effect on breakage ratio with the increase of impact velocity.

7.7.5 Summary of parametric study on the breakage ratio

This parametric study investigates how the variation of key input parameters influences the breakage ratio of bonded particles subjected to normal impact loading. Four relatively influential parameters are chosen for parametric study in this work: bond Young's modulus, mean tensile bond strength, coefficient of variation of bond strength, and restitution coefficient between particles. It was found that the breakage ratio increases with decreasing mean tensile strength or increasing particle & particle restitution coefficient. The bond Young's modulus, mean tensile bond strength and

particle & particle restitution coefficient have an increasing influence on the breakage ratio with the increase of impact velocity. However, the influence of coefficient of variation on the breakage ratio is more pronounced under medium impact velocities (16 m/s and 20 m/s). A summary of the parametric study on breakage ratio is shown in Table 7.6.

Table 7.6 Summary of parametric study on the breakage ratio

Parameters	**Description**	**Breakage ratio**
E_b	Bond Young's modulus	√
S_t	Mean bond tensile strength	↓
ζ	Coefficient of variation of bond strength	√
e_{rp}	Particle & Particle coefficient of restitution	↑

where ↑, ↓ and √ indicate an increase, decrease and non-monotonic influence respectively to the breakage ratio.

7.8 Summary

A DEM simulation of single particle breakage subject to normal impact loading was conducted to characterize the breakage behaviour. A newly developed DEM bond model based on Timoshenko beam theory was utilized, which considers axial, shear and bending behaviour. The DEM simulation of bonded particle breakage subject to normal impact loading was first studied through a reference case using a proposed set of input parameters. Two breakage patterns, chipping and fragmentation, were reproduced under the impact velocity regime. With the increase of impact velocity, the breakage pattern changes from chipping to fragmentation. The main failure mode of bonds is through tension whilst compressive and shear failures are negligible, which provides some micromechanical insight into impact breakage. It suggests that higher impact

velocities lead to a higher plate force, number of broken bonds and damage ratio. With the unification of breakage criteria in DEM simulation and experiment, the predicted breakage ratio shows good agreement with the impact test results although the breakage ratio of DEM simulations is overestimated at l0 m/s.

Combined with previous systematic investigations of input parameters in TBBM and the indication of breakage results from the reference case, four critical parameters were chosen for a parametric study in this work: bond Young's modulus, mean tensile bond strength, coefficient of variation of bond strength, and restitution coefficient between particles. The parametric study investigates how the variation of key input parameters influences the breakage ratio. The breakage ratio increases with decreasing mean tensile strength and increasing particle & particle restitution coefficient. The bond Young's modulus, mean tensile strength and particle & particle restitution coefficient have an increasing influence on the breakage ratio with the increase of impact velocity.

Another point to be highlighted is to project the numerical results from bonded DEM simulation to selection function, which provides an alternative way to scale up the particle-level information to a population balance model (PBM). The upscaling of bonded DEM simulation into the selection function will be presented in the next chapter. As a collaborative project with Hosokawa Ltd UK is continued, the breakage simulation subject to oblique impact and a calibration procedure of the bonded model are underway, which will be reported in due course.

Chapter 8

Population balance model (PBM)

8.1 Introduction

A typical scale-up procedure based on population balance model (PBM) was proposed for milling design in industrial scale by Herbst and Fuerstenau (1980). The scale-up procedure could be divided to three steps according to Datta and Rajamani (2002). First, lab scale milling experiments are carried out under identical or similar operating conditions to obtain the breakage properties of particulates. Second, these properties obtained at lab scale are scaled to larger mills with suitable mathematical models. Finally, the product size distributions are estimated based on the feed particles and milling configuration. In the scale-up procedure utilizing the population balance model (PBM), two functions, i.e. selection and breakage functions have to be considered. As noted in Chapter 2, the breakage probability of a particle is determined by a selection function in the grinding zone, which depends on the operation mode of the grinding machine and the intrinsic quality of the particle. The breakage function describes the size distribution of product particles after grinding, which gives the probability of particles contained in a given size. Both selection and breakage functions are determined from the laboratory scale experiment. By means of selection and breakage functions, PBM has demonstrated its capacity to predict product size in a milling operation (Vogel and Peukert, 2002; Powell and Morrison, 2007; Weerasekara et al., 2013). However, some limitations have been observed in the traditional population balance model to predict the behaviour of industrial-scale mills using the scale-up information from lab-scale experiments. For example, Datta and Rajamani (2002) pointed out that the differences in charge motion between plant-scale and lab-scale mills introduce significant inaccuracies in the prediction. Other criticisms include implicit assumptions of breakage linearity and a lack of link to fundamental breakage parameters (Herbst, 2004).

As noted by Carvalho and Tavares (2009), traditional population balance model is dependent on both the material and milling functions. In other words, the functions determined for a specific type of milling machine cannot be applied to another machine.

With the first application of DEM to comminution by Mishra and Rajamani (1992), the widespread use of DEM has made possible to simulate the mechanical environment inside mills in great details using a combination of Newtonian physics, appropriate contact models and powerful computer routines (Barrios et al., 2011). Furthermore, an alternative way to predict product size distribution is the coupling between DEM and PBM. In this method, DEM is used to describe the mechanical environment whereas the population balance model is used to determine breakage in a mill (King and Bourgeois, 1993; Datta and Rajamani, 2002; Lichter et al., 2009; Carvalho and Tavares, 2009). Quoted from King (1993), it states that 'The really significant advances in comminution technology in the forthcoming decades will only come from the exploitation of basic fundamental understanding of the fracture process to improve industrial comminution processes.' It is thus advocated that the physical development of particle breakage in pursuit of more appropriate selection and breakage functions is greatly needed.

This chapter describes the exploration of population balance model (PBM) by upscaling the information from lab scale to industrial scale. Section 8.2 describes the general form of PBM for a batch grinding process and a microscale breakage model which distinguishes chipping and fragmentation as well as damage accumulation. Section 8.3 presents a flow chart of PBM for product size prediction in a milling operation when coupling with DEM is mobilised. In Section 8.4, the selection and breakage functions determined from single particle impact at lab scale are discussed. Then the information of single particle impact from lab scale is introduced into both selection and breakage functions. Section 8.5 shows an example of PBM to predict product size distribution based on the milling results from impact pin experiments in Chapter 6. DEM simulation of particle breakage in UPZ100 is presented in Section 8.6. A temporal averaging method is utilized to analyse the spatial and temporal distribution of particle size and solid fraction. The radial distribution of particle size and impact velocity is depicted as well using the same temporal averaging method. Concluding remarks are drawn in Section 8.7.

8.2 Population balance models

A general form of population balance model for a batch grinding is given by,

$$\frac{dw_i(t)}{dt} = -S_i w_i(t) + \sum_{j=1}^{i-1} b_{i,j}\, S_j w_j(t) \tag{8.1}$$

where i and j are the size-class indices of size interval; w_i, S_i and $b_{i,j}$ represent mass fraction in class i, selection function or specific breakage rate parameter, and breakage function respectively. The breakage rate (S_i) is assumed to be first-order in the batch mill and the basis of modelling breakage in tumbling mills (Tavares and Carvalho, 2009). In view of uniform breakage rate, Eq. (8.1) is referred to as the linear, time-invariant (LTINV) PBM because the specific breakage rate of particles is only dependent on the particle size, but not on population density and/or time inherently. However, it has been observed by other investigators that the breakage rate often becomes non-first-order for long milling time and coarse particles grinding (Austin, 1971; Austin et al., 1973; Bilgili and Scarlett, 2005; Bilgili, 2007). The possible reasons for the variation of breakage rate during long milling times are due to the temporally changing particle population, interactions among particles of all sizes and force transmission among particles (Bigili and Scarlett, 2005; Wang, 2012).

With the deficiency identified in LTINV model, Austin and Bagga (1981) and Austin et al. (1981) introduced the feature of time-dependence to the specific breakage rate in Eq. (8.1) leading to,

$$\frac{dw_i(t)}{dt} = -S_i w_i(t) + \sum_{j=1}^{i-1} b_{i,j}\, S_j(t) w_j(t) \tag{8.2}$$

As compared to LTINV model, Eq. (8.2) is referred to as linear, time-variant (LTVAR) model.

Since finding an analytical solution to Eq. (8.2) and estimating the pertinent parameters are relatively difficult and laborious, the following assumption is made:

$$S_i(t) = k(t)S_i(t=0) \equiv k(t)S_{i0} \tag{8.3}$$

This means that all specific breakage rate parameters change with time in accordance with the same acceleration-deceleration function $k(t)$. Defining θ as an effective first-order grinding time by $\theta = \int_0^t k(t)dt$ or $d\theta = k(t)dt$. Eq. (8.2) becomes

$$\frac{dw_i(\theta)}{d\theta} = -S_i(0)w_i(\theta) + \sum_{j=1}^{i-1} b_{i,j}\, S_j(0)w_j(\theta) \tag{8.4}$$

Further details of LTVAR model and non-linear models of PBM as well as their solutions can be found elsewhere (e.g. Bilgili et al., 2006; Wang, 2012).

Carvalho and Tavares (2009) proposed a general microscale breakage model based on the synergy of breakage mechanisms, material characteristics and mechanical environment to overcome the limitations of traditional PBMs. The generalized population balance model for particles in size class i and component class j is

$$\begin{aligned}\frac{d[w_{ij}(t)M(t)]}{dt} &= w_{ij}^{in}(t)W^{in}(t) + \omega\left[-D_{ij,b} - D_{ij,s} + A_{ij,b} + A_{ij,s}\right] \\ &\quad - w_{ij}^{out}(t)W^{out}(t)\end{aligned} \tag{8.5}$$

where $M(t)$ is the mass of material at time t inside the mill, namely hold-up. $w_{ij}(t)$, $w_{ij}^{in}(t)$ and $w_{ij}^{out}(t)$ are the mass fractions of particles contained in class $i\ j$ in the mill, in the feed and in the discharge streams, respectively. W^{in} and W^{out} are the feed and discharge mass flow rates, respectively. ω is the frequency of stressing events in the comminution machine. Functions A and D represent the rate of appearance and disappearance of material in class $i\ j$ due to fracture whilst subscripts b and s denote body and surface breakage mechanisms. This model was applied to describe grinding in a ball mill, where the mechanical environment was predicted using the Discrete Element Method (DEM). Since this model is based on a description of each stressing event, it can be used to describe particle size reduction in different types of mills using the same fundamental material characteristics (Carvalho and Tavares, 2009). Some key assumptions based on this model are summarized as below:

1. Breakage results are only from the normal component of the collisions.

2. The batch mill is perfectly mixed and all the particles are involved in each collision in the mill.

3. The fracture strength of a particle does not vary if it was produced as a progeny of a low-energy or a high-energy stressing event.

4. Once particles contained in a given size break their fragments, the fracture energy is assumed the same as the original material.

5. The collision energy is equally split by particles present in the active breakage zone.

6. Surface breakage, namely chipping, abrasion and attrition are described by the first-order kinetics with a single rate constant.

8.3 Flow chart of PBM-DEM

Following the footsteps of the work originally carried out in the University of Utah in the early 1990s (King and Bourgeois, 1993), the research group at the Universidade Federal do Rio de Janeiro presented a DEM-PBM coupling to predict breakage in comminution processes. The feature of this approach is to merely use DEM to simulate motion of media and to track the collisions among particles. The task of projecting the collision energy to the models determining the particle response under stressing events is accomplished by the population balance model (PBM). A flow chart of PBM-DEM coupling (Carvalho and Tavares, 2011) is shown in Figure 8.1. The left side of Figure 8.1 shows the model inputs consisting of the information from both feed particles and milling equipment. In terms of DEM simulations, the initial size distribution and contact parameters from the feed particles as well as the design and operational parameters are required. What DEM provides to PBM is the impact energy distribution of feed particles. As the kernel of this coupling approach, the PBM determines the particle size distribution and flow rate as the outcome. Note that the coupling is called one-way if the particle size distribution is not updated to inform the impact energy spectrum.

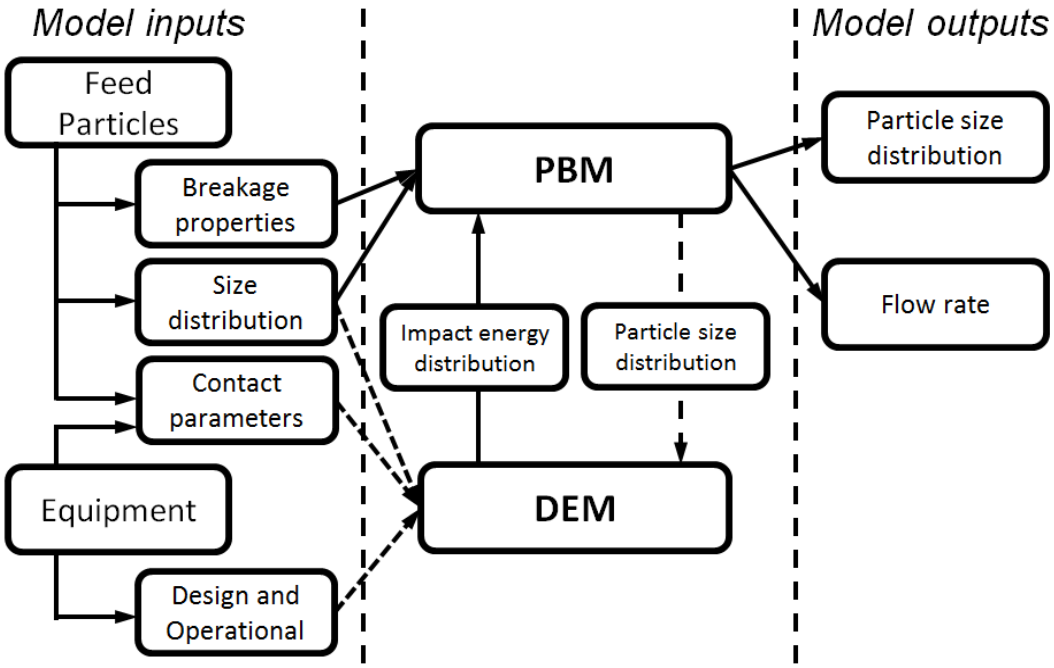

Figure 8.1 Flow chart of population balance modelling for particle size prediction in milling (Modified from Carvalho and Tavares, 2011)

Capece et al. (2014) formulated a particle-scale breakage rate constant of the linear time-variant population model (PBM) for batch dry-milling. It was found that a threshold impact energy must be considered in the analysis of DEM results based on the point that the majority of low energy impacts do not contribute to particle breakage. A framework of unified DEM-PBM to model milling process is shown schematically in Figure 8.2.

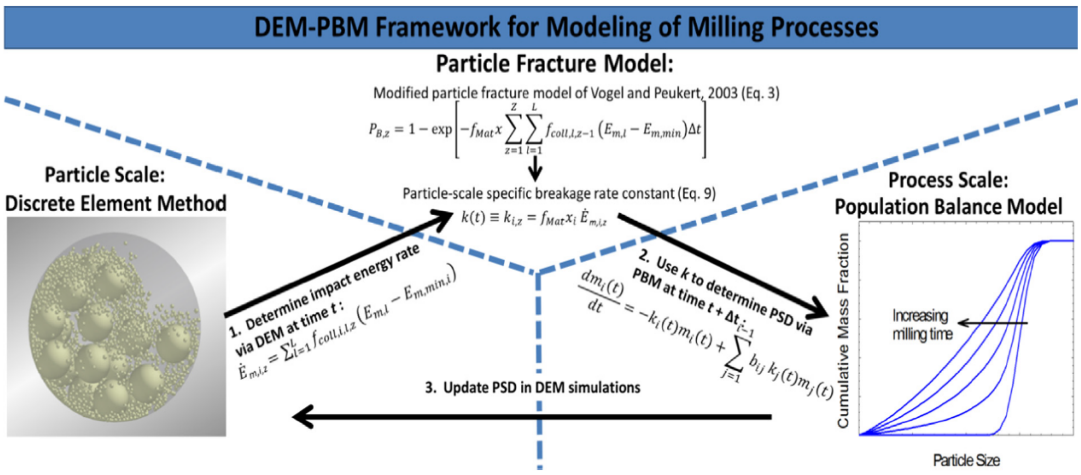

Figure 8.2 A framework of unified DEM-PBM coupling model in milling process After (Capece et al., 2014)

8.4 Scale-up from single particle impact test to PBM

This section explores the information obtained from single particle impact and describes how the information is related to the population balance model. Two functions, the selection and breakage functions are briefly reviewed although they are comprehensively described in Chapter 2. The breakage results obtained in Chapter 3 combined with the numerical results from bonded DEM simulation are exploited to establish its relationship with selection and breakage functions.

8.4.1 Selection function

As noted in Chapter 2, selection function is defined to describe the breakage rate of a particle in a given size range. There are several methods to characterise the selection function on the basis of single particle impact. For example, breakage rate proposed by Ghadiri et al. (1986, 1998, 2002) calculates the mass of debris divided by the total mass of mother particles and debris, which is also adopted to develop a particle breakage model in Chapter 5. Salman and co-workers (1995, 2002) proposed a breakage model defined by the number of broken particles to study particle fragmentation. Vogel and Peukert (2003) defined the breakage probability as the mass fraction of particles smaller than the feed size of a narrow size distribution. As demonstrated by Tavares and King (1998), a threshold of impact energy is required to break a particle catastrophically. This mode of breakage is defined as body breakage, which is represented by the particle fracture energy. The particle fracture energy is dependent on the individual size, shape, internal defection and composition (Barrios et al., 2011). The criterion for body breakage is defined as at least 10% loss of the original particle mass (Tavares, 2007). For a narrow size range of particles, the fracture energy distribution of particles at a given size could be well expressed by an up-truncated log-normal distribution (Tavares and King, 1998).

$$P(E) = \frac{1}{2}\left[1 + erf\left(\frac{lnE^* - lnE_{50}}{\sqrt{2}\sigma_e}\right)\right] \tag{8.6}$$

where E_{50} and σ_e are the median energy and the standard deviation of the distribution. $E^* = \frac{E_{max,i}E}{E_{max,i}-E}$ is the upper truncation of the log-normal distribution.

It should be noted that the particle fracture energy is achieved by stressing a great number of feed particles (typically more than 100) individually of a given size under fixed value of stressing mode. Tavares and King (1998) measured the impact fracture energy for a limestone sample with different size ranges, as shown in Figure 8.3. Note that the results shown in Figure 8.3 were measured by the drop weight impact tester (Tavares and King, 1998).

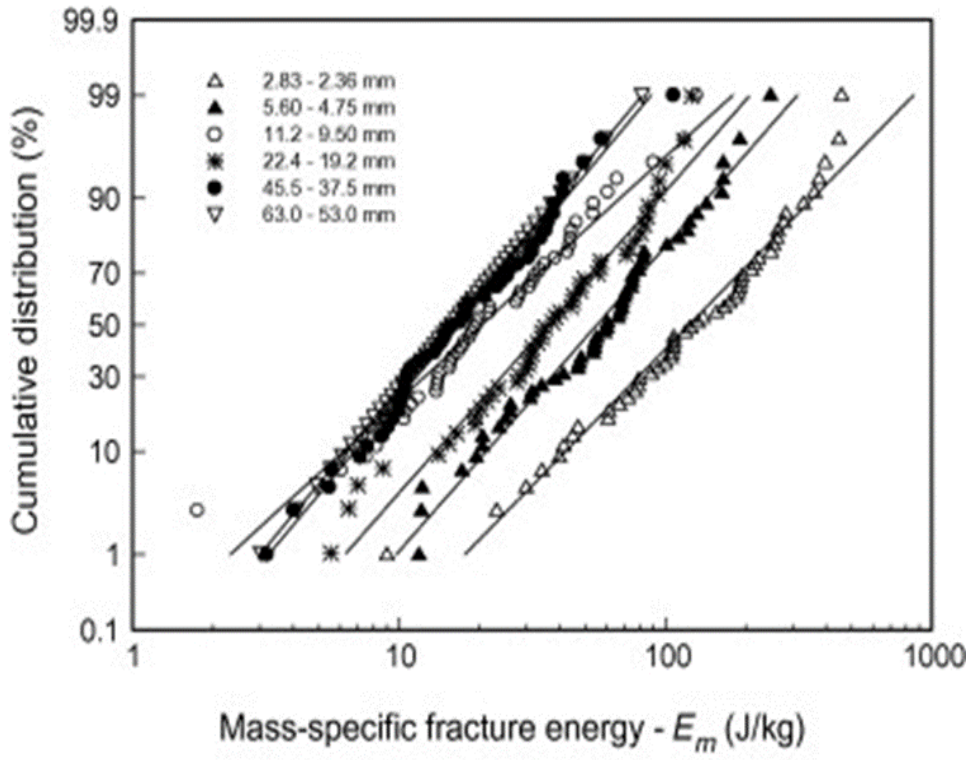

Figure 8.3 Distribution of particle fracture energies of limestone with different sizes (Adopted from Barrios et al., 2011)

As can be seen from Figure 8.3, the specific fracture energy witnesses an increase with decreasing particle size since finer particles become tougher to break. The following equation which relates the specific fracture energy to particle size is given:

$$E_{m50} = E_{m\infty}\left[1 + \left(d_{p,o}/d_p\right)\right]^{\emptyset} \tag{8.7}$$

where E_{m50} is the median of the fracture energy log-normal distribution. $E_{m\infty}$, $d_{p,o}$ and $\emptyset$ are models constants estimated by least-square method. $E_{m\infty}$ and $d_{p,o}$ denote residual fracture energy at larger size and characteristic size of material microstructure.

For simplicity, as noted by Tavares and Carvalho (2009), the maximum fracture energy of particle for a given size is expressed by $E_{max,i} = \eta E_{50,i}$ where η is a constant determined by experimental data.

The results from single particle impact test presented in Chapter 3 indicates that the dominant breakage mechanism is chipping in the impact velocity regime. The particle breakage results subject to impact are limited to the regime where the impact velocity is lower than 30 m/s. The particle size distribution of the zeolite under varying impact velocity is tabulated in Table 8.1.

Table 8.1 Cumulative undersize distribution of single particle impact tests on zeolite (1.4-1.7 mm)

Impact velocity (m/s)	Mass specific impact energy (J/kg)	Cumulative undersize				
		0.6 mm	0.8 mm	1.0 mm	1.18 mm	1.4 mm
8.3	34.45	0.16%	0.21%	0.21%	0.53%	8.75%
13.6	92.48	0.76%	0.93%	1.02%	1.69%	12.71%
15.9	126.41	1.47%	2.03%	2.39%	4.24%	24.49%
19	180.5	2.73%	4.00%	4.78%	6.34%	25.85%
21.5	231.13	5.95%	9.79%	11.71%	14.59%	34.74%
22.4	250.88	4.17%	9.17%	13.33%	18.33%	42.50%
25.3	320.05	8.18%	14.36%	18.70%	27.38%	49.08%
26.4	348.48	12.57%	23.89%	32.39%	44.78%	69.56%

However, analogous to the definition of breakage by Tavares (2007), the fracture probability on the basis of mass-specific fracture energy is illustrated in Figure 8.4, where the breakage is defined as the event in which a particle loses at least 37.5% of its original size. The reason for choosing 37.5% loss of original size is to keep consistent with the breakage ratio defined in Chapter 3. For the zeolite particle ranging from 1.4-1.7 mm, the debris particles below 1.0 mm are defined as breakage. Thus, the breakage probability in this work is the ratio of 1.0 mm to the representative particle size 1.6 mm, which accounts for at least 37.5% size loss as compared to the feed particle.

The fracture energy distribution of zeolite particle (1.4-1.7 mm) is thus obtained based on the collective data from single particle impact test and the breakage probability is shown in Figure 8.4 as well as the fracture energy distribution for smaller particle sizes. The fracture energy distribution for zeolite particle (1.4-1.7 mm) is assumed to follow Eq. (8.6) and the median fracture energy for different zeolite sizes is assumed to follow Eq. (8.7).

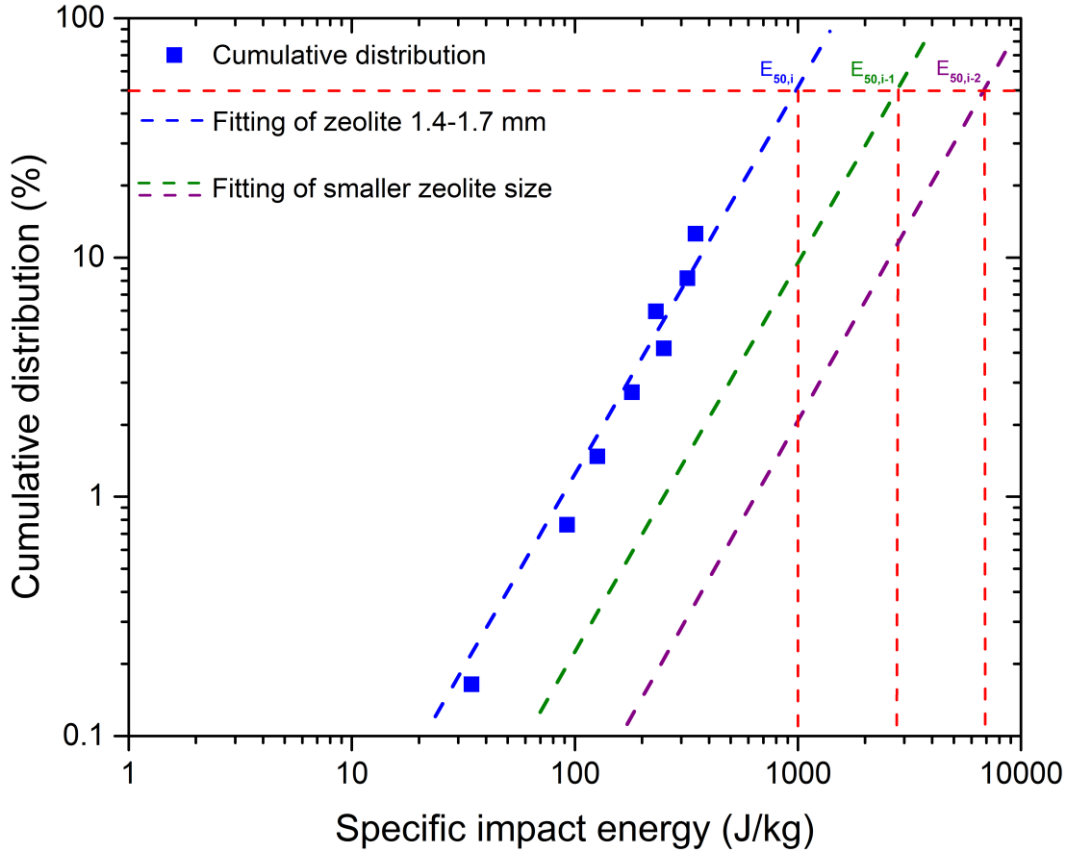

Figure 8.4 Specific impact energy vs. cumulative distribution and extrapolation curve for smaller size zeolite particle

As seen in Figure 8.4, the cumulative distribution arrives at 18.70% under the largest impact velocity of 26.4 m/s whereas the cumulative distribution beyond 26.4 m/s is needed. In addition, the numerical results of the reference case using bonded DEM in Chapter 7 is converted to fracture energy distribution with the same breakage definition as the experiment and plotted for comparison. It can be seen that the fracture energy distribution increasingly converges with the increase of specific impact energy although the disparity at lower specific impact energy is observed. The median fracture energy of smaller size particle could be achieved by further single particle impact or through a calibrated DEM model, which can be the subject for the future research.

8.4.2 Breakage function

Particle size distribution (PSD) is a list of value defined by the mass or size of granular materials. Breakage function is a mathematical function which describes the size distribution of fragments and number of fragments if a particle breaks (Rozenblat et al., 2012). The breakage function is an important indicator of the comminution process and is critically important for modelling purpose. A detailed description of breakage functions found in the literature has been provided in Chapter 2. Amongst these functions, Narayanan and Whiten (1983) proposed a method to characterise the particle size distribution by a one-parameter family of curves since a single reference parameter is used to infer the complete size distribution. In this context, the reference parameter is called t_{10}, which denotes the cumulative percentage passing 1/10 of the initial size. Similarly, the parameter t_n is defined as the cumulative percentage passing 1/n of a given fraction of the initial size. The uniqueness of this method is that the reference parameter t_{10} could be related to other t_{10} parameters on a family of size distribution curve (Shi and Kojovic, 2007). The adaptability of t_n-family curves has been verified for a variety of materials over a wide range of fracture energies by Pauw and Mare (1988) and King and Bourgeois (1993). Therefore, the whole size distribution of particle subject to impact can be determined on condition that the reference parameter t_{10} is measured. The t_n-family curves for a specific size of ore material are depicted in Figure 8.5 (Tavares, 2007), in which the relationships t_{10}-t_2, t_{10}-t_4, t_{10}-t_{25}, t_{10}-t_{50} and t_{10}-t_{75} are established through spline regression analysis.

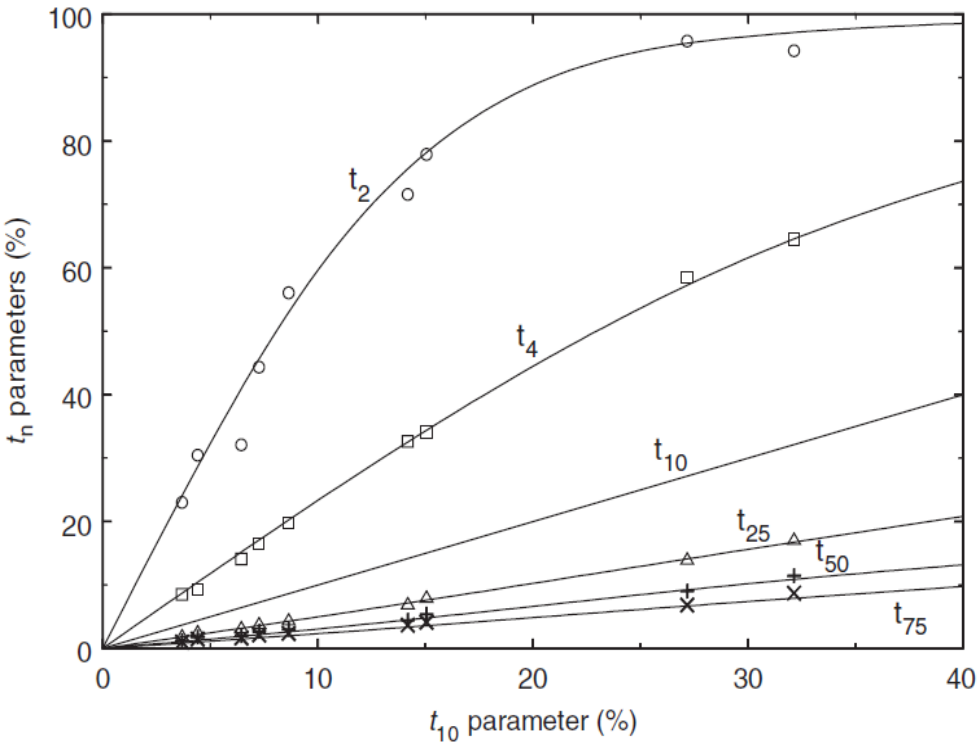

Figure 8.5 Relationship between t_{10} and t_ns for a copper ore. Symbols denote experimental data and lines are fitting curve by splines
(Adopted from Tavares, 2007)

Apart from spline regression analysis, the t_n-family curves can be interpolated by several alternatives including truncated Rosin-Rammler function (King, 2001), logistic distribution and incomplete beta function (Tavares and Carvalho, 2013). For instance, the truncated Rosin-Rammler or logistic distributions can be generated through a transformed size scale (King, 2001). The truncated Rosin-Rammler distribution is expressed

$$P(D) = 1 - \exp\left(-\left(\frac{\eta}{\eta_{63.2}}\right)^{\alpha}\right) \quad for\ D < d_p \tag{8.8}$$

According to the definition of t_{10}

$$t_{10} = P\left(\frac{d_p}{10}\right) = 1 - \exp\left(-\left(\frac{1}{(10-1)\eta_{63.2}}\right)^{\alpha}\right) \tag{8.9}$$

And likewise, t_n is given

$$t_n = P\left(\frac{d_p}{n}\right) = 1 - \exp\left(-\left(\frac{1}{(n-1)\eta_{63.2}}\right)^{\alpha}\right) \tag{8.10}$$

With $\eta_{63.2}$ eliminated from Eqs. (8.9) and (8.10), the relationship between t_{10} and t_n is given

$$t_n = 1 - (1 - t_{10})^{\frac{10-1}{n-1}} \tag{8.11}$$

Similarly, the relationship between $t_{2.67}$ and t_ns for zeolite particle (1.4-1.7 mm) is tabulated in Table 8.2, which can be established by incomplete beta function.

Table 8.2 t_{n} family parameters based on single impact test in Chapter 3

Product size after impact vs. t_n family parameters				
0.6 mm	0.8 mm	1.0 mm	1.18 mm	1.4 mm
$t_{2.67}$	$t_{2.0}$	$t_{1.6}$	$t_{1.36}$	$t_{1.14}$

The incomplete beta function is given by

$$I_x(a,b) = \frac{B_x(a,b)}{B(a,b)} = \frac{1}{B(a,b)}\int_0^x t^{a-1}(1-t)^{b-1}dt \tag{8.12}$$

where $a > 0, b > 0;\ 0 \le x \le 1$. A historical profile of $B_x(a,b)$ is given elsewhere (Dutka, 1981).

The beta function $B(a,b)$ gives

$$B(a,b) = \frac{\Gamma(a)\Gamma(b)}{\Gamma(a+b)} \tag{8.13}$$

where $\Gamma(a)$, $\Gamma(b)$ and $\Gamma(a+b)$ are Gamma Function. For instance, $\Gamma(a)$ is defined by

$$\Gamma(a) = \int_0^\infty t^{a-1} e^{-t} dt \tag{8.14}$$

The incomplete beta function has the symmetry relation

$$I_x(a,b) = 1 - I_{1-x}(b,a) \tag{8.15}$$

Figure 8.6 depicts the incomplete beta function for numerous pairs (a, b).

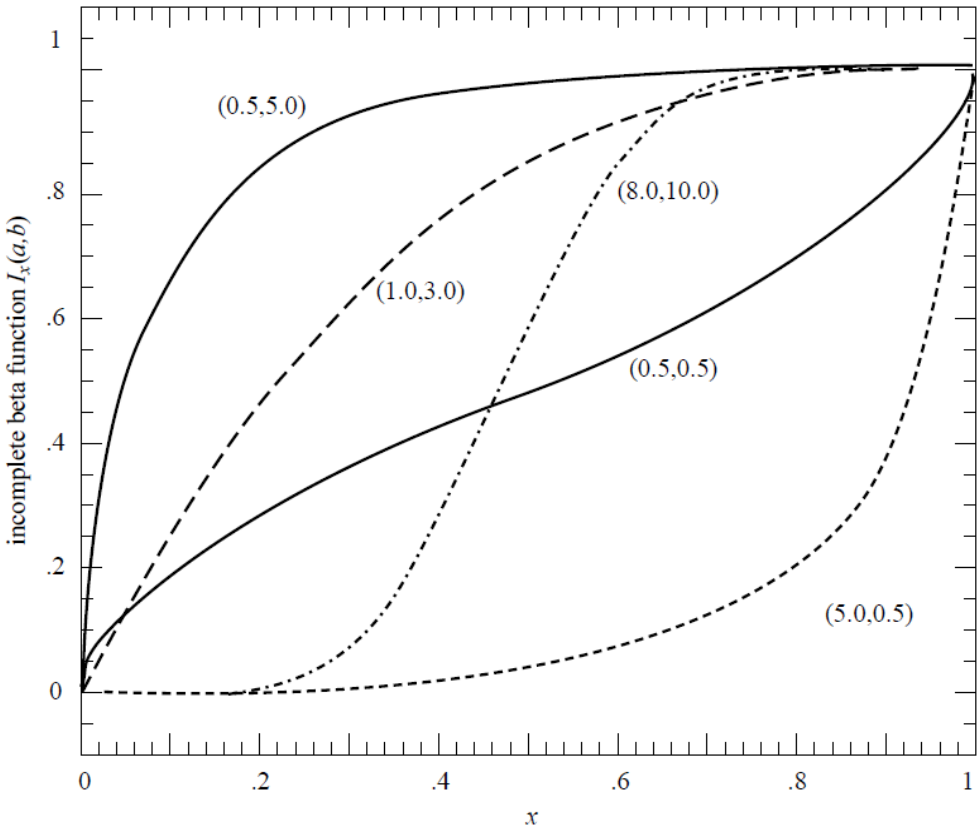

Figure 8.6 The incomplete beta function Ix(a,b) for five different pairs of (a,b). Notice that the pairs (0.5,5) and (5.0,0.5) are related by reflection symmetry around the diagonal (Adopted from The Art of scientific computing second edition)

The pairs of a and b for t_ns as a function of reference parameter $t_{2.67}$ are summarized in Table 8.3 through the incomplete beta function. The relationship between $t_{2.67}$ and t_ns for zeolite (1.4-1.7 mm) is shown in Figure 8.7.

Table 8.3 Relationship between $t_{2.67}$ and t_n family parameters based on single impact test in Chapter 3

t_n \ $t_{2.67}$	*a*	*b*
$t_{2.0}$	1.27	3.08
$t_{1.6}$	1.51	5.43
$t_{1.36}$	1.69	8.71
$t_{1.14}$	0.63	4.34

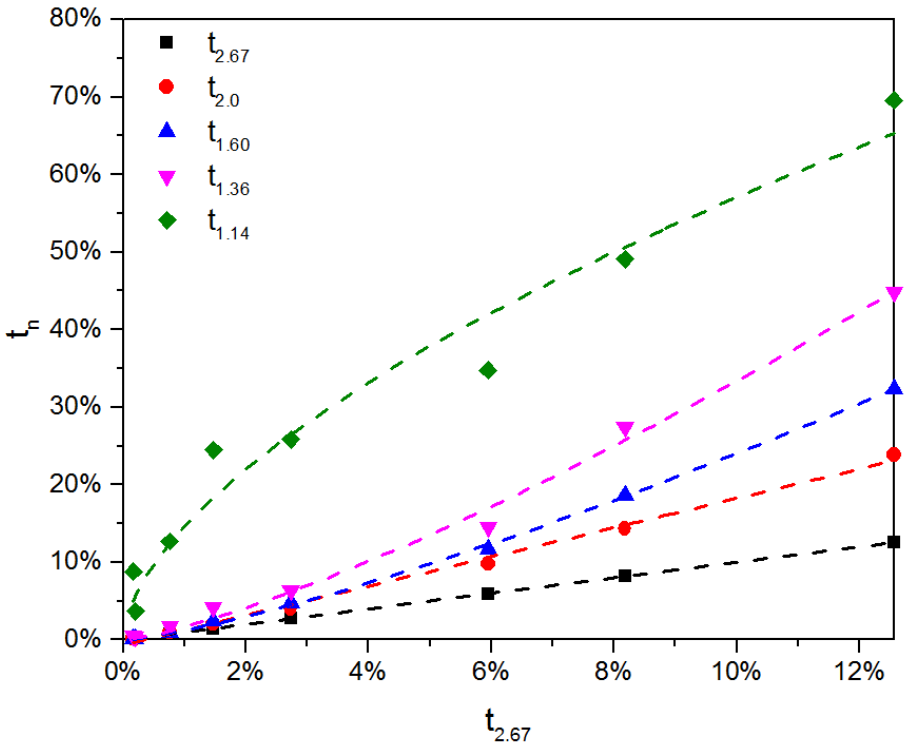

Figure 8.7 Relationship between $t_{2.67}$ and t_ns for zeolite particle (1.4-1.7 mm)

8.5 Example from PBM to predict product size distribution

An example of PBM based on two simple selection and breakage functions is shown below to predict the product size distribution in the impact pin mill. The program used in this work is based on the dissertation of Chimwani (2014) and related paper (Chimwani et al., 2013).

8.5.1 Selection function-Austin et al. (1984)

An empirical selection function proposed by Austin et al. (1984) is as follow

$$S_i = A \cdot x_i^{\alpha} \cdot Q_i = A \cdot x_i^{\alpha} \cdot \frac{1}{1 + \left(\frac{x_i}{\mu}\right)^{\Lambda}} \tag{8.16}$$

where x_i is the maximum limit in the screen size interval i in mm; A is a parameter dependent on mill conditions and material properties, which indicates how fast the grinding is Makokha and Moys (2006); Q_i is the correction factor accounting for abnormal breakage; μ is a parameter dependent on mill conditions; Λ and α are positive constants which are dependent on material properties.

8.5.2 Breakage function-Austin et al. (1984)

An empirical model relating the cumulative breakage function to particle size has been formulated by (Austin et al., 1984):

$$B_{ij} = \phi_j \left(\frac{x_{i-1}}{x_j}\right)^{\gamma} + (1 - \phi_j)\left(\frac{x_{i-1}}{x_j}\right)^{\beta} \tag{8.17}$$

where β is a parameter characteristic of the material used, the value of which is generally greater than 2.5; γ is a material-dependent parameter, the value of which is typically found to be greater than 0.6; ϕ_j is a material-dependent parameter representing the fraction of fines that is produced in a single fracture step. Its value ranges from 0 to 1.

The breakage function in Eq. (8.1) gives

$$b_{ij} = B_{ij} - B_{i-1,j} \tag{8.18}$$

b_{ij} denotes the mass fraction arriving in size interval i from breakage of size j.

8.5.3 Solution scheme

The general solution to Eq. (8.2) is given by Reid (1965) ,

$$w_i(t) = \sum_{j=1}^{i} a_{i,j}\, e^{-S_j t} \tag{8.19}$$

where $a_{i,j}$ is physically interpreted as the fraction f feed size j transferred to size i via the breakage process over time t. Austin et al. (1984) proposed the following expression for the mill transfer function:

$$a_{i,j} = \begin{cases} w_i(0) - \sum_{j=1}^{i-1} a_{i,j} & if\ i = j \\ 0 & if\ i < j \\ \frac{1}{S_i - S_j} \sum_{k=j}^{i-1} S_k \cdot b_{i,k} \cdot a_{k,j} & if\ i > j \end{cases} \tag{8.20}$$

Eqs. 8.16-8.17 give the comprehensive expression of the relationship between feed and product particle size. More information about the above selection and breakage functions as well as the solution scheme for Eq. (8.2) could found in Chimwani (2014). A flow chart for the milling prediction is schematically shown in Figure 8.8 (Chimwani et al., 2013).

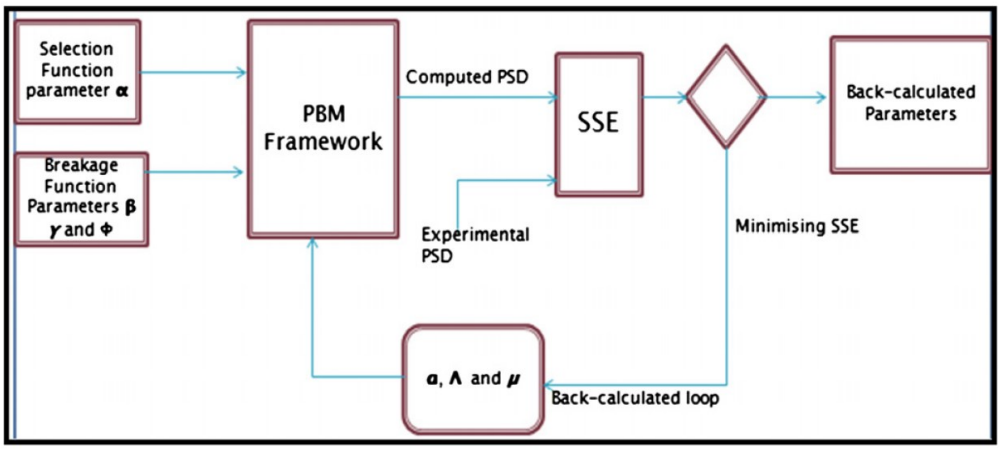

Figure 8.8 Diagrammatic representation of the simulator used for PBM framework After Chimwani et al. (2013)

The parameter α of selection function in Eq. (8.16) was determined based on the plot between the specific breakage rate and particle size. The value of α is defined as the slope of the linear portion of the curve. The three parameters β, γ and ϕ of breakage function in Eq. (8.17) are determined based on the product size distribution, which are considered to be independent of milling conditions. The remaining parameters in selection function are estimated by enabling the best combination of all the parameters to minimize the sum of squared errors (SSEs) between the predicted and experimental product size distribution. The calculation procedure is executed through a parameter fmincon that uses a Sequential Quadratic Programming (QP) method. Once the parameters are determined, the proposed framework is able to predict product size distribution for any given milling period.

8.5.4 PBM prediction results

The predictive product size distribution via PBM is shown in Figure 8.9 based on the milling results under 10000 RPM with four feed rates 9, 14, 19, 24 kg/h. Note that the feed rate is converted to milling time corresponding to 3.75, 2.31, 1.67 and 1.3 minutes respectively. The circle refers to the impact milling results whilst the solid line refers to the predictive results through PBM. The PBM results are in generally good agreement with the milling results.

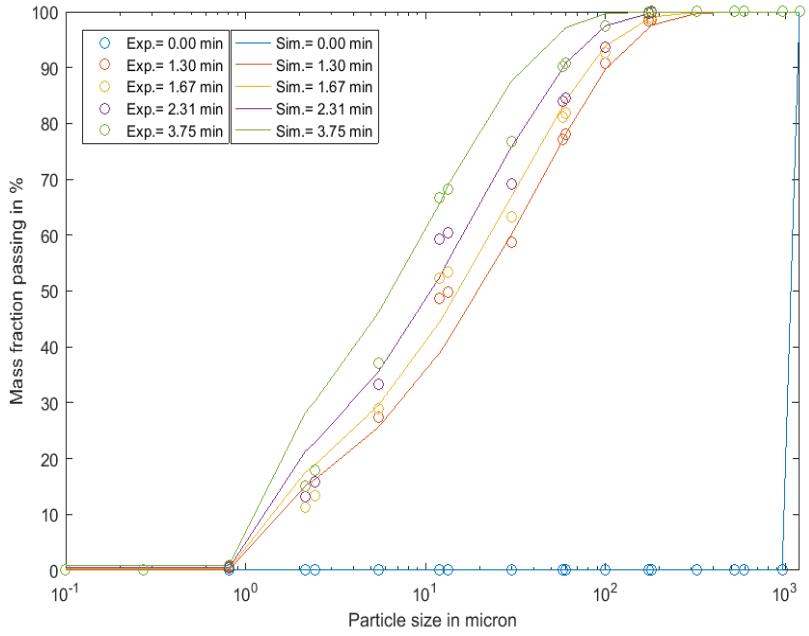

Figure 8.9 Particle size distribution predicted by PBM corresponding to milling results with feed rates 9, 14 19, 24 kg/h under 10000 RPM

8.6 Particle breakage from DEM

The discrete element method (DEM) has been widely used to model the motion and interaction of particles in a number of milling process (Tuzcu and Rajamani, 2011; Wang et al., 2012; Tavares, 2016). The particle dynamics and the interaction between particle and machine kinematics have been shown in the previous section (Labra et al., 2013). This section presents preliminary results of DEM simulation in the real-geometry impact pin mill and discusses how the particle dynamics could be utilized as a function of impact energy spectrum. The particle breakage in UPZ 100 is investigated as an exploratory study. This section was collaborated with Dr. Carlos Labra.

8.6.1 Model of impact pin mill UPZ 100

The real geometry model of the impact pin mill UPZ100 is adopted for the numerical modelling. The specification of the numerical model is exactly the same as the selective impact pin mill in Chapter 6. The mill is 600 mm in diameter and consists of eight rings of pin with four stationary rings and four rotary pins respectively. The pins in each ring are 3 mm in diameter and 15 mm in length. The pin spacing is radially reduced outwards considering the reduction of particle size. The numerical model of the impact pin mill UPZ100 is shown in Figure 8.10. The diameter of feed particle is fixed as 0.956 mm as the nominal size. The particle density is normalized as 1000 kg/m^3.

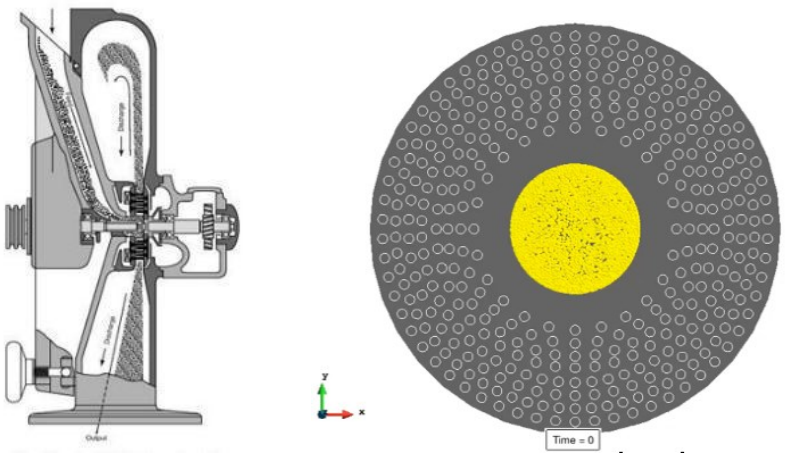

(a) (b)

Figure 8.10 Schematics of pin mill (a) and real-geometry numerical model (b)

The normal contact stiffness and tangential contact stiffness are assumed to be 106 N/m and 10.6 N/m respectively. The Coulomb friction coefficient is assumed to be 0.5.

Initially the particles are fed into the milling chamber through the central inlet at the constant velocity 10 m/s. Note that the influence of the initial feed velocity is not considered significant, which was reported in the IFPRI Annual report (Labra et al., 2013). Once the particles are fed into the mill, they are accelerated by the centrifugal forces and transmitted towards the impact zone where the rotary and stationary pin rings are interlaced. Labra et al. (2013) presented a DEM simulation of particle dynamics and impact events in a simplified impact pin mill in which a DEM model with unbreakable particles is employed. It was found that particle-pin impact accounts for 88% of the statistic of overall impact events with particle-particle 5% and particle-mill discs 7%. This underpins the fact that the particle-pin impact is the dominant impact event in the configured mill. An important finding arising from the analysis of impact events is that only one third of the impacts have incidence angles of more than 80^o (normal for 90^o). This implies that the published literature on measuring particle breakage with normal impact may underestimate the size reduction ratio. Besides, it was shown that the number of impacts per particle reduces exponentially as the impact velocity increases. The frequency, velocity and force distribution between particles and mill components can be found in more details in Labra et al. (2013).

8.6.2 Exploration of particle dynamic from DEM

As DEM provides the particle dynamics in a milling operation, it then comes up with the question how to define the impact energy spectrum based on the particle dynamics. The schematic of impact energy spectrum based on particle dynamics is shown in Figure 8.11. E_k is the collision energy and λ_k is the frequency of the *k*th level collision in collisions per second. As indicated from the literature survey, three methods are usually adopted to define the impact energy by researchers (Tavares, 2016), namely the kinetic energy, the dissipated energy and the maximum impact energy.

The kinetic energy in the collision is defined as:

$$E_k = 1/2mv_{ij}^2 \tag{8.21}$$

where $v_{ij} = v_i - v_j$ is the relative normal velocity at the collision and $m = 1/2(m_i + m_j)$ is the average mass for particle-particle collision whereas the reduced mass $m_r = 2m_i m_j/(m_i + m_j)$ is often used to calculate the collision energy (Kwan et al., 2005).

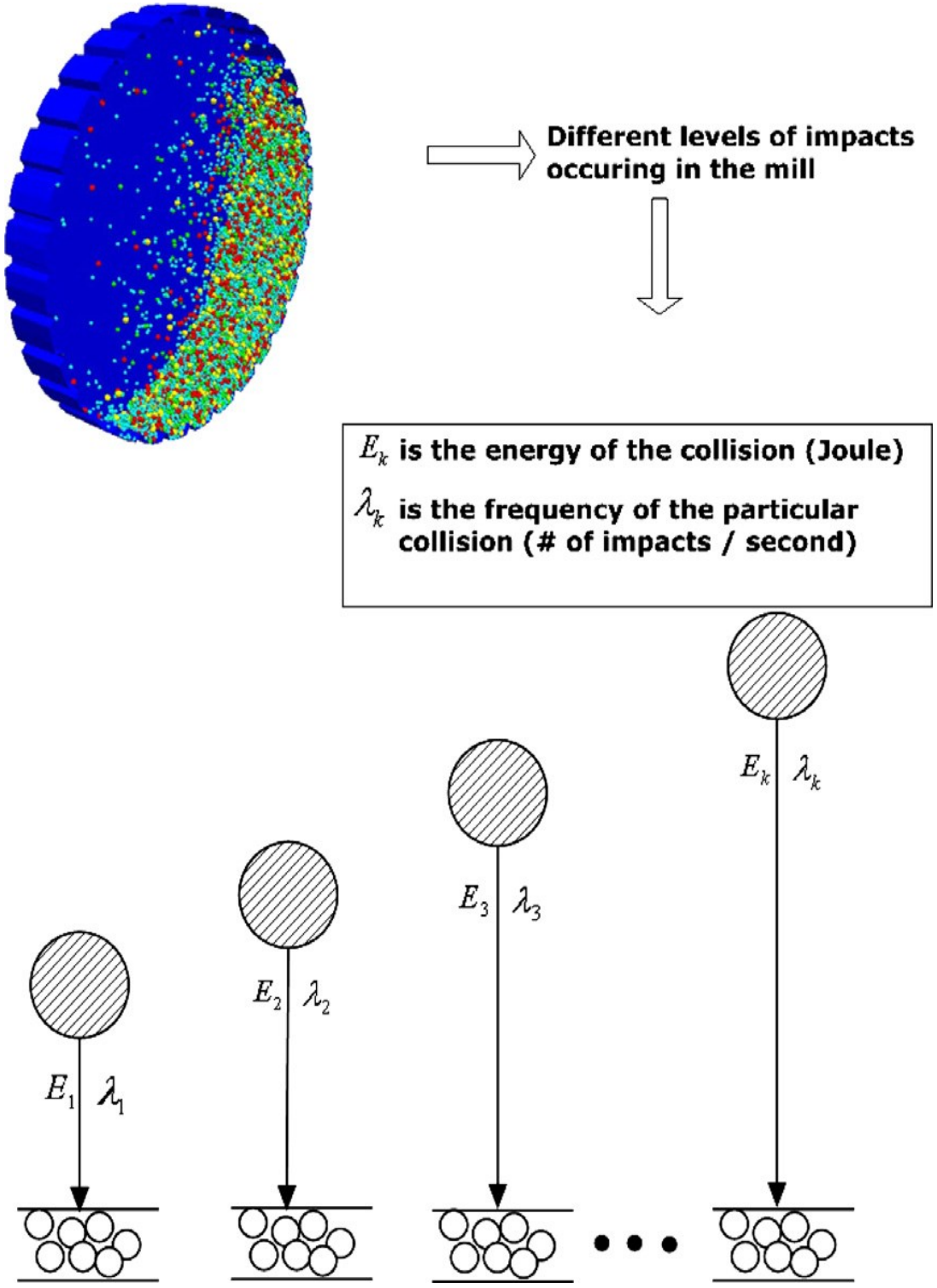

Figure 8.11 Frequency of collisions occurring in a grinding mill

(After Tugcan and Rajamani, 2011)

The dissipated energy results from inelastic contact between the milling media and particle during processes such as plastic deformation or breakage. It is defined as the integral of the damping force with regard to the displacements, including the contributions of both the normal and the shear component of the contact.

$$E = E_n + E_s = \int_0^{t_{contact}} (F_n d\varepsilon_n + F_s d\varepsilon_s) \tag{8.22}$$

where F_n and F_s are the components of the contact force in the normal and shear directions respectively. $t_{contact}$ is the total contact time during a collision.

The maximum impact energy is to characterize the maximum stress experienced by a particle and is the integral of the contact force and displacement in the normal direction when the overlap between two particles reaches the maximum (Wang et al., 2012).

$$E = \int_0^{\varepsilon_{n,max}} \left(F_{ij}^n d\varepsilon_n\right) \tag{8.23}$$

The three types of impact energy have been investigated by Wang et al. (2012). By linking the impact energy with PBM, the product size distributions in a ball mill were predicted with the three types of impact energy. It was found that the kinetic energy can be used directly to predict produce sizes without a need of data fitting. Another two types of impact energy, on the other hand, requires an adjustable parameter which needs to be calibrated.

8.6.3 UPZ100 with particle breakage

Particle breakage in the UPZ100 impact pin mill is investigated via DEM in which the breakage criteria based on relative normal velocity is used. It is assumed that mother particle is broken into 2 daughter particles with half size and without overlap when relative normal velocity is over 30 m/s. The representative diameter of feed particles is 0.956 mm and the rotary speed is set as 10000 RPM with milling duration 1s. The result of particle breakage in milling time 0.1125s is depicted in Figure 8.12. It can be seen that the minimum particle diameter is reduced to 0.239 mm at the milling time of 0.1125s.

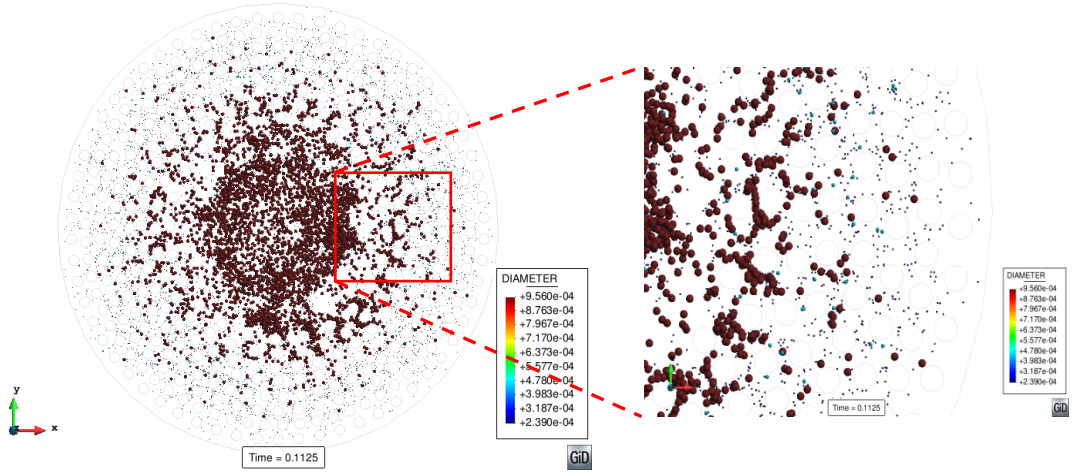

Figure 8.12 Particle breakage in UPZ100 at a specific time step (0.1125s)

As shown in Figure 8.12 is an instantaneous snapshot of the particle breakage at a specific time step. However, due to the large scale simulations of industrial problems and a significantly small time step, a temporal technique stacking successive time steps is needed to allow for a better visualization of the computed breakage results. A technique developed by Particle Analytics (2015) is used to analyse the temporal average of the breakage results. In terms of spatial averaging, a Gaussian weight function is selected with a width of 2 mm and a cutoff value of 6 mm. The temporal averaging is assigned with a Heaviside function considering a sampling frequency of 2 kHz. Further details of the implementation and influence of the parameters have been reported in Labra et al. (2013). The temporal average of particle size distribution and solid fraction over 1 second of simulation is shown in Figure 8.13.

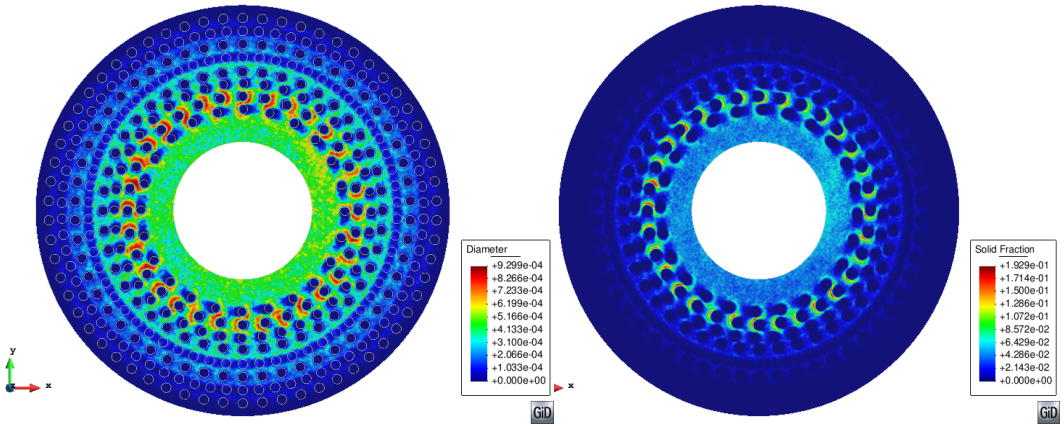

(a) (b)

Figure 8.13 Spatial and temporal averaging of diameter (a) and solid fraction (b)

In Figure 8.13 (a), the averaging of particle size is reduced when heading to the first ring of rotary pin. Then the averaging of particle size is increased towards the first ring of stationary pin. This is due to the fact that more particles are broken at rotary pin ring as compared to the stationary pin ring. Then the averaging of particle size gradually decreases towards the outer pin ring. The averaging of solid fraction in Figure 8.13 (b) appears to follow the same trend of particle size distribution. It would be very interesting to plot the particle size distribution along the radial direction as shown in Figure 8.14.

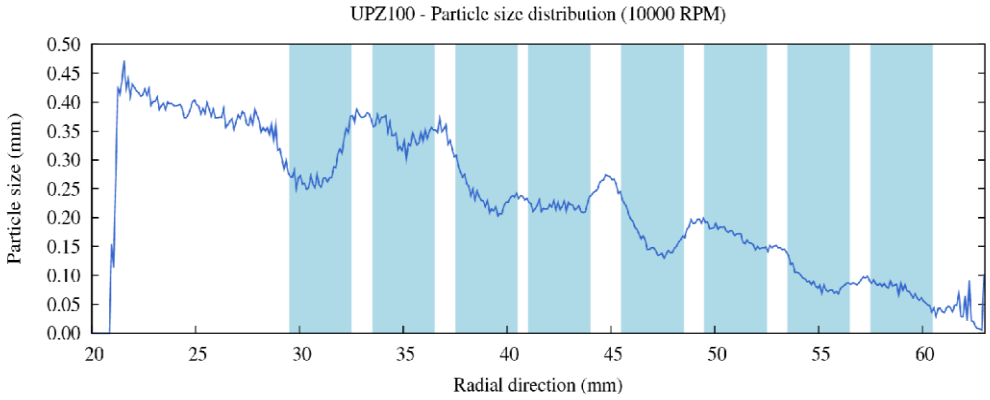

Figure 8.14 Particle size (radius) distribution along the radial direction

Figure 8.14 shows that the particle size gradually decreases when heading to the first rotary pin ring and then increases between the neighbouring pin rings. The particle size in rotary pin mill is smaller than that in the neighbouring stationary pin mill. This may lead to a conclusion that the rotary pin ring is more effective than the stationary pin ring in the UPZ100 pin mill. It indicates from Figure 8.14 that the particle size distribution does not decrease monotonically along the radial direction. This infers that the rotary pin is most effective in particle breakage whilst the gap between the rotary and stationary pin is least effective in particle breakage.

Another important aspect is the velocity distribution along the radial direction as shown in Figure 8.15. It can be seen that the total velocity in the rotary pin ring is basically larger than that in the neighbouring stationary pin ring. It should be noted that the tangential component velocity is much larger than the radial component velocity. This suggests that more attention of the contribution from tangential component velocity should be paid in the UPZ100 pin mill.

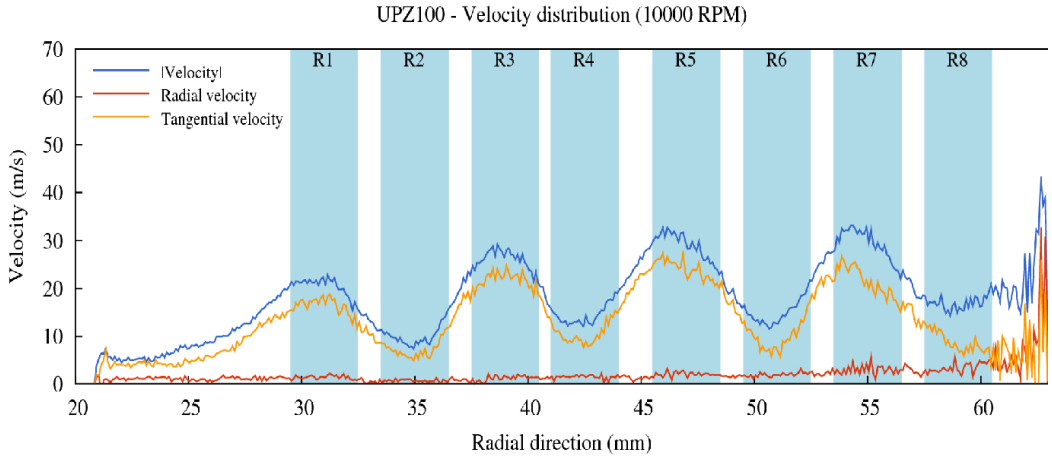

Figure 8.15 Velocity distribution along radial direction

The exploration of particle dynamics and the breakage behaviour under different rotary speeds is beyond the scope of this thesis considering the time constraint, which will form an interesting topic in the follow-on research.

8.7 Summary

This chapter aims to improve the understanding of population balance model (PBM) by upscaling the information from lab scale to industrial scale. Because of its simplicity and flexibility, the population balance model is widely used in the comminution process. As indicated by the general form of PBM, it shows that two functions, i.e. breakage and selection functions have to be considered. The two functions are explored based on the information from single particle impact test in Chapter 3 and the bonded DEM simulation of particle impact in Chapter 7. The bonded DEM simulation of particle impact has shown its potential as an alternative to make a connection with selection function on condition that a proper calibration process is conducted. The capacity of PBM is exemplified by predicting product size distribution in the impact pin mill considering two simple selection and breakage functions. A good closeness is reached between the milling results and the predictive results via PBM.

A preliminary study of particle dynamics in impact pin mill UPZ 100 was carried out to characterise the impact events and explore the impact energy spectrum. It has shown that the particle-pin impact is the dominant impact event in the configured mill. Another finding infers that measuring particle breakage only with normal impact may underestimate the size reduction ratio. The literature survey indicates that the impact

energy linking with PBM is expressed by three types, namely kinetic energy, dissipated energy and the maximum impact energy. It was found that kinetic energy can be used directly to predict produce sizes without a need of data fitting. A temporal averaging method of particle breakage in impact pin mill was utilized to analyse the spatial and temporal distribution of particle size and solid fraction. The radial distribution of impact velocity suggests that more attention of the contribution from tangential component velocity should be paid in the UPZ100 pin mill. The significance of these findings will be further investigated by coupling DEM with PBM, leading to a deeper scientific understanding of the grindability of granular solids.

Chapter 9

Conclusions and recommendations

The research in this thesis has been carried out to study particle breakage mechanics associated with stressing events that occur in a milling operation. A comprehensive investigation of particle breakage was conducted through a hybrid of experimental, theoretical and numerical methods. The mechanical properties were measured by indentation whilst particle breakage subject to impact loading was characterised. The synergy of X-ray μCT and DIC under in-situ loading reveals that strain localisation has formed before fracture at peak force. Considering the limitation of existing models in predicting breakage under oblique impact and the significance of tangential component velocity identified from experiment, a new particle breakage model was proposed incorporating the effect of impact angle, which enables the contribution of normal and tangential velocity component to be rationalized. The assessment of breakage models including chipping and fragmentation under oblique impact suggests that the equivalent normal velocity proposed in the new model is able to give close prediction with experimental results sourced from the literature. The DEM simulation of particle breakage subject to normal impact loading was carried out using a bonded contact model. The bonded DEM results were validated against experiment where the disparity is highlighted. An exploratory study of population balance model (PBM) was conducted based on single particle impact as a scale-up procedure.

This chapter summarizes the key conclusions emerging from this thesis and gives some recommendations for future research.

9.1 Characterisation of selected solids

Two materials: zeolite 4AK and alumina have been chosen as the test particles with semi-brittle and brittle failure expected respectively. The hardness and Young's modulus were determined by nanoindentation whilst fracture toughness was determined by microindentation combined with SEM to measure the length of initiated crack. It was found that alumina has the greater value of hardness and Young's modulus than zeolite. The coefficient of variation for zeolite was varied 20-40% whereas the

coefficient of variation for alumina was varied 40-50%. The fracture toughness of alumina was greater than that of zeolite, which indicates that alumina is more resistant to fracture than zeolite. The coefficient of variation of fracture toughness for alumina was relatively low but very high for zeolite with 58% and 89% for the smaller and bigger particles respectively.

Single particle impact test was carried out in a range of impact velocity up to 30 m/s. The breakage propensity of zeolite (1.4-1.7mm) was evaluated subject to impact loading. The breakage ratio of zeolite was observed to increase with the increase of impact velocity and normal component velocity was found to be dominant in particle breakage under oblique impact. The effect of impact angle was investigated by keeping the normal component velocity constant while changing the tangential component velocity. The significance of tangential component velocity was identified to play an increasing role in particle breakage with the increasing impact velocity. This infers that the contribution of tangential component velocity should be considered in the particle breakage model.

In-situ loading test of particle under X-ray μCT was conducted to evaluate the progressive failure of zeolite particle under compression. To ensure a high quality of image, a linear interpolation method was proposed to alleviate the spatial orientation in data collection process. It was observed that the cracks first initiate from the contact area and then propagate parallel to the loading direction resulting in the radial cracks. The dominant breakage pattern was found to be splitting failure with some fragments generated. The combined use of X-ray μCT and DIC allows for the evaluation of strain localization under incremental loading. It was highlighted that the localized zone forms before the peak force and the localized zone is not uniform.

As an exploitation of X-ray μCT, principal curvature at the contact point and its influence on the Young's modulus based on Hertz contact theory were investigated taking the particle shape into account. Two fitting methods, namely 3rd polynomial fitting and circular (spherical at 3D) fitting were used to estimate the principal curvature. A good agreement of principal curvature was reached under 2D and 3D condition for each fitting method. It was found that the Young's modulus changes significantly from

global fitting to local fitting, which demonstrates a non-negligible variation when the influence of principal curvature is considered. A criterion for Young's modulus is thus required in which the particle shape is an important factor.

9.2 Development of particle breakage model subject to impact loading

A breakage model for brittle particulate solids was developed based on a mechanistic approach assuming that the subsurface lateral crack accounts for chipping mechanism. With the deficiencies identified in the existing breakage models and the significance of tangential component velocity confirmed from experiment, the effect of impact angle is incorporated in the developed breakage model, which enables the contribution of normal and tangential component velocity to be rationalized. The assessment of existing breakage (chipping) models as well as the proposed model shows a relatively large scatter in terms of breakage ratio. This infers that one breakage model based on limited test data is likely not to be reliable in another breakage model. Particularly, the velocity exponent cannot be unified for all the literature data and the reason for the lack of velocity exponent generality could be attributed to the complicated load transfer mechanism, simplified assumption of chipping et al. The assessment of breakage models including both chipping and fragmentation under oblique impact suggests that the equivalent normal velocity is able to give close prediction with experimental results. It was found that the breakage propensity only considering normal component velocity is likely to be underestimated if the tangential component velocity is ignored. The mobilization of dynamic friction under oblique impact enables a remarkable unification curve of breakage propensity prediction for various impact angles.

9.3 Bonded DEM simulation of particle impact breakage

A DEM simulation of single particle breakage subject to normal impact loading was conducted to characterize the breakage behaviour. A newly developed DEM bond model based on Timoshenko beam theory was used, which considers axial, shear and bending behavior. Through a reference case with a proposed set of input parameters, the bonded DEM simulation of particle breakage subject to normal impact loading was studied. With the increase of impact velocity, it was found that the breakage pattern was transmitted from chipping to fragmentation. The main failure mode of bonds is through tension whilst compressive and shear failures are negligible. It suggests that higher

impact velocities lead to higher plate force, number of broken bonds and damage ratio. With the same breakage criterion in DEM simulation and experiment, the bonded DEM simulation results were validated against experimental results, which shows good agreement despite the overestimation of breakage ratio from DEM simulation at 10 m/s.

Four critical parameters were chosen for parametric study, including bonded Young's modulus, mean tensile bond strength, coefficient variation of bond strength, and restitution coefficient between particles. It demonstrates that the breakage ratio increases with the decrease of mean tensile bond strength and the increase of particle & particle restitution coefficient. The bond Young's modulus, mean tensile strength and particle & particle restitution coefficient have an increasing influence on the breakage ratio with the increase of impact velocity.

9.4 Milling tests in impact pin mill

Impact pin mill test was carried out to study particle breakage through an impact pin mill UPZ 100. Two types of particles, zeolite (1.2-2.0 mm; 2.0-2.5 mm) and alumina (1.0-1.18 mm) are chosen under impact pin milling operation. The rotary speed was varied at 8000, 10000, 12000 and 18000 RPM whilst the feed rate was varied at 9, 14, 19, 24 kg/h in every rotary speed test. The effect of rotary speed and feed rate on the milling performance was analyzed. It was found that the rotary speed is more influential on the product particle size distribution than the feed rate. Considering the popularity and ease of interpretation, six parameters, namely fineness, median product size, relative size span, bond's grinding energy, size reduction ratio and specific surface area were selected to characterize the milling results. It shows that the minimum median particle size and fineness of product are achieved at the highest rotary speed 18000 RPM and the lowest feed rate 9 kg/h. The smallest relative size span for zeolite (1.2-2.0 mm and 2.0-2.5 mm) is obtained at the rotary speed 18000 RPM whilst the smallest relative size span for alumina (1.0-1.18 mm) is obtained at the rotary speed 8000 RPM. It was observed that the grinding energy follows a linear relationship with the size reduction ratio. The alumina particle needs more grinding energy as compared to the zeolite particle. The specific surface area was observed to follow a power law with the median size of product size. The collective data presented via impact pin mill provides the basis for the validation of numerical simulation.

9.5 Population balance model and its coupling with DEM

Population balance model (PBM) was investigated by upscaling the information from lab scale to industrial scale. Two functions, i.e. breakage and selection functions were emphasized in the general form of PBM. The two functions were explored based on the information from single particle impact test and the bonded DEM simulation of particle impact. The single particle impact tests were exploited to establish the fracture energy distribution in the selection function. As an alternative, the bonded DEM simulation of particle impact has shown its potential to make connection with selection function on condition that a proper calibration process is conducted. The predictive capacity of PBM is shown by predicting the product size distribution in the impact pin mill considering two simple selection and breakage functions. A good closeness was reached between the milling results and the predictive results via PBM. A preliminary study of particle dynamics in impact pin mill UPZ 100 was carried out to characterise the impact events and explore the impact energy spectrum. It was found that the particle-pin impact is the dominant impact event in the configured mill. It should also be noted that measuring particle breakage only with normal impact may underestimate the size reduction ratio. From the perspective of impact energy spectrum based on particle dynamics, it was found that kinetic energy can be used directly to predict produce sizes without a need of data fitting. The radial distribution of impact velocity suggests that more attention of the contribution from tangential component velocity should be paid in the UPZ100 pin mill.

9.6 Recommendation for future research

The thesis has presented the particle breakage mechanism subject to various stressing events pertinent to a milling process. Several areas for future research are outlined below:

- The indentation test was carried out to characterise the mechanical properties of two selected particles: zeolite and alumina. However, the coefficient of variation for the Young's modulus, hardness and fracture toughness was found to be relatively high. The reason for the big scatter of mechanical properties should be investigated.

- Single particle impact test was conducted to evaluate the breakage propensity up to 30 m/s. The impact test beyond 30 m/s is required to establish a full fracture

probability curve for zeolite particles. Since zeolite particles are mostly tested in the thesis, tests with alumina particle will be helpful to quantify its breakage subject to impact loading.

- X-ray μCT has been used to characterize the progressive failure of particle under compression and to investigate the influence of contact curvature on the Young's modulus. Improved DIC analysis should be performed to quantify the relative displacement of deformed particle after peak load with large discontinuities. A criterion for Young's modulus should be proposed in which the particle shape is a non-negligible factor.

- A new particle breakage model was developed based on a mechanistic approach in the regime of chipping. The equivalent normal velocity has shown its applicability to unify the breakage curve for various impact angles. However, the assessment of velocity exponent in all the breakage models presents a lack of velocity exponent generality. Furthermore, a physical foundation for a fragmentation model is still lacking. A physical sound breakage model including both chipping and fragmentation will be an interesting subject for the future research.

- The particle breakage subject to normal impact loading was investigated with a bonded contact model. A reference case simulation of particle breakage was shown using a proposed set of input parameters. Four critical parameters were chosen for parametric study. A full examination of input parameters in the contact model and a proper calibration process for the bonded contact model should be studied. Furthermore, the particle breakage subject to oblique impact loading is required and the breakage results should be compared with the proposed breakage model under oblique impact.

- The population balance model was investigated with emphasis on selection and breakage functions. This work exemplifies the predictive capacity of PBM with two simple selection and breakage functions. With further impact tests at higher impact velocity or a properly calibrated bonded contact model, the parameters in both selection and breakage functions will be properly estimated. Current work does not

compare the performance of three types of impact energy in predicting product size distribution. The coupling of DEM with PBM should be studied considering the influence of impact energy selection and the contribution of tangential component velocity in product size prediction.

Reference

Akono, A.T., Reis, P.M., Ulm, F.J., 2011. Scratching as a fracture process: From butter to steel. Physical Review Letters 106, 2–5.

Ali, M., Bonakdar, T., Ghadiri, M., Tinke, A., 2015. Particle Breakage in a Scirocco Disperser. Powder Technology 285, 138–145.

Allais, I., Edoura-Gaena, R.B., Gros, J.B., Trystram, G., 2006. Influence of egg type, pressure and mode of incorporation on density and bubble distribution of a lady finger batter. Journal of Food Engineering 74, 198–210.

Alshibli, K. a., Cil, M.B., 2012. 3D assessment of fracture of sand particles using discrete element method. Géotechnique Letters 2, 161–166.

Alvarado, S., Alguerno, J., Auracher, H., Casali, A., 1998. Energy and Exergy Optimization of Comminution. Energy 23, 153–158.

Aman, S., Tomas, J., Kalman, H., 2010. Breakage probability of irregularly shaped particles. Chemical Engineering Science 65, 1503–1512.

André, D., Iordanoff, I., Charles, J.L., Néauport, J., 2012. Discrete element method to simulate continuous material by using the cohesive beam model. Computer Methods in Applied Mechanics and Engineering 213–216, 113–125.

Andrew, J.P., 1930. Theory of collision of spheres of soft metals. Philosophical Magazine 9 (58), 593.

Andrews, E.W., Kim, K.S., 1999. Threshold conditions for dynamic fragmentation of glass particles. Mechanics of Materials 31, 689–703.

Anstis, G.R., Chantikul, P., Lawn, B.R., Marshall, D.B., 1981. A critical evaluation of indentation techniques for measuring fracture toughness: I, Direct crack measurements 46, 533–538.

Antonyuk, S., Heinrich, S., Tomas, J., Deen, N.G., Van Buijtenen, M.S., Kuipers, J.A.M., 2010. Energy absorption during compression and impact of dry elastic-plastic spherical granules. Granular Matter 12, 15–47.

Antonyuk, S., Khanal, M., Tomas, J., Heinrich, S., Mörl, L., 2006. Impact breakage of spherical granules: Experimental study and DEM simulation. Chemical Engineering and Processing: Process Intensification 45, 838–856.

ASAE Standard, 1998. Compression test of food materials of convex shape. American Society of Agricultural Engineering S368.3, 580–587.

Austin, L.G., 1971. Introduction to the mathematical description of grinding as a rate process. Powder Technology 5, 1–17.

Austin, L.G., 1973. A commentary on the Kick, Bond and Rittinger laws of grinding. Powder Technology 7, 315–317.

Austin, L.G., Bagga, P., 1981. An analysis of fine dry grinding in ball mills. Powder Technology 28, 83–90.

Austin, L.G., Klimpel, R.R., P.T., L., 1984. Process Engineering of Size Reduction: Ball Milling, Society of. ed. New York.

Austin, L.G., Luckie, P.T., 1971. Methods for determination of breakage distribution parameters. Powder Technology 5, 215–222.

Austin, L.G., Luckie, P.T., 1972. The estimation of non-normalized breakage distribution parameters from batch grinding tests. Powder Technology 5, 267–271.

Avizo, 2012. https://www.fei.com/software/amira-avizo/.

Barrios, G.K.P., De Carvalho, R.M., Tavares, L.M., 2011. Modeling breakage of monodispersed particles in unconfined beds. Minerals Engineering 24, 308–318.

Bergstrom, B.H., 1966. Empirical modification of the Gaudin-Meloy equation. AIME Transactions 45.

Bilgili, E., Scarlett, B., 2005. Population balance modeling of non-linear effects in milling processes. Powder Technology 153, 59–71.

Bilgili, E., Yepes, J., Scarlett, B., 2006. Formulation of a non-linear framework for population balance modeling of batch grinding: Beyond first-order kinetics. Chemical Engineering Science 61, 33–44.

Bonakdar, T., Ghadiri, M., Ahmadian, H., Bach, P., 2015. Impact strength distribution of placebo enzyme granules. Powder Technology 285, 68–73.

Bond, F.C., 1952. Transactions AIME 193, 484.

Bowman, E., Soga, K., Drummond, T.W., 2000. Particle shape characterisation using Fourier analysis. Géotechnique 315, 1–20.

Broadbent, S.R., Callcott, T.G., 1956. A matrix analysis of processes involving particle assemblies. Philosophical Transactions of the Royal Society of London A: Mathematical, Physical and Engineering Sciences 960, 99–123.

Brown, N.J., 2013. Discrete Element Modelling of Cementitious Materials. PhD dissertation, The University of Edinburgh 270.

Brown, N.J., Chen, J.F., Ooi, J.Y., 2014. A bond model for DEM simulation of cementitious materials and deformable structures. Granular Matter 16, 299–311.

Capece, M., Bilgili, E., Davé, R., 2014. Insight into first-order breakage kinetics using a particle-scale breakage rate constant. Chemical Engineering Science 117, 318–330.

Carvalho, R.M., Tavares, L.M., 2009. Dynamic modeling of comminution using a general microscale breakage model, Computer Aided Chemical Engineering. Elsevier Inc.

Carvalho, R.M. de, Tavares, L.M., 2011. DEM-PBM coupling to predict breakage in comminution processes. EDEM Conference.

Chen, Y., Ding, Y., Papadopoulos, D.G., Ghadiri, M., 2004. Energy-Based Analysis of Milling a -Lactose Monohydrate 93, 886–895.

Cheng, Y.., Nakata, Y., Bolton, M.D., 2003. Discrete element simulation of crushable soil. Géotechnique 53, 633–641.

Cheong, Y.S., Salman, A.D., Hounslow, M.J., 2003. Effect of impact angle and velocity on the fragment size distribution of glass spheres. Powder Technology 138, 189–200.

Chimwani, N., 2014. An attainable region approach to optimizing product size distribution for flotation purposes. PhD dissertation, University of the Witwatersrand.

Chimwani, N., Glasser, D., Hildebrandt, D., Metzger, M.J., Mulenga, F.K., 2013. Determination of the milling parameters of a platinum group minerals ore to optimize product size distribution for flotation purposes. Minerals Engineering 43–44, 67–78.

Cho, H., Austin, L.G., 2003. An equation for the breakage of particles under impact. Powder Technology 132, 161–166.

Cho, N., Martin, C.D., Sego, D.C., 2007. A clumped particle model for rock. International Journal of Rock Mechanics and Mining Sciences 44, 997–1010.

Chung, Y.C., Ooi, J.Y., 2011. Benchmark tests for verifying discrete element modelling

codes at particle impact level. Granular Matter 13, 643–656.

CIMNE, 2010. DEMPACK. www.cimne.upc.edu/dempack

CIMNE, 2012. GiD. International Center for Numerical Methods in Engineering. www.gidhome.com

Clayton, C.R.I., Heymann, G., 2001. Stiffness of geomaterials at very small strains. Géotechnique 51, 245–255.

Cleaver, J.A.S., Ghadiri, M., Rolfe, N., 1993. Impact attrition of sodium carbonate monohydrate crystals. Powder Technology 76, 15–22.

Craig R.F., 2004. Craig's soil mechanics, London: Sp. ed.

Cundall, P.A., 1971. A computer model for simulating progressive large-scale movements in blocky rock systems. Proceedings of the Symposium of the International Society of Rock Mechanics, Nancy, France 1, II-8.

Cundall, P.A., Strack, O.D.L., 1979. A discrete numerical model for granular assemblies. Géotechnique 29, 47–65.

Danjo, K., Kato, H., Otsuka, A., Ushimaru, K., 1994. Fundamental study on the evaluation of strength of granular particles. Chemical Pharm. Bull. 42, 2598–2603.

Datta, A., 1999. A model of batch grinding with impact energy spectra. University of Utah.

Datta, A., Rajamani, R.K., 2002. A direct approach of modeling batch grinding in ball mills using population balance principles and impact energy distribution. International Journal of Mineral Processing 64, 181–200.

De Vegt, O., Vromans, H., Faassen, F., Van Der Voort Maarschalk, K., 2005. Milling of organic solids in a jet mill. part 1: Determination of the selection function and related mechanical material properties. Particle and Particle Systems Characterization 22, 133–140.

Deniz, V., 2004. Relationships between Bond's grindability (Gbg) and breakage parameters of grinding kinetic on limestone. Powder Technology 139, 208–213.

Dodds, J., Guigon, P., Pons, M.N., 1998. An experimental study of fragmentation by high velocity impacts on a target and by air jet milling. International Fine Particle Research Institute (IFPRI), ARR27-05.

Du Plessis, H., Kearsley, E.P., Matjie, H., 2007. Effect of grinding time on the particle size distribution of gasification ash and Portland cement clinker. Journal of the South African Institution of Civil Engineering 49, 28–34.

Dutka, J., 1981. The Incomplete Beta Function-a Historical Profile 24.

EDEM 2.6, 2015. DEM Soutions.

EDEM User Guide, 2015. DEM Solutions.

Eisenhart, L.P., 2004. A Treatise on the Differential Geometry of Curves and Surfaces. ISBN 0-486-43820-1, Dover.

Ergenzinger, C., Seifried, R., Eberhard, P., 2011. A discrete element model to describe failure of strong rock in uniaxial compression. Granular Matter 13, 341–364.

Euler, L., 1760. Recherches sur la courbure des surfaces. Memoires de l'academie des sciences de Berlin 119–143.

Evans, A.G., Gulden, M.E., Rosenblatt, M., 1978. Impact Damage in Brittle Materials in the Elastic-Plastic Response Regime. Proceedings of the Royal Society A: Mathematical, Physical and Engineering Sciences 361, 343–365.

Evans, A.G., Wilshaw, T.R., 1976. Quasi-static solid particle damage in brittle solids -- I. Observations, analysis and implications. Acta Metallurgica 24, 939–956.

Finnie, I., 1972. Some observations on the erosion of ductile metals. Wear 19, 81–90.

Folk, R.R.L., Ward, W.W.C., 1957. Brazos River Bar: A study in the significance of grain size parameters. SEPM Journal of Sedimentary Research.

Fuerstenau, D.W., Abouzeid, A.Z., 2002. The energy efficiency of ball milling in comminution. International Journal of Mineral Processing 67, 161–185.

Gaudin, A.M., Meloy., T.P., 1962. Model and a Comminution Distribution Equation for Single Fracture. Trans. SME-AIME 223, 40–43.

Gentzler, M., Michaels, J.N., 2004. Impact attrition of brittle structured particles at low velocities: Rigorous use of a laboratory vibrational impact tester. Chemical Engineering Science 59, 5949–5958.

Ghadiri, M., Moreno-Atanasio, R., Hassanpour, A., Antony, S.J., 2007. Chapter 19 Analysis of Agglomerate Breakage. Handbook of Powder Technology 12, 837–872.

Ghadiri, M., Ning, Z., Kenter, S.., Puik, E., 2000. Attrition of granular solids in a shear cell. Chemical Engineering Science 55, 5445–5456.

Ghadiri, M., Zhang, Z., 2002. Impact attrition of particulate solids. Part 1: A theoretical model of chipping. Chemical Engineering Science 57, 3659–3669.

Goldman, L.W., 2007. Principles of CT and CT technology. Journal of nuclear medicine technology 35, 115-28-30.

Goldman, R., 2005. Curvature formulas for implicit curves and surfaces. Computer Aided Geometric Design 22, 632–658.

Hall, S.A., 2006. A methodology for 7D warping and deformation monitoring using time-lapse seismic data. Geophysics 71, O21.

Hall, S.A., Bornert, M., Desrues, J., Pannier, Y., Lenoir, N., Viggiani, G., Bésuelle, P., 2010. Discrete and continuum analysis of localised deformation in sand using X-ray μCT and volumetric digital image correlation. Géotechnique 60, 315–322.

Hanley, K.J., O'Sullivan, C., Huang, X., 2015. Particle-scale mechanics of sand crushing in compression and shearing using DEM. Soilds and Foundations, 55(5), 1100-1112.

Hare, C., Wang, L.G., Ooi, J.Y., 2014. Characterisation of Particle Grindability by Indentation and Impact. International Fine Particle Research Institute (IFPRI) Annual Report, CRR2014-01.

Harris, C.C., 1968. The application of size distribution equations to multi-event comminution processes. AIME Transactions 343–358.

Herbst, J.A., 2004. A microscale look at tumbling mill scale-up using high fidelity simulation. International Journal of Mineral Processing 74.

Herbst, J.A., Fuerstenau, D.W., 1980. Scale-up procedure for continuous grinding mill design using population balance models. International Journal of Mineral Processing 7, 1–31.

Hertz, H., 1881. Über die Berührung fester elastischer Körper. Journal für die reine und angewandte Mathematik 156–171.

Hosokawa Micron Ltd., http://hosokawa.co.uk/.

Hsieh, J., 2009. Computed tomography: principles, design, artifacts, and recent

advances. Bellingham, WA: SPIE.

Hu, J., Stroeven, P., 2006. Shape Characterization of Concrete Aggregate. Image Analysis and Stereology 25, 43–53.

Hutchings, I.M., 1994. Wear resistant materials-into the next century. Material Science and Technology,10,513-517.

ImageJ, 2013. https://imagej.nih.gov/ij/.

Ipek, H., Goktepe, F., 2011. Determination of grindability characteristics of zeolite. Physicochemical Problems of Mineral Processing 47, 183–192.

Jaeger, J.C., 1967. Failure of rocks under tensile conditions. International Journal of Rock Mechanics and Mining Sciences 4, 219–227.

Johann, R., 1917. On the determination of functions from their integrals along certain manifolds. Translation in [Deans, 2007].

Johnson, K.L., 1992. Contact Mechanics, University of Cambridge.

Johnstone, M., 2010. Calibration of DEM models for granular materials using bulk physical tests. The University of Edinburgh.

Kafui, K.D., Thornton, C., 1993. Powders & Grains 93, the proceedings of the 2nd International Conference on Micromechanics of Granular Media. Balkema, Rotterdam 401–406.

Kalman, H., Rodnianski, V., Haim, M., 2009. A new method to implement comminution functions into DEM simulation of a size reduction system due to particle-wall collisions. Granular Matter 11, 253–266.

Kanda Y. and Kotake N., 2007. Comminution energy and evaluation in fine grinding. Handbook of powder technology 12, 526–547.

Karatza, Z., 2013. Mechanisms of inelastic deformation in sandstone studied by x-ray tomography and image analysis, Master Thesis, Universite Joseph Fourier.

Ketcham, R.A., Carlson, W.D., 2001. Acquisition, optimization and interpretation of x-ray computed tomographic imagery: Applications to the geosciences. Computers and Geosciences 27, 381–400.

Kick, F., 1885. Das Gesetz der proportionalen Widerstande und seine anwendung felix.

Leipzig, Germany.

Kim, J.Y., Lee, J.J., Lee, Y.H., Jang, J. il, Kwon, D., 2006. Surface roughness effect in instrumented indentation: A simple contact depth model and its verification. Journal of Materials Research 21, 2975–2978.

King, R.P., 1993. Comminution research—a success story that has not yet ended. Proceedings XVIII Int Min Proc Congress,Sydney, Publ. AUSIMM 39–45.

King, R.P., 2001. Modeling and Simulation of Mineral Processing Systems. Butterworth-Heinemann.

King, R.P., Bourgeois, F., 1993. Measurement of fracture energy during single-particle fracture. Minerals Engineering 6, 353–367.

Klotz, K., Schubert, H., 1982. Crushing of single irregularly shaped particles by compression: size distribution of progeny particles. Powder Technology 32, 129–137.

Kumara, G.H. a., Hayano, K., Ogiwara, K., 2012. Image analysis techniques on evaluation of particle size distribution of gravel. International Journal of GEOMATE 3, 290–297.

Kun, F., Herrmann, H.J., 1996. A study of fragmentation processes using a discrete element. Computer Methods in Applied Mechanics and Engineering 138, 3-18.

Kun, F., Herrmann, H.J., 1999. Transition from damage to fragmentation in collision of solids. Physical Review E 59, 2623–2632.

Kwan, C.C., Chen, Y.Q., Ding, Y.L., Papadopoulos, D.G., Bentham, A.C., Ghadiri, M., 2004. Development of a novel approach towards predicting the milling behaviour of pharmaceutical powders. European Journal of Pharmaceutical Sciences 23, 327–336.

Kwan, C.C., Mio, H., Chen, Y.Q., Ding, Y.L., Saito, F., Papadopoulos, D.G., Bentham, A.C., Ghadiri, M., 2005. Analysis of the milling rate of pharmaceutical powders using the Distinct Element Method (DEM). Chemical Engineering Science 60, 1441–1448.

Labra, C., 2012. Advances in the development of the discrete element method for excavation processes. Universitat Politecnica de Catalunya.

Labra, C., Ooi, J.Y., Wang, L., Chen, J.-F., 2013. IFPRI Grindability Project 2013 Annual Report.

Lawn, B.R., Marshall, D.B., 1979. Mechanism of Microcontact Fracture in Brittle

Solids. Lithic Use-Wear Analysis.

Lawn, B.R., Swain, M. V., Phillips, K., 1975. On the mode of chipping fracture in brittle solids. Journal of Materials Science 10, 1236–1239.

Lawn, M.V., Swain, B.R., 1975. Microfracture Beneath Point Indentation in Brittle Solids. Journal of Materials Research 113–122.

Lecoq, O., Chamayou, A., Dodds, J.A., Guigon, P., 2012. Application of a simplifying model to the breakage of different materials in an air jet mill. International Journal of Mineral Processing 112–113, 7–12.

Leschonski, K., 1982. Particle size analysis. Wiley Heydon 437–445.

Lichter, J., Lim, K., Potapov, A., Kaja, D., 2009. New developments in cone crusher performance optimization. Minerals Engineering 22, 613–617.

Makokha, A.B., Moys, M.H., 2006. Towards optimising ball-milling capacity: Effect of lifter design. Minerals Engineering 19, 1439–1445.

Malkin, S., Hwang, T.W., 1996. Grinding mechanisms for ceramics. CIRP Annals-Manufacturing Technology 45, 569–580.

Manohar, B., Sridhar, B.S., 2001. Size and shape characterization of conventionally and cryogenically ground turmeric particles. Powder Technology 292–297.

Marrow, J., Reinhard, C., Vertyagina, Y., Saucedo-Mora, L., Collins, D., Mostafavi, M., 2014. 3D Studies of Damage by Combined X-ray Tomography and Digital Volume Correlation. Procedia Materials Science 3, 1554–1559.

McDowell, G.R., Harireche, O., 2002. Discrete element modelling of soil particle fracture. Géotechnique 52, 131–135.

Meier, M., John, E., Wieckhusen, D., Wirth, W., Peukert, W., 2008. Characterization of the grinding behaviour in a single particle impact device: studies on pharmaceutical powders. European journal of pharmaceutical sciences : official journal of the European Federation for Pharmaceutical Sciences 34, 45–55.

Meier, M., John, E., Wieckhusen, D., Wirth, W., Peukert, W., 2009. Generally applicable breakage functions derived from single particle comminution data. Powder Technology 194, 33–41.

Meier, M., Peukert, W., 2007. Characterization of grinding behaviour of fine particulate

solids in a single particle impact device. Partec 2007.

Miller, M., Bobko, C., Vandamme, M., Ulm, F.J., 2008. Surface roughness criteria for cement paste nanoindentation. Cement and Concrete Research 38, 467–476.

Mindlin, R.D., Deresiewicz, H., 1953. Elastic Spheres in Contact Under Varying Oblique Forces. Applied Mechanics 327–344.

Mishra, B.K., 2003. A review of computer simulation of tumbling mills by the discrete element method: Part I-contact mechanics. International Journal of Mineral Processing 71, 73–93.

Mishra, B.K., Thornton, C., 2001. Impact breakage of particle agglomerates. International Journal of Mineral Processing 61, 225–239.

Mishra, B.K.K., Rajamani, R.K., 1992. The discrete element method for the simulation of ball mills. Applied Mathematical Modelling 16, 598–604.

Misra, A., Cheung, J., 1999. Particle motion and energy distribution in tumbling ball mills. Powder Technology 105, 222–227.

Misra, A., Huang, S., 2012. Micromechanical stress-displacement model for rough interfaces: Effect of asperity contact orientation on closure and shear behavior. International Journal of Solids and Structures 49, 111–120.

Moreno-Atanasio, R., Ghadiri, M., 2006. Mechanistic analysis and computer simulation of impact breakage of agglomerates: Effect of surface energy. Chemical Engineering Science 61, 2476–2481.

Moreno, R., Ghadiri, M., Antony, S.J., 2003. Effect of the impact angle on the breakage of agglomerates: A numerical study using DEM. Powder Technology 130, 132–137.

Mori, H., Mio, H., Kano, J., Saito, F., 2004. Ball mill simulation in wet grinding using a tumbling mill and its correlation to grinding rate. Powder Technology 143–144, 230–239.

Morrison, R.D., Cleary, P.W., 2004. Using DEM to model ore breakage within a pilot scale SAG mill. Minerals Engineering 17, 1117–1124.

Morrissey, J.P., 2013. Discrete element modelling of iron ore pellets to include the effects of moisture and fines, PhD thesis, University of Edinburgh.

Müller, P., Seeger, M., Tomas, J., 2013. Compression and breakage behavior of r-Al_2O_3

granules. Powder Technology 237, 125–133.

Müller, P., Tomas, J., 2012. Compression behavior of Moist Spherical Zeolite 4A Granules. Chemical Engineering and Technology 35, 1677–1684.

Narayanan, S.S., 1985. Development of a laboratory single particle breakage technique and its application to ball mill modelling and scale-up. The University of Queensland.

Narayanan S.S. and Whiten S.S., 1983. Breakage characteristics of ores for ball mill modelling. Proceedings of AusIMM 31–39.

O'Sullivan, C., Coop, M., Cavarretta, I., 2010. The influence of particle characteristics on the behaviour of coarse grained soils. Géotechnique 60, 413–423.

Octopus Imaging, 2012. https://octopusimaging.eu/.

Oliver, W.C., Pharr, G.M., 1992. An improved technique for determining hardness and elastic modulus using load and displacement sensing indentation experiments.Journal of Materials Research 6, 1564-1583.

Oliver, W.C., Pharr, G.M., 2004. Measurement of hardness and elastic modulus by instrumented indentation: Advances in understanding and refinements to methodology. Journal of Materials Research 19, 3–20.

Pan, B., Xie, H., Xu, B., Dai, F., 2006. Performance of sub-pixel registration algorithms in digital image correlation. Measurement Science and Technology 17, 1615–1621.

Papadopoulos, D.G., 1998. Impact breakage of particulate solids, PhD dissertation, University of Surrey.

Papadopoulos, D.G., Ghadiri, M., 1996. Impact breakage of poly-methylmethacrylate (PMMA) extrudates: I. Chipping mechanism. Advanced Powder Technology 7, 183–197.

Parab, N.D., Claus, B., Hudspeth, M.C., Black, J.T., Mondal, A., Sun, J., Fezzaa, K., Xiao, X., Luo, S.N., Chen, W., 2014. Experimental assessment of fracture of individual sand particles at different loading rates. International Journal of Impact Engineering 68, 8–14.

Particle Analytics, 2015. http://www.particle-analytics.com/.

Pauw, O.G., Maré, M.S., 1988. The determination of optimum impact-breakage routes for an ore. Powder Technology 54, 3–13.

Peleg, M., Normand, M.D., 1986. Enlargement Processes by a Modified Version of the Beta Distribution Function 32, 1928–1930.

Petukhov, Y., Kalman, H., 2003. A new apparatus for particle impact tests. Particle and Particle Systems Characterization 20, 267–275.

Petukhov, Y., Kalman, H., 2004. Empirical breakage ratio of particles due to impact. Powder Technology 143–144, 160–169.

PFC 3D, 2001., Itasca. http://www.itascacg.com/software/pfc.

Piret, 1953. Fundamental aspects of grinding. Chemical Engineering Progress 49, 56–63.

Potapov, A. V, Campbell, C.S., 1994. Computer Simulation of Particle Breakage. Powder Technology 81, 207–216.

Potyondy, D.O., Cundall, P.A., 2004. A bonded-particle model for rock. International Journal of Rock Mechanics and Mining Sciences 41, 1329–1364.

Powell, M.S., Morrison, R.D., 2007. The future of comminution modelling. International Journal of Mineral Processing 84, 228–239.

Przemieniecki, 1968. Theory of Matrix Structural Analysis, McGraw-Hill, New York.

Reid, K.J., 1965. A solution to the batch grinding equation. Chemical Engineering Science 20, 953–963.

Robertson, D., Bolton, M.. D., 2001. DEM simulations of crushable grains and soils. Powders and Grains 2001: 4th International Conference on Micromechanics of Granular Media.

Rosin, P., Rammler, E., 1933. The laws governing the fineness of powdered coal. Journal of the Institute of Fuel 7, 29–36.

Rozenblat, Y., Portnikov, D., Levy, A., Kalman, H., Aman, S., Tomas, J., 2011. Strength distribution of particles under compression. Powder Technology 208, 215–224.

Rumpf, H., 1973. Physical aspects of comminution and new formulation of a law of comminution. Powder Technology 7, 145–159.

Russell, A., Schmelzer, J., Müller, P., Krüger, M., Tomas, J., 2015. Mechanical properties and failure probability of compact agglomerates. Powder Technology 286,

546–556.

Sadrai, S., 2007. High velocity impact fragmentation and the energy efficiency of comminution. The University of British Columbia.

Salman, A.D., Biggs, C.A., Fu, J., Angyal, I., Szabó, M., Hounslow, M.J., 2002. An experimental investigation of particle fragmentation using single particle impact studies. Powder Technology 128, 36–46.

Salman, A.D., Fu, J., Gorham, D.A., Hounslow, M.J., 2003. Impact breakage of fertiliser granules. Powder Technology 130, 359–366.

Salman, A.D., Gorham, D.A., 2000. The fracture of glass spheres. Powder Technology 107, 179–185.

Salman, A.D., Gorham, D.A., Verba, A., 1995. A study of solid particle failure under normal and oblique impact. Wear 186–187, 92–98.

Samimi, A., Ghadiri, M., Boerefijn, R., Groot, A., Kohlus, R., 2003. Effect of structural characteristics on impact breakage of agglomerates. Powder Technology 130, 428–435.

Samimi, A., Moreno, R., Ghadiri, M., 2004. Analysis of impact damage of agglomerates: effect of impact angle. Powder Technology 143–144, 97–109.

Scala, F., Montagnaro, F., Salatino, P., 2007. Attrition of limestone by impact loading in fluidized beds. Energy and Fuels 21, 2566–2572.

Schönert, 1972. The Role Of Fracture Physics In Understanding Comminution Phenomena. Society for Mining, Metallurgy & Exploration 252, 21–26.

Schreier, H., Sutton, M.A., 2002. Systematic Errors in Digital Image Correlation Due to Undermatched Subset Shape Functions. Experimental Mechanics 42, 303–310.

Schumann, R., 1940. Size distribution and surface calculations. Technical publication, American Institute of Mining and Metallurgical Engineers.

Shashidhar, M.G., Murthy, T.P.K., Girish, K.G., Manohar, B., 2013. Grinding of Coriander Seeds: Modeling of Particle Size Distribution and Energy Studies. Particulate Science and Technology 31, 449–457.

Shi, F., Kojovic, T., 2007. Validation of a model for impact breakage incorporating particle size effect. International Journal of Mineral Processing 82, 156–163.

Shipway, P.H., Hutchings, I.M., 1993. Attrition of brittle spheres by fracture under compression and impact loading. Powder Technology 76, 23–30.

Sikong, L., Hashimoto, H., Yashima, S., 1990. Breakage behavior of fine particles of brittle minerals and coals. Powder Technology 61, 51–57.

Spivak, 1975. A comprehensive introduction to differential geometry.

Couroyer, C., Ghadiri, M., Brunard, N., Kolenda, F., 2005. Analysis of catalyst particle strength by impact testing: The effect of manufacturing process parameters on the particle strength. Powder Technology 160, 67–80.

Subero, J., 1999. Effect of interface energy on the impact strength of agglomerates. Powder Technology 105, 66–73.

Subero, J., Ghadiri, M., 2001. Breakage patterns of agglomerates. Powder Technology 120, 232–243.

Sukovic, P., 2003. Cone beam computed tomography in craniofacial imaging. Orthodontics and craniofacial research 6 Suppl 1, 31-36-182.

Sukumaran, B., Ashmawy, A.K., 2001. Quantitative characterisation of the geometry of discret particles. Géotechnique 51, 619–627.

Sutton, M., Wolters, W., Peters, W., Ranson, W., McNeill, S., 1983. Determination of displacements using an improved digital correlation method. Image and Vision Computing 1, 133–139.

Swain, B.R., Lawn, M.V., 1976. Indentation fracture in brittle rocks and glasses. International journal of rock mechanics and mining science & Geomechanics Abstracts 13, 311–319.

Tabor D., 1951. The hardness of metals. Oxford: Clarendon Press.

Tavares, L.M., 2004. Optimum routes for particle breakage by impact. Powder Technology 142, 81–91.

Tavares, L.M., 2007. Chapter 1 Breakage of Single Particles: Quasi-Static. Handbook of Powder Technology 12, 3–68.

Tavares, L.M., 2016. Hosokawa A review of advanced ball mill modelling 34, 1–19.

Tavares, L.M., de Carvalho, R.M., 2009. Modeling breakage rates of coarse particles in

ball mills. Minerals Engineering 22, 650–659.

Tavares, L.M., King, R.P., 1998. Single-particle fracture under impact loading. International Journal of Mineral Processing 54, 1–28.

Taylor, L.J., Papadopoulos, D.G., Dunn, P.J., Bentham, A.C., Mitchell, J.C., Snowden, M.J., 2004. Mechanical characterisation of powders using nanoindentation. Powder Technology 143–144, 179–185.

The Canadian Fertilizer Institute Guide of Material Selection for the Production of Quality Blends, 1982. , Canadian Fertilizer Institute Ottawa, Ontario, Canada.

Thornton, C., Ciomocos, M.T., Adams, M.J., 1999. Numerical simulations of agglomerate impact breakage. Powder Technology 105, 74–82.

Thornton, C., Yin, K.K., 1991. Impact of elastic spheres with and without adhesion. Powder Technology 65, 153–166.

Thornton, C., Yin, K.K., Adams, M.J., 1996. Numerical simulation of the impact fracture and fragmentation of agglomerates. J. Phys. D: Appl. Phys. 29, 424.

Timoshenko, S.P., 1922. On the transverse vibrations of bars of uniform cross-section. Philosophical Magazine 43, 125–131.

Tong, W., 2005. An evaluation of digital image correlation criteria for strain mapping applications. Strain 41, 167–175.

Tsoungui, O., Vallet, D., Charmet, J.C., 1999. Numerical model of crushing of grains inside two-dimensional granular materials. Powder Technology 105, 190–198.

Tsuji, Y., Tanaka, T., Ishida, T., 1992. Lagrangian numerical simulation of plug flow of cohesionless particles in a horizontal pipe. Powder Technology 71, 239–250.

Tuzcu, E.T., Rajamani, R.K., 2011. Modeling breakage rates in mills with impact energy spectra and ultra fast load cell data. Minerals Engineering 24, 252–260.

Van Veen, B., 2003. Compaction of Powder Blends Effect of pores, particles and percolation on tablet strength. Thesis.

Verheezen, J.J.A.M., Van Der Voort Maarschalk, K., Faassen, F., Vromans, H., 2004. Milling of agglomerates in an impact mill. International Journal of Pharmaceutics 278, 165–172.

Viggiani, G., 2007. Volumetric Digital Image Correlation Applied to X-ray Microtomography Images from Triaxial Compression Tests on Argillaceous Rock 193–205.

Vlassenbroeck, J., Dierick, M., Masschaele, B., Cnudde, V., Van Hoorebeke, L., Jacobs, P., 2007. Software tools for quantification of X-ray microtomography at the UGCT. Nuclear Instruments and Methods in Physics Research, Section A: Accelerators, Spectrometers, Detectors and Associated Equipment 580, 442–445.

Vogel, L., Peukert, W., 2002. Characterisation of Grinding-Relevant Particle Properties by Inverting a Population Balance Model. Particle & Particle Systems Characterization 19, 149.

Vogel, L., Peukert, W., 2003. Breakage behaviour of different materials - Construction of a mastercurve for the breakage probability. Powder Technology 129, 101–110.

Vogel, L., Peukert, W., 2004. Determination of material properties relevant to grinding by practicable labscale milling tests. International Journal of Mineral Processing 74, 329–338.

Vogel, L., Peukert, W., 2005. From single particle impact behaviour to modelling of impact mills. Chemical Engineering Science 60, 5164–5176.

Von Rittinger, P., 1867. Lehrbuch der Aufbereitungskunde. Berlin.

Walker, Lewis, McAdams, and G., 1937. Principles of chemical engineering. MCGraw-Hill, New York.

Wang, M.H., Yang, R.Y., Yu, A.B., 2012. DEM investigation of energy distribution and particle breakage in tumbling ball mills. Powder Technology 223, 83–91.

Weedon, D.M., 2001. A perfect mixing matrix model for ball mills. Minerals Engineering 14, 1225–1236.

Weerasekara, N.S., Powell, M.S., Cleary, P.W., Tavares, L.M., Evertsson, M., Morrison, R.D., Quist, J., Carvalho, R.M., 2013. The contribution of DEM to the science of comminution. Powder Technology 248, 3–4.

Wittel, F.K., Carmona, H.A., Kun, F., Herrmann, H.J., 2008. Mechanisms in impact fragmentation. International Journal of Fracture 154, 105–117.

Yokoyama, T., Inoue, Y., 2007. Chapter 10 Selection of Fine Grinding Mills. Handbook

of Powder Technology 12, 487–508.

Yoneyama, Satoru; Kitagawa, Akikazu; Kitamura, Koji; Kikuta, H., 2006. In-Plane Displacement Measurement Using Digital Image Correlation with Lens Distortion Correction. JSME International Journal Series A 49, 458–467.

Yoneyama, S., Murasawa, G., 2009. Digital Image Correlation. Experimental Mechanics.

Yuregir, K.R., Ghadiri, M., Clift, R., 1986. Observations on Impact Attrition of Granular Solids. Polymer Engineering & Science 49, 53–57.

Zhang, Z., 1994. Impact attrition of particulate solids. PhD dissertation, University of Surrey.

Zhang, Z., Ghadiri, M., 2002. Impact attrition of particulate solids. Part 2: Experimental work. Chemical Engineering Science 57, 3671–3686.

Zhao, B; Wang, J; Coop, M.R.; Viggiani, G.J.M., 2015. An investigation of single sand particle fracture using X-ray micro-tomography. Géotechnique 65, 625–641.

Zhu, H.P., Zhou, Z.Y., Yang, R.Y., Yu, A.B., 2007. Discrete particle simulation of particulate systems: Theoretical developments. Chemical Engineering Science 62, 3378–3396.

Appendix A

```
#!/usr/bin/python
# Authors:  Edward Ando, Lige Wang, Zeynep Karatza
# Date:     2013-12-02
# Program to shift radiographs from x-ray tomography when we see that
#   there is a significant displacement between the first and last radiographs.
# The displacement between first and last should be measured manually
#  (this could be implemented by DIC of course).
# Input:  A. radiographs (folder and filename)
#         B. Number of radiographs
#         C. y,x displacement in pixels (could consider also correcting zoom...)
#         D. output directory
# Output: A. Shifted radiographs
NUMBER_OF_RADIOS = 1000

# base directory of where your scan is
#RADIOS_BASE_DIR = "/media/TOSHIBA EXT/XR-CT/XR-CT/DIC/Undeformed"
RADIOS_BASE_DIR = "/media/TOSHIBA EXT/XR-CT/XR-CT/DIC/Deformed"

# this shouldn't change, X-Act always writes Acquis
RADIOS_IN_DIR   = "normalised"

# directory for output
RADIOS_OUT_DIR  = "normalised_shifted"

# base name for radios to which "_NNNNN.tif" will be appended
RADIOS_NAME     = "Image"

# Displacement for last image
x_displacement = -5
y_displacement = 14
```

```
#########################################################################
###
## DON'T CHANGE THINGS BELOW THIS LINE                    ##
#########################################################################
###
# 0. Load libraries
import numpy
import Image
import os
import sys
import time
import scipy.ndimage
import tifffile as tiff

# for output when running remotely
sys.stdout = os.fdopen(sys.stdout.fileno(), 'w', 0)

# start the timer...
time_start = time.time()

# this is going to eb a displacement table for displacements fopr each radiograph
#   first column = y, second column = x
displacement_table = numpy.zeros( (NUMBER_OF_RADIOS, 2), dtype=numpy.float )

# fill in the table with displacements, Y FIRST
for i in range( 1, NUMBER_OF_RADIOS ):
    # fill in the y-displacement for this
    displacement_table[ i, 0 ] = ( ( i ) / float( NUMBER_OF_RADIOS-1 ) ) *
float(y_displacement)

    # fill in the x-displacement for this
    displacement_table[ i, 1   ] = ( ( i ) / float( NUMBER_OF_RADIOS-1 ) ) *
float(x_displacement)
```

```
# check existence of output folder. If it doesn exist create it
if not os.path.exists( "%s/%s"%(RADIOS_BASE_DIR,RADIOS_OUT_DIR) ):
os.mkdir( "%s/%s"%(RADIOS_BASE_DIR,RADIOS_OUT_DIR) )

# get dimensions by loading the first image...
firstImage =
Image.open( "%s/%s/%s%i.tif"%(RADIOS_BASE_DIR,RADIOS_IN_DIR,RADIOS
_NAME,1) )
radioDimensions = firstImage.size

# generate coordinates for interpolation
mgrid_temp = numpy.mgrid[ 0:radioDimensions[1], 0:radioDimensions[0] ]

# allocate 2xN array fo coordinates
coordinates = numpy.zeros( (radioDimensions[0]*radioDimensions[1], 2),
dtype=numpy.float )

# y-coordinates
coordinates[ :, 0 ] = mgrid_temp[0].flat

# x-coordinates
coordinates[ :, 1 ] = mgrid_temp[1].flat

# tidy up
del firstImage
del mgrid_temp

# 1. Load radiographs
print "Processing data from %s"%(RADIOS_BASE_DIR)
print "\tand applying a displacement of x=%f and y=%f"%( x_displacement,
y_displacement )

for i in range( NUMBER_OF_RADIOS ):
   print "\r\t\tRadiograph [%04i/%04i]"%(i+1,NUMBER_OF_RADIOS),
```

```
   # Load radiograph directly into numpy -- the Image library, or the TIFF output from Octopus does not work,
   #  U16 is interpreted as I16.
   im_in = tiff.imread(  "%s/%s/%s%i.tif"%(RADIOS_BASE_DIR,RADIOS_IN_DIR,RADIOS_NAME,i+1) )

   # copy coordinates
   displaced_coordinates = coordinates.copy()

   # Apply displacement
   displaced_coordinates[:,0] -= displacement_table[i,0]
   displaced_coordinates[:,1] -= displacement_table[i,1]

   # interpolate image
   im_out = scipy.ndimage.interpolation.map_coordinates( im_in, displaced_coordinates.T, order=1 )

   # Save radiograph
   # converting this filtered radio back to array back to image, need to do a strange hack of making it
   #   a string, Image.fromarray doesn't seem to work...
   im = Image.fromstring('I;16',radioDimensions,im_out.astype('<u2').tostring())

   # write to file.

im.save("%s/%s/%s_%05i.tif"%(RADIOS_BASE_DIR,RADIOS_OUT_DIR,RADIOS_NAME,i+1))

# print out how long this took.
time_end = time.time()
print "\n\nDone. I think I ran for: ", time_end - time_start, " Seconds\n"
```

Appendix B

```
clear all;
ima_name=dir('*.tif');
pixel2mum=0.00434; %%%%% 1 pixel  = 24 mu m
delta_z=0.0476; %%%%% separation between images in mu_m
Nima=length(ima_name); %%%% number of images
Amin=10; %%% Minimum are of the object
pos_pos=[]; %%%% matrix to store the position of the surface
curva=zeros(Nima,3); %%%% matrix for curvature of each slice

for cont_ima=1:Nima;
   ima1=imread(ima_name(cont_ima).name);
   ima2=edge(ima1);
   etiq=bwlabel(ima2);
   objprops=regionprops(etiq,'PixelList','Area','Centroid');
   pos_surf_ima=[];
   for cont2=1:max(etiq(:));
      if objprops(cont2).Area > Amin;
        pos_surf_ima=[pos_surf_ima;              pixel2mum.*objprops(cont2).PixelList
delta_z.*(cont_ima-1).*ones(size(objprops(cont2).PixelList,1),1)];
      end
   end
   pos_pos=[pos_pos; pos_surf_ima];
%
abs(gradient(gradient(pos_surf_ima(:,1:2))))/(1+gradient(pos_surf_ima(:,1:2)).^2).^1.
5;
%   gradient(gradient(pos_surf_ima(:,1:2)))/(1+gradient(pos_surf_ima(:,1:2)).^2).^1.5;
%   curva(cont_ima,1)=cont_ima;
%   curva(cont_ima,2)=k;
%   curva(cont_ima,3)=kk;
   clear pos_surf_ima;
end
data=pos_pos;
```

```
results3=[];

%test_values=1.4:0.1:2.3;
%for k=1.4:0.1:2.3;
for i=1:1:20
sp=i;
results=[];
results1=[];
results2=[];
k=1.4;
for i=0:0.0476:1.428
%ind=data(:,3)==i & data(:,2)>test_values(1,k);
ind=data(:,3)==i & data(:,2)>k;
f61=pos_pos(ind,1);
f62=pos_pos(ind,2);
f63=pos_pos(ind,3);
f71=f61(1:sp:end);
f72=f62(1:sp:end);
f73=f63(1:sp:end);
No=length(f61);
results=[results;f61 f62 f63];
results1=[results1;f71 f72 f73];
results2=[results2;No];
end
results;
results1;
results2;
Fitting_points=length(results1);
xdata=results1(:,1);
ydata=results1(:,3);
zdata=results1(:,2);
%% Fit: 'untitled fit 1'.
[xData, yData, zData] = prepareSurfaceData( xdata, ydata, zdata );
% Set up fittype and options.
```

```
ft = fittype( 'poly33' );
opts = fitoptions( ft );
opts.Lower = [-Inf -Inf -Inf -Inf -Inf -Inf -Inf -Inf -Inf -Inf];
opts.Upper = [Inf Inf Inf Inf Inf Inf Inf Inf Inf Inf];

% Fit model to data.
[fitresult, gof] = fit( [xData, yData], zData, ft, opts );
rsquare=vpa(gof.rsquare,4);

syms x y z
digits(5)
A=[1; x; y; x^2; x*y; y^2; x^3; x^2*y; x*y^2; y^3];
B=[fitresult.p00 fitresult.p10 fitresult.p01 fitresult.p20 fitresult.p11
  fitresult.p02 fitresult.p30 fitresult.p21 fitresult.p12 fitresult.p03 ];
f1=B*A;
f=f1-z;
Fx=diff(f,x,1);
Fy=diff(f,y,1);
Fz=diff(f,z,1);
Fxx=diff(Fx,x,1);
Fxy=diff(Fx,y,1);
Fxz=diff(Fx,z,1);
Fyx=diff(Fy,x,1);
Fyy=diff(Fy,y,1);
Fyz=diff(Fy,z,1);
Fzx=diff(Fz,x,1);
Fzy=diff(Fz,y,1);
Fzz=diff(Fz,z,1);
x=2.7689; y=0.714;
par_gra=[Fx Fy Fz];
H=[Fxx Fxy Fxz;Fyx Fyy Fyz;Fzx Fzy Fzz];
hes_matrix=vpa(hessian(f));
d1=eval(Fx);
d2=eval(Fy);
```

```
d3=eval(Fz);
d11=eval(Fxx);d12=eval(Fxy);d13=eval(Fxz);
d21=eval(Fyx);d22=eval(Fyy);d23=eval(Fyz);
d31=eval(Fzx);d32=eval(Fzy);d33=eval(Fyz);
d=[d1 d2 d3];
dh=[d11 d12 d13;d21 d22 d23;d31 d32 d33];
[n,m]=size(dh);
   A=zeros(n,m);
   for i=1:n
      for j=1:m
         dhij=H;
         dhij(i,:)=[];
         dhij(:,j)=[];
         df(i,j)=(-1)^(i+j)*det(dhij);
      end
   end
digits(5);
T=trace(dh);
abs_par=sqrt(sum(d1.^2+d2.^2+d3.^2));
KG=vpa((d*df*(d)')/((abs_par)^4));
KM=((d*hes_matrix*(d)')-((abs_par)^2)*T)/(2*(abs_par)^3);
k1=vpa(eval(KM+sqrt(KM^2-KG)))
R1=1/k1;
k2=vpa(eval(KM-sqrt(KM^2-KG)))
R2=1/k2;
E=0.338*6*0.91*((2*1.35*(k1+k2)^(1/3))^(3/2))/(0.02^(3/2));
E1=0.338*6*0.91*((1.35*(k1+k2)^(1/3)+1.351*1.74^(1/3))^(3/2))/(0.02^(3/2));
results3=[results3; Fitting_points k1 k2 E E1 rsquare]
%end
end
plot(results3(:,1), results3(:,4),'-o','LineWidth',2,...
   'Marker','diamond')
xlabel('Fitting points No.','FontSize',28,'FontName','Abyssinica SIL');
ylabel('Young''s Modulus (MPa)','FontSize',28,'FontName','Abyssinica SIL');
```

Appendix B

Table B1 Value of K for various values of θ (Adapted from ASAE, 1998)

θ	50	55	60	65	70	75	80	85	90
$cos\theta$	0.6428	0.5736	0.5000	0.4226	0.3420	0.2588	0.1736	0.0872	0.0
K	1.198	1.235	1.267	1.293	1.314	1.331	1.342	1.349	1.351

Appendix C

1. Dataset 2 plotting and fitting by equivalent normal velocity

1.1 Data source of chipping-PS1 Particles (Papadopoulos 1998)

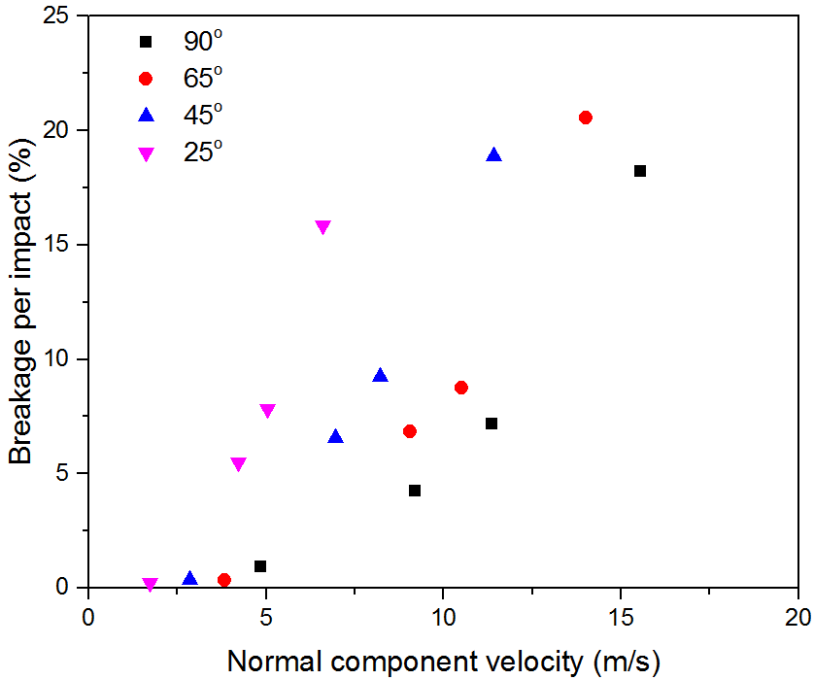

Figure C1 Breakage ratio of the PS1 particles as a function of the normal component velocity

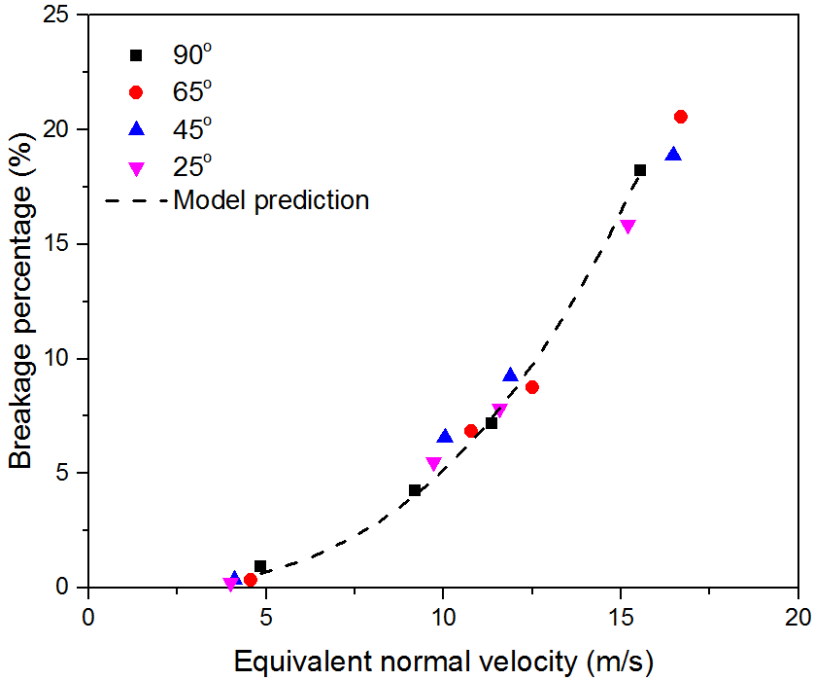

Figure C2 Model prediction (Wang 2016) vs. breakage data of PS1 particles

1.2 Data source of chipping-PS3 Particles (Papadopoulos 1998)

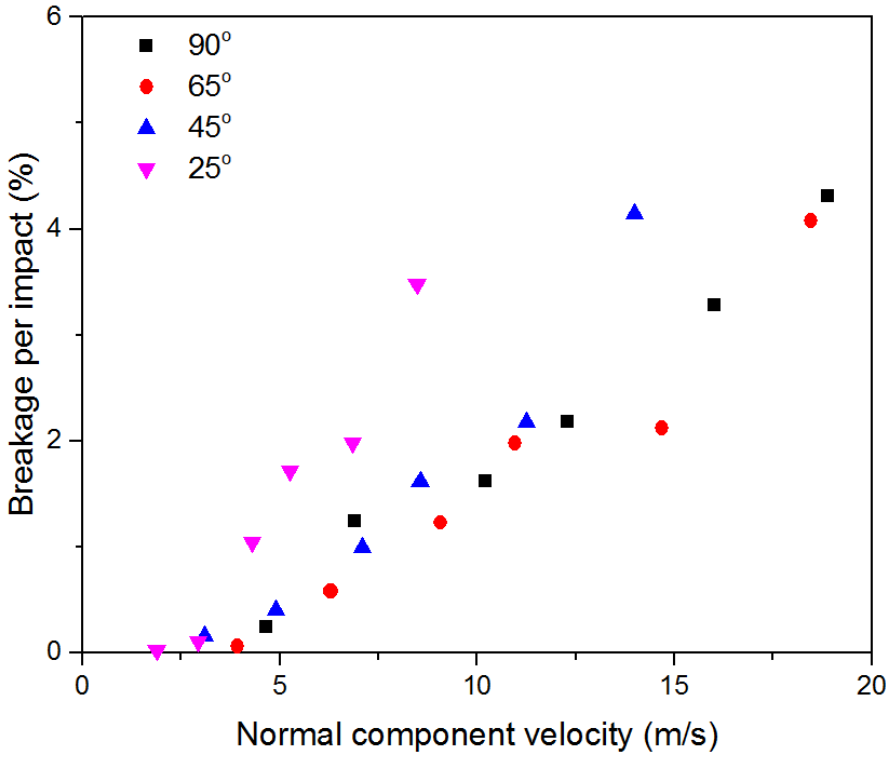

Figure C3 Breakage ratio of the PS3 particles as a function of the normal component velocity

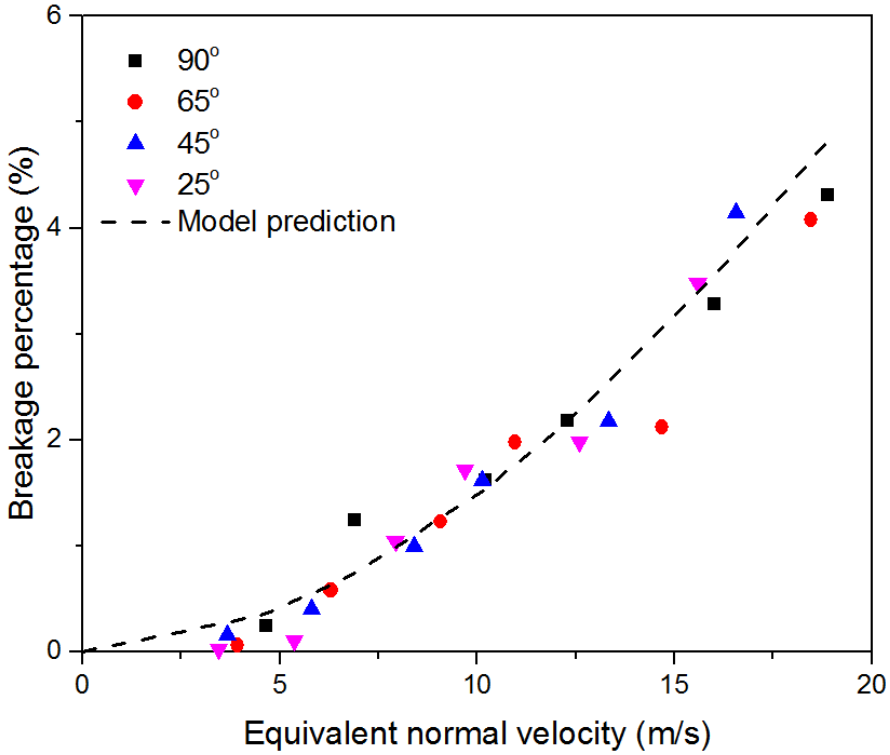

Figure C4 Model prediction (Wang 2016) vs. breakage data of PS3 particles

2. Dataset 3 plotting and fitting by equivalent normal velocity

2.1 Data source of D3.2mm Particles (Salman et al., 2003)

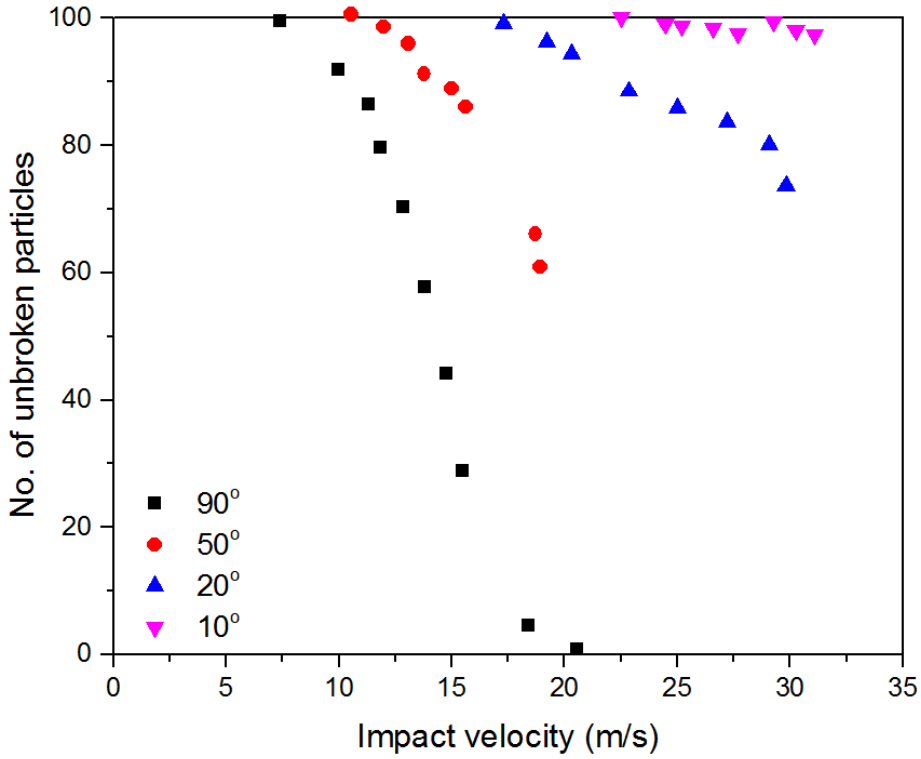

Figure C5 Breakage data collection

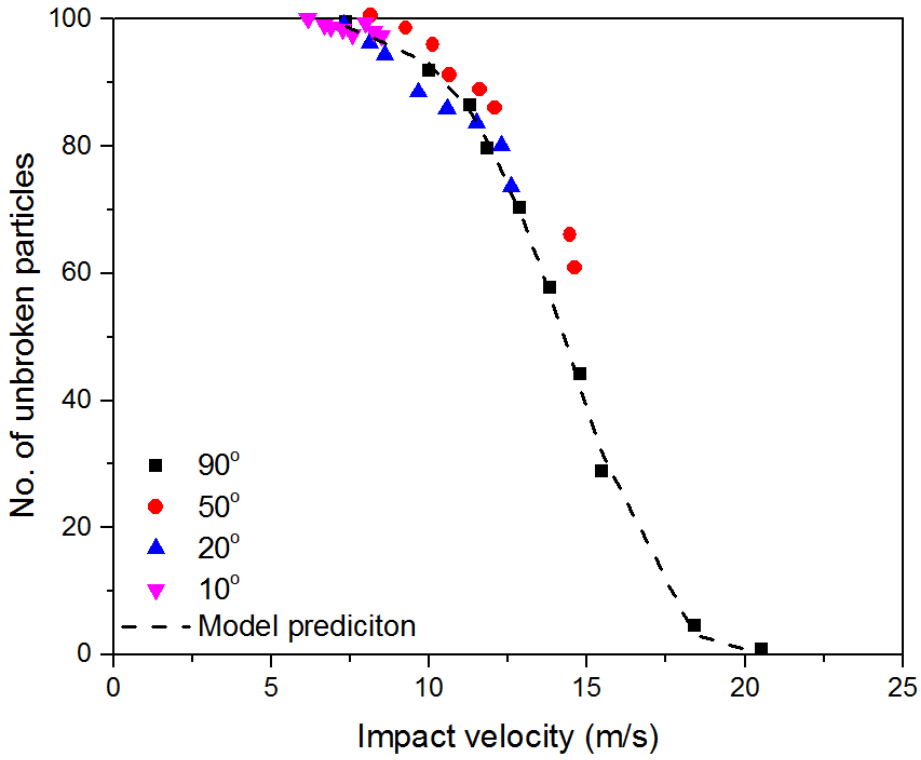

Figure C6 Model prediction (Wang 2016) vs. breakage data collection

2.2 Data source of D5.3mm Particles (Salman et al., 2003)

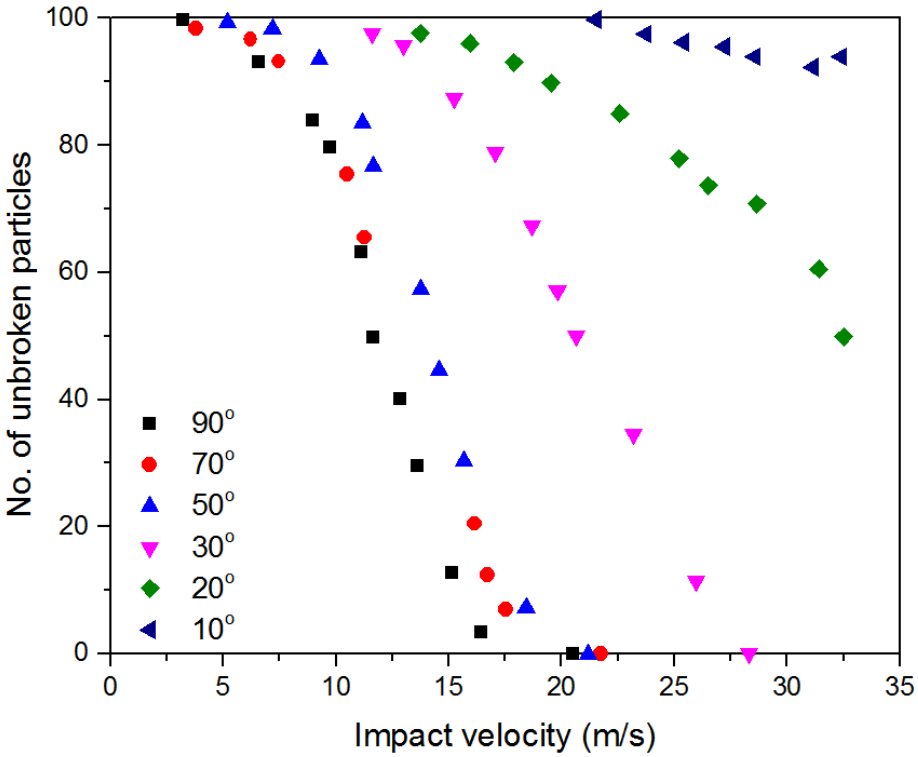

Figure C7 Breakage data collection

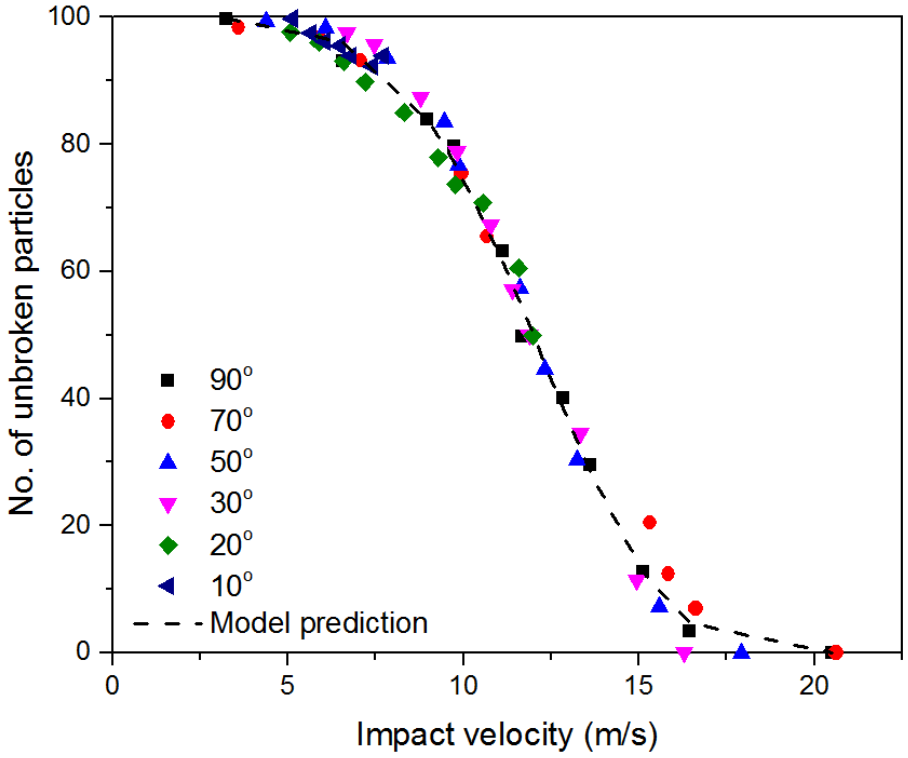

Figure C8 Model prediction (Wang 2016) vs. breakage data collection

2.3 Data source of D7.2mm Particles (Salman et al., 2003)

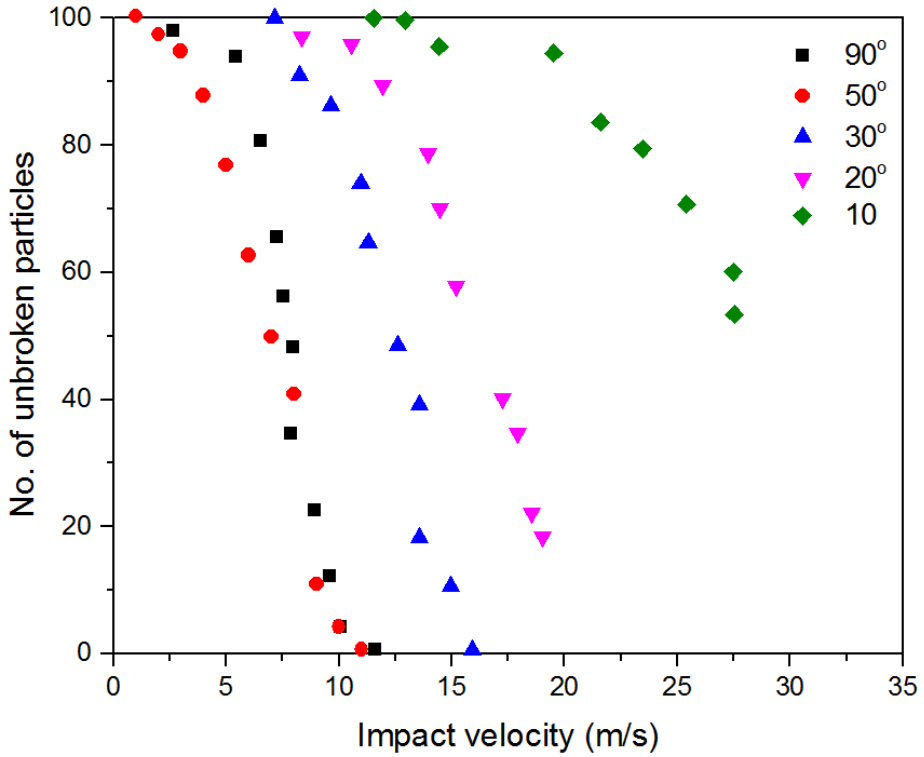

Figure C9 Breakage data collection

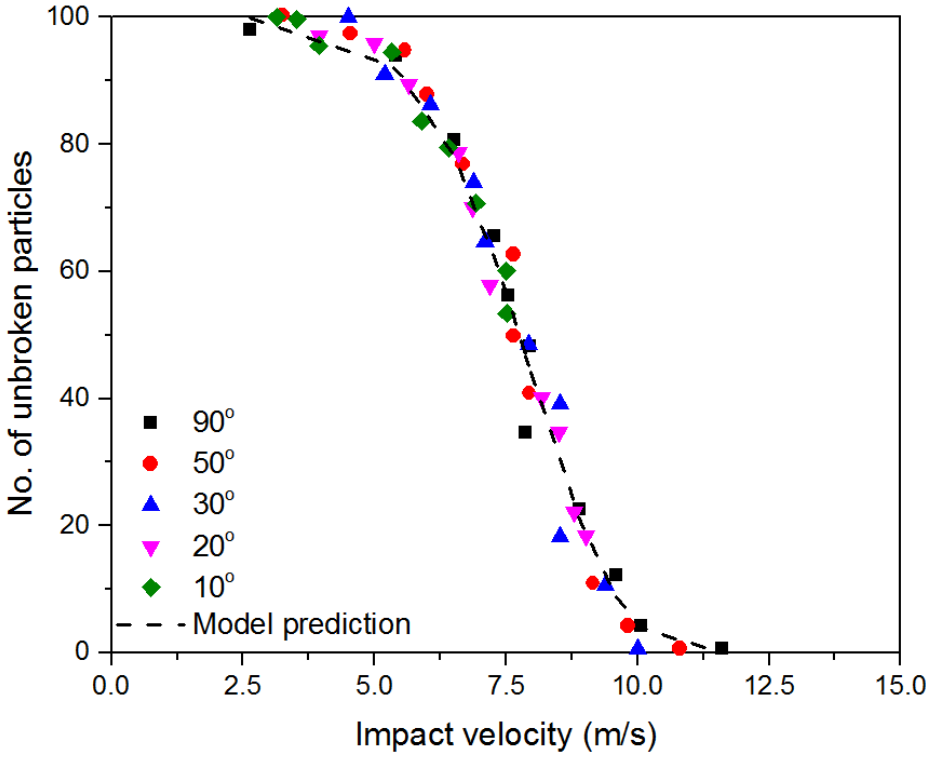

Figure C10 Model prediction (Wang 2016) vs. breakage data collection

Appendix C

Table C1 Value of two fitting parameters in the equivalent normal velocity

Data source	**Particle type and size (mm)**	**Impact angle (°)**	**α**	**μ**	$\alpha * \mu$	**Breakage type**
Wang, 2016	Zeolite, 1.4-1.7	90	x	x	x	Chipping
		60	5.0	0.2	1.0	
		45	5.0	0.2	1.0	
		30	5.0	0.2	1.0	
Papadopoulos, 1998	Porous silica 1 (PS1), 3.35-4.0	90	x	x	x	Chipping
		65	5.30	0.2	1.1	

		45	6.80	0.2	1.4
		25	11.42	0.2	2.3
	Porous silica 2 (PS2), 1.0-1.18	90	x	x	x
		65	5.20	0.2	1.0
		45	5.99	0.2	1.2
		25	10.24	0.2	2.0
Papadopoulos, 1998	Porous silica 3 (PS3), 2.0-2.36	90	x	x	x

		65	3.20	0.2	0.6
		45	4.50	0.2	0.9
		25	8.52	0.2	1.7
Salman et al. 1995	Alumina, 5.15	90	x	x	x	Fragmentation
		80	4.97	0.2	1.0	
		70	4.97	0.2	1.0	
		60	4.97	0.2	1.0	

		50	6.20	0.2	1.2	
		40	6.56	0.2	1.3	
		35	5.82	0.2	1.2	
		30	5.16	0.2	1.0	
		20	3.65	0.2	0.7	
Salman et al. 2003	Fertiliser, 3.2	90	x	x	x	Fragmentation
		50	1.00	0.2	0.2	

		20	3.86	0.2	0.8	
		10	6.16	0.2	1.2	
Salman et al. 2003	Fertiliser, 5.3	90	x	x	x	Fragmentation
		70	2.00	0.2	0.4	
		50	3.64	0.2	0.7	
		30	3.29	0.2	0.7	
		20	2.13	0.2	0.4	

		10	4.76	0.2	1.0	
Salman et al. 2003	Fertiliser, 7.2	90	x	x	x	Fragmentation
		50	4.47	0.2	0.9	
		30	4.40	0.2	0.9	
		20	5.10	0.2	1.0	
		10	6.16	0.2	1.0	

Appendix D

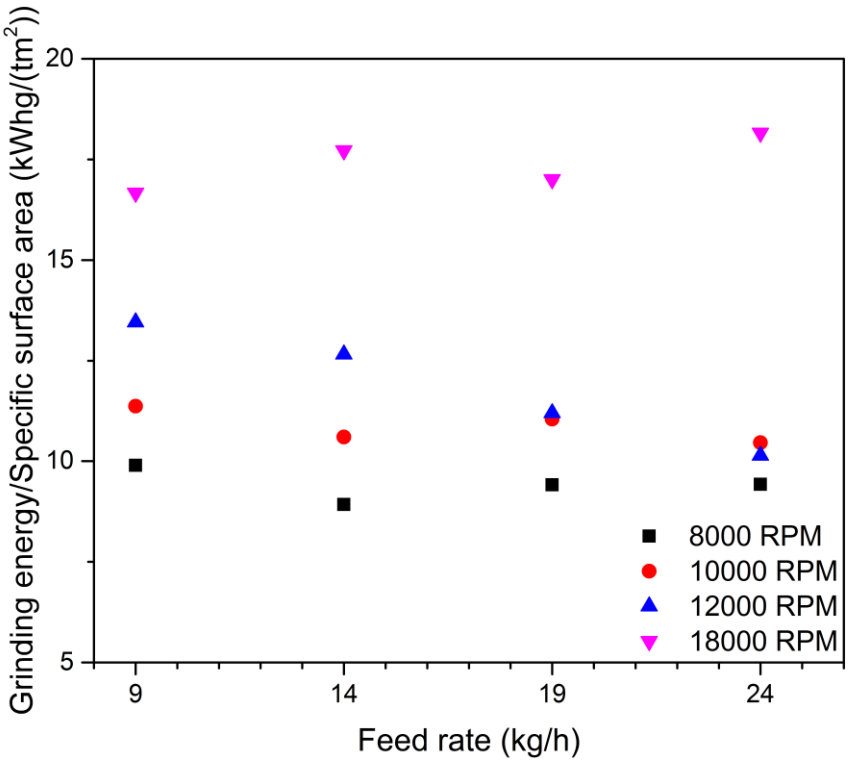

Figure D1 Grinding energy/Specific surface area vs feed rate for zeolite (1.2-2.0 mm)

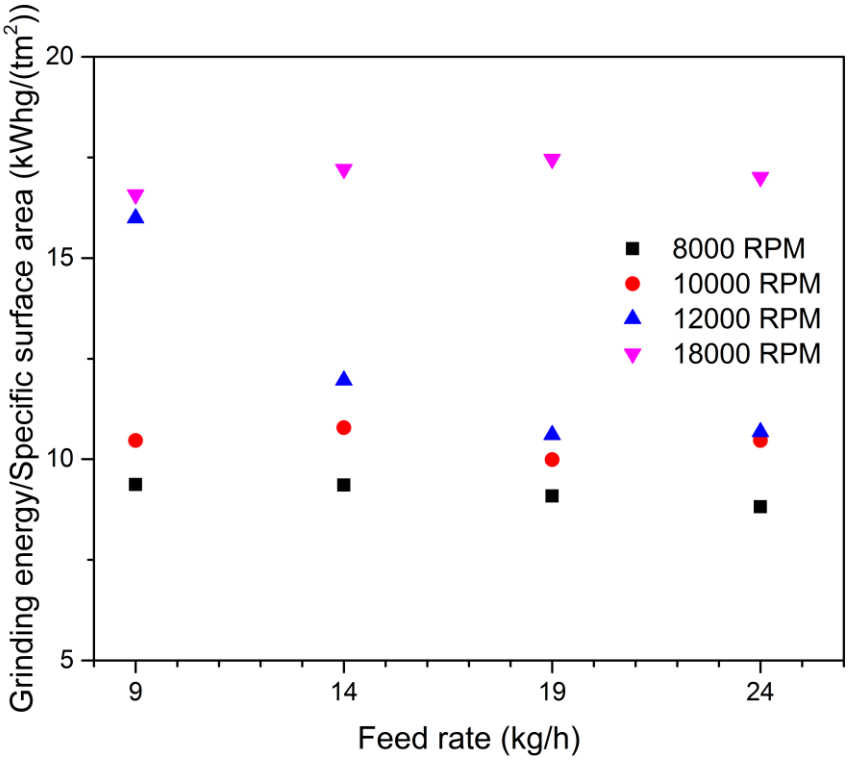

Figure D2 Grinding energy/Specific surface area vs feed rate for zeolite (2.0-2.5 mm)

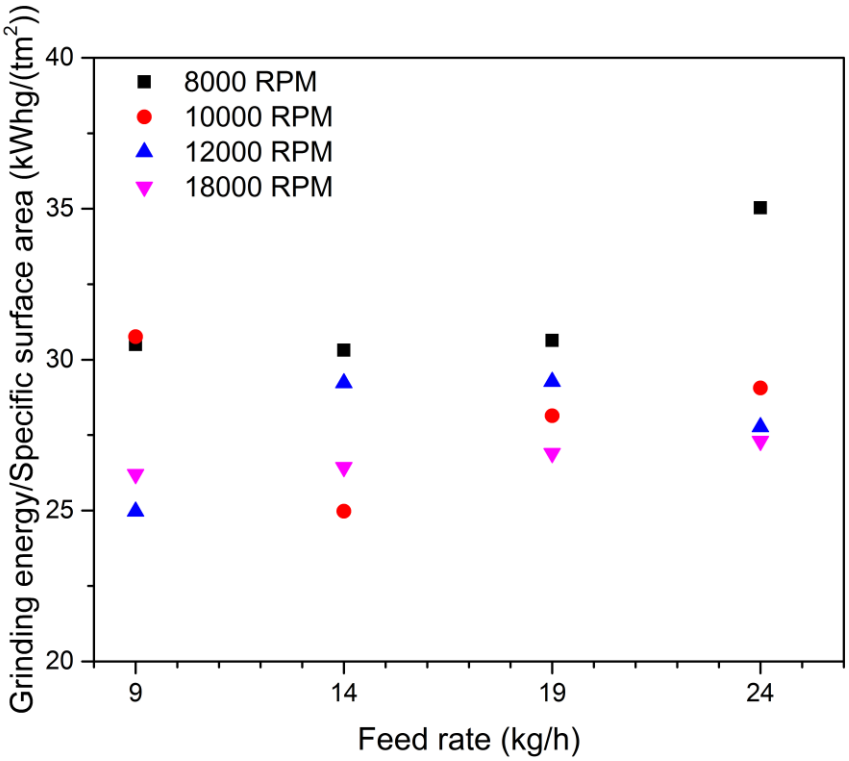

Figure D3 Grinding energy/Specific surface area vs feed rate for alumina (1.0-1.18 mm)